NASA/CR—1999-209303

PSU CGTP 9901

Numerical Simulation of Complex Turbomachinery Flows

A.A. Chernobrovkin and B. Lakshminarayana
The Pennsylvania State University, University Park, Pennsylvania

July 1999

The NASA STI Program Office . . . in Profile

Since its founding, NASA has been dedicated to the advancement of aeronautics and space science. The NASA Scientific and Technical Information (STI) Program Office plays a key part in helping NASA maintain this important role.

The NASA STI Program Office is operated by Langley Research Center, the Lead Center for NASA's scientific and technical information. The NASA STI Program Office provides access to the NASA STI Database, the largest collection of aeronautical and space science STI in the world. The Program Office is also NASA's institutional mechanism for disseminating the results of its research and development activities. These results are published by NASA in the NASA STI Report Series, which includes the following report types:

- TECHNICAL PUBLICATION. Reports of completed research or a major significant phase of research that present the results of NASA programs and include extensive data or theoretical analysis. Includes compilations of significant scientific and technical data and information deemed to be of continuing reference value. NASA's counterpart of peer-reviewed formal professional papers but has less stringent limitations on manuscript length and extent of graphic presentations.
- TECHNICAL MEMORANDUM. Scientific and technical findings that are preliminary or of specialized interest, e.g., quick release reports, working papers, and bibliographies that contain minimal annotation. Does not contain extensive analysis.
- CONTRACTOR REPORT. Scientific and technical findings by NASA-sponsored contractors and grantees.
- CONFERENCE PUBLICATION. Collected papers from scientific and technical conferences, symposia, seminars, or other meetings sponsored or cosponsored by NASA.
- SPECIAL PUBLICATION. Scientific, technical, or historical information from NASA programs, projects, and missions, often concerned with subjects having substantial public interest.
- TECHNICAL TRANSLATION. English-language translations of foreign scientific and technical material pertinent to NASA's mission.

Specialized services that complement the STI Program Office's diverse offerings include creating custom thesauri, building customized data bases, organizing and publishing research results . . . even providing videos.

For more information about the NASA STI Program Office, see the following:

- Access the NASA STI Program Home Page at ***http://www.sti.nasa.gov***
- E-mail your question via the Internet to help@sti.nasa.gov
- Fax your question to the NASA Access Help Desk at (301) 621-0134
- Telephone the NASA Access Help Desk at (301) 621-0390
- Write to:
  NASA Access Help Desk
  NASA Center for AeroSpace Information
  7121 Standard Drive
  Hanover, MD 21076

NASA/CR—1999-209303

PSU CGTP 9901

Numerical Simulation of Complex Turbomachinery Flows

A.A. Chernobrovkin and B. Lakshminarayana
The Pennsylvania State University, University Park, Pennsylvania

Prepared under Grants NAG3–1736 and NAG3–2025

National Aeronautics and
Space Administration

Glenn Research Center

July 1999

Acknowledgments

The research was sponsored by the NASA Grants NAG3–1736, with Robert Boyle as the technical monitor, and NAG3–2025, with Dr. David Ashpis as the technical monitor. Additional support was obtained through a grant from Pratt & Whitney, a division of United Technologies Corporation, West Palm Beach, Florida, with Mr. Martin Tabbita as the technical monitor. We wish to acknowledge NASA Ames, NASA Glenn, Pittsburgh NSF Supercomputer Center, and San Diego NSF Supercomputing Center for providing supercomputer resources.

Trade names or manufacturers' names are used in this report for identification only. This usage does not constitute an official endorsement, either expressed or implied, by the National Aeronautics and Space Administration.

Available from

NASA Center for Aerospace Information
7121 Standard Drive
Hanover, MD 21076
Price Code: A14

National Technical Information Service
5285 Port Royal Road
Springfield, VA 22100
Price Code: A14

ABSTRACT

Wider acceptance of CFD methods in the design and the analysis require development of CFD techniques that should satisfy two main criteria; provide results within a reasonable time frame and with apriori known accuracy. Major efforts have been spent in recent years to establish the accuracy of numerical solvers. However more research is required to develop reliable and robust numerical solvers suitable for modeling of complex turbomachinery flows.

An unsteady viscous flow solver based on the Runge-Kutta scheme has been developed. Pseudo–time step technique has been incorporated to provide efficient simulation of unsteady flows. Utilization of the pseudo-time approach reduces the computational time by a factor varying from 5 to 25 times in comparison with the original solver. The results of the stability analysis of the dual time step scheme are used to establish an optimum pseudo-time step based on the local CFL, VonNeuman numbers and the ratio of pseudo-to-physical time steps. Code has been modified to incorporate multi-block capabilities. This modification is essential for the modeling of complex multidomain configurations such as the rotor-stator interaction, film cooling. etc. Multoblock feature simplifies the complexity of the grid generation process. It also improves the quality of the grid, thus contributing to the enhanced accuracy of the numerical modeling.

The code has been validated against the analytical and experimental data. The influence of the numerical aspects (artificial dissipation, grid density etc.) on the accuracy of the prediction of the wake decay, transition, flow over a cylinder has been analyzed. Based on the results of the test cases, modifications to the k-ε model to improve the accuracy in the regions with dominant normal stresses are incorporated.

Numerical simulation of the unsteady flow in a compressor cascade has been performed to assess the ability of the code to simulate unsteady flow in a turbomachinery cascade. Three low Re k-ε turbulence models have been assessed for their ability to predict the unsteady transitional flows. Good agreement with the measured data and with an earlier Euler/boundary layer prediction has been achieved. The numerical solver was able to predict major features, associated with the wake induced transition on a compressor blade (wake induced transitional strip, wake induced turbulent strip, etc.). Analysis and interpretation of the results from the unsteady flow simulation have been carried out to understand additional flow physics associated with the transitional flow.

A coupled experimental and computational study of the effects of the nozzle wake-rotor interaction in a turbine is carried out to understand the cause and effects of the unsteady flow in turbine rotors. The result of the numerical prediction correlates well with the Laser Doppler Velocimeter data and dynamic pressure measurements. An assessment of the viscous and the inviscid contribution to the nozzle wake decay and the unsteady loss distribution in the rotor passage reveals the dominant effect of the viscous decay upstream of the leading edge. Inside the passage, the inviscid effects have a significant influence. The predicted flow at the off-design condition has been interpreted to understand the nature of the unsteady flow field at a high negative incidence angle.

Variation of the flow Reynolds number between the take off and cruise conditions significantly affects the boundary layer development on a low-pressure turbine blading. A decreased Reynolds number leads to flow separation on the suction surface of the blading, thus increasing losses. A numerical simulation has been carried out to assess the ability of the Navier-Stokes solver to predict transitional flows in a wide range of Reynolds numbers and inlet turbulence intensities. A number of turbulence (including the Algebraic Reynolds Stress Model) and transition models have been employed to analyze the reliability and accuracy of the numerical simulation. A comparison between the prediction and the experimental data reveals a good correlation. However, the analysis shows that the artificial dissipation in the numerical solver may have a profound effect on the transition in a separated flow.

The viscous flow solver has been employed for the numerical investigation of the aerothermal field due to the leading edge film cooling at a compound angle. Good agreement with the measured data has been achieved. Results of the numerical investigation have been used to analyze the vortex structure associated with the coolant jet-freestream interaction to understand the effect of different vortices on the cooling effectiveness and aerothermal losses. Two counter-rotating vortices generated by the interaction between the mainflow and the coolant jet have been found to have a major influence in decreasing the cooling efficiency through strong entrainment of the hot fluid. Results of the numerical simulation indicate that the turbulence length scale has a significant effect on the accuracy of the numerical prediction of the film cooling. Not only the inlet turbulence intensity but also the turbulence length scale should be accurately prescribed to achieve reliable numerical prediction of the heat and the mass transfer due to the film cooling.

Numerical analysis of the tip leakage flow in a turbine is utilized to investigate physics of the secondary flow in a rotor including interaction between secondary vortices, tip leakage vortex, and rotor wake. Analysis of the leakage flow development shows that the relative motion of the blade and the casing wall reduces the propagation of the leakage flow into the mainflow. The tip leakage vortex is confined to the suction surface corner of the casing. Most of the leakage losses is due to the mixing of the tip leakage vortex downstream of the trailing edge.

TABLE OF CONTENTS

LIST OF FIGURES ix

LIST OF TABLES xvi

NOMENCLATURE xvii

ACKNOWLEDGMENTS xxv

Chapter 1 INTRODUCTION 1

- 1.1 Significance 1
  - 1.1.1 Unsteady Flow 3
  - 1.1.2 Transition to turbulence 7
  - 1.1.3 Film Cooling 12
  - 1.1.4 Three dimensional flow in turbine including tip leakage effect 14
- 1.2 Objectives and thesis organization. 16
- 1.3 Contribution of the thesis 18
- 1.4 Thesis organization 20

Chapter 2 GOVERNING EQUATION AND NUMERICAL PROCEDURE 25

- 2.1 Governing equations and numerical procedure 25
  - 2.1.1 Turbulence closure 27
  - 2.1.2 Two-equation models 28
  - 2.1.3 Algebraic Reynolds Stress Model 30
- 2.2 Development of the multiblock solver 32
  - 2.2.1 Structure of the multiblock solver 33
- 2.3 Pseudo-time Acceleration 37
  - 2.3.1 Stability analysis of the scheme with pseudo time acceleration 40
  - 2.3.2 Artificial dissipation term adjustment for the solver with pseudo-time stepping 44

Chapter 3 CODE VALIDATION AND MODIFICATION 51

- 3.1 Verification against analytical solution 51
- 3.2 Influence of the artificial dissipation on the wake propagation and decay 54

3.3 Steady turbulent and transitional boundary layer 56
3.4 Modification of the k-ε model for the flows with dominant normal stresses.. 58
    3.4.1 Modification of the turbulence model for leading edge flow 59
    3.4.2 Turbulence flow field in the freestream 63

Chapter 4 NUMERICAL SIMULATION OF THE UNSTEADY TRANSITIONAL FLOW IN A COMPRESSOR CASCADE 70

4.1 Compressor cascade description 70
4.2 Sensitivity studies 72
4.3 Unsteady pressure field.. 75
4.4 Development of the unsteady transitional flow.. 76
4.5 Stator wake... 81

Chapter 5 UNSTEADY FLOW IN TURBINE.. 93

5.1 Experimental Program... 94
    5.1.1 Laser Doppler Velocimeter Data 97
    5.1.2 Dynamic Pressure Measurements.. 99
5.2 Numerical Procedure... 101
5.3 Sensitivity Studies 102
5.4 Time-Averaged Flow Field... 103
5.5 Unsteady Pressure Field on the Blade Surface (Design) 105
5.6 Unsteady Pressures at Off-Design Conditions... 109
5.7 Unsteady Flow Field Due to Rotor-Stator Interaction................................ 111
5.8 Discussion of Unsteady Flow Physics 112
5.9 Nozzle Wake Decay Through the Rotor Passage.. 116
5.10 Loss Generation Due To Unsteady Flow 122
5.11 Unsteady Transitional Flow on the Suction Surface 125
5.12 Rotor Wake Development... 132
5.13 Off-Design Flow... 133
5.14 Effect of Inlet Turbulence.. 135

Chapter 6 NUMERICAL SIMULATION OF THE TRANSITION OVER LAMINAR SEPARATION BUBBLE 160

6.1 Description of the Test Case.. 161
6.2 Numerical Procedure.. 162
6.3 PREDICTION USING k-ε MODEL... 165
    6.3.1 Case Re=200000, Tu=10%.. 165
    6.3.2 Case Re=50000, Tu=10% 167
    6.3.3 Case Re=50000, Tu=2.5% 169
6.4 Prediction Using Hybrid ARSM/K-ε Model... 171
6.5 Prediction Using k-ε Model in Conjunction with the Transition Model......... 172

6.6 Effect of Artificial Dissipation on the Transition Prediction 178
6.7 Concluding remarks 181

Chapter 7 NUMERICAL SIMULATION OF LEADING EDGE FILM COOLING 190

7.1 Flat Plate Film Cooling 191
7.2 Leading edge cooling at compound angle 192
    7.2.1 Numerical modeling 193
    7.2.2 Comparison with the experiment 196
    7.2.3 Discussion of aerothermal flow physics 198
    7.2.4 Mach number effect 203
    7.2.5 Influence of the high inlet turbulence 204
    7.2.6 Influence of the inlet turbulence length scale. 206
7.3 Concluding remarks. 208

CHAPTER 8 THREE DIMENSIONAL FLOW IN TURBINE ROTOR 228

8.1 Computational details 228
8.2 Comparison with the experimental data 229
8.3 Vortex field development 235
8.4 Secondary and leakage flow losses 239
8.5 Influence of the tip clearance height on the tip leakage vortex development 242

Chapter 9 SUMMARY 267

9.1 Summary 267
9.2 Conclusions 269
    9.2.1 Unsteady transitional flow in compressor cascade 270
    9.2.2 Rotor-stator interaction in turbine stage 272
    9.2.3 Transition to turbulence over laminar separation bubble in LP turbine 274
    9.2.4 Leading edge film cooling 276
    9.2.5 Secondary flow in turbine including tip leakage flow 278
9.3 Recommendations for the future work 280

Appendix A LINEARIZED SOLUTION OF THE WAVE PROPAGATION 282

BIBLIOGRAPHY 285

LIST OF FIGURES

Fig. 1-1 Research program 24

Fig. 2-1 Block scheme of the multiblock solver 46

Fig. 2-2 Allowable multiblock topology (in computational space) 46

Fig. 2-3 Stability limits and amplification factor distribution for scheme 1a 47

Fig. 2-4 Stability limits and amplification factor distribution for scheme 2a 48

Fig. 2-5 Stability limits and amplification factor distribution for scheme 1 49

Fig. 2-6 Stability limits and amplification factor distribution for scheme 2 49

Fig. 2-7 Stability limits and amplification factor distribution for scheme 3 50

Fig. 2-8 Stability limits and amplification factor distribution for scheme 4 50

Fig. 3-1 Total velocity distribution along the stagnation streamline, inviscid simulation, "H" type gird 65

Fig. 3-2 Computational error 65

Fig. 3-3 Wake decay due to artificial dissipation 66

Fig. 3-4 Flat plate wake decay 66

Fig. 3-5 Steady transition on a flat plate 67

Fig. 3-6 Steady transition on a flat plate, correlation from Abu-Ghannam and Shaw (1980) 67

Fig. 3-7 Effect of the artificial dissipation on the skin friction coefficient on a rotor blade 68

Fig. 3-8 Turbulence intensity at midpitch inside the rotor blade passage 68

Fig. 3-9 Turbulence intensity at midpitch inside the rotor passage (FLUENT) 69

Fig. 3-10 Predicted distribution of the normal Reynolds stresses along midpassgae streamline (FLUENT) 69

Fig. 4-1 Scheme of the experiment 84

Fig. 4-2 Computational grid 84

Fig. 4-3 Influence of number of inner iterations on the amplitude of unsteady pressure 85

Fig. 4-4 Influence of number of inner iterations on the amplitude of skin friction coefficient 85

Fig. 4-5 Influence of the physical time step on the amplitude of unsteady pressure 86

Fig. 4-6 Blade pressure distribution 86

Fig. 4-7 Unsteady pressure distribution, suction surface 87

Fig. 4-8 Skin friction coefficient 88

Fig. 4-9 Shape factor 89

Fig. 4-10 Velocity profile 90

Fig. 4-11 Momentum thickness, suction surface 91

Fig. 4-12 Amplitude of the total velocity in the stator wake 91

Fig. 4-13 Unsteady turbulent kinetic energy in the stator wake 92

Fig. 4-14 Blade to blade distribution of the total velocity $x/C_x=1.29$ 92

Fig. 5-1 LDV and Kulite measurement locations in rotor passage (velocity triangle is based on design) 136

Fig. 5-2 Variation of rotor inlet static and stagnation pressure coefficients, velocity and turbulence quantities at $x/c_x = -0.244$, design conditions (case A).... 136

Fig. 5-3 Decomposition of the revolution periodic data into blade periodic (average passage) and blade aperiodic 137

Fig. 5-4 Averaged blade pressure and unsteady pressure envelope at design conditions, ... 137

Fig. 5-5 Averaged blade pressure coefficient on the rotor blade midspan at off design 138

Fig. 5-6 Blade-to-blade distribution of relative velocity 139

Fig. 5-7 Measured and predicted time history of unsteady pressures on the suction surface (design condition) 140

Fig. 5-8 Measured space-time distribution of blade unsteady pressure, case A (design) 141

Fig. 5-9 Measured and predicted harmonics of blade unsteady pressure suction surface 141

Fig. 5-10 Measured space-time surface pressure distribution at midspan, case C 142

Fig. 5-11 Measured and predicted time history of unsteady pressure, case C (off design) 143

Fig. 5-12 Maximum variation of surface unsteady pressure, cases A-D 144

Fig. 5-13 Nozzle wake defect at the nozzle-LDV position N1 145

Fig. 5-14 Unresolved unsteadiness at nozzle-LDV position N4 146

Fig. 5-15 Wake defect decay 147

Fig. 5-16 Unsteady velocity field in the rotor passage 148

Fig. 5-17 Unsteady pressure field inside the rotor passage 149

Fig. 5-18 Transport of the nozzle wake turbulence in the rotor passage 150

Fig. 5-19 Normalized unsteady relative total pressure coefficient 151

Fig. 5-20 Unsteady velocity and pressure field with different inlet B.C 152

Fig. 5-21 Measured and predicted time history of the surface pressure with different inlet B.C 153

Fig. 5-22 Unsteady pressure coefficient, suction surface 154

Fig. 5-23 Wake decay balance 155

Fig. 5-24 Mass average loss coefficient 155

Fig. 5-25 Maximum turbulence kinetic energy in the boundary layer, suction surface 156

Fig. 5-26 Unsteady skin friction coefficient, suction surface 156

Fig. 5-27 Rotor wake decay as a function of streamwise 157

Fig. 5-28 Space-time distribution of the total velocity at x/C_x=132% 157

Fig. 5-29 Unsteady pressure and velocity fields, case C 158

Fig. 5-30 Variation of the maximum blade unsteady pressure at different inlet turbulence levels 159

Fig. 5-31 Variation of the maximum wake defect at different inlet turbulence levels.. 159

Fig. 6-1 Schematic of the experiment 182

Fig. 6-2 Surface pressure distribution 183

Fig. 6-3 Transition in attached boundary layer 184

Fig. 6-4 Transition over a laminar separation bubble 184

Fig. 6-5 Velocity and turbulence intensity, Tu=10%, Re=200000 185

Fig. 6-6 Velocity and turbulence intensity, Tu=10%, Re=50000 185

Fig. 6-7 Velocity and turbulence intensity, Tu=2.5%, Re=50000 186

Fig. 6-8 Velocity and turbulence intensity, Tu=2.5%, Re=50000, prediction based on hybrid ARSM/k-ε approach 186

Fig. 6-9 Velocity and turbulence intensity, Tu=10%, Re=50000, effect of the transition model utilization a) 1d model Var1, b) 1d model Var2, c) "step" model, d) 2d model Var1, e) 2d model Var2 187

Fig. 6-10 Turbulent kinetic energy balance, Tu=10%, Re=50000 188

Fig. 6-11 Effect of artificial dissipation on predicted location of transition and separation inception, , Tu=10%, Re=50000 188

Fig. 6-12 Influence of the artificial dissipation; Tu=10%, Re=50000 189

Fig. 6-13 Influence of the artificial dissipation, Tu=10%, Re=50000 189

Fig. 7-1 Flat plate film cooling, grid 209

Fig. 7-2 Adiabatic effectiveness along the jet centerline 209

Fig. 7-3 Schematic of the test case 210

Fig. 7-4 Grid structure and boundary conditions 211

Fig. 7-5 Surface adiabatic effectiveness, Tu=0.5% 212

Fig. 7-6 Lateral distribution of adiabatic effectiveness, Tu=0.5% a) s/d=1.24; b) s/d= 4.86; c)s/d=9.88 213

Fig. 7-7 Laterally averaged adiabatic effectiveness, Tu=0.5% 214

Fig. 7-8 Normalized temperature at s/d=9.88 214

Fig. 7-9 Vortex structure due to the upper hole jet-mainstream interaction, a) 215

Fig. 7-10 Vortex structure due to the upper hole jet-mainstream interaction, b) 216

Fig. 7-11 Vortex structure due to the upper hole jet-mainstream interaction, c) 217

Fig. 7-12 Vortex structure due to the upper hole jet-mainstream interaction, d) 218

Fig. 7-13 a) Streamwise vorticity; b) normalized total pressure; c) normalized temperature at s/d=9.88 219

Fig. 7-14 a) Streamwise vorticity; b) normalized total pressure; c) normalized temperature at s/d=6 219

Fig. 7-15 a) Streamwise vorticity; b) normalized total pressure; c) normalized temperature at s/d=4.2 219

Fig. 7-16 Surface pressure distribution, Tu=0.5% 220

Fig. 7-17 Velocity distribution , Tu=0.5%, contours represent distribution of normalized temperature, h 221

Fig. 7-18 Velocity distribution , Tu=0.5%, contours represent distribution of normalized temperature, h 222

Fig. 7-19 Laterally averaged adiabatic effectiveness, influence of the Mach number .. 223

Fig. 7-20 Surface pressure distribution at z/d=5 223

Fig. 7-21 Laterally averaged adiabatic effectiveness, influence of high turbulence intensity 223

Fig. 7-22 Streamwise vorticity at s/d=8.4, a) Tu=0.5%, b) Tu=10, μ_t/μ_l=30, c) Tu=10%, μ_t/μ_l=120 224

Fig. 7-23 Normalized temperature at s/d=8.4 a) Tu=0.5%, b) Tu=10%, μ_t/μ_l=30, c) Tu=10%, μ_t/μ_l=120 224

Fig. 7-24 Surface adiabatic effectiveness 225

Fig. 7-25 Streamlines from the bottom hole, Tu=0.5%; 226

Fig. 7-26 Streamlines from the bottom hole, Tu=10% 226

Fig. 7-27 Laterally averaged adiabatic effectiveness, influence of the length scale 227

Fig. 8-1 Penn State rotor, computational grid 244

Fig. 8-2 Pressure distribution, pressure surface 245

Fig. 8-3 Pressure distribution , suction surface 246

Fig. 8-4 Normalized axial velocity field at x/C_x=1.10 247

Fig. 8-5 Normalized axial vorticity at x/C_x=1.10 248

Fig. 8-6 Normalized axial velocity at x/C_x=50% 249

Fig. 8-7 Normalized axial vorticity at x/C_x=50% 249

Fig. 8-8 Normalized axial velocity at x/C_x=80% 250

Fig. 8-9 Normalized axial vorticity at x/C_x=80% 250

Fig. 8-10 Streamline vorticity ($\omega_s/2\omega$), crossflow planes are located at x/C_x=60%, x/C_x=80%, and x/C_x=110% respectively, streamlines are initiated 5% of the chord upstream of the leading in hub and casing boundary layers 251

Fig. 8-11 Streamline vorticity ($\omega_s/2\omega$), crossflow planes are located at x/C_x=60%, x/C_x=80%, and x/C_x=110%, streamlines are initiated inside tip gap at 20% and 55% of the cord 252

Fig. 8-12 Massflow through the tip gap a) case with τ_c=0.61%. b) case with τ_c=0.75%. c) case with τ_c=1.1% 253

Fig. 8-13 Velocity field at Z_g=0.75 254

Fig. 8-14 Velocity field at Z_g=0.33 255

Fig. 8-15 Velocity field at Z_g=-10 256

Fig. 8-16a Secondary velocity (calculated as velocity vector consisting of normal to the 2d design streamlines component and radial component), background contours - streamline velocity 257

Fig. 8-17 Normalized streamline vorticity ($\omega_s/2\omega$), crossflow planes are located at x/C_x=60%, x/C_x=80%, and x/C_x=110%, streamlines are initiated at the location of the tip vortex inception and represent mean flow fluid particles 260

Fig. 8-18 Normalized streamline vorticity ($\omega_s/2\omega$), crossflow planes are located at x/C_x=60%, x/C_x=80%, and x/C_x=110%, streamlines are initiated inside tip gap at 70% and 90% of the chord 261

Fig. 8-19 Loss coefficient 1) case with τ_c=1.1%. 2) case with τ_c=0.75%. 3) Two-dimensional simulation 262

Fig. 8-20 Loss coefficient, ζ 263

Fig. 8-21 Loss coefficient, ζ, no tip clearance 264

Fig. 8-22 a)-d) Flowfield at x/C_x=110%, influence of tip clearance height a) Normalized vorticity, 0.61% clearance a) Normalized vorticity, 1.1% clearance, c) Normalized axial velocity, 0.61% clearance, d) Normalized axial velocity, 1.1% clearance 265

LIST OF TABLES

Table 2-1 Low-Reynolds-number functions used in turbulence model 28

Table 2-2 Low-Reynolds-number functions used in turbulence models 29

Table 4-1 Compressor cascade characteristics 71

Table 5-1 Operating Conditions 96

Table 5-2 Zone boundaries 118

Table 5-3 Wake decay, zone 4 and 5 122

Table 6-1 Location of the experimental data points on the suction blade surface 162

Table 6-2 Inception and length of the transition, separation and reattachment points, Re=200000, Tu=10%. 165

Table 6-3 Inception and length of the transition, separation and reattachment points, Re=50000, Tu=10%. 168

Table 6-4 Inception and length of the transition, separation and reattachment points, Re=50000, Tu=2.5%. 170

Table 7-1 Flow conditions 193

Table 7-2 Boundary conditions 194

NOMENCLATURE

A	Wake amplitude, $A=(U-U_c)/U$
Amp[]	Amplitude of the first harmonic
C	Chord
c_μ, $c_{\varepsilon 1}$, $c_{\varepsilon 2}$	Constants in low Re turbulence models
C_f	Skin friction coefficient, $\tau_w / (\rho_1 \overline{W_1}^2)$
CFL, λ	Courant-Fredrich-Levy number
C_p	Pressure coefficient, $C_p = (p - \overline{p}_{refl}) / (\rho_1 \overline{W}_{ref}^2 / 2)$, reference velocity is inlet total absolute velocity for the stator or inlet total relative velocity for the rotor
c_μ	Constant in k-ε model
c_p	Specific heat at constant pressure
C_p'	Pressure coefficient, $C_p' = (p - \overline{p}_2) / (\rho_1 \overline{W}_{x1}^2 / 2)$
C_p''	Pressure coefficient, $C_p'' = (\overline{p}_{01} - p) / (\overline{p}_{01} - p_2)$
C_{pI}	i-th harmonic of C_p,
C_{po}	Total pressure coefficient, $C_{p0} = (P_0 - \overline{P}_{01}) / (\rho_1 \overline{W}_1^2 / 2)$
C_x	Axial chord length
d	Injection hole diameter
$D=\rho_j/\rho_o$	Density ratio

e	Internal energy per unit mass
e''	Fluctuation component of internal energy
f_μ	Near wall function in k-ε model
$\tilde{g}_{k_1k_2}$	Average amplification factor, $\tilde{g}_{k_1k_2} = \int_{k_1}^{k_2} \frac{g(k)dk}{(k_2 - k_1)}$
G, g	Amplification factor
H	Shape factor
h and η	Normalized temperature and adiabatic efficiency, $(T_0-T)/(T_0-T_c)$
H_b	Normalized distance in spanwise direction, $H_b=(r-r_{hub})/(r_{tip}-r_{hub})$
h_b	Blade height (Chapter 8)
i	Incidence angle
k	Turbulent kinetic energy, wave number
k_{2ke}	Coefficient of the second-order artificial dissipation, turbulence equations
k_4	Coefficient of the 4th order artificial dissipation
l	Injection hole length
M	Blowing ratio $M=\rho_jU_j/\rho_oU_o$
Ma	Mach number
m_l	Leakage mass flow rate
m_t	Total mass flow rate
n	Number of grid points per wave length
p	Static pressure
P	Turbulent kinetic energy production

P^*, P_0	Total pressure
Ph[]	Phase of the first harmonic
P_{ij}	Production rate of Reynolds stress
Pr	Prandtl number
PS	Pressure surface
Q	Vector of conservative variables
q	heat flux
r	distance n radial direction
R	Residual, Radius of cylinder
$\overline{\overline{R}}$, R_{ij}	Rotation rate tensor
Re	Reynolds number, based on chord and outlet velocity
Re_θ, Re_x	Reynolds number, based on θ , x and local velocity
Re_1	Reynolds number based on chord and inlet velocity
Re_d	Reynolds number, based on hole diameter
Re_t	Turbulent Re number, $k^2 / \nu\varepsilon$
Re_y	Turbulent Re number, $\sqrt{k}\, y/\nu$
S	Rotor blade spacing
s	Surface length from the leading edge
$\hat{S}^k$	Numerical discretization of the physical time derivatives at k stage of the Runge-Kutta scheme
$\overline{\overline{S}}$, S_{ij}	Strain rate tensor
S_l	Local passage width (rotor)

S_n	Vane spacing
SS	Suction surface
T^*	Total temperature
T	Period, Temperature
t	Physical time
T_u	Turbulence intensity, $\sqrt{(k*2/3)}/W_{inl}$
Tu_r	Unresolved unsteadiness
Tu_t	Turbulence intensity based on local total relative velocity
U	Total velocity
u''	Fluctuation component of velocity
u'	Total fluctuating velocity (RMS value)
u',v',w'	x, y, and z components of fluctuating velocity
u_τ	Friction velocity, $\sqrt{\tau_w}/\rho$
U_i	i-component of velocity
U_m	Rotational velocity at midspan
V,U	Absolute total velocity
	y-component of velocity
v	y-component of velocity
V_{ow}	Wave, wake velocity in y-direction
W	Total relative velocity
x	Axial length measured from leading edge

x_c	Chordwise distance measured from leading edge
y	Distance in normal to surface
y	Distance in pitchwise direction
y'	Direction normal to x (Chapter 7)
y^+	Inner variable, $u_\tau y/\nu$
Z_g	Normalized gap distance, $Z_g=(r-r_{tip})/(r_{cas}-r_{tip})$

Greek

α	Absolute flow angle
α''_k, α'_k	Coefficient of Runge-Kutta scheme with pseudo-time stepping
α_k	Coefficient of Runge-Kutta scheme
β	Relative flow angle
Δ	Difference between maximum and minimum values during the period
δ	$\delta=\Delta\tau/\Delta t$
ΔCp	$Cp-Cp_{aver}$
δ_{ij}	Kronecker delta
ΔV	Wake defect
ε	Turbulence dissipation rate
ε_{ijk}	Alternating tensor
γ	Intermittency
μ, μ_l	Molecular viscosity

μ_t	Eddy viscosity coefficient
ν	Kinematic viscosity
θ	Momentum thickness
ζ	Loss coefficient, $\varsigma = (\overline{P}_{01} - P_0)/(\rho_1 \overline{W}_{ref}^{\,2}/2)$
ξ	Normalized total pressure, $(P^*-P^*_0)/(\rho_0 U^2_0)$
ρ	Density
$\sigma_k,\sigma_\varepsilon$	Turbulent Prandtl numbers
σ	VonNeuman number
δ_{xxxx}	Fourth order spatial operator
τ	Pseudo time, stress
τ_w	Wall shear stress
Ω	Reduced frequency, $\Omega=\varpi C_x/U_x$
ϖ	Wake passing frequency
ω	Vorticity, wake width parameter, rotation vector
ω_s	Projection of normalized vorticity, $\omega d/U_0$ on streamwise direction

Subscript

δ,e	At edge of the boundary layer
0,inl	Total, inlet, free stream
1	Rotor inlet
2	Outlet

ARSM	Based on Algebraic Reynolds Stress Model
aver	Time average
c	Values at the wake center line, Coolant, Projection on chord
cas	Casing
dis	Viscous dissipation
inv	Inviscid
j	Jet
hub	Hub
k-ε	Based on k-ε model
loc	Local
max	Maximum outside rotor wake
pot	Pressure gust effect
ref	Reference value
s	Separation inception Projection on s direction
str	Inviscid stretching
t	Turbulent
t_e	Trailing edge
tip	Blade tip
tr	Transition inception
vis	Viscous

w	Quantity at the wall
x	Axial
y	Projection on y direction
z	Projection on z direction
Superscript	
~	Ensemble average
′	Unresolved unsteadiness
*	Total
–	Time average, Laterally average

ACKNOWLEDGMENTS

The research was sponsored by the NASA Grants NAG 3-1736, with Dr. Robert Boyle as the technical monitor, and NAG 3-2025, with Dr. David Ashpis as the technical monitor. Additional support was obtained through a grant from Pratt & Whitney, a division of United Technologies Corporation, West Palm Beach, Florida, with Mr. Martin Tabbita as the technical monitor. We wish to acknowledge NASA Ames, NASA Lewis, Pittsburgh NSF Supercomputer Center, and San Diego NSF Supercomputing Center for providing supercomputer resources.

Chapter 1

INTRODUCTION

1.1 Significance

Significant research efforts and design advances have led to thermal efficiency of up to 60% in modern gas turbines. The modern compressor stage has efficiency of about 90% and the modern turbine stage has efficiency of up to 95%. Further improvements in efficiency become more and more difficult and require a much deeper understanding of the flow field inside turbomachines.

Three methods have been widely used in the analysis and design of modern turbomachinery; experimental research, analysis in conjunction with empirical data base, and numerical methods. The development of the accurate numerical methods and computer hardware have made the numerical simulation more efficient, reliable and affordable. However, questions of affordability and reliability of the numerical simulation are the key factors in the future development of the numerical analysis for the turbomachinery design and analysis.

Wider acceptance of CFD methods in the design and the analysis requires CFD techniques that should satisfy two main criteria; provide results within reasonable time frame and with apriori knowledge of accuracy. Ideally, engineer need to have a technique (i.e. implementation of correct physical models etc.) and solution with a fixed level of precision. Despite complexity of the process, it is possible to establish reliability of the numerical technique. Reliability and suitability of the mathematical model, including such aspects as the turbulence model, as well as mutual influence of the model and the numerical technique can not be verified for a general case. Major efforts have been spent in recent years to establish the accuracy of numerical models utilizing the benchmark data. These attempts had only limited success. Further development of the CFD requires more systematic approach to the assessment of the numerical accuracy. Melnik et al., 1995, suggested three major steps in assessing the capability of the CFD code; code verification, validation and certification. Code verification against known analytical solutions, reveals numerical accuracy of the numerical technique used. The second step is the code validation. This step is critical in assessing the ability of the code to provide an accurate solution for the benchmark test cases in a relatively narrow range of flow features. Last step is the code certification, which includes predictive capabilities of the code for complex and realistic cases. This step includes a systematic simulation of flow cases and a comparison with the existing experimental data.

Flows in turbomachinery blade rows are very complex. They are strongly three-dimensional, viscous, with several types of secondary flows and vortices (horseshoe vortex, passage vortex, leakage flow, etc.). Their interaction with the blade, boundary layers and wakes results in mixing losses. Transitional flows and the high turbulence intensity result in additional complexities. Because of the complex nature of the flow, analytical methods are scarce and not accurate. Results of experimental investigations are limited to a narrow range of flow parameters in modeled turbomachines.

One of the major features of the flow in the blade passage is the unsteadiness caused by the relative motion of the stator and rotor. While the unsteadiness plays an important role in the flow through turbomachinery blade rows, majority of flow simulations are carried out assuming a steady flow approximation. The inlet flow pattern is prescribed as uniform and steady. This approach leads to the neglection of such phenomena as a rotor/stator interaction, vortex shedding and other unsteady flow effects. The unsteadiness has a major influence on the surface pressure distribution and shear stresses at the wall. The unsteady dynamic and thermal loading can reduce the life of the blades. To ensure reliable operation, the natural frequency of the blade should be different from the frequency of the vibration caused by the flow unsteadiness. The main sources of the unsteadiness are; potential effect, wake-blade interaction, vortex-blade interaction random unsteadiness of the mean flow.

Another problem which is closely connected to the unsteady nature of the flow in turbomachines is the heat transfer. Prediction of the heat transfer and film cooling effect is crucial to an understanding of the turbine flow field. Excessive blade temperature may lead to a thermal fatigue. Accurate analysis of this phenomenon is essential for good design.

1.1.1 Unsteady Flow

Unsteady interaction increases losses, blade vibration, and noise generation; and affects heat transfer in turbines. An understanding of the physics of the unsteady flow will enable an improvement in the overall aerodynamic and mechanical performance of the turbine. Increases in the available computer resources and the development of more efficient computational algorithms in recent years have made the numerical simulation of unsteady flows more affordable.

There are three main approaches to unsteady calculations in the blade passage. The utilization of the linearized Euler equation is the earliest and the least numerically intensive approach. The simulation based on the full Euler equation or the coupled Euler/boundary layer approximation, is used in the second approach. The last approach is the numerical simulation using Reynolds averaged Navier-Stokes equations with an adequate turbulence model.

The linearized inviscid theory is based on the approximation that the perturbations of the mean flow are small and hence, these parameters are presented through Taylor series neglecting higher order terms. The more complex approach is the modeling of the flow using non-linear Euler equations. In this method, full Euler equation is used and only the inviscid approximation is invoked. This approach was used in Giles (1988), He (1989), Dorney and Verdon (1994), Fan and Lakshminarayana (1994). Giles (1988) analyzed the flow using the Lax-Vendroff scheme with non-reflecting boundary condition. He (1989) used a multi-step Runge-Kutta scheme to simulate two dimensional flow over an oscillating blade. A moving grid zone was implemented near the blade surface to treat blade oscillations. One of the approaches which combines the advantages of both the Euler and the boundary layer method is due to Fan and Lakshminarayana (1994). Fan and Lakshminarayana (1994) used a multi-step Runge-Kutta scheme with non-reflecting boundary conditions. The results of the inviscid solution were used as an input for unsteady boundary layer calculations. Numerical results showed a good agreement with the experimental data.

The last and the most complex approach is the Navier-Stokes simulation. Codes based on this approach were used by Rai (1987), Dorney and Davis (1991), Ho and Lakshminarayana (1993), Fourmaux (1994), Arnone et al. (1994), One of the earliest works in this field is the simulation done by Rai (1987). He used a thin layer approximation of the Navier-Stokes equations and a third order upwind difference scheme. An O-type overlaid grid was used. Ho and Lakshminarayana (1993) developed an unsteady Navier-Stokes solver based on a pressure correction method. Code was validated for the grid sensitivity and artificial dissipation. Numerical simulation of the rotor-stator interaction showed good correlation with experimental results. Fourmaux (1994) implemented four-step Runge-Kutta numerical scheme with combined H-O type grid. Arnone et al. (1994) also applied the explicit four-step Runge-Kutta scheme where, for economy, the viscous terms were evaluated only on the first stage.

A number of additional problems must be solved when the numerical modeling is based on unsteady Navier-Stokes equations. Unsteady numerical simulation results in a significant increase in required CPU time. Wave dissipation and dispersion characteristics of the steady state numerical scheme are not suitable for unsteady flow simulations. Problems associated with efficiency and accuracy of unsteady simulations can be overcome through the utilization of dual-step approach. The utilization of the inner cycle to relax a time step limitation of the explicit schemes (e.g. Arnone, 1994), or to remove the linearization error in the implicit scheme (Rai, 1987) was found to be essential for unsteady simulations.

The choice of physically realistic turbulence model suitable for the unsteady calculation is a difficult one. Most of the turbulence models have been developed for the steady flow. Special attention needs to be paid to the ability of the model to resolve time scales associated with the flow unsteadiness. Many authors used simple models which had been validated only for steady flows, such as the 2 layer Baldwin-Lomax turbulence model (Arnone et. al. (1994) and Dorney et al. (1994)). Partially, this may be attributed to the additional stability and convergence problems caused by the incorporation of more complex turbulence models in unsteady computations. Turbulence models, as well as their improvements for unsteady flows, need to be more carefully investigated. Fan, Lakshminarayana, and Barnett (1993) modified two-equation k-ε model for a application in the unsteady flow and showed good agreement with the experimental data for the flat plate and cascade unsteady flows.

Even though many attempts have been made to develop and use unsteady Navier-Stokes solvers, none have been satisfactory validated against accuracy, especially in respect to the unsteady viscous layer near blade and wall surfaces. This is one of the major objectives of this thesis.

1.1.2 Transition to turbulence

One of the challenging problems in turbomachinery is to understand the flow physics due to transitional flows associated with the laminar separation and the rotor-stator interaction in low pressure turbines. The rotor-stator interaction flow is inherently unsteady and transitional. Additional complexities arise due to these transitional boundary layers along the blade surfaces. Such complex unsteady and transitional boundary layer flow is known to affect the aerodynamic and thermal performance of a turbomachine (Simon and Ashpis, 1996). The transition from the laminar to turbulent flow on the blade surface is a common, yet complex, phenomenon in turbomachinery. The boundary layer development, losses, efficiency, and heat transfer are greatly affected by the transition. The ability to accurately predict the onset and length of the transition is very important in the design of efficient machines.

There are three types of transition. The first is called the "natural" transition, where the laminar boundary layer develops the Tollmein-Schlichting wave, followed by an amplification of instabilities and finally the fully turbulent flow. Natural transition usually occurs with small freestream disturbances. The second type of transition is caused by large external flow disturbances. It is called the "bypass" mode because there is no Tollmein-Schlichting instability. The third type is called the "separated-flow" transition, which happens within the laminar boundary layer separation and may or may not involve the T-S wave. In turbine flows, the freestream turbulence level is usually high. Transition in these flows is of the bypass mode most of the time. Natural transition is almost non-existent in practical flows. Separated flow transition is also common in low pressure turbines.

The periodic passing of upstream wakes can also lead to transition patches on the downstream blade surface. This modification of the transition process is called the "wake-induced" transition. When the upstream wake impinges on the downstream blade surface, within a laminar boundary layer, transition occurs because of the sudden and large disturbance caused by the wake and the high turbulence level inside the wake. Periodic turbulence and transition patches may develop and transport downstream at the certain fraction of the period while laminar regions exist at the rest of the period.

High performance and durability of turbines can be realized through an improved understanding of the physics associated with the transition and rotor-stator interaction phenomena. Considerable attention has been paid in recent years in developing computer codes to predict unsteady aerodynamics and heat transfer, but these efforts are hampered by a lack of understanding of the basic physics associated with these interactions and the lack of adequate physical modeling (transition/turbulence models), and validation of the codes. The ultimate solution of this problem has to come from a systematic, scientific, and building block approach. The measurement in an actual engine is not only complicated, but will rarely provide an insight into numerous sources of unsteadiness and mechanisms. Likewise, a computational code with the artificial dissipation and the numerical error may mask some of the important physics. The code has to be validated at several stages to ensure that the flow physics is captured accurately. The past computational effort was mainly concerned with the large code development for the steady and the unsteady viscous flow in turbomachines using simple algebraic eddy viscosity models. Even the steady flow prediction with higher order turbulence models is not satisfactory due to inadequacy of physical models employed. The models do not adequately account for effects of rotation, curvature, heat transfer, compressibility, three-dimensional strain field, flow separation, and the unsteady flow. These codes are among the most sophisticated and comprehensive available for turbomachinery flows. There is a need to assess these numerical techniques and improve the computational efficiency.

Mayle (1991) reviewed the transition phenomena in gas turbines. From a theoretical perspective, first transition is viewed as a sudden jump from the laminar to the turbulent flow. Laminar flow is separated from the turbulent flow by a single line or section. Through the modification to the boundary layer properties, two zones are patched together. This is the approach most numerical methods adopt (Launder and Spalding, 1974; Schmidt and Patankar, 1991).

Experimental results show that that the transition is not an abrupt process. Emmons (1951) is the first to propose that the transition is a three-dimensional and unsteady process, which has a region where laminar and turbulent flows co-exist. At a certain point in space, the flow could be laminar at sometime and turbulent at other times. This is the "intermittency" phenomenon. Most of the earlier theoretical investigations were concerned with the intermittency factor. Narasimha (1957) modified the Emmons theory through the hypothesis of concentrated breakdown and showed good agreement between his model and the intermittency measured by Schubauer and Klebanoff (1955). Dhawan and Narasimha (1958) developed a model for the intermittancy based on a Guassian distribution. This model can only be used in combination with analysis/computational techniques to predict onset location and transition length. Mayle and Paxson (1991) later proposed a new theory that accounts for the extra terms due to the interaction between non-turbulent and turbulent flows in molecular and heat flux stresses. Models based on the experimental data are used to derive onset and transition. These models are formulated to account for the effects of turbulence intensity (Gostelow and Blunden, 1989; Abu-Ghannam and Shaw, 1980), pressure gradient (Gostelow and Walker, 1991), and other factors like curvature and surface roughness.

Computations of transitional flows can be classified into four groups. The simplest one is a linear combination model. Transitional flow is divided into turbulent and laminar parts according to the intermittency parameter. Predictions using the model by Dhawan and Narasimha (1958) give an excellent agreement for two-dimensional flows without pressure gradient. But the extension to more complex flow situations has not been successful. The second method is incorporated in the framework of algebraic turbulence models. The total viscosity is assumed to be the sum of the molecular viscosity and the product of the intermittency and the eddy viscosity. The third group employs the one- or two-equation turbulence models, and will be discussed in the next paragraph. The fourth method uses the direct numerical simulation of three-dimensional unsteady flows. No models are needed in this case.

Computation of the flow field including the transition by two-equation turbulence models is a popular approach (Jones and Launder, 1972; Schmidt and Patankar, 1991; Fan and Lakshminarayana, 1996). The low-Reynolds-number form of two-equation models are capable of capturing the transition inception location to a certain accuracy. Schmidt and Patankar (1991) examine the effects of inlet locations, inlet profile of the turbulence kinetic energy and the dissipation rate, and the freestream turbulence intensity on the transition using low-Reynolds-number two-equation models by Jones and Launder (1972), and Lam and Bremhost (1981). Through the modification of the turbulence production term and the introduction of two parameters to their model, onset and end of transition on a flat plate are accurately predicted. Fan and Lakshminarayana (1996) proposed a new model which modifies near wall functions and obtaine improved wake-induced transitions.

There has been very limited computational effort to resolve the flow physics and provide an accurate prediction of the unsteady viscous layers in turbines. Fan and Lakshminarayana (1996) used an Euler-boundary layer approach and modified the turbulence models to predict unsteady transitional viscous layers in compressors and turbines for which detailed data is available (Schulz et al., 1990 and Halstead et al., 1995). No attempts have been made to assess the capability of the Navier-Stokes code to predict these unsteady transitional viscous layers due to the wake-blade interaction. The effect of the grid sensitivity, the time step, and an artificial dissipation have to be assessed along with the capability of existing turbulence models to capture unsteady flow physics and the transitional boundary layer. The Euler boundary layer procedure developed by Fan and

Lakshminarayana (1996) is very efficient due to the parabolic nature of viscous layers. But, this procedure is restricted to thin unseparated viscous layers, and its accuracy depends on the accuracy of the Euler solution. The Navier-Stokes code, on the other hand, is more general and does not depend on inviscid/viscid uncoupled procedure. But its disadvantage is in large CPU time due to large number of grids (typically $y^+=u_\tau y/\nu=1$) required for the computation of the amplitude and phase angle of various flow properties inside the viscous layers.

1.1.3 Film Cooling

The theoretical limit of the efficiency of a thermal power plant is governed by the Carnot cycle. The temperature of the heat sink is usually equal to or higher than the ambient temperature, thus the only way to improve the thermal efficiency is to increase the temperature of the heat source. An increase in the inlet turbine temperature is one of the most efficient means of advancing efficiency and weight characteristics of turbines. In gas turbines, the relation between the inlet turbine temperature and turbine efficiency is complex, and includes the compressor pressure ratio and bypass ratio as well as other parameters.

Combustion of modern gas turbine fuels can provide stochastic temperature in excess of 2200 K, while modern materials cannot stand temperatures higher than 1200 - 1400K. If the cycle temperature exceeds these values, blades should be cooled. The most common techniques for cooling are the convection cooling and the film cooling. For the engines with turbine inlet temperature in excess of 1600K, only film cooling or a hybrid convective and film cooling techniques can provide acceptable surface temperature.

A significant amount of research, predominately experimental, has been done during the last several decades to improve the efficiency of film cooling and to understand the aerothermal flow physics associated with the process. Early experimental research were carried out using simplified experimental conditions such as injection from a single hole in the direction of the flow on a flat plate. More advanced research utilized configurations of practical interest. The main problem associated with these efforts is in making accurate heat transfer measurements in a real machine. The influence of different characteristics, such as, blowing ratio, hole shape, injection angle, and turbulence intensity of the freestream on the film cooling effectiveness were investigated by Goldstein et al., (1987), Bergeles et al.,(1977), and Pietrzyk et al., (1990). Tekeishi et al., (1991) measured the film cooling effectiveness on the rotating turbine stage. Abhari and Epstein (1994) measured the time-resolved heat transfer on the rotor of a transonic turbine stage. A review of some works can be found in Margason (1993), Lakshminarayana (1996).

Early attempts to predict film cooling effects were based on the parabolic or the partially-parabolic equations. Craward et al., (1980) used a boundary layer code to predict laterally averaged film cooling. Bergeles et al. (1977) used a semi-elliptic code with the prescribed constant velocity at the jet inlet. While codes based on partially parabolic equations and especially boundary layer codes are extremely effective, the predictions are at best qualitative. Fully coupled procedures should be used to improve the accuracy of the prediction.

Almost all current efforts in numerical modeling of the film cooling are based on coupled solutions. Current numerical efforts can be divided into two groups. The first group of researchers attempt to simulate simplified geometries such as a flat plate (Lylek and Zerkle (1993)) or a magnified model of the leading edge cooling (He et al. (1996)). This approach provides good numerical resolution of the jet structure and is aimed at resolving the physics of cooling jet-mainstream interaction. Another approach is to simulate the flow in the real turbine geometry. Numerical simulations of film cooling flow in a turbine were performed by Hall et al.(1994), Vogel (1996), Garg and Abhari (1996). Due to the memory and CPU time limitation, only a limited number of grid points were distributed inside the film cooling hole. Lack of an adequate grid density reduces the accuracy of the prediction.

The prediction of the film cooling is in its infant stage. Even though recent attempts are promising, none have been able to predict the film cooling effectiveness and jet-mainstream interaction accurately. This is mainly due to the numerical inaccuracy, turbulence model, and grid sensitivity. These issues will be addressed in this thesis.

1.1.4 Three dimensional flow in turbine including tip leakage effect

Most of axial turbomachines have a small clearance between the rotor blade tip and the casing. The presence of the tip gap generates the tip leakage flow, which has a profound effect on the stage aerodynamics, efficiency, and noise vibration. According to Schaub et al. (1993), in a modern high performance high-pressure turbine, up to 30% of losses can be attributed to the presence of the tip leakage flow. Tip leakage flow results in reduced loading of the blade. Another significant effect is the modification of the heat transfer pattern due to the interaction between the tip leakage flow and the mainflow. The interaction between the tip leakage flow and the succeeding blade row results in an additional source of unsteadiness. Chopping of the tip vortex by the leading edge of the downstream blade produces turbulence and mixing, contributing to increased losses.

The leakage flow has a complex three-dimensional structure. Development of the tip leakage flow is characterized by the complex interaction between the passage secondary flow, tip clearance vortex, blade wake, and the the endwall boundary layer. Significant efforts have been made to improve an understanding of the tip clearance and secondary flows in turbine. A comprehensive review of the experimental and computational research in this field can be found in Sjolander (1997).

Due to the complexity of flow measurements, most of the research work was limited to the cascade flows; Langston et al. (1977), Gregory-Smith et al. (1988), and Yamamoto (1989). It is only recently that the emphasis is placed on the experimental work in real turbine stage configurations. Experimental measurements in actual rotors, (Joslyn and Dring, 1992 and Ristic et al., 1998) indicate significantly different leakage and secondary vortex structure in comparison with those observed in a linear cascade. One of the main conclusions of the experimental investigation by Ristic et al. (1998) is that the tip clearance vortex is confined to the suction side corner of the blade, unlike in a cascade where the considerable pitchwise flow transport is observed.

Several models based on the inviscid consideration of the tip leakage vortex (e.g., Lakshminarayana, 1970; Senoo and Ishida, 1987) are successfully used by the turbine industry in their design systems. However, further efficiency improvement requires a better understanding of the complex secondary vortex structure including the analysis of the loss origin. Utilization of the numerical modeling is a valuable tool in the achieving this objective.

1.2 Objectives and thesis organization.

Many aspects of the turbomachinery flow physics are still unresolved. Further progress can be achieved through a systematic application of the computational technique to the investigation of turbomachinery flows. Extensive validation and certification process is a necessary step in order to establish confidence in numerical simulations. The main objective of the thesis is to contribute to a better understanding of the turbomachine aerothermodynamics through the development and utilization of the numerical modeling, with special emphasis on the code validation and calibration, turbulence and transition modeling aspects.

The main objective of the research is achieved through the accomplishment of the following tasks:

(1) Development of the unsteady Navier-Stokes solver, which can provide an efficient and flexible modeling of turbomachinery flows. This task includes an improvement in the computational efficiency of the solver for unsteady applications (dual time step approach) and improvements in the code flexibility and physical models (i.e. incorporation of the multiblock, flexible boundary conditions, incorporating of wide range of turbulence and transition models etc.).

(2) Establishment of the solver's reliability range for turbomachinery unsteady flows.

(3) Application of the solver to the investigation of complex turbomachinery flows in order to gain a better understanding of flow physics. This task includes the analysis of:

(3.1) Unsteady transitional boundary layer: Assessment of the turbulence models for their ability to simulate wake induced transition. Analysis of the effect of the unsteady transitional boundary layer development on the turbomachinery performance.

(3.2) Different modes of steady transition varying from bypass transition in the attached flow to the transition over a laminar separation bubble. Effect of the numerical scheme on the accuracy of the prediction.

(3.2) Rotor-stator interaction in the form of the upstream wake transport through the stage. Analysis of the upstream wake decay mechanism (e.g. contribution of inviscid stretching and viscous dissipation), and its effect on the unsteady flow loss generation.

(3.3) Flow physics of the rotor-stator interaction at off-design conditions.

(3.4) Analysis of secondary flows due to the jet-mainstream interaction in film cooling configurations. Identification of the sources of the aerodynamic and heat losses due to the presence of the vortices.

(3.5) Analysis of the secondary flow in a turbine rotor, including the tip vortex - passage vortex interaction. Effect of the tip clearance flow on the rotor efficiency. Development and decay of the tip clearance vortex.

The main steps of the research presented in this thesis are illustrated in Fig. 1-1.

1.3 Contribution of the thesis

An unsteady compressible Navier-Stokes code based on the pseudo-time acceleration technique has been developed. Incorporation of the pseudo-time approach has enabled efficient unsteady simulation with CPU utilization improvement from 5 to 25 times in comparison with the original code. An analysis of the scheme has been carried out to assess different approaches to the discretization of the time derivatives in the pseudo-time based scheme. Results of this analysis have been used to establish correction for the local pseudo-time step (iterative parameter) to provide efficient and stable unsteady calculations. Multiblock feature has been added to the code in order to simplify grid generation process and improve grid quality for cases with complex multidomain configurations such as the film cooling and the rotor-stator interaction.

Extensive validation of the code has been performed to assess sensitivity of the solver to grid characteristics and artificial dissipation for the complex turbomachinery flows (e.g., preservation of the accurate decay of the unsteady wake, the accurate development of the unsteady boundary layer etc.)

The code has been used for the investigation of the unsteady flow physics in turbomachinery blade rows. Analysis of the wake induced transition on a turbine and a compressor blade has been carried out. A number of turbulence models have been assessed for their ability to provide an accurate prediction of the rotor-stator interaction effects, including the wake induced transition.

Detailed simulation has been performed to investigate the transport of the upstream wake through the turbine rotor and the mechanism responsible for the wake decay. The contribution of different physical mechanisms; potential interaction viscous dissipation, and inviscid stretching has been analyzed. The viscous dissipation has been found to be a major contributor into the overall wake decay. However, the wake stretching inside the blade passage is predominantly inviscid. Distribution of losses correlates with this conclusion, as most of the losses due to the unsteady interaction are concentrated upstream of the leading edge (wake mixing losses).

The flow in a low pressure turbine at different Reynolds numbers and freestream turbulence levels has been studied. Variation of the flow condition results in a different type of transition, varying from a bypass transition to a separated flow transition. Different approacheas to the transition modeling (different turbulence and transition models) have been assessed to establish their ability to predict the transitional flow in a low pressure turbine within the range of flow conditions encountered in practice. The analysis performed shows that the prediction of the flow with the transition over a separation bubble is more sensitive to the numerical aspects of the scheme in comparison with the attached flow transition.

Investigation of the complex aerothermal field due to the leading edge at a compound angle has been carried out. Results of the modeling have been used to analyze the vortex structure associated with the coolant jet-freestream interaction to understand the effect of different vortices on the cooling effectiveness and aerothermal losses. The system of vortices has been found to be essentially different from those observed in a flat plate configurations. Effect of the inlet turbulence and the length scale on the aerothermal field has been examined. It has been found that the inlet turbulence scale has a profound effect on the accuracy of the prediction. This influence is significantly higher in comparison with those observed in the boundary layer flow due to the intense mixing and entrainment of the ambient fluid into the coolant jet vortex structure.

Numerical modeling is employed to gain a better understanding of the secondary flow in the Penn State rotor. Result of the simulation is used to interpret tip vortex development, its interaction with secondary flow and vortices. Secondary flow vortex structure is analyzed to estimate its contribution in overall loss generation.

1.4 Thesis organization

The governing equation and numerical scheme employed are described in Chapter 2. Code development includes two major components; the development of an efficient unsteady solver based on a pseudo-time step approach and incorporation of the multiblock capabilities. The results of the stability analysis of the dual time step scheme are used to establish the optimum pseudo-time step based on local CFL, Von Neuman numbers and the ratio of pseudo-to-physical time steps.

The application of CFD analysis to the investigation of the physical problem requires the establishment of the reliability and the accuracy of the code. Results of the code validation and verification are presented in Chapter 3. The emphasis is on the assessment of flow features crucial for the numerical model developed in the thesis. The influence of the numerical aspects (artificial dissipation, grid density etc.) on the accuracy of the prediction of the freestream wake propagation, transition, flow over a cylinder is analyzed. Based on the results of the test cases, modifications to the k-ε model to improve the accuracy in regions with dominant normal stresses are discussed.

Investigation of the unsteady flow in a compressor stage is presented in Chapter 4. This research is carried out in three major aspects. First aspect is the validation of the code against the experimental data and the establishment of the number of pseudo time and physical time steps required for the accurate simulation of the unsteady flow. Another aspect considered is a comparison of the current prediction with the prediction based on the Euler/boundary layer approach from the point of view of accuracy and efficiency. Development of the unsteady boundary layer, including the unsteady transition zone, as well as the upstream wake–profile wake interaction effects is also discussed.

Chapter 5 is aimed at an improved understanding of the flow physics in turbines through the integrated computational and experimental study. The prediction has been validated not only against the blade surface experimental data (i.e., unsteady surface pressure distribution), but also against instantaneous blade-to-blade velocity acquired from an LDV. The sources of additional losses due to the unsteady interaction are analyzed. The physics of the upstream wake transport and decay are investigated. The emphasis is on the contribution of different mechanisms responsible for the overall wake decay. The results presented on the wake induced transition show the ability of the code to simulate major features associated with the unsteady transition, with the exception of the calmed region.

Chapter 6 incorporates research efforts on the numerical simulation of the flow in a low pressure turbine. A range of parameters are considered. These variations correspond to different types of transition, from bypass transition in the attached flow to the transition over a laminar separation bubble. Assessment of different turbulence and transition models is presented. Predictions of the transitional flow based on k-ε and ARS turbulence models are compared with the prediction based on the utilization of the transition model. Extensive evaluation of the effect of the artificial dissipation on the accuracy of the transition prediction is carried out to estimate the accuracy range.

Jet-main flow interaction may lead to the generation of a vortex structure and, consequently, to additional aerodynamic losses and heat transfer. Examples of this type of flows are the leading edge film cooling considered in Chapter 7, and the tip clearance flow in turbine, discussed in Chapter 8. The emphasis of this research is on an achievement of a better understanding of the vortex structure due to the jet-mainflow interaction, including the identification of sources of vortices and associated losses (both aerodynamic and thermal). Comparison of the simulated flow of the leading edge film cooling model with the experimental data shows the ability of the code to predict complex vortex structure associated with the film jet-main flow interaction. Results of the simulation are used to gain better understanding of factors affecting thermal and aerodynamic efficiency of the leading edge film cooling. Numerical analysis of the tip leakage flow in a turbine is utilized to investigate secondary flow physics in the rotor, including interaction between secondary vortices, tip leakage vortex, and rotor wake.

Conclusions from the current research as well as suggestions for the future research are summarized in Chapter 9.

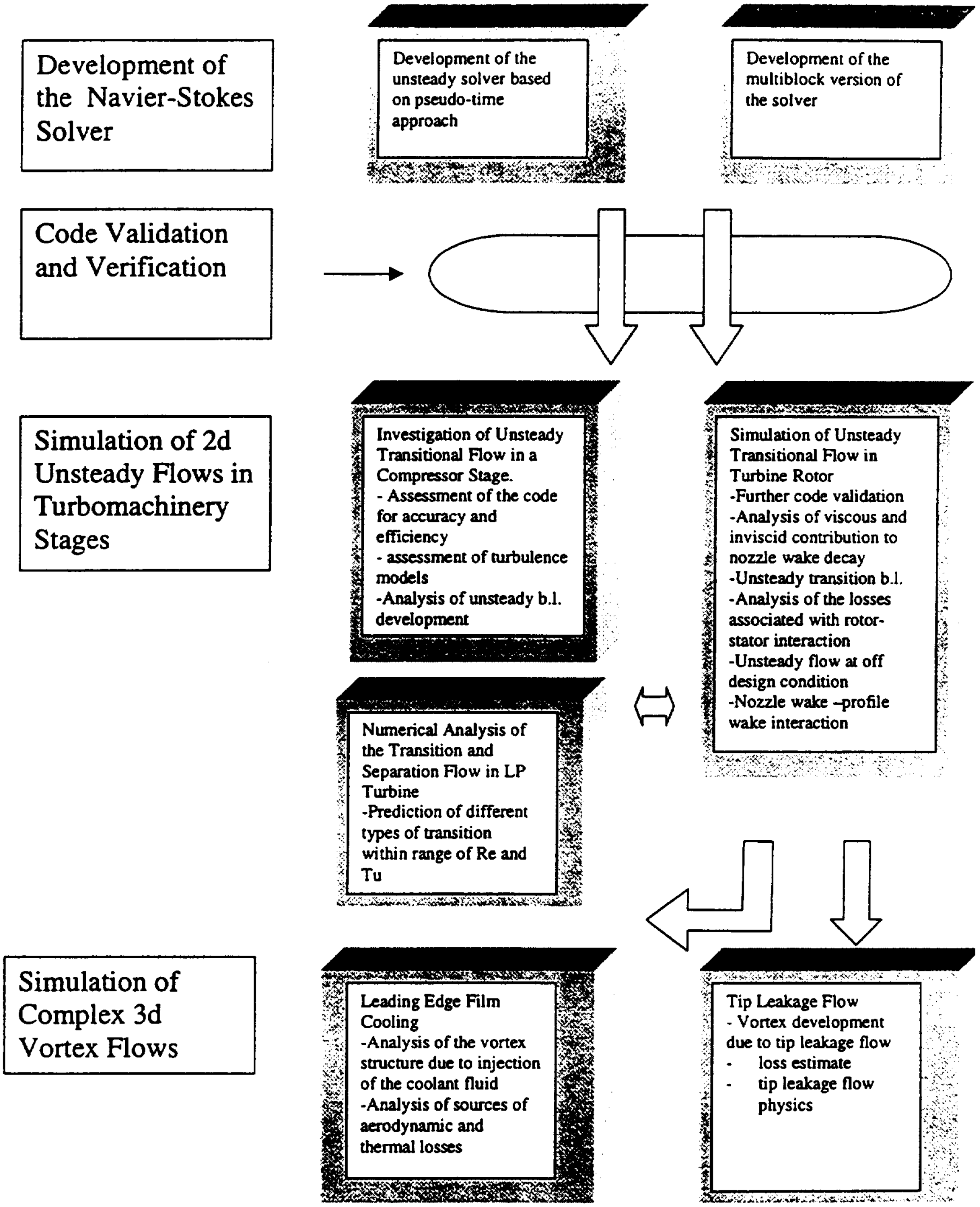
Development of the Navier-Stokes Solver
Development of the unsteady solver based on pseudo-time approach
Development of the multiblock version of the solver
Code Validation and Verification
Simulation of 2d Unsteady Flows in Turbomachinery Stages
Investigation of Unsteady Transitional Flow in a Compressor Stage.
- Assessment of the code for accuracy and efficiency
- assessment of turbulence models
-Analysis of unsteady b.l. development
Simulation of Unsteady Transitional Flow in Turbine Rotor
-Further code validation
-Analysis of viscous and inviscid contribution to nozzle wake decay
-Unsteady transition b.l.
-Analysis of the losses associated with rotor-stator interaction
-Unsteady flow at off design condition
-Nozzle wake –profile wake interaction
Numerical Analysis of the Transition and Separation Flow in LP Turbine
-Prediction of different types of transition within range of Re and Tu
Simulation of Complex 3d Vortex Flows
Leading Edge Film Cooling
-Analysis of the vortex structure due to injection of the coolant fluid
-Analysis of sources of aerodynamic and thermal losses
Tip Leakage Flow
- Vortex development due to tip leakage flow
- loss estimate
- tip leakage flow physics

Fig. 1-1 Research program

Chapter 2

GOVERNING EQUATION AND NUMERICAL PROCEDURE

A three-dimensional steady/unsteady Navier-Stokes solver has been developed in this thesis. Present development is based on the extension of the original solver developed earlier (Kunz and Lakshminarayana, 1992). Pseudo-time stepping has been incorporated to enable an efficient unsteady computation. Multiblock feature has been incorporated to make the code more flexible for the computation of the flow in complex topologies. A description of the code development as well as the numerical procedure, and turbulence models utilized are described in this chapter.

2.1 Governing equations and numerical procedure

Applying the Favre averaging procedure to the continuity, momentum, and energy equations, the five mean flow equations can be written in Cartesian tensor form as :

$$\frac{\partial\bar{\rho}}{\partial t}+\frac{\partial}{\partial x_j}(\bar{\rho}\tilde{U}_j)=0$$

$$\frac{\partial(\bar{\rho}\tilde{U}_i)}{\partial t}+\frac{\partial}{\partial x_j}(\bar{\rho}\tilde{U}_i\tilde{U}_j)=-\frac{\partial\bar{p}}{\partial x_i}+\frac{\partial}{\partial x_i}\tau_{ij}-\bar{\rho}\varepsilon_{ijk}\omega_j\varepsilon_{klm}\omega_l x_m-2\bar{\rho}\varepsilon_{ijk}\omega_j\tilde{U}_k$$

$$\frac{\partial(\overline{\rho\tilde{e}_{0R}})}{\partial t}+\frac{\partial}{\partial x_j}(\bar{\rho}(\tilde{e}_{oR}+\frac{\bar{p}}{\bar{\rho}})\tilde{U}_j)=\frac{\partial}{\partial x_j}(\tilde{U}_j\tau_{ij}-q_i)$$

[2-1]

Where: $\bar{f}=\frac{\lim}{t\rightarrow\infty}\frac{1}{t}\int_{t_0}^{t_0+t}f\,dt$ - time averaging of f

$\tilde{f} = \frac{\overline{\rho f}}{\bar{\rho}}$ - Favre averaging

$\tau_{ij} = \tau_{lij} - \overline{\rho u_i'' u_j''}$ - effective stress tensor

$q_i = q_{li} + \overline{\rho u_i'' e''}$ - effective heat flux vector

$e_{0R} = \rho(e + W^2/2 - \omega^2 r^2/2)$ -energy transport variable, assuming rotation vector is coincident with x-axis and r is a distance to the axis

Reynolds stresses and heat flux components are calculated using the eddy viscosity hypothesis or higher order turbulence closure.

For the stability analysis of the numerical scheme presented below equations [2-1] can be rewritten in a matrix form:

$$\frac{\partial Q}{\partial t} = \frac{\partial(E_i + E_v)}{\partial x} + \frac{\partial(F_i + F_v)}{\partial y} + \frac{\partial(G_i + G_v)}{\partial z} + S$$

[2-2]

$Q = (\bar{\rho} \quad \bar{\rho}\tilde{U}_x \quad \bar{\rho}\tilde{U}_y \quad \bar{\rho}\tilde{U}_z \quad \bar{\rho}\tilde{e}_{oR})$ - vector of conservative variables

E_i, F_i, G_i - inviscid flux vectors,

E_v, F_v, G_v - vectors of viscous terms,

S - source vector.

Explicit four-stage Runge-Kutta scheme is used for time integration of both main-flow and turbulence equations. A compact second order accurate central difference flux evaluation scheme is employed for the convection terms. Diffusion terms are discretized using second order accurate central differences. For the mean flow equations a fourth order artificial dissipation is included to damp high wave number errors. Second order dissipation is used to improve the shock capturing. Eigenvalue and velocity scaling are used to optimize the amount of the artificial dissipation. Multigrid and an implicit residual smoothing are used to improve the convergence characteristics of the steady solver.

Numerical simulation of the unsteady flow requires special efforts to reduce possible reflection at the boundaries. One and two-dimensional, Giles' type, non-reflecting boundary conditions are incorporated to minimize the reflection at boundaries and to minimize the computational domain (Fan and Lakshminarayana, 1996).

2.1.1 Turbulence closure

Turbulence equations are descretized in a manner similar to those for mean flow equations. "Lagged" approach is utilized for the computation of turbulence equations, i.e., k and ε values at previous time step are used to calculate the eddy viscosity at the current step. The presence of the source term in the turbulence equation results in a stability problem during the initial convergence period. Two mechanisms are used to ensure a stable calculation; utilization of the underelaxation factor, ϕ, for k and ε equations in addition to the time step based on the mean equation and enforcement of an eddy viscosity limit. The maximum ratio of μ_t/μ_l is set equal to 10~100 during the initial convergence period with yhe further increase to 1000~10000 to ensure the correct solution. It was found that the utilization of ϕ=0.6 in the case of two-dimensional flow and ϕ=0.75 for the three-dimensional flow improves convergence characteristics of the solver.

2.1.2 Two-equation models

In eddy-viscosity models effective stress tensor and effective heat flux vector are defined:

$$\tau_{ij} = \tau_{lij} - \overline{\rho u_i'' u_j''} \text{ and } q_i = q_{li} + \overline{\rho u_i'' e''}$$

Reynolds stress is calculated from

$$-\overline{\rho u_i'' u_j''} = \mu_t \left[\left(\frac{\partial \tilde{U}_i}{\partial x_j} + \frac{\partial \tilde{U}_j}{\partial x_i} \right) - \frac{2}{3} \delta_{ij} \frac{\partial \tilde{U}_k}{\partial x_k} \right] - \frac{2}{3} \delta_{ij} \bar{\rho} \tilde{k}$$

heat flux component is given

[2-3]

$$q_{li} = -c_p \frac{\mu_t}{\mathrm{Pr}_t} \frac{\partial \bar{T}}{\partial x_i}$$

Turbulent eddy viscosity is computed using Prandtl-Kolmogorov relation

$$\mu_t = \frac{c_\mu f_\mu \bar{\rho} \tilde{k}^2}{\tilde{\varepsilon}}$$

[2-4]

Transport equations for turbulence kinetic energy and turbulence dissipation ratio (for the simplification, in subsequent equations averaging symbols are omitted)

$$\frac{\partial (\rho k)}{\partial t} + \frac{\partial (\rho U_i k)}{\partial x_i} = \frac{\partial}{\partial x_j} \left[\left(\mu_l + \frac{\mu_t}{\sigma_k} \right) \frac{\partial k}{\partial x_j} \right] + \rho P_k - \rho (\varepsilon + D)$$

[2-5]

$$\frac{\partial (\rho \varepsilon)}{\partial t} + \frac{\partial (\rho U_i \varepsilon)}{\partial x_i} = \frac{\partial}{\partial x_j} \left[\left(\mu_l + \frac{\mu_t}{\sigma_\varepsilon} \right) \frac{\partial \varepsilon}{\partial x_j} \right] + \rho \frac{\varepsilon}{k} \left[C_{\varepsilon 1} f_1 P_k - C_{\varepsilon 2} f_2 \varepsilon \right] + \rho \mathrm{E}$$

[2-6]

Here f_1, f_2, f_μ, $c_{\varepsilon 2}$, $c_{\varepsilon 1}$,D, E are low Reynolds number functions and constants described below.

$$P_k = -\overline{u_i'' u_j''} \frac{\partial \tilde{U}_i}{\partial x_j} \text{ - production of turbulent kinetic energy}$$

A number of low-Reynolds number k-ε turbulence models; Chien (1982), denoted as CH, Lam-Bremhost (1981), denoted as LB, and Fan-Lakshminarayana-Barnett (1993), denoted as FLB, are utilized for the turbulence closure. A summary of the constant and near wall function for different turbulence models is given in Table 2-1 and Table 2-2. The solution of the turbulence transport equations is numerically coupled with the solution of the main flow equations. A second and fourth order artificial dissipation is included in the turbulence transport equations.

Table 2-1 Low-Reynolds-number functions used in turbulence model

Model	Code	f_μ
Chien	Ch	$1-\exp(-0.0115y^+)$
Lam-Bremhost	LB	$[1-\exp(-0.0165Re_y)]^2(1+20.5/Re_t)$
Fan-Lakshminarayana-Barnett	FLB	$0.4f_w/\sqrt{Re_t}+(1-0.4f_w/\sqrt{Re_t})[1-\exp(-Re_y/42.63)]^3$

Table 2-2 Low-Reynolds-number functions used in turbulence models

Code	f_1	f_2	D	E
CH	1.0	$1-0.22\exp(-Re_t^2/36))$	$2\nu k/y^2$	$-2\nu(\varepsilon/y^2)\exp(-0.5y^+)$
LB	$1+(0.06/f_\mu)^3$	$1-\exp(-Re_t^2)$	0	0
FLB	1.0	$1-2/9\exp(-Re_t^2/36))f_w^2$	0	0

where the near-wall function in the FLB model is given by

$$f_w = 1 - \exp\left\{\frac{\sqrt{Re_y}}{2.30} + \left(\frac{\sqrt{Re_y}}{2.30} - \frac{Re_y}{8.89}\right)\left[1 - \exp\left(-\frac{Re_y}{20}\right]^3\right\}$$

Constants C_μ=0.09,$C_{\varepsilon1}$=1.44,$C_{\varepsilon2}$=1.92,σ_k=1.0,σ_ε=1.3 in the LB and FLB models are the same as those used in the standard (high-Reynolds-number) k-ε model given by Launder and Spalding (1974). Chien's k-ε model has slightly different values for $C_{\varepsilon1}$=1.35,$C_{\varepsilon2}$=1.80.

2.1.3 Algebraic Reynolds Stress Model

Numerical simulation based on the first order turbulence closure can be applied to a wide range of cases and may improve the accuracy of the prediction in comparison with algebraic turbulence models. However, deficiency of these models associated with the Boussinesq approximation and empirical correlation used to derive these models leads to less precise solution in the case of complex flows (Lakshminarayana, 1986). Non-equilibrium flows, flows with streamwise curvature and rotation, flows with injection (e.g., film cooling) are examples when the first order turbulence closure does not provide an adequate level of accuracy. Flow computation based on a second degree closure and a subgrid turbulence modeling (LES) demonstrated the potential for the improvement in the turbulence flow prediction. Complex models generally require more CPU time. Another factor affecting the wide acceptance of more complex models is a potentially increased dependence on the numerical stability. More complex structure may lead to a less robust and, as a result, less reliable prediction. It is more difficult to develop a stable code in the case of full Reynolds Stress (FRSM) models. To overcome stability limitations many FRSM solvers utilized a simplified approach for the near wall region (wall function, one-equation models), thus decreasing the accuracy of the flow resolution near the wall.

Rodi, 1976, suggested a simplified algebraic expression for the component of the Reynolds stress tensor. This model is based on the assumption that the transport of Reynolds stress components is locally proportional to the transport of the turbulent kinetic energy. ARSM may be considered as a compromise between the two-equation and higher order models. Implementation of the ARSM does not lead to a significant increase in the CPU time and requires an inversion of the 6X6 (multidimensional case, implicit ARSM). ARSM uses the following expression to calculate Reynolds Stress component:

$$-\overline{u_i''u_j''} = -k\left[R_{ij}(2-C_2)/2 + (P_{ij} - P_{kk}\delta_{ij}/3)(1-C_2)\right] / \left[\frac{1}{2}P_{kk} + \varepsilon(C_1 - 1)\right] - \frac{2}{3}\delta_{ij}k \qquad [2\text{-}7]$$

where: $P_{kk} = P_k = -\overline{u_i''u_j''}\dfrac{\partial \tilde{U}_i}{\partial x_j}$ - production of k

$P_{ij} = -\overline{u_i''u_k''}\dfrac{\partial \tilde{U}_j}{\partial x_k} + \overline{u_j''u_k''}\dfrac{\partial \tilde{U}_i}{\partial x_k}$ - production of Reynolds stresses

$R_{ij} = -2\omega_p(\varepsilon_{ipk}\overline{u_j''u_k''} + \varepsilon_{jpk}\overline{u_i''u_k''})$

$C_1=1.5$, $C_2=0.6$ - model constants

In current research, a hybrid model is utilized in a near wall region. Laminar sublayer and overlap region are calculated using k-ε equation. Matching function based on Re_y is incorporated to smooth the transition between regions calculated using k-ε and ARS models:

$$f_m = \frac{1}{2}\left(\frac{\tanh\left(\beta\dfrac{Re_y}{1.83}/y^{+}_{match} - 1\right)}{\tanh(\beta)} + 1\right)$$

where: β is a slope constant

y^{+}_{match} - matching location

$$R_{vis} = f_m R_{ARSM} + (1 - f_m) R_{k-\varepsilon}$$

2.2 Development of the multiblock solver

The quality of the grid used in the numerical simulation has a serious impact on the accuracy of the numerical simulation. In the case of the complex computational topology, it is appropriate to divide the computational domain into sub-domains and consider these sub-domains as separate computational blocks. Utilization of the multidomain structure enables better optimization of the grid point distribution, thus leading to an improved grid quality. The multiblock approach is also useful in single-connected regions with relatively simple topology, such as a turbomachinery blade row. In this case, different grid types can be more suitable for different regions. A C-type grid is better suited for the near blade region including the leading edge, while an H-type grid can be utilized for a mid passage and inlet/outlet regions. The multiblock approach can also simplify the implementation of the zonal approach, i.e., application of different mathematical models in different regions. Numerical simulation of configurations, with relative motion is another case where a multiblock approach is very helpful. An example of this type of problem is the stator/rotor interaction. Simultaneous calculation of the flow field in several rows improves the accuracy of the numerical prediction. A multiblock approach, with grids stationary in relation to the corresponding blade row and moving relatively to each other, is the best approach for the computation of flows with rotor/stator interaction.

2.2.1 Structure of the multiblock solver

The three-dimensional viscous code has been extended to include a multiblock feature to enable a computation of the rotor/stator interaction and other complex turbomachinery flows. A number of alternative approaches to the development of the multiblock solver have been considered. The first approach is the extension of the existing array structure with an additional index representing a block number. This variant has two essential drawbacks. First, it leads to an excessive use of memory. The total required memory is equal to the memory required for the storage of the largest block times the number of blocks. Therefore, efficient memory allocation can not be achieved in the case of uneven block sizes. Another significant drawback is the need to rewrite the whole program, resulting in extensive additional debugging and incompatibility with previous version of the solver. Utilization of Fortran 90 array type with variable element length has been the second considered approach. Preliminary tests have indicated that this may lead to a certain level of the performance degradation (about 15-20%).

The replacement of multi-dimensional array structure with one-dimensional arrays enables an efficient memory allocation. However, it still requires a significant rewriting of the code. A multilevel approach has been adopted in the current research to combine advantages of one-dimensional arrays with the original code preservation. The code is divided into three modules: "control", "communication" and "kernel" (Fig. 2-1). The main purpose of the control module is to provide the switching between "kernel" and "communication" modules:

```
DIMENSION X(nelem), ....
........
```

```
   DO  block_number =1,number_of_block

         CALL   kernel   (id(block_number),jd(block_number),
kd(block_number),X(i_lock(block_number),...)

      CALL  communication (X,....)

   enddo
......
......
   SUBROUTINE kernel (idim,jdim,kdim,X,...)
   DIMENSION  X(idim,jdim,kdim)
.......
.......
   end  !kernel

SUBROUTINE communication (X,...)
   DIMENSION  X(nelem)
.......
.......
   end  !communication
```

In “control” module all data is represented as one-dimensional array structure. “Kernel” module interface works as a switch between one-dimensional and multidimensional data representation. Fortran passes an actual argument of subroutine as a reference. *i_lock(block_number)* corresponds to the first element of array *X*, belonging to *block_number*. The specification of *X(...)* as actual argument is equal to the employment of a pointer to indicate the position of corresponding block in X array. Inside the “kernel” module there is no information about existence of other blocks. Same routines as in the original single block version of the code are used to perform calculations. “Communication” module is the only module with the simultaneous access to the elements belonging to different blocks. Interblock data transfer requires knowledge of the position of the interface elements in one-dimensional array structure. This task is performed during the preprocessor stage based on a given grid and interblock topology description.

The current structure of the multiblock is well suited for the parallel computer implementation. The development of the Message Passing Interface, MPI, based version of the code for parallel computers requires the modification of three locations only. "Kernel" routine calls should be set to be executed in parallel. In "communication" module, MPI send/receive routine should be added to provide the data exchange between elements stored in memory blocks situated at different CPU. Utilization of pointers makes it easy to move the code from distributed memory systems to shared memory systems. Based on the system type, the preprocessor can calculate `i_lock` suitable for the corresponding system. For example, for the distributed memory system n_{elem} can be set equal to the number of elements in the largest block, while `i_lock(block_number)` will be equal to one for all blocks. For the shared memory system n_{elem} is equal to total number of elements in all blocks.

The information exchange between blocks is a crucial component for the successful development of the multiblock solver. The communication procedure must be efficient, robust and be able to preserve conservation properties. Overlaid and patched grids are the most common types of multiblock grids. The current solver uses overlaid grids. At each interface grids are overlapped by one grid point. Data assigned to this point is based on the solution in the adjustment block. To achieve an accurate preservation of conservative properties a conformal interface has been chosen as a primary mechanism for the information transfer. Conformal interface requires that the boundary ghost cell must be coincident with the inner cell of the adjustment block. No interpolation is required. Data is directly passed from one block to another. For some computational topologies conformal interface may complicate grid generation. To increase a flexibility of the code, the second type of the interface with data interpolation has been added. However, all multiblock results presented in the current thesis are based on the conformal interface approach.

The explicit nature of the numerical solver utilized in this research limits the distance information can propagate during each iteration. Thus, the separation of the computational domain into subdomains does not affect convergence characteristics. Interblock interfaces (in the case of the conformal interfaces) are essentially invisible for the solver. Simulations based on multiblock and the single block configuration (assuming that the multiblock topology can be represented as single block) result in identical solutions. Convergence behavior is also practically identical. The only exemption is the flow with rapidly changing conditions across the interblock interface. This is due to the fact that an artificial dissipation is calculated using one-side finite differences at each side of the interblock interface. One side differences are used because one cell overlap does not provide enough grid point to calculate the 4th artificial dissipation term.

In comparison with the original version, boundary conditions are treated point-by-point in the multiblock version. This enables simulation of any general configuration (Fig. 2-2). Point-by-point boundary conditions lead to an extensive calling of small subroutines and the problem with vectorization of this part of the code. The first problem can be overcome by the inlining during the compilation. According to test cases CPU, overhead due to non-vectorization is less then 1-2%.

Developed multiblock version of the solver has been utilized for the computation of the multidomain film cooling configuration presented in Chapter 7. Implementation of the multiblock approach has simplified the grid generation process and has improved the quality of the computational grid.

2.3 Pseudo-time Acceleration

Time-marching schemes are one of the most widely used methods for the numerical simulation of the compressible Navier-Stokes equations. Even though these schemes approximate unsteady equations, discretization errors and acceleration techniques can totally destroy time accuracy. During a steady code development the main emphasis is done on the minimization of the amplification matrix amplitude $G = \frac{Q^{n+1}}{Q^n}$ in order to increase the convergence rate. Phase error does not play any significant role. In contrast, time accurate computations require that the amplitude of G should be close to unity for all harmonics to be resolved. Phase angle error also has a major influence on the time accuracy. Thus special efforts should be undertaken in order to apply time marching schemes, developed for the steady state calculation, to the unsteady numerical simulation. One of the additional limitations is the restriction on a time step, i.e., the time step should be constant for all cells to preserve temporal accuracy. When an explicit, time marching code is employed for the unsteady computation, the time step is limited by the minimum time based on stability considerations. Due to this, the actual time step is much smaller than the time step needed to achieve required temporal accuracy, especially in the case of highly stretched grids in viscous flows. Furthermore, it is impossible to use common acceleration techniques, such as multigrid and implicit residual smoothing. These techniques generally affect the temporal accuracy of computations. These limitations lead to a large increase in CPU time utilization for unsteady viscous computations on highly stretched grids.

Implicit schemes do not imply direct limitations on a time step. However, most implicit schemes introduce additional linearization error, especially if special technique (e.g. approximate factorization) is used to simplify matrix inversion. The amplitude of the error is proportional to the utilized time step. Thus, implicit schemes developed for steady solvers do not provide the efficient and accurate simulation for unsteady problems also. These difficulties can be overcome through the introduction of dual step calculations.

For example, the governing equation [2-2] for two dimensional time marching problems can be written in the form:

$$\frac{\partial Q}{\partial t}=R(Q)$$

$$\text{Where } R(Q)=-\frac{\partial(E_i+E_v)}{\partial x}-\frac{\partial(F_i+F_v)}{\partial y} \qquad [2\text{-}8]$$

Original scheme uses one iteration to obtain the solution at a new time level, $t^{n+1}=t^n+\Delta t$. Iteration parameter t plays a role of the physical time step. In a dual step or pseudo-time step approach physical time derivative $\frac{\partial Q}{\partial t}$ is considered as an additional term in the equation. To obtain the solution at $t^{n+1}= t^n+\Delta t$ iterations are performed in mathematical space τ rather than in physical temporal space:

Equation [2-8] can be rewritten in the form:

$$\frac{\partial Q}{\partial \tau}=\frac{\partial Q}{\partial t}+R(Q) \quad \text{or} \quad \frac{\partial Q}{\partial \tau}=R'(Q) \qquad [2\text{-}9]$$

Physical derivative $\frac{\partial Q}{\partial t}$ can be discretized in an implicit manner, thus removing limitation on the physical time step. There is no direct influence of the solver characteristics on the temporal accuracy. The original steady solver may be used as an iterative procedure during the inner cycle to achieve the time accurate solution at $t^{n+1}= t^n+\Delta t$. The only effect of the discretization scheme (temporal in a pseudo time space) on the temporal accuracy is the level of convergence during the inner cycle.

Equations [2-8] and [2-9] are similar, the only difference is the presence of additional terms in the residual. Steady computational codes which were developed to solve the equation [2-8] can be applied to the equation [2-9] with minor modifications. The same acceleration techniques that are used in steady state calculations can be utilized in the inner cycle. However, the presence of the source term and the rate of convergence during inner iterations can affect the efficiency of the code and should be carefully analyzed. The form of discretization used for physical temporal derivatives is the factor affecting the stability and convergence rate of the internal cycle. This factor should be also taken into consideration.

Implicit schemes with approximate-Newton methods can be considered as a subgroup of schemes with a dual time step. Different schemes with the dual time stepping have been successfully used to simulate unsteady problems during recent years (Arnone et al. (1995), Hall (1995), Alonso et al. (1994) Daily et al. (1995)).

2.3.1 Stability analysis of the scheme with pseudo time acceleration

Different approaches have been used in the discretization of the physical derivative in pseudo-time step techniques. These approaches for the discretization of the equation [2-9], can be expressed as follows:

$$(1+\alpha'_k \frac{\Delta\tau}{\Delta t}c)\Delta Q^k = -\alpha_k \Delta\tau(\hat{S}^{k-1}+\hat{R}^{k-1})+\alpha''_k \frac{\Delta\tau}{\Delta t}c\Delta Q^{k-1} \qquad [2\text{-}10]$$

where: α_k - coefficients of Runge-Kutta scheme

α'_k α''_k - auxiliary coefficient of Runge-Kutta scheme with pseudo time stepping

$\hat{S}$ - additional source term due to the pseudo-time stepping

Second-order accurate discretization of time derivatives can be written as: $\frac{\partial Q}{\partial t} = \hat{S} = \frac{3Q^{k-1} - 4Q^n + Q^{n-1}}{2\Delta t}$, in this case constant c=2/3. Values of the coefficients used by various authors are given below:

1) $\alpha'_k = 0, \alpha''_k = 0$; explicit treatment of physical derivatives in internal cycle (Arnone et al. (1995) and Hall(1995)), denoted as scheme 1.

2) $\alpha'_k = 1, \alpha''_k = 0$; implicit discretization of physical derivatives (Weiss et al.(1995)), denoted as scheme 2.

3) $\alpha_k' = \alpha_k, \alpha_k'' = \alpha_k$; also implicit discretization of physical derivatives (Melson et al. (1994)), denoted as scheme 3.

4) $\alpha_k' = \alpha_k, \alpha_k'' = 0$, denoted as scheme 4

The presence of the additional source term in equation [2-10] changes the behavior of the scheme. Melson et al.(1994) carried out VonNeuman stability analysis of a five-stage Runge-Kutta scheme. This analysis has been applied to the four-stage scheme and has been extended to include different cases described above. The following two-dimensional model equation has been utilized for this analysis:

$$\frac{du}{d\tau} + \frac{du}{dt} + a\frac{du}{dx} + b\frac{du}{dy} = \upsilon\left(\frac{d^2u}{dx^2} + \frac{d^2u}{dy^2}\right) + k_4\left(a\Delta x^3 \frac{d^4u}{dx^4} + b\Delta x^3 \frac{d^4u}{dy^4}\right) \tag{2-11}$$

where: a,b - model transport velocities

Equation [2-11] is discretized using a four-stage Runge-Kutta scheme with following coefficients; $\alpha_1=1/4$ $\alpha_2=1/3$ $\alpha_3=1/2$ $\alpha_4=1$. A numerical scheme with the evaluation of all terms at all stages (denoted as scheme 1, scheme 2, etc.) as well as schemes with the evaluation of source and viscous terms only at the first stage (denoted as scheme 1a, scheme 2a, etc.) has been considered. An amplification factor of $g = g(\lambda_x = \frac{a\Delta\tau}{\Delta x}, \lambda_y = \frac{b\Delta\tau}{\Delta y}, \sigma_x = \frac{\upsilon\Delta\tau}{\Delta x^2}, \sigma_y = \frac{\upsilon\Delta\tau}{\Delta y^2}, \sigma_x' = \frac{k_4 a\Delta\tau}{\Delta x}, \sigma_y' = \frac{k_4 b\Delta\tau}{\Delta y}, \delta = \frac{\Delta\tau}{\Delta t})$ has been derived using the symbolic computation program Mathematica. Only one-dimensional results are presented here for the sake of clarity. The second dimension does not principally alter the results, but makes the evaluation and interpretation more difficult.

The ratio of the pseudo-time step to the physical time step, $\delta=\Delta\tau/\Delta t$, plays a crucial role in the behavior of the scheme. The results of the stability analysis are summarized in Fig. 2-3-Fig. 2-8. An average amplification factor $\tilde{g}_{0\pi/2}$ is plotted as a function of the CFL number, VonNeuman number, and δ. This approach has been chosen instead of a more standard plot (real and imaginary parts of the amplification factor) to clarify the influence of various parameters. The plot is bounded by the stability surface with $|g|=1$. Explicit discretization of the physical derivative leads to a linear decrease in the maximum allowable VonNeuman number with the increasing δ (scheme 1a, Fig. 2-3). On the contrary, an implicit evaluation of the physical time derivative (scheme 2a) results in an extended stability region at higher δ (Fig. 2-4). The extended stability region indicates an advantage of the implicit evaluation of the physical temporal derivative. However, the distribution of $\tilde{g}_{0\pi/2}$ suggests that within the stability region, a scheme with an explicit evaluation of the physical time derivative may possess better convergence characteristic as a result of lower $\tilde{g}_{0\pi/2}$. For both schemes, 1a and 2a, “optimal” λ and σ (at each value of δ) provide identical amount of error damping. Numerical modeling confirmed that scheme 2a and scheme 1a achieve similar convergence rate during the inner cycle if the “operational curve” (Fig. 2-3, Fig. 2-4) is used to adjust the calculation of the pseudo-time step τ. These curves are used to adjust the time step according to the local value of δ.

The presence of the additional source term results in another positive feature. The higher the ratio of the pseudo time step to the physical time step the more intensive decrease of the amplification factor is observed at low wave numbers. This is especially beneficial for the numerical simulation of the wake propagation in a turbomachinery stage. At the beginning of each inner cycle an error spectrum is close to the spectrum of the local unsteadiness. Local unsteadiness is dominant by the frequencies associated with a relative rotor-stator movement. Usually only first few harmonics, based on the rotation passing frequency, have significant amplitude. These harmonics correspond to low wave numbers. Therefore, the utilization of the pseudo time stepping provides a very efficient mechanism of the error elimination in the region outside of the boundary layer (i.e., the zone with high δ). Damping at low wave numbers is more profound in scheme 1a. Flat distribution of g at low wave numbers can be also used to explain the reduced efficiency of the multigrid acceleration when it is used in conjunction with a pseudo-time stepping. For the standard Runge-Kutta scheme the amplification factor is rapidly decreasing for low frequency errors. Calculations on a coarse grid effectively double a local wave number improving convergence. Practically constant distribution of the amplification factor at low wave numbers diminishes the effect of the multigrid acceleration in the case of a pseudo-time scheme.

Figures Fig. 2-5 and Fig. 2-6 show an average amplification factor for schemes 1 and 2 respectively. Evaluation of viscous and source terms at all stages extends the stability limit for both schemes. Low wave damping is also improved in scheme 1. However, simular to the steady state case, the advantage of the evolution of viscous and source terms at all stages is not significant enough to justify an additional CPU time required for this modification.

Last two schemes with the implicit evaluation of the physical time derivatives behave similar to those of scheme 2 (Fig. 2-7, Fig. 2-8). Scheme 3 possess more rapid decay of the $\tilde{g}_{0\pi/2}$ in comparison with the scheme 2. It is possible to expect that this may provide better convergence of the inner cycle for regions with δ~0.3-1. An interesting feature of the scheme 4 is the independence of its stability limit from the ratio of pseudo time to physical steps. However, similar to all other schemes it provides better low frequency error elimination with increased δ.

2.3.2 Artificial dissipation term adjustment for the solver with pseudo-time stepping

Explicit treatment of the physical derivative in pseudo-time stepping imposes a limitation on the pseudo-time step during the inner iteration for the grid cell located in the middle of the blade passage. Thus the Courant-Fredrichs-Levy number for these grids may be significantly smaller than the maximum CFL_{max}. Meanwhile, the artificial dissipation term is based on the local maximum CFL number. A one-dimensional simplified form of the governing equation [2-2] can be written as:

$$\frac{\partial Q}{\partial \tau} + A\frac{\partial Q}{\partial x} + D(Q) + S(Q) = 0 \qquad [2\text{-}12]$$

where the artificial dissipation term :

$$D(Q) = \frac{k_4 * \delta_{xxxx} Q * \rho(A)}{CFL * \Delta x} \qquad [2\text{-}13]$$

here ρ(A) - spectral radius of A

For $CFL<CFL_{max}$, D(Q) may become large even with a small variation in Q. To avoid an excessive level of the artificial dissipation , D(Q) was modified:

$$D'(Q)=D(Q)CFL/CFL_{max}. \qquad [2-14]$$

Incorporation of the pseudo-time acceleration has allowed an efficient simulation of unsteady turbomachinery flows, presented in subsequent chapters. Code based on pseudo-time approach requires from 5 to 30 times less CPU time in comparison with the original code. Scheme with explicit evaluation of the physical time step (scheme 1a) has been used, because it provides the same level of convergence as the scheme with the implicit evaluation of the physical time step (scheme 2a).

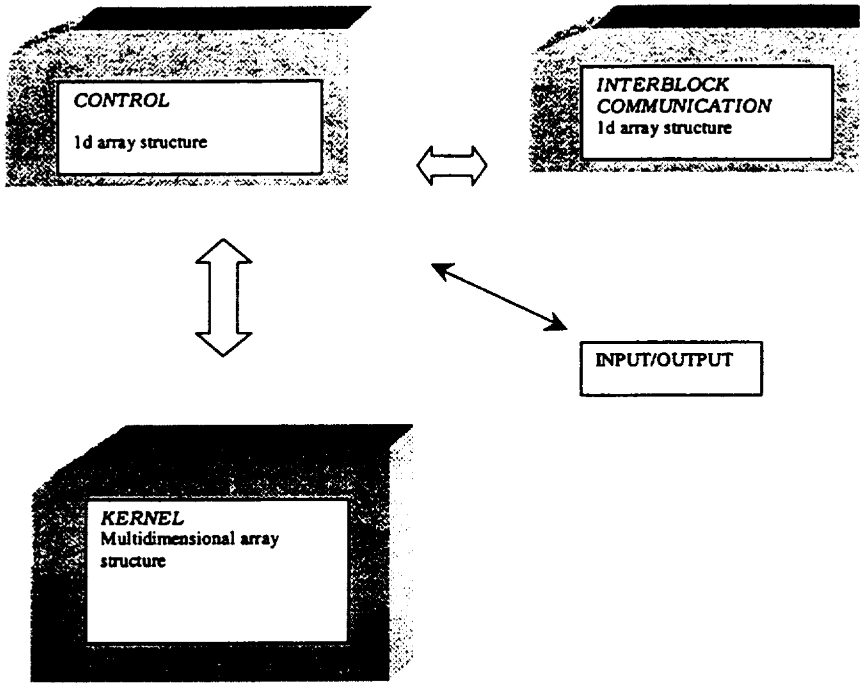
CONTROL
1d array structure
INTERBLOCK COMMUNICATION
1d array structure
INPUT/OUTPUT
KERNEL
Multidimensional array structure

Fig. 2-1 Block scheme of the multiblock solver

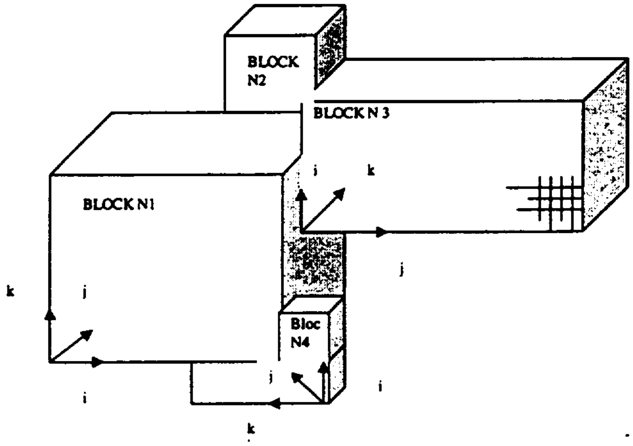
BLOCK N2
BLOCK N 3
i
k
j
BLOCK N1
k
j
i
Bloc N4
j
i
k

Fig. 2-2 Allowable multiblock topology (in computational space)

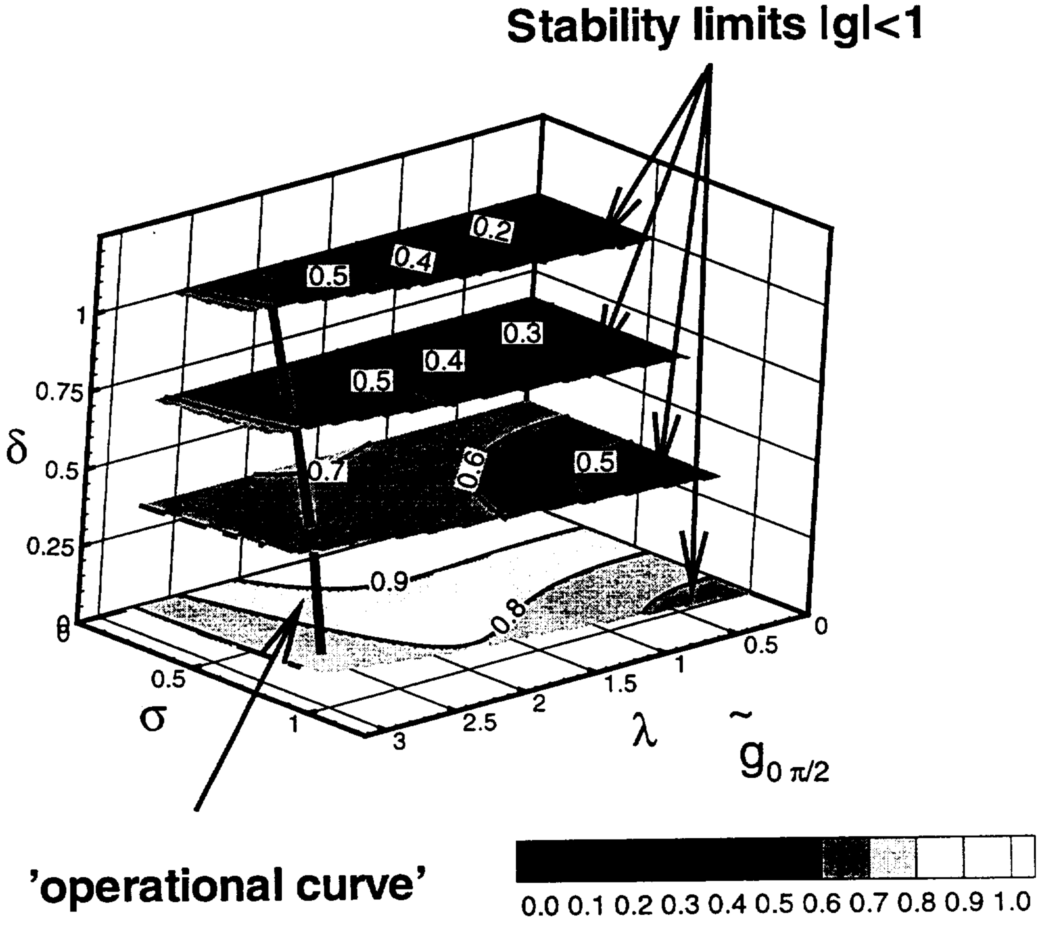

Fig. 2-3 Stability limits and amplification factor distribution for scheme 1a

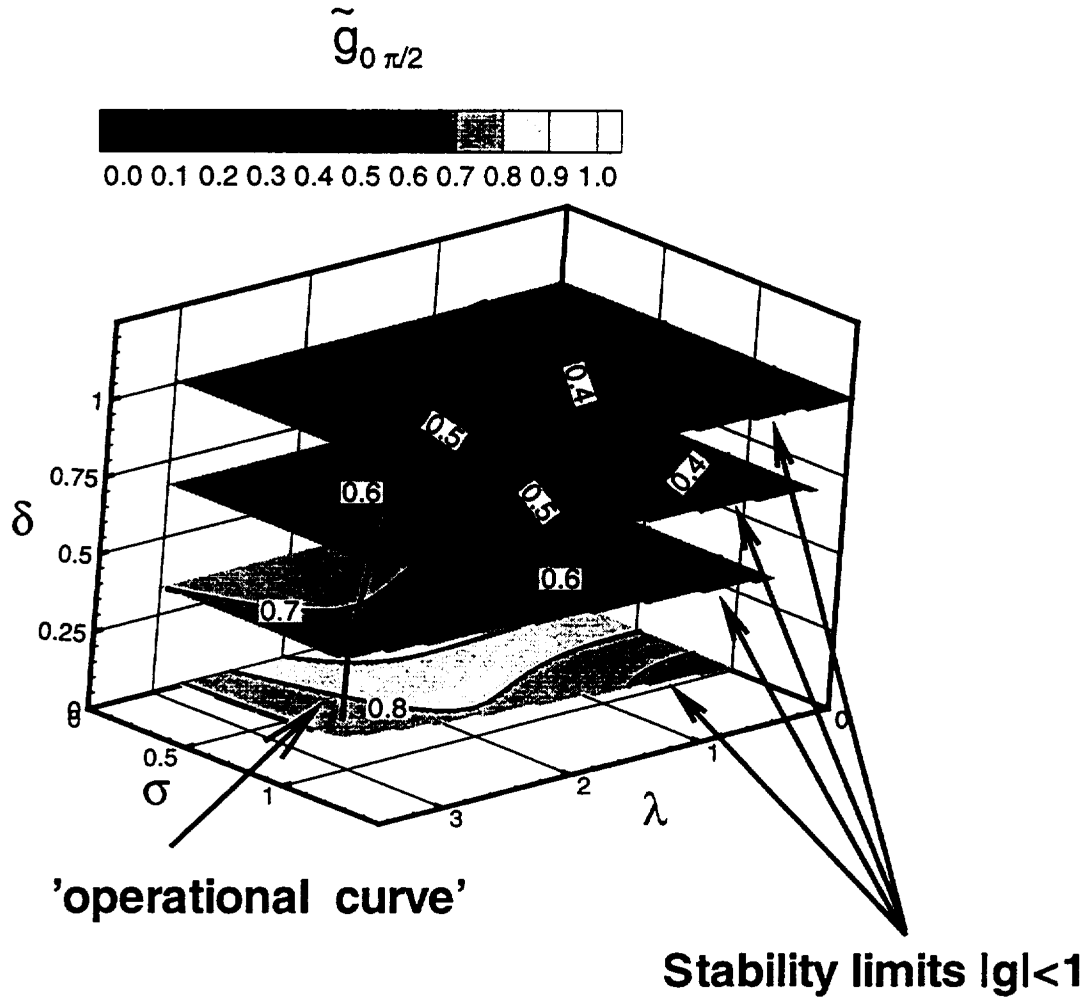

'operational curve'

Stability limits |g|<1

Fig. 2-4 Stability limits and amplification factor distribution for scheme 2a

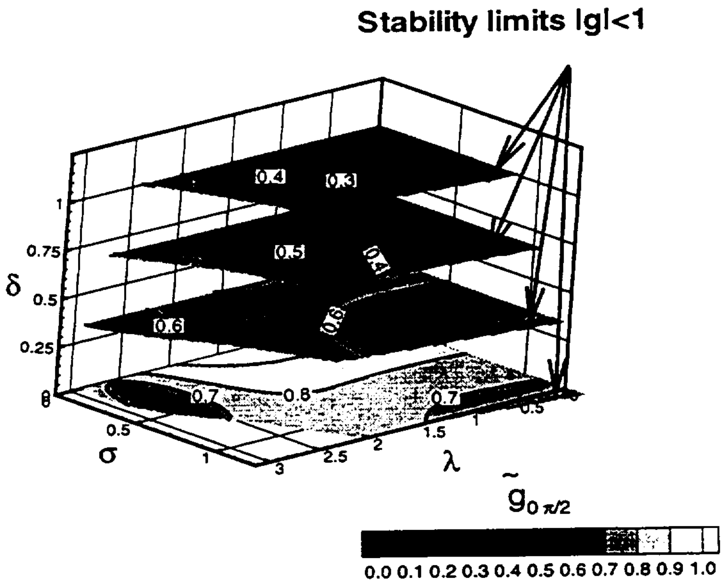

Fig. 2-5 Stability limits and amplification factor distribution for scheme 1

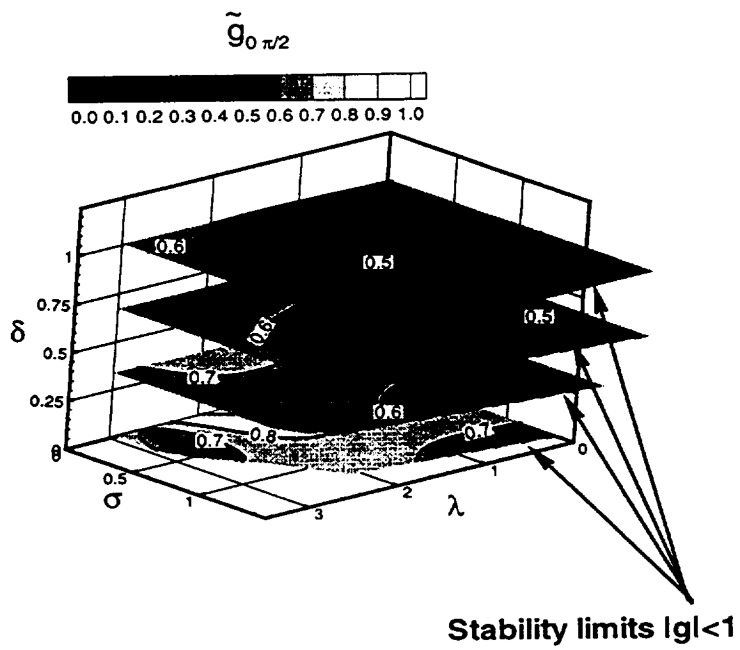

Fig. 2-6 Stability limits and amplification factor distribution for scheme 2

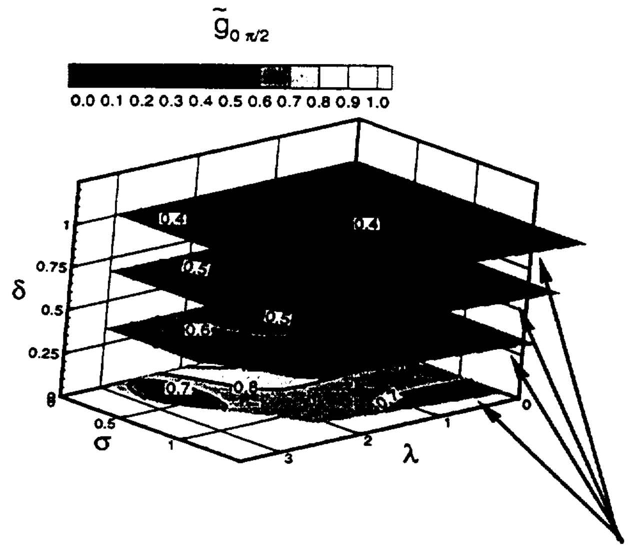

Stability limits |g|<1

Fig. 2-7 Stability limits and amplification factor distribution for scheme 3

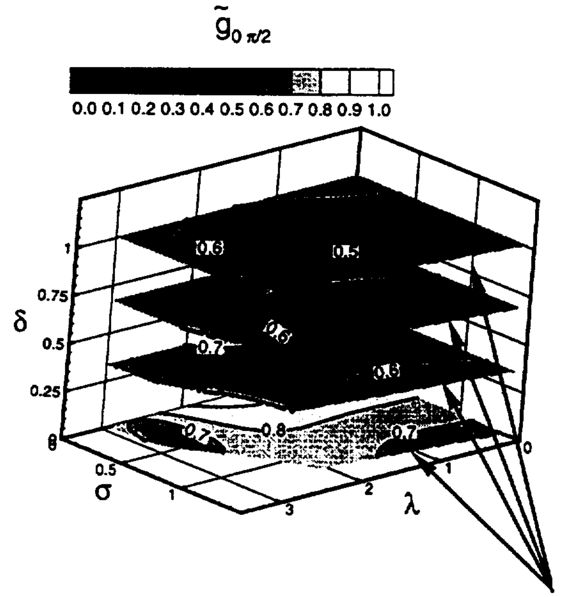

Stability limits |g|<1

Fig. 2-8 Stability limits and amplification factor distribution for scheme 4

Chapter 3

CODE VALIDATION AND MODIFICATION

Code validation and verification are essential parts of the development of the CFD solver. Validation process of the current solver can be divided into two stages. First stage of the validation includes test cases to verify that the development and modification of the code did not introduce additional errors. The objective of the second stage of the validation process is to simulate test cases with complex features essential for accurate flow simulations in turbomachinery. In addition to results presented in this chapter, code validation against the existing experimental data for flow configurations discussed in following chapters is carried out to achieve confidence in the code and numerical simulations.

3.1 Verification against analytical solution

Numerical simulation of the inviscid, irrotational flow over a cylinder with inlet Mach number equal to 0.1 has been carried out to verify accuracy of the code against the analytical solution. Flow over a cylinder possess a number of flow features which can be found in turbomachinery cascades, i.e., decelerating flow along the stagnation line near the leading edge etc. The existence of the analytical (potential) solution makes possible a quantitative comparison to assess the accuracy of the code. Utilization of the finite difference approach to the solution of the partial differential equations results in the procedure that effectively solves the equation, which is different from the original differential equation. Effect of the discretization procedure can be analyzed using partial differential approximation (PDA) (Shokin and Janenko, 1985) of the equations. Deviation from the form of the original PDE may result in numerical errors, even if the computation could be carried out with the unlimited precision. To ensure stable calculation, most of the numerical codes include artificial dissipation terms. The absence of explicit artificial terms does not constitute the absence of the artificial dissipation but rather its increased value in the partial differential approximation. The analysis of PDA provides significant amount of information on the characteristics of the scheme, including the effect of the explicit and the implicit numerical dissipation. However, from the practical point of view, the verification and the validation of the code are more appropriate, even taken into the consideration the limited and empirical nature of the validation process.

Flow over the cylinder has been simulated using 151 x 41, "H" type grid. Grid density is similar to the grid density (inviscid simulations and grids for viscous simulation outside the boundary layer) typically used for the computational analysis presented in following chapters. The comparison between the analytical solution and computational results (Fig. 3-1) reveals very good agreement for the computations with the appropriate amount of the artificial dissipation. Decelerating flow upstream of the cylinder is not very sensitive to the level of the artificial dissipation. Only use of very high values of k_4 results in a deviation of the numerical solution from the exact one. Flow prediction downstream of the cylinder is not as accurate as the prediction of the upstream region. For cases with fourth order artificial dissipation coefficient $k_4 > 0.015$ a small separation zone develops near the downstream stagnation point. This phenomenon results in a flat velocity from x/R

= 1 to x/R = 1.05 (Fig. 3-1). Further increase of the artificial dissipation provides fully attached flow near the trailing edge. However, this results in a velocity field which has noticeably asymmetric downstream and upstream zones. The decreased total pressure indicates the unphysical energy dissipation. Quantitative analysis of the numerical error is presented in Fig. 3-2. First norm, $\|\cdot\|_1 = \max_{ij}(\cdot)$ represents the local error, while the second norm $\|\cdot\|_2 = \frac{\sqrt{\sum_{ij}(\cdot)^2}}{n_i \cdot n_j}$ is an indication of an overall accuracy of the prediction (n_i,n_j are grid dimensions). The computational error was calculated separately for the zone with x/R > 0 and x/R < 0. Stagnation points are the locations of the maximum errors for all cases with $k_4 < 0.04$. Within a range of small values of $k_4 = [0.05 - 0.015]$, the numerical error is practically zero outside a small zone near stagnation points. The development of the separation zone downstream of the cylinder results in $\|\cdot\|_1$ jump at $k_4 = 0.15$.

High artificial dissipation $k > 0.04$ leads to monotonic increase in $\|\cdot\|_1$ and $\|\cdot\|_2$ throughout the flow. This is an indication that at this level of the artificial dissipation, the type of the flow (accelerating or decelerating) as well as the flow grid alignment is irrelevant. Computations based on a doubled grid result in 30% decrease in $\|\cdot\|_1$ and have no significant effect on $\|\cdot\|_2$ for $k_4 \in [0.005, 002]$. Based on this analysis, $k_4 < 0.02$ may be established as a requirement for the accurate flow simulation.

3.2 Influence of the artificial dissipation on the wake propagation and decay

The correct simulation of the wake decay is an essential component of the rotor-stator interaction analysis. Excessive wake dissipation would result in the improper unsteady blade loading and unsteady losses. Numerical analysis of the freestream decay of the moving wake has been used to establish the requirement on grid characteristics and the level of an artificial dissipation.

Moving wake has been simulated using nonuniform time dependent inlet boundary condition. Inlet total velocity was prescribed as $U=U_o+f(y-V_{ow}t)$. Time average flow angle is set at 45°. Function f is either Gaussian distribution or sine wave with different reduced frequencies. This configuration imitates the wake propagation in an axial gap in a relative frame of reference (without the potential effect).

If inviscid flow model is considered, then any wake decay is due to the numerical dissipation. Numerical analysis has been carried out to establish the criteria (grid density, artificial dissipation) required to obtain an accurate wake propagation.

Results of the numerical simulation are summarized in Fig. 3-3. The influence of the artificial dissipation on a wake decay is shown for two typical values of the fourth-order artificial dissipation coefficient, k_4. Twenty to thirty grid points per each wave width is necessary for an accurate prediction of the wake propagation.

This flow can be analytically solved using the linearization procedure (see Appendix A):

$$A(\xi) = A_0 \exp(-(2\pi\varpi)^2(\frac{1}{\mathrm{Re}} + (k_4 \frac{(2\pi\varpi)^2}{n^3}(1+\frac{1}{Ma}))\xi)$$

where $\xi = y - V_{ow}x$

This formula correlates well with results of the numerical simulation and can be used to establish grid and k_4 requirement depending on the spectrum of the incoming unsteadiness.

The results of this analysis are used as a guideline in generating grids for two additional test cases. The numerical solver was utilized to simulate the wake downstream of the flat plate measured by Chevray et al. (1969) (Fig. 3-4). The prediction is in good agreement with the data. The comparison of the numerical prediction of the far wake decay with the correlation due to Reynolds et al. (1979) for a cascade wake is also found to be in good agreement.

Another objective of the current analysis is to verify the wake-outlet boundary condition interaction. Even though non-reflection boundary conditions are used in the current solver, certain amount of the wake damping occurs near the outlet boundary. This affect is limited by two-three grid points upstream of the outlet boundary. It does not generate any reflection wave. Thus, there is no adverse affect on the unsteady solution of near the boundary region.

3.3 Steady turbulent and transitional boundary layer

Numerical simulation of the transitional flow on a flat plate has been carried out to assess the ability of the code to predict the inception and the length of the transition. The test case chosen for this validation is T3a described by Savill (1992). The predictions from all three turbulence models (CH, LB, FLB) are compared with the data. A number of investigators have used boundary layer codes to analyze the ability of the low-Re number turbulence models to predict the transition. This prediction is feasible since low-Re k-ε equations model the transitional behavior of the boundary layer through low-Re functions. However, this prediction may not be very accurate, since low-Re functions employed are based on the fully turbulent flow.

Uniform inlet flow and turbulence distribution are prescribed at the inlet, upstream of the leading edge. Numerical experiments indicate that the grid should be extensively stretched near the leading edge of the flat plate to minimize an effect of the singularity point and to ensure an accurate prediction of the transitional boundary layer. The skin friction coefficient distribution, shown in Fig. 3-5, indicates that the LB model shows the best agreement with the data for the low turbulence intensity, while the CH model predicts a very premature transition and the longest transitional length. Several 'numerical' factors (artificial dissipation, grid density etc.) are found to have an appreciable effect on the prediction of the transitional region in comparison with laminar and fully turbulent zones. Possible variation of the C_f coefficient due to the variation of 'numerical' factors is shown for the LB and FLB models. Numerical simulation of the flat plate flow with the higher inlet turbulence intensity, more typical for turbomachinery applications, shows that the LB model gives an earlier transition; while the FLB model is in better agreement with the data. This can be explained by the fact that the LB model is numerically less stable than the FLB model. The momentum Reynolds number at the start and at the end of the transition, predicted from the Navier-Stokes code, is compared with the correlation of Abu-Ghannam and Shaw (1980) and the boundary layer prediction (Fan & Lakshminarayana (1996)) in Fig. 3-6. The time-marching code predicts an earlier inception of the transition at low values of the turbulent intensity. Overall, the transition prediction by the Navier-Stokes code is close to the prediction by the boundary layer code based on the same turbulence model.

In addition to the quality of the particular low-Re turbulence model, the level of the artificial dissipation plays a crucial role in the prediction of the transition region. For the configuration more complex than a flat plate flow, the potential error due to the presence of the artificial dissipation is even more serious. For example, for the transitional flow in Penn State turbine, the location of the transition and the skin friction coefficient beyond the transition, strongly depend on the value of k_4 (Fig. 3-7). An excessive level of the artificial dissipation delays transition inception and ultimetely leads to the fully laminar boundary layer. An increase in k_4 results in the transition onset shifting from $x/C_x=0.65$ to the trailing edge on the suction surface. Grid refinement reduced this dependency, however, as shown in Chapter 6, it is practically impossible totally eliminate the effect of artificial dissipation on the transitional prediction. The essential feature of the current solver is that for the calculations with $k_4< 0.015$, the transition prediction is found to be independent of the level of the artificial dissipation coefficient. This value of the k_4 coefficient is found to be universal for other configurations (the flat plate, compressor cascade, LP turbine), under the condition that the solution is otherwise grid independent.

3.4 Modification of the k-ε model for the flows with dominant normal stresses

Models based on the eddy viscosity do not provide an accurate solution for the flow that deviates from linear stress-strain relation. The problem is aggravated if two-equation turbulence model is applied to flows that are essentially different from those used for the derivation of the model coefficients. Flow with dominant normal stresses is the case where k-ε model fails to provide a realistic prediction of the turbulence field. K-ε model developed for the shear flow tends to overpredict the local level of turbulent kinetic energy produced by the normal stresses. A significant amount of work both experimental and computational were carried out to investigate these type of flow (e.g., Cooper et al., 1993). Most of these efforts were concentrated on the analysis of the heat transfer associated with the impinging jet. Less attention to this problem was paid in aerodynamic simulations without heat transfer focus. This lack of attention can be explained by the relatively small influence of this problem on the overall accuracy of the prediction in many cases. Error in the energy redistribution between the mean flow and turbulence is about 1% for flows with Ma=0.4 and T_u=8%. However, an excessive level of turbulence prediction seriously affects the transition development in a turbomachinery stage, even in the case of the utilization of the transition model. In the turbomachinery stage an overprediction of turbulence occurs at two major locations. First zone is the stagnation flow near the leading edge. The correct prediction of the turbulence kinetic energy at this location is especially needed if the boundary layer has the transition inception close to the leading edge (compressor cascade, Chapter 4). Adequate turbulence intensity near the leading edge also makes the solver less "numerically" dependent (LP turbine, Chapter 6). The second region with the dominant normal stresses is the accelerated flow near the suction surface of the turbine blade. If no attention is paid to this region, turbulence intensity may be overpredicted by 3-7%, resulting in an earlier transition inception (turbine flows, Chapters 5 and 6).

Application of more complex, in comparison with standard k-ε, models (e.g., k-ε-v^2, Behnia et al., 1996) and second-moment closures (Craft et al., 1993) showed an improved prediction of flows with dominant normal stresses. However, current analysis is limited to the modifications for a k-ε model.

3.4.1 Modification of the turbulence model for leading edge flow

The modification of the turbulence near the leading edge of the blade results in an elevated level of k, strongly affecting the development of the turbulent boundary layer along the blade. Large flow turning and curvature effects, present in these leading edge flows, influence the development of the flow near the stagnation point. The experimental data on this effect, especially in turbomachinery stages, is scarce. The k-ε turbulence model predicts the level of the turbulent kinetic energy. As a result, the boundary layer becomes fully turbulent, with the transition occurring very close to the leading edge.

It is possible to separate the flow near the stagnation point into three regions. The first region is a freestream flow. In this region turbulent kinetic energy is balanced by the dissipation term in the k-equations. The second region is the thin boundary layer, developing from the stagnation point. In this region the mean flow and the turbulence equations are strongly coupled and should be solved simultaneously. The third region is the buffer zone between previous two zones. Despite the fact that the mean flow can still be considered inviscid and the development of the turbulence does not affect the mean flow variables in this region, the velocity gradients severely affect the development of the turbulence.

The modification of the k-ε model to improve the accuracy have been suggested by many investigators. The first group of modifications suggested consists of change in the production term. The production of the turbulence kinetic energy can be expressed (incompressible flow):

$$P = \nu_t((\frac{\partial U_j}{\partial x_i} + \frac{\partial U_i}{\partial x_j}) - \frac{2}{3}\delta_{ij}k)\frac{\partial U_i}{\partial x_j} = 2\nu_t S_{ij} \cdot S_{ij} \qquad [3\text{-}1]$$

Launder (1974) suggested the use of the rotation rate to modify the production term: $P = 2\nu_t\sqrt{(S_{ij})^2 \cdot (R_{ij})^2}$. The flow near (upstream) the stagnation point is nearly irrotational, while in the shear layer : $\sqrt{(S_{ij})^2 \cdot (R_{ij})^2}$ and: $(S_{ij}) \cdot (S_{ij})$ are practically equal. This modification reduces the production of turbulence only near the stagnation point, while the boundary layer is not affected. Jin and Braza (1994) proposed the production term of the form: $P = 2\nu_t R_{ij} \cdot R_{ij}$. This modification can be used only in a limited region near the stagnation point However, the experimental data gives an increase of k up to three times of the freestream value along the stagnation line. $P = 2\nu_t R_{ij} \cdot R_{ij}$ is zero along the stagnation line and correspondingly k will be about uniform.

In the second approach, the dissipation rate equation is modified. The equation for the turbulence dissipation rate is one of the 'weakest' parts of any turbulence model. The derivation of this equation is based on numerous assumptions. Strahle et al. (1987) suggested setting $C_{\varepsilon 2}$ and $C_{\varepsilon 1}$ (Eq. 2-6, Chapter 2) near the stagnation point in the dissipation equation. This modification is based on the consideration of the analytical solution for k and ε equations near the stagnation point. The potential solution was used to define velocities, i.e., it was assumed that the mean flow and turbulence equations are uncoupled in this region. According to Strahle et al. (1987), a consistent solution can be obtained only if $C_{\varepsilon 2}$ and $C_{\varepsilon 1}$ are equal. Due to the fact that $C_{\varepsilon 2}$ is based on the decay of grid turbulence $C_{\varepsilon 1}$ is chosen to be modified.

Numerical simulations have been carried out to assess various modifications to the turbulence model indicated above. In the case of time marching scheme, stiffness of k-ε equations and a highly stretched grid near the stagnation point lead to an additional difficulties near the leading edge. Viscous flow in the compressor cascade, described in Chapter 4, has been simulated using these modifications to the FLB k-ε model for the leading edge flow. The ratio of the normal to the shear stresses has been used as a switching function to switch from the modified $C_{\varepsilon 1}$ near the stagnation point to the original $C_{\varepsilon 1}$ in the shear layer. Results based on the original k-ε model, without the modification, predict a very high level of the turbulent kinetic energy near the leading edge, while models with the modified ε-equation predict smaller production of k, closer to the observed values. The original model predicts very low turbulent dissipation rate near the stagnation point. Due to an excessive production of the turbulent kinetic energy and a low level of ε, very large values of eddy viscosity are predicted. This leads to an excessive diffusion, which is not physical. As a result of this, the boundary layer becomes fully turbulent at the leading edge. All modifications improve the distribution of the turbulent kinetic energy and enable a reasonably good prediction of the transition. Predicted transition zone is located from about 33% of chord to 50% (this correlates well with the experimental data), with 5% variation between various modifications. The modification, due to Jin et al. (1994), leads to earliest transition inception while the modification of the ε equation tends to predict the latest transition inception. Due to a lack of the experimental data on the budget of the turbulent kinetic energy along the stagnation line, it is difficult to assess various modifications suggested. Approaches, based on the modification of the ε-equation and the modification of the production term, due to Launder and Spalding, have been chosen for the simulation of the unsteady transition described in following chapters and they are found to be crucial for the accurate prediction of the unsteady transitional flow.

3.4.2 Turbulence flow field in the freestream

The flow in turbine passage is another example of the case with normal stress dominance. Rapid flow acceleration/deceleration outside boundary layers generate normal Reynolds stresses (in streamwise direction) that are higher than a shear stress.

Comparisons between the predicted flow in Penn State turbine rotor (Chapter 5), based on k-ε model, and the measured data shows that turbulence intensities may be overpredicted by more than ΔTu= 5% (Fig. 3-8). This problem has two main consequences. First is the effect on the boundary level transition. For the unsteady numerical simulation it also affects the decay of the upstream wake through the turbine passage. In contrast to the stagnation point flow, this problem is not contaminated by the near wall effect, thus results are independent of low-Re part of the model. Simulations based on the Fluent code have been used to get more insight into the turbulence flow at a midpassage of the turbine blade. Three different turbulence models are utilized for this analysis; standard k-ε model, renormalized group k-ε model (Orszag et al., 1993) and Full Reynolds stress model. Fluent tends to predict more radical rise in the turbulence level (ΔTu=2-3%) in comparison with Penn State code, therefore the comparison is done between different turbulence models using the same code (Fluent, Fig. 3-9 and Penn State, Fig. 3-8). Utilization of the RNG k-ε model provides only a moderate improvement. This difference may be attributed to a modified coefficient of the RNG k-ε model rather than to improved physics. Second-order turbulence model significantly improves the predicted distribution of the turbulent kinetic energy (Fig. 3-9). Error in the prediction based on the k-ε model may be separated into two components; inadequate coefficient of the model and lack of the flow physics. A comparison of the streamwise and crossflow Reynolds stresses presented in Fig. 3-10 (note different scales for k-ε and FRSM predictions), indicates that the predicted normal stress differs not only in amplitude, but has essentially different distribution. Comparison of pseudo viscosity coefficient ε at the location of the maximum turbulence intensity shows that $\varepsilon_s \sim 2\varepsilon_n$. Therefore the adjustment of the k-ε model coefficient will not lead to the correct solution (e.g. RNG k-ε model can only moderately improve the solution). Application of the second-order turbulence closure for turbomachinery flows is beyond the framework of this thesis. Hence, modifications similar to those analyzed for the stagnation flow have been considered for the k-ε model modification. Only the modification of the prediction term based on $P = 2\nu_t\sqrt{(S_{ij})^2}(R_{ij})^2$ is found to be suitable for the current task (Fig. 3-8). The modification with the prediction in the form: $P = 2\nu_t R_{ij} R_{ij}$ has been found to underpredict the upstream wake dissipation in the case of the rotor-stator interaction.

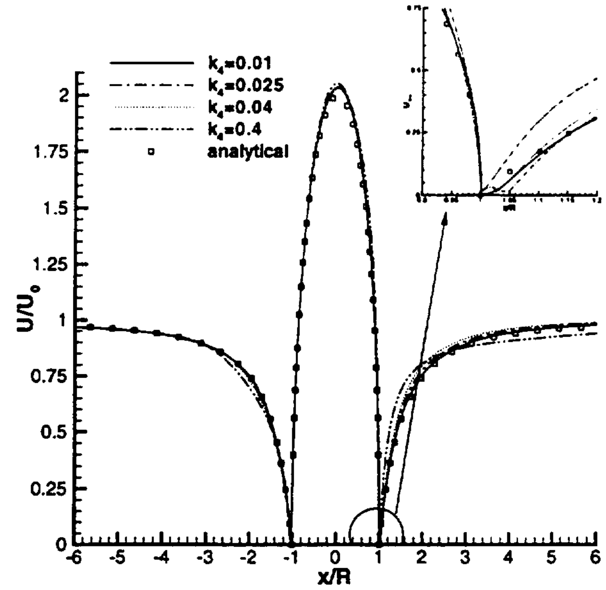

Fig. 3-1 Total velocity distribution along the stagnation streamline, inviscid simulation, “H” type gird

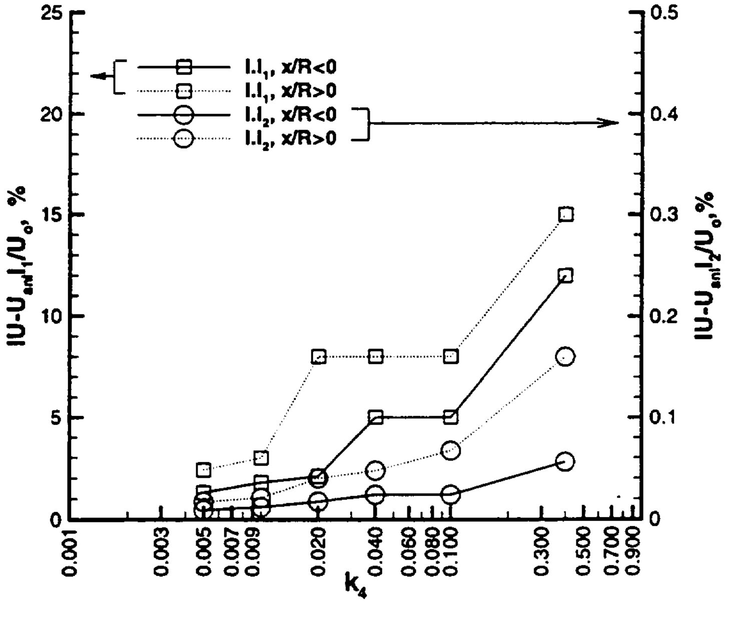

Fig. 3-2 Computational error

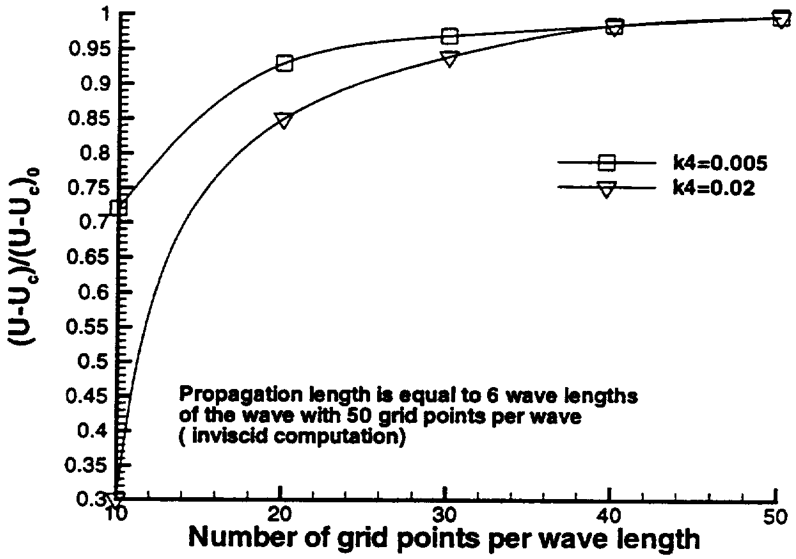

Fig. 3-3 Wake decay due to artificial dissipation

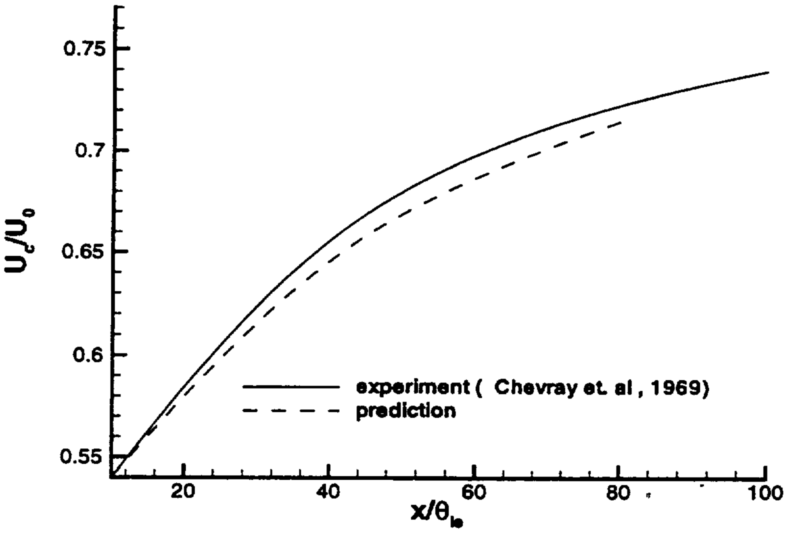

Fig. 3-4 Flat plate wake decay

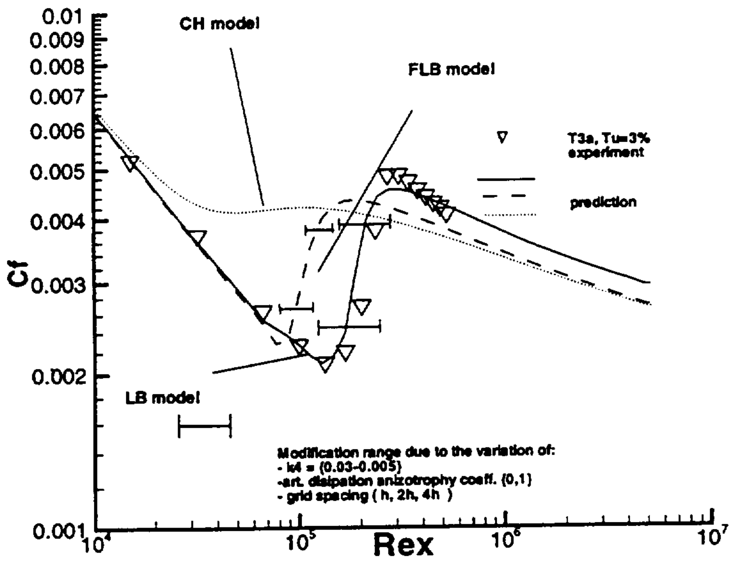

Fig. 3-5 Steady transition on a flat plate

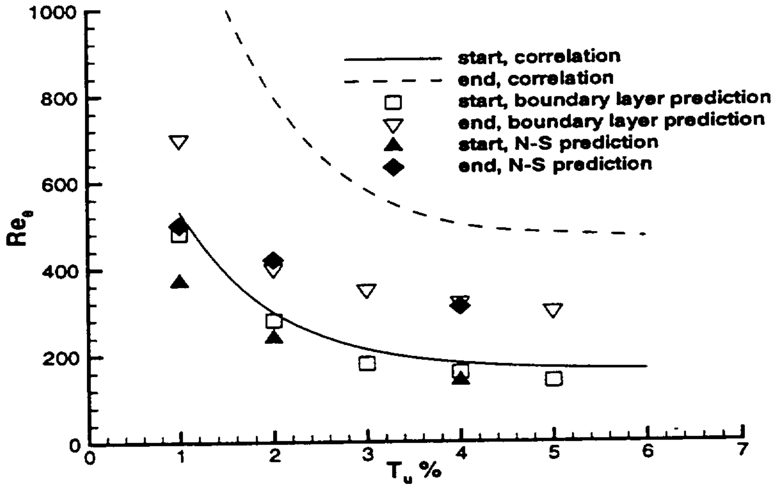

Fig. 3-6 Steady transition on a flat plate, correlation from Abu-Ghannam and Shaw (1980)

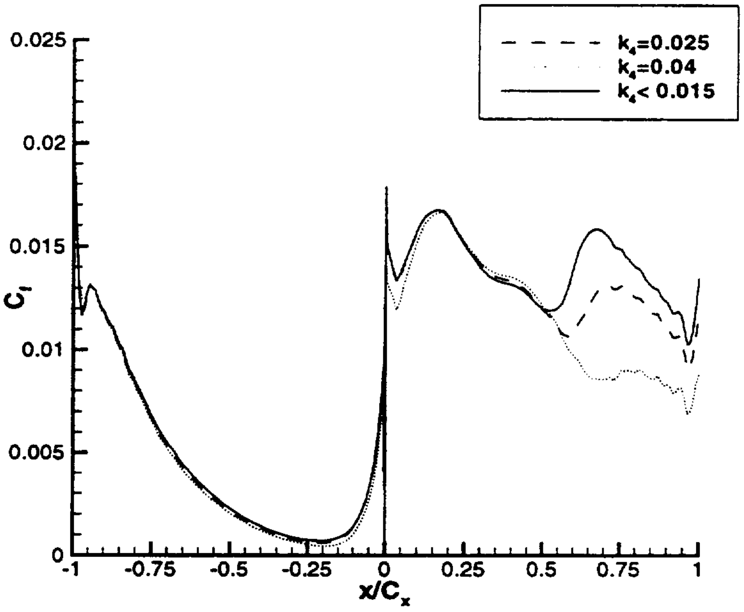

Fig. 3-7 Effect of the artificial dissipation on the skin friction coefficient on a rotor blade

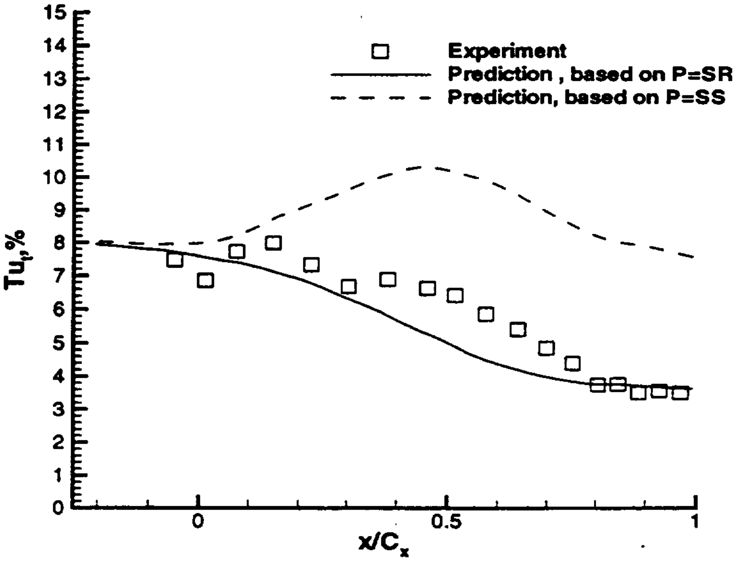

Fig. 3-8 Turbulence intensity at midpitch inside the rotor blade passage data due Zaccaria and Lakshminarayana, 1997b

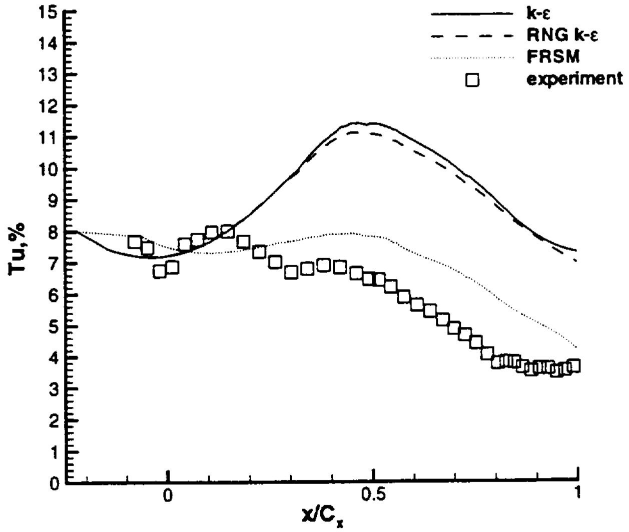

Fig. 3-9 Turbulence intensity at midpitch inside the rotor passage (FLUENT)

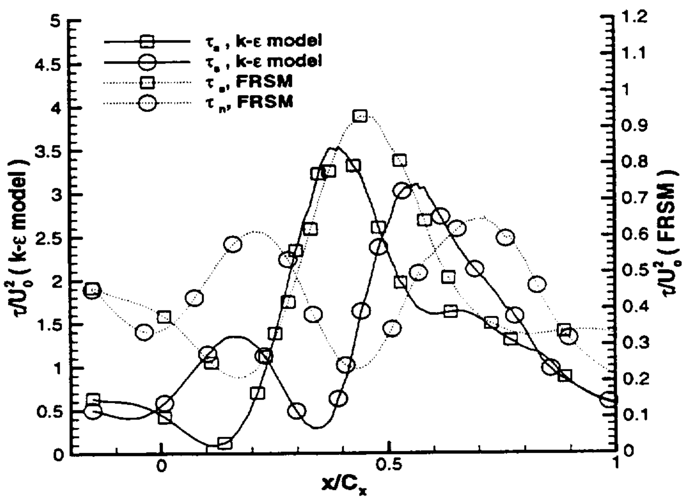

Fig. 3-10 Predicted distribution of the normal Reynolds stresses along midpassgae streamline (FLUENT)

Chapter 4

NUMERICAL SIMULATION OF THE UNSTEADY TRANSITIONAL FLOW IN A COMPRESSOR CASCADE

Simulations of the test cases, presented in the Chapter 3, establish the accuracy of the code for basic flows. Numerical analysis of the unsteady transitional flow in a compressor cascade, presented in this chapter, is carried out to assess the ability of the code to simulate realistic turbomachinery configurations. Even though attempts have been made to develop and use unsteady Navier-Stokes solvers for the prediction of rotor-stator interaction effects, none have been satisfactorily validated against accuracy, especially for its ability to capture the unsteady transitional viscous layers near blade and wall surfaces. This is the main objective of the research presented in this chapter. Characteristics of the different low-Reynolds k-ε turbulence models have direct impact on the ability of the code to simulate the unsteady transitional boundary layer. Further research is required to assess the applicability of the k-ε models for the unsteady flow modeling. Temporal accuracy of the code depends on the adequate choice of the number of inner cycles and the physical time iterations. Numerical simulation of the compressor flow is used to evaluate the influence of these factors on the accuracy of the prediction.

4.1 Compressor cascade description

Fan & Lakshminarayana (1996) used an unsteady inviscid two-dimensional code coupled with an unsteady boundary layer code to predict the unsteady flow caused by the transport of a simulated upstream rotor wake through an annular compressor cascade and compared the prediction with the data due Schulz et al (1990). The simulated rotor wake was generated using a rotor consisting of rotating rods (Fig. 4-1). The annular cascade had twenty four untwisted blades. Characteristics of the cascade are given in Table 4-1. Fan and Lakshminarayana (1996) used 241(streamwise) X 61(blade-to-blade) grid for inviscid calculation. For the boundary layer solution, 120 streamwise stations and 121 grid point normal to the wall were used.

Table 4-1 Compressor cascade characteristics

Pitch/Chord	0.78	Stager angle	29°
Steady inflow angle, α	44°, 49.2°	Inlet Ma	0.299
Re	4×10^6	Wake inflow angle	15.55°
Reduced frequency, Ω	6.12	Wake width parameter, ω	0.095
Wake velocity defect, A_0	28.3%	Variation of the turbulence intensity, ΔT_u	8 %

In the numerical simulation, the inlet wake was prescribed as a Gaussian distribution, this was found to be a good approximation of the measured wake:

$$V = V_0 + A_0 \exp(-\frac{(y - V_{0w}t)^2}{2\omega^2})$$

Similar distribution is used to prescribe an inlet distribution of turbulence characteristics. Amplitude and width are adjusted according to experimental parameters:

$$T_u = T_{u0} + \Delta T_u \exp(-\frac{(y - V_{ow}t)^2}{2\omega^2})$$

Where V_{ow} - wake pitchwise velocity.

To assess the accuracy of the code, predictions based on the Navier-Stokes procedure are compared with the data and with predictions from the Euler/boundary layer approach. In some instances, the comparison is done only with the Euler/boundary layer prediction, due to a lack of the experimental data. Cases with 44° and 49° inlet flow angles have been chosen for numerical simulations.

4.2 Sensitivity studies

Flow simulations have been performed using three different grids: 179x61, 189x95 (Fig. 4-2), and 201X193 to investigate the grid dependency. The distance between the first grid point and the wall varies from y+=1.6 for the coarse grid to y+=0.6 for the fine grid. Numerical simulation of the steady flow (C_p and C_f distributions) do not show any significant difference between predictions with 201x193 and 189x95 grids. Numerical simulation of unsteady flows impose additional requirements on the grid generation. Grid should be fine enough to allow a correct propagation and decay of the unsteady wake through the passage. The numerical analysis presented earlier (Chapter 3) is used to satisfy this requirement. Fourier decomposition of the inlet wake shows that it has five essential harmonics (based on blade passing frequency). Amplitude of the fifth harmonic is found to be only 1.3 % of an amplitude of the first harmonic. The grid with 193 grid points in the y-direction enables the wake to propagate through the cascade without non-physical decay, caused by numerical factors. In the case of 95 grid points in y-direction, only the fifth harmonic is affected by the artificial dissipation. This effect can be neglected, because the fifth harmonic is dispersed rapidly by the physical dissipation. As a result of the grid dependency analysis, 189x95 grid has been chosen in all computations.

The choice of the number of physical time steps per period and the number of inner iterations at each physical time step is an additional factor which affects the accuracy of the unsteady flow simulation. An increase in the number of physical time steps leads to a growth in the temporal accuracy and reduced phase errors. The main requirement is that the physical time step should be small enough to resolve the smallest time scales. Previous research indicated that about 500 physical time steps per period is required for the accurate solution of the wake-blade interaction effect. An increase in the number of physical time steps also affects the number of inner iterations, because of the smaller initial error. The change in the number of physical time steps modifies convergence characteristic of the scheme with a pseudo time stepping. For the case when $\Delta t \rightarrow \infty$ (a steady state solution), the additional source term due to the presence of the physical time derivative vanishes. Additional damping at low wave numbers disappears and correspondingly, the convergence of the inner cycle in the freestream slows down. To analyze the effect of the number of physical and inner iterations on the accuracy of numerical results, a number of numerical tests have been carried out.

Numerical simulations were performed with 500 physical time steps and 10, 20, 50 inner iterations. About 1.5 order of magnitude drop in the maximum residual (mean flow equations) was achieved with 10 inner iteration at each physical time steps, this number increased to 2.5 for 50 inner iterations. A comparison of the predicted amplitude of the first harmonic of the unsteady pressure (ΔC_p) on the blade is shown in the Fig. 4-3. There is no significant difference between 20 and 50 inner iterations. Similar results were obtained for other harmonics and phase angles. On the other hand (Fig. 4-4), there is a significant change in the amplitude C_f variation on the suction surface, when the number of inner iterations is increased to 50. Additional numerical experiments showed that further increase in the number of inner iterations does not affect the accuracy of the unsteady C_f distribution. Unsteady skin friction coefficient on the pressure surface is less sensitive to this factor because of the thin boundary layer. The convergence of the unsteady pressure depends on the convergence characteristics of the numerical scheme in the freestream. As it was indicated previously, inlet wake has five essential harmonics. This corresponds to the wave number range of 0.03 to 0.15. The ratio of the pseudo time step to the physical time step is high outside the boundary layer. As a result, an additional damping of the low wave number harmonics provides very rapid convergence of the unsteady freestream flow. During first 10 iterations the inner cycle convergence is equal to an analytical value based on the freestream $\Delta\tau/\Delta t$ ratio. This fact also supports the previous conclusion. On the contrary, the correct prediction of the unsteady C_f requires an accurate simulation of the unsteady velocity in the boundary layer. In addition to employing smaller inner steps due to the fine grid, there is no 'positive' effect of the source term in this region ($\Delta\tau/\Delta t \sim 0$). Thus the prediction of the unsteady velocity requires more inner iterations.

Numerical simulations with 250, 500, 1000 physical time steps were carried out to estimate the influence of the number of physical time steps. The number of inner iterations was 20 for all cases. According to the previous analysis, this number is sufficient to achieve a converged pressure field. The comparison, presented in Fig. 4-5, indicates that at least 500 steps are required for the accurate prediction.

4.3 Unsteady pressure field

The predicted pressure distribution and the unsteady pressure envelope on the blade are shown in Fig. 4-6. The time averaged blade pressure distribution from the Navier-Stokes code is more accurate than the prediction from the Euler code and is also in a good agreement with the experimental data. This is due to the presence of the separated region at about 90%-95% of the chord. The predicted time history of the unsteady pressure is compared with the experimental data in Fig. 4-7. There is a good agreement between predictions and the experimental data. Numerical simulation correctly predicts the maximum unsteadiness near the leading edge, where the wake hits the blade. This is caused by a change in the incidence angle and chopping of the wake by the blade. Beyond 20% of the chord, the development of the recirculating flow pattern, induced by the passing wake, plays a dominant role in the development of the unsteady pressure. This leads to the region of an increased instantaneous pressure along the wake path. Fig. 4-7 indicates that unsteady pressures are predicted well up to 20 percent of the chord, which is the most important and crucial part of the blade. Both the Euler and the Navier-Stokes code predict smaller pressure variation in comparison with the experimental data, especially from x/Cx=60% to x/Cx=80% on the suction surface. This discrepancy is due to three-dimensional effects in the annular cascade. Flow visualization (Schulz et al, 1990) showed a strong corner separation. Interaction between the upstream wake and the corner separation leads to an amplification of the pressure oscillations. As expected, the Navier-Stokes solution predicts smaller amplitude in the unsteady pressure at the midchord in comparison with the Euler prediction due to the wake decay caused by the physical dissipation. There is a region of an increased unsteadiness in pressure near the trailing edge. This is due to the interaction between the passing wake and the separated region near the trailing edge. The Navier-Stokes code correctly predicts this feature (Fig. 4-5 and Fig. 4-7). While the flow is attached up to 97% of chord, velocity profiles from 85% of chord indicate a 'near separation' character of the flow.

The development of the unsteady pressure field can be explained on the basis of two main mechanisms: wake cutting by the leading edge with the associated modification of the incidence angle and the development of the recirculating pattern due to the passing wake. Both phenomena are predominantly inviscid. As a result, both the Euler and the Navier-Stokes code predict nearly identical unsteady pressure field.

4.4 Development of the unsteady transitional flow

Prediction of the unsteady transitional flow is crucial in evaluating loses, efficiency and cooling requirements of turbomachinery. None of the Navier-Stokes procedures have been validated for their ability to predict the unsteady transitional flow. Numerical simulations have been carried out using three low Re k-ε models: CH, FLB and LB. The leading edge modification of k-ε models, described earlier, was found to be crucial for correct prediction of the transitional flow. Despite the modifications for the leading edge effect, the calculation with the CH model predicts fully turbulent flow all along the blade. Hence, the numerical simulation based on the CH model is not presented.

As shown in Fig. 4-8a, in the boundary layer solution the transitional region extends from $x/C_x=0.1$ to $x/C_x=0.30$. An examination of the skin friction coefficient distribution in conjunction with the turbulence field shows that the Navier-Stokes code with the FLB model predicts transition from $x/C_x=0.12$ to $x/C_x=0.4$, while the computation based on the LB model predicts transition from $x/C_x=0.1$ to $x/C_x=0.3$. An understanding of the complex transitional process on the suction surface can be obtained from a study of the time history of the skin friction coefficient presented in Fig. 4-8. The trend predicted by both the Navier-Stokes code and the Euler/boundary layer code are in a very good agreement, unsteady fluctuations predicted by the Navier-Stokes code are slightly lower due to the decay of the wake, which is neglected in the Euler code.

Wake induced transition is a very complex phenomenon driven by the interaction between the mean flow and the turbulence field. In this compressor cascade, the transitional region is located near the leading edge. Amplification and modification of the wake and turbulence due to the interaction with the leading edge affect the development of the transitional process. In Fig. 4-8b, path I corresponds to the upstream wake propagation at the edge of the boundary layer, based on the maximum wake defect at that location. Path II (Fig. 4-8b) is the location of the maximum velocity fluctuations in the boundary layer. Beyond 20% of chord, an increase in phase lag between the convection velocity in the boundary layer and in the freestream is observed. An interesting phenomenon takes place in zone A (Fig. 4-8b), along path II. At t/T=0, the wake is located at the leading edge (path I). Change in the incidence angle seriously affects the pressure distribution near the leading edge of the suction surface. As a result of this interaction, a zone with a reduced velocity is generated from 5% to 15% of the chord above the suction surface. This region modifies the development of the boundary layer. A zone of a low mean flow is located near the leading edge from about t/T=-0.1 to t/T=0.15 (Fig. 4-7 and Fig. 4-8) and disappears after passing of the wake. This phenomenon accounts for the difference in the location of the minimum C_f predicted by the Navier-Stokes and the boundary layer code shown in Fig. 4-8. Following the classification suggested by Halstead et.al. (1995), it is possible to identify various regions associated with the wake induced transitional flow. In Fig. 4-8b, A is the region of the wake induced transition. Disturbance due to the wake-boundary interaction leads to an earlier transition. The region B is a region with a transition between wakes and a zone with some features associated with the becalmed region. This region is located downstream of the small, fully laminar zone L. There is a smooth decrease in the shape factor H in the zone B (line Z, Fig. 4-9), while in the region of the wake induced transition, a sharp drop of H (line Y) indicates an abrupt transition from the laminar to the turbulent flow. A comparison between predictions based on the FLB model and the LB model shows that the LB model predicts an early transition (Fig. 4-9). Zone C is the wake induced turbulence strip. Two counterrotating vortices inside the boundary layer, generated by the interaction of the upstream wake with the cascade flow, have a major influence on the unsteady boundary layer downstream of the transitional region. A clockwise rotating vortex near the leading edge of the wake, leads to a smaller C_f in the region C. The skin friction coefficient in the region D (trailing edge of the wake) has an increased level of C_f as a result of the counterclockwise vortex. Boundary layer simulation predicts no change in the skin friction coefficient in this region. The Navier-Stokes simulation provides more accurate simulation of the wake behavior in the outer region of the boundary layer and predicts the extended region of this counterclockwise vortex (about 20% of chord). Due to the presence of this vortex, the boundary layer profile has larger gradients near the wall resulting in increased shear stresses between wakes.

The transitional flow and the unsteady boundary development are controlled by both the mean velocity defect and turbulence variation in the wake. These two factors have dissimilar influence in different regions. Unsteady interaction between the mean flow and the turbulence field, with a phase lag between the velocity, the pressure, and the turbulence quantities make the flow very complex. It is possible to estimate the importance of these two mechanisms from an analysis of the unsteady flow field simulated by the Navier-Stokes solver. In the wake induced transitional strip (zone A in Fig. 4-8 and Fig. 4-9), the influence of the velocity defect has the dominant influence. While the turbulence intensity in the wake reaches 10%, the phase lag between k in the freestream and k in the boundary layer reduces the influence of the increased turbulent kinetic energy at this location. An opposite effect is felt in the region B, which is located between wake paths. The amplification of the unsteady turbulence near the leading edge leads to an increased level of k from 10% to 30% of the chord. Additional diffusion of the turbulence from the freestream results in a smoother transition, as seen along line Z in Fig. 4-9b.

One of the characteristic features of the unsteady boundary layer is the phase lag between the velocity at the edge and inside the boundary layer. The distance between path I and path II (Fig. 4-8b) is widening with the development of the boundary layer downstream of the leading edge. This is an indication of an increased phase lag in the velocity field. The amplitude and the phase angle of velocity fluctuations are shown in Fig. 4-10. This phase lag increases from about 30° at $X_c/C=0.4$ to 100° at $X_c/C=0.76$ (Fig. 4-10b). The predicted phase angle and the amplitude of the first harmonic of the total velocity correlate well with predictions from the boundary layer code. The Navier-Stokes solution predicts sudden increase of the phase lag in the laminar sublayer. This can be attributed to an inadequate grid resolution in this region. It should be remarked here that the boundary layer code employs 121 grid points inside the boundary; nearly four times as many as that used in the Navier-Stokes solver. Considering this, the agreement is good. This is one of the most important and critical steps in the validation of the Navier-Stokes code. With proper control of the artificial dissipation, grid, and time step, the Navier-Stokes code can be used to predict the unsteady transitional boundary layer accurately.

The predicted momentum thickness, shown in Fig. 4-11, reveals an excellent agreement with the experimental data and the Euler/boundary layer prediction. Similar to the boundary layer solution, the Navier-Stokes solver predicts a higher level of the time-averaged momentum thickness in a comparison with the steady state solution. This is an indication of an increased loss due to the unsteady interaction. According to the flow visualization, the flow separation occurs near 90% chord. The main drawback of the boundary layer approach is its inability to simulate the separated flow. The Navier-Stokes code correctly predicts separation zone, existing from 87% of chord. The predicted separation has an unsteady character, flow conditions vary from the fully attached to the separated flow. A sharp increase in the momentum thickness beyond 85% of chord is due to an earlier separation caused by the passing wake.

4.5 Stator wake

The development of the stator wake is influenced by its interaction with the upstream rotor wake. As described previously, the passing wake generates two counterrotating vortices which have considerable influence on the development of both the pressure and suction side boundary layers. The amplitude and extent of the secondary vortices inside the pressure surface boundary layer are smaller due to extremely thin boundary layers. Vortices inside the suction surface boundary layer play a dominant role in the development of the unsteady wake. This is evident from the unsteady velocity and turbulent kinetic energy distribution in the static wake shown in Fig. 4-12, Fig. 4-14, and

Fig. 4-13 respectively. The unsteadiness is higher away from the wake center. This distribution is very similar to that inside the boundary layer shown in Fig. 4-10a. The fluctuations are zero at the wall and this is reflected in a very low unsteadiness inside the wake center. Maximum unsteadiness in kinetic energy occurs on the suction side of the wake and the reasons for this are explained below.

The convective speed of the upstream wake is different for the pressure and suction surfaces. At the trailing edge, the phase angle difference between the passing wake near the suction surface and the pressure surface approaches 100°. This is an additional source of the unsteadiness in the wake. Clockwise vortex generated inside the boundary layer due to the wake-boundary layer interaction is shed into the stator wake, thus amplifying unsteadiness due to the wake passing. Clockwise rotating vortex, located above the stator wake, produces a system of counterrotating vortices in the stator wake. The presence of the unsteady vortices in the boundary layer creates an additional unsteady amplification of the wake turbulence. Fig. 4-13 indicates that this amplification is much higher on the suction side of the profile wake in comparison with the pressure side. The unsteady total velocity and turbulence kinetic energy distribution in the wake (Fig. 4-12 and Fig. 4-13) indicate that the disturbance due to the passing wake is mainly concentrated in the first harmonic. The effect of the counterrotating vortices and its shedding is mainly confined to second and third harmonics. Interaction between vortices also leads to an amplification of the spatial oscillation of the wake. The deviation in the trajectory of the center line of the wake is about 3% of the chord at x/Cx=1.29.

The interaction between the passing wake and the profile wake results in complex vortex structure, increased unsteadiness in the profile wake and high level of turbulent kinetic energy. These effects result in increased dissipation and faster decay of the stator wake. Thus the presence of the unsteadiness due to the rotor-stator interaction tends to decay profile wake faster. The time history of the instantaneous velocity, shown in Fig. 4-14, clearly reveals the location and the extent of the maximum interaction region. This occurs when the passing wake is directly inside the profile wake. The effect of additional shed vortices, causing additional oscillations, is also evident from this plot.

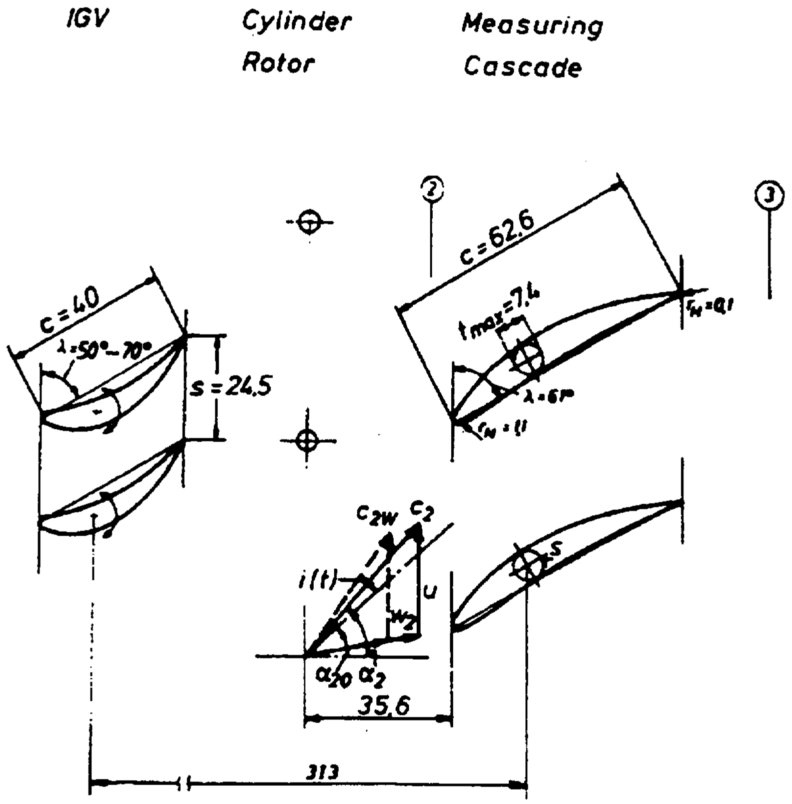
IGV
Cylinder Rotor
Measuring Cascade
②
③
c=40
λ=50°–70°
s=24,5
c=62,6
tmax=7,4
rN=0,1
rN=1,1
c2w
c2
i(t)
u
w2
α20
α2
s
35,6
313

Fig. 4-1 Scheme of the experiment

Fig. 4-2 Computational grid

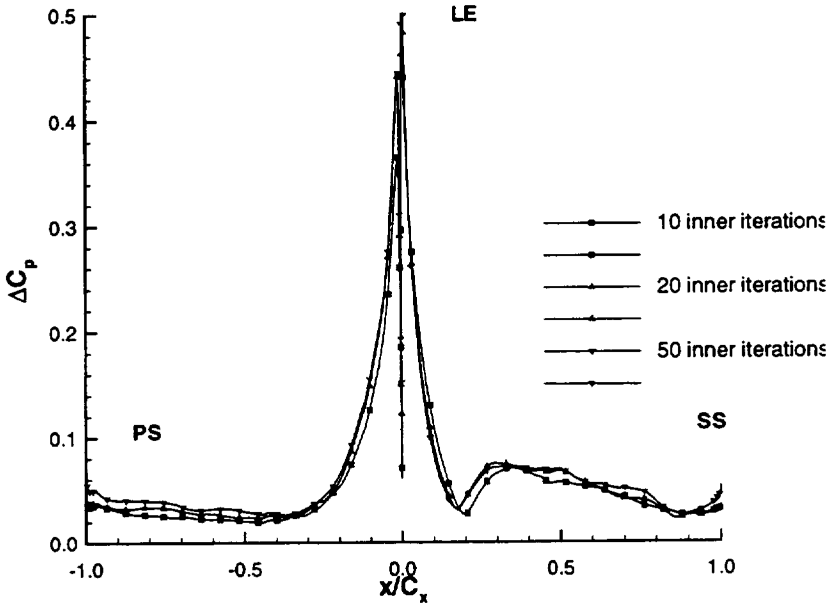

Fig. 4-3 Influence of number of inner iterations on the amplitude of unsteady pressure

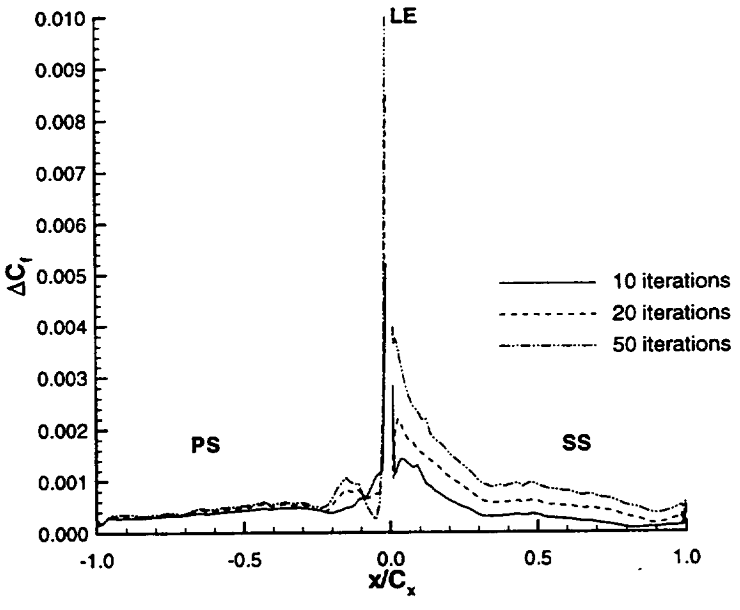

Fig. 4-4 Influence of number of inner iterations on the amplitude of skin friction coefficient

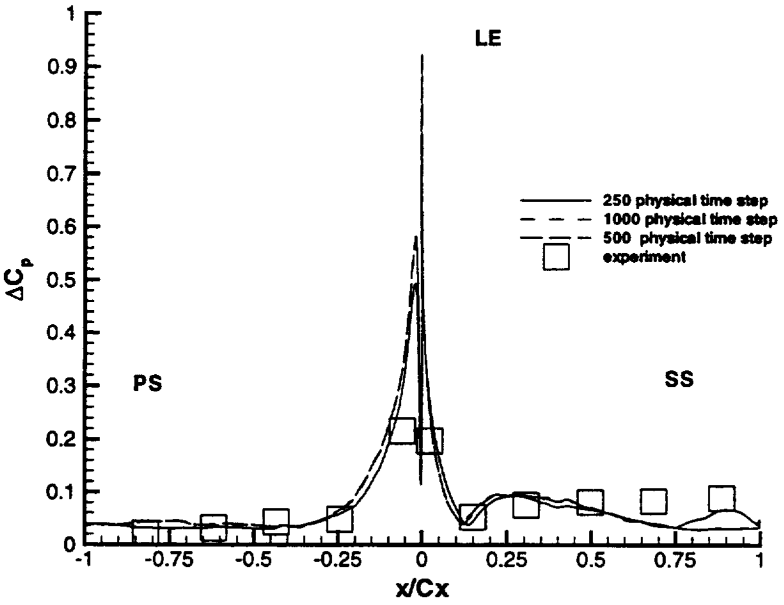

Fig. 4-5 Influence of the physical time step on the amplitude of unsteady pressure

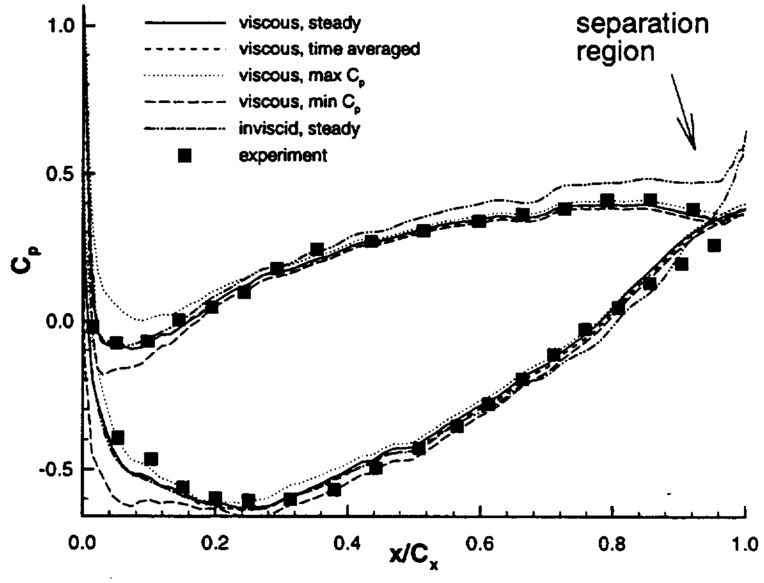

Fig. 4-6 Blade pressure distribution

a) Navier-Stokes prediction

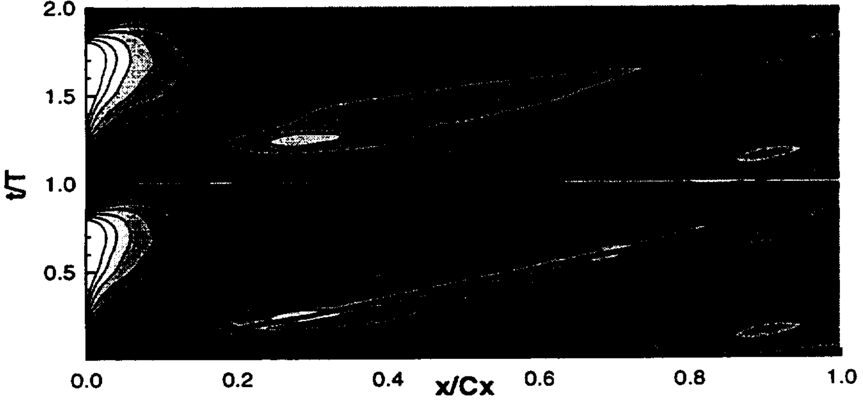

b) Euler/boundary layer prediction

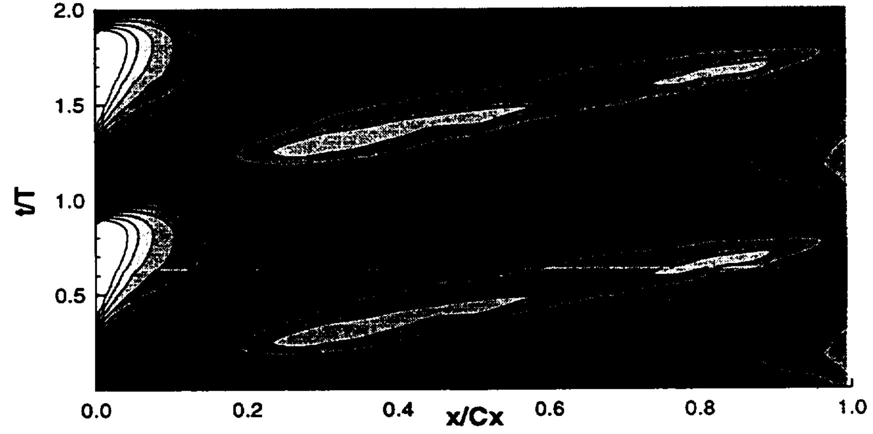

c) Experiment

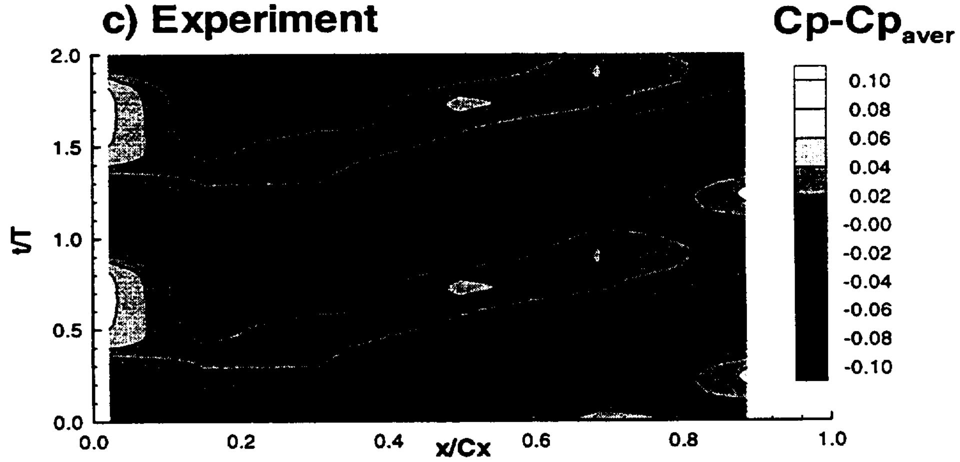

Fig. 4-7 Unsteady pressure distribution, suction surface

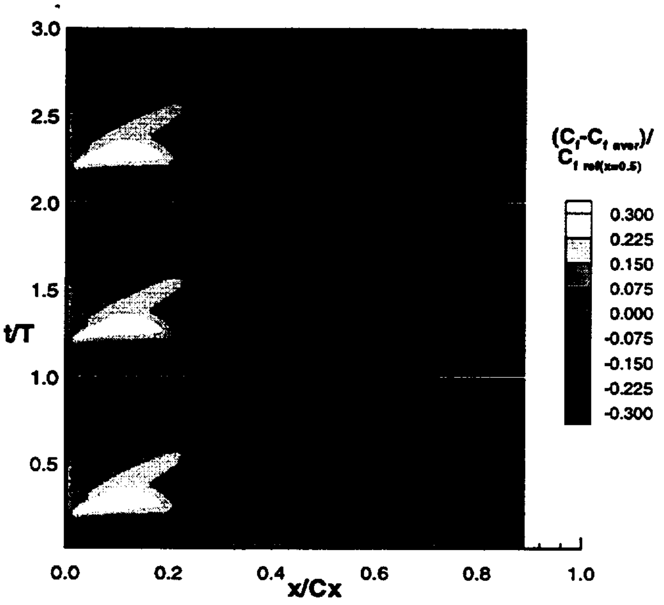

a) boundary layer prediction, FLB model

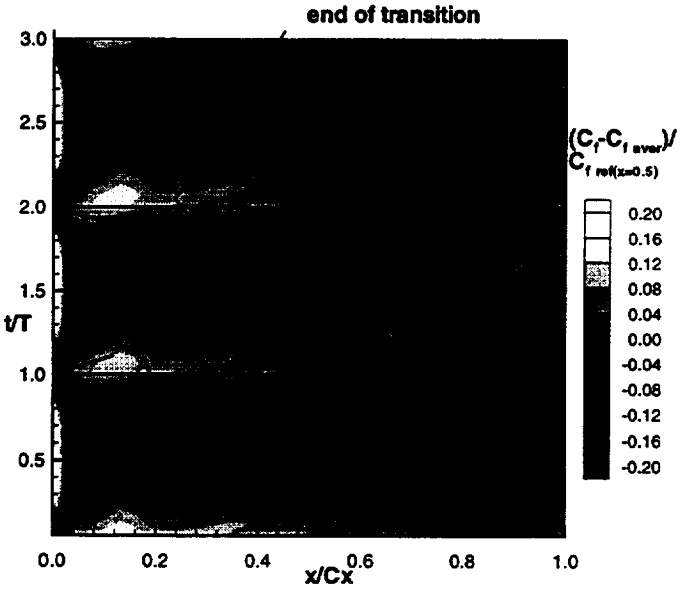

b) full Navier Stoke prediction, FLB model

Fig. 4-8 Skin friction coefficient

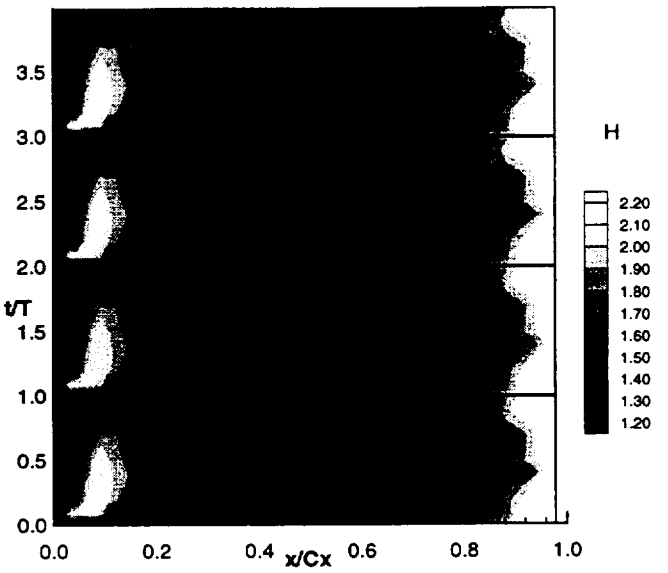

a) Navier-Stokes prediction, LB model

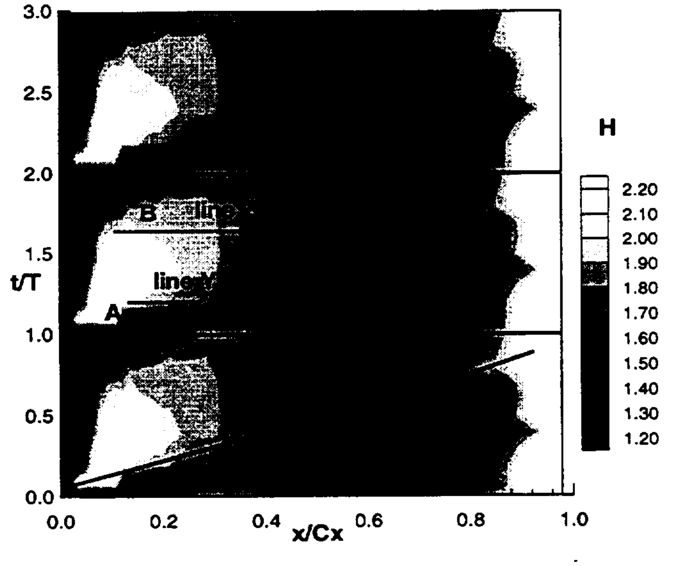

b) Navier-Stokes prediction FLB model

Fig. 4-9 Shape factor

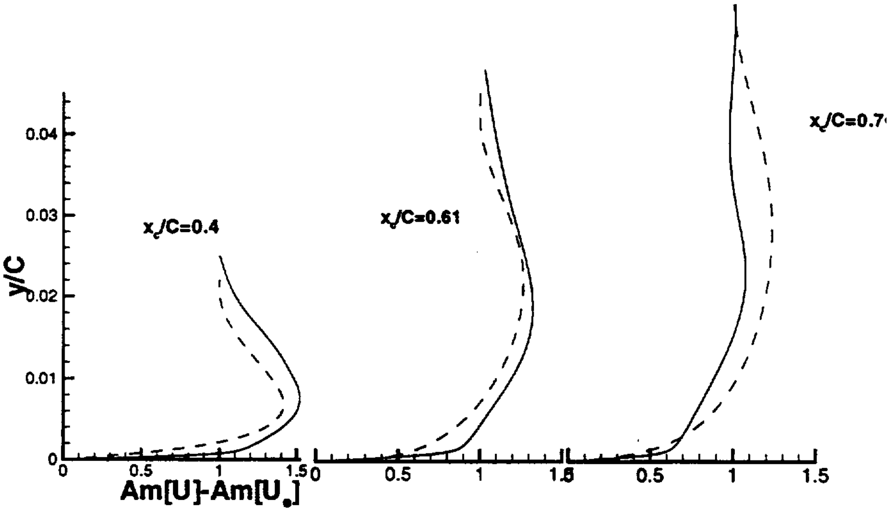

a) amplitude

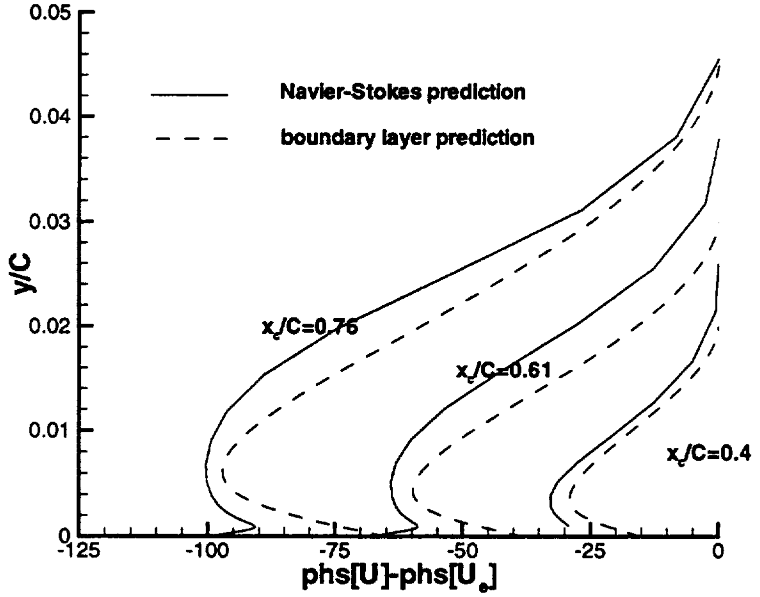

b) phase angle
Fig. 4-10 Velocity profile

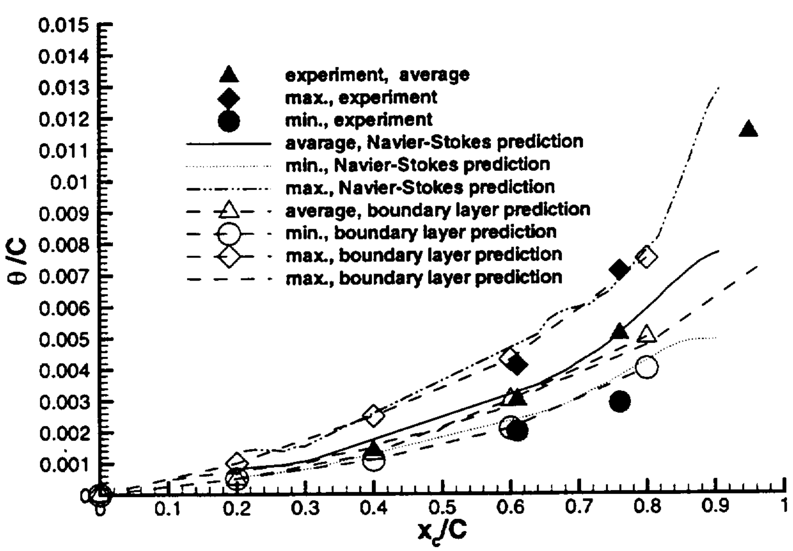

Fig. 4-11 Momentum thickness, suction surface

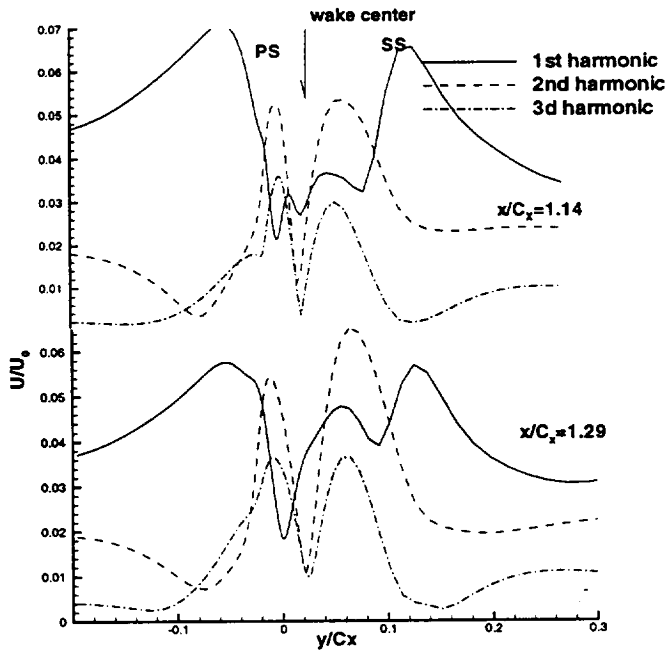

Fig. 4-12 Amplitude of the total velocity in the stator wake

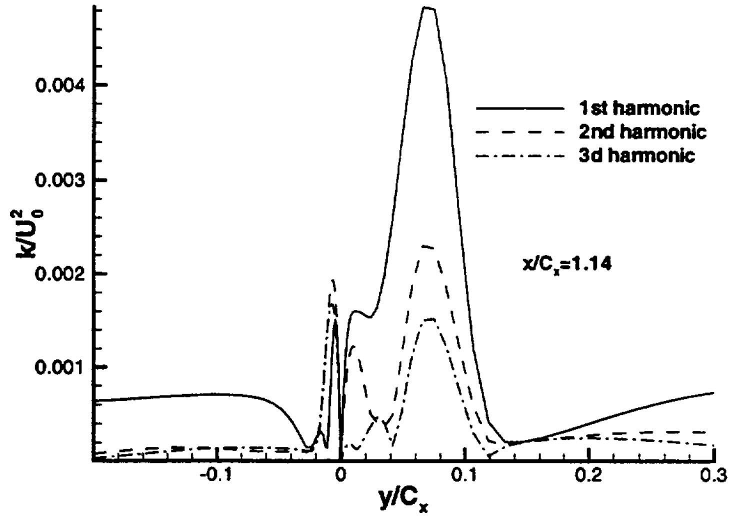

Fig. 4-13 Unsteady turbulent kinetic energy in the stator wake

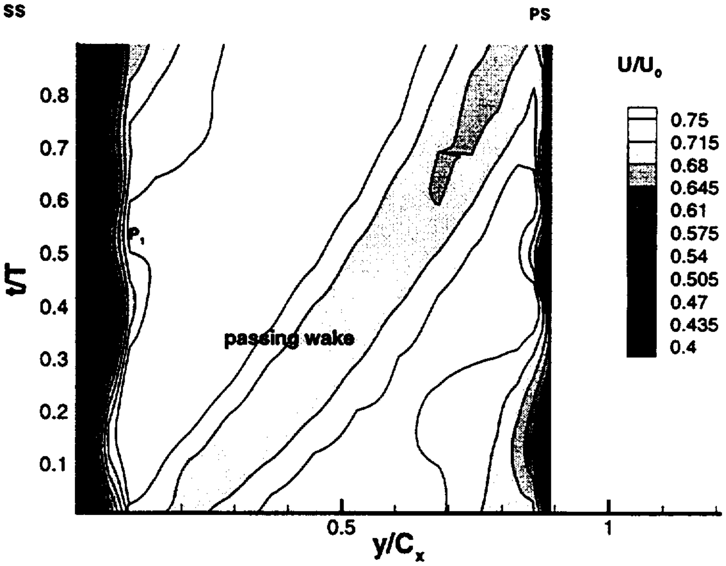

Fig. 4-14 Blade to blade distribution of the total velocity x/C_x=1.29

Chapter 5

UNSTEADY FLOW IN TURBINE

Rotor-stator interaction in a turbine stage has more complex structure in comparison with the unsteady flow in the compressor cascade analyzed in the previous chapter. In a compressor, the upstream wake propagates as a set of straight segments. The shape of each wake segment undergoes only minor distortion when the wake is transported through the compressor stage. Significantly higher turning and acceleration of the flow in a turbine stage results in a strong distorution, twisting and stretching of the wake segment. There is an increased phase lag between the flow at the midpitch and at the edge of the boundary layer. The difference in the relative wake-flow alignment also contributes to the modified rotor-stator interaction in a turbine stage. The ultimate solution of the rotor-stator interaction has to come from a systematic, scientific, and building block approach. The measurement in an actual engine is not only complicated, but will rarely provide an insight into numerous sources of unsteadiness. Likewise, a computational code with artificial dissipation and numerical error may mask some of the important physics. The major objective of this research is to understand the nature and magnitude of unsteadiness in turbines and develop insight for incorporation of these effects in the design and analysis. This objective is accomplished through a coupled experimental and computational study. Author has carried out the computational part and participated in the interpretation of the experimental data. The experimental data was acquired by D.Ristic (Lashminarayana et al., 1998).

The coupled experimental and computation study carried out at Penn State, which is more comprehensive than hither to attempted, should provide a detailed understanding of the flow physics. Almost all earlier experimentalists have concentrated their effort on blade surface measurements (e.g., pressure, skin friction, and transition). The present approach is to derive information on both the velocity field and the blade surface properties due to rotor-stator interaction. Likewise, the computational approach involves a development of a two-dimensional unsteady Navier-Stokes code, incorporating the transition and turbulence models to predict the nozzle wake, unsteady rotor blade boundary layers, unsteady free stream flow field and blade pressures accurately, and carrying out a simulation study to understand the sources of unsteady viscous flow through turbomachinery stages, including its effects on the transition and aero-thermodynamic losses.

5.1 Experimental Program

The Axial Flow Turbine Research Facility (AFTRF) of The Pennsylvania State University is an open circuit facility 0.9166 m (3 feet) in diameter and a hub-to-tip radius ratio of 0.73, with an advanced axial turbine blading configuration (Fig. 5-1). The facility consists of a large bellmouth inlet, followed by a test section with a nozzle vane guide row and a rotor. There are 23 nozzle guide vanes and 29 rotor blades followed by outlet guide vanes. A window for LDV measurements covering the entire flow field from upstream of the nozzle to downstream of the rotor passage is also incorporated. Detailed design of the facility, performance, and geometric features are described in Lakshminarayana et al. (1992). Some important performance and geometric parameters are as follows: ratio = 0.7269; Nozzle, axial chord (midspan) = 11.23 cm, turning angle = 70 degrees; Rotor : hub/tip axial blade chord (midspan) = 9.294 cm, turning angle = 95.42 degrees at tip, and 125.69 degrees at root, tip clearance = 0.97 mm; Reynolds number of nozzle flow (based on exit flow) = 10^6, mass flow rate = 11.05 kg/s, loading coefficient ($2\Delta P_0 / \rho U_m^2$) = 3.88, rotational speed = 1330 rpm. The vane-blade spacing is 22.6 % of the nozzle axial chord at the midspan. The design velocity triangles at the inlet and exit of the rotor are shown in Fig. 5-1.

Comprehensive data was acquired within and downstream of the nozzle during the earlier phase of the research program. A complete five-hole probe survey was carried out at 2.5 and 9% nozzle chord downstream of the nozzle trailing edge (Zaccaria and Lakshminarayana, 1995). Furthermore, LDV measurements carried out at midspan of the rotor (upstream to downstream) establishe the details of the distortion and the nozzle wake profile upstream of the rotor (Zaccaria and Lakshminarayana, 1997b). Hence all the rotor inflow properties (time dependent in rotor frame) are known and shown in Fig. 5-2. The LDV measurements at the rotor midspan are carried out at the design condition (Table 5-1). The blade dynamic pressure data at midspan and hub are acquired at design and three off-design conditions, and these are shown in Table 5-1. This was achieved by varying the turbine speed and the mass flow. The off-design data listed in Table 5-1 is based on the one-dimensional consideration. The upstream flow field was not acquired at the off-design conditions. The inlet flow properties (x/C_x = -0.224) are shown in Fig. 5-2 at mid span (H = 0.5) of the rotor and near the hub (H = 0.035). These are also the inlet conditions used for the computation. It is clear that substantial velocity, flow angle, stagnation, and static pressure gradients exist in the nozzle wake, both at the hub and the midspan regions. Most of the earlier research was carried out at larger nozzle-rotor spacing, where the pressure wakes do not exist as they decay rapidly downstream. The present measurement is carried out at practical spacing; and hence, all the features of modern turbines are present, including both the pressure and velocity gusts due to the viscous wakes. The flow field near the hub includes secondary flow regions as evidenced by the defect in velocity, static pressure, and stagnation pressure near the outer edge (suction side) of the wake.

Table 5-1 Operating Conditions

Operating Conditions	A Design	B	C	D
Mass flow (Kg/s)	10.42	10.42	5.82	5.82
RPM	1330	1235	1100	800
V_x (ms)	30.43	30.43	16.8	16.8
U_m (ms)	55.32	51.35	45.75	33.27
Rotor inlet flow angle , β_1, (deg)	41.44	45.76	-4.75	33.4
Incidence (deg)	-1.9	2.06	-44.9	-7.6
$\Omega = \varpi C_x / V_x$	4.89	4.54	7.32	5.82
Re	2.15x 10^5	2.15x10^5	1.19x10^5	1.19x 10^5

The reduced frequency based on the upstream nozzle wake frequency, rotor axial chord and axial velocity upstream of nozzle varies from 4.54 to 7.32. Since there are significant differences between the condition A (design) and C (off design), only the data at these two conditions are presented and interpreted.

5.1.1 Laser Doppler Velocimeter Data

Detailed steady and unsteady flow data were acquired at midspan of the rotor blade using a two-dimensional laser doppler velocimeter. Since the flow is two-dimensional at this spanwise location, only the axial and tangential velocity components were measured. The measurements were carried out at 37 axial locations upstream of the rotor (x/C_x=-0.088) to one chord downstream of the rotor (Zaccaria and Lakshminarayana, 1997b). To account for the non-uniformity of the rotor absolute inlet flow field, measurements were made at six tangential locations in the absolute frame equally spaced over one nozzle pitch (Fig. 5-1). These six tangential positions represent six different relative positions between the nozzle and the rotor (labeled position 1 through 6) or if viewed from the nozzle frame of reference, six different time-resolved positions of the rotor in relation to the nozzle.

At each survey point, approximately 120,000 velocity measurements were acquired. Since all the velocity components were spatially phase-lock averaged, which result in a representative rotor passage with 50 measurement windows, there were 2400 velocity measurements on average in each measurement window. After all instantaneous velocity measurements were acquired for each particular survey point, the velocity was ensemble-averaged at each measurement window. The unresolved velocity for each measurement window can be calculated as

$$V' = V_i - \overline{V} \qquad \text{[Eq. 5-1]}$$

where V_i is the instantaneous velocity measured at a particular rotor measurement window. The variance is given by:

$$\overline{(V')^2} = \frac{\left[\sum\limits_{i=1}^{n} (V_i - \overline{V})^2 \right]}{(n-1)} \qquad \text{[Eq. 5-2]}$$

The level of unresolved unsteadiness in each measurement window is determined by the variance. For the LDV measurements in the rotor, the instantaneous velocity, V_{in}, is decomposed as follows

$$V_{in} = \overline{V} + \tilde{V} + V' \qquad \text{[Eq. 5-3]}$$

where $\overline{V}$ is the time-averaged velocity, $\tilde{V}$ is the periodic velocity and V' is the unresolved velocity component as calculated in Eq.5-1 .

The cycle-averaged values were obtained by averaging the ensemble-averaged (and phase-lock averaged) properties in each rotor measurement window for one nozzle/rotor location over the six nozzle/rotor locations (see Fig. 5-1).

It should be emphasized here that the experimental procedure and data processing are designed to obtain spatially and "temporal" measurements (i.e., rotor shaft positions; not real time) of the wake-rotor interaction generated unsteadiness in the rotor. The laser is located at a fixed position relative to the nozzle wake for each nozzle/rotor location.

Hence, the averaging is based on identical rotor-nozzle blade positions. These measurements are similar to those reported by earlier investigators (e.g., Hathaway, 1986).

The LDV measurements are subject to numerous errors, most of which can be quantified. A complete error analysis for these measurements is given in Zaccaria and Lakshminarayana (1997a). Based on this error analysis, the uncertainty for a 95% confidence level is as follows: outside the rotor wake 0.4% and 2.8%, respectively for the ensemble-averaged velocity and the unresolved component of velocity; inside the rotor wake, 4.0% and 14.8% for the ensemble-averaged and unresolved velocity, respectively. The LDV data is presented and interpreted in Zaccaria and Lakshminarayana (1997b). This data is used in this thesis to validate the code and to derive new insight on the nozzle-rotor viscous interaction in view of the additional blade surface data acquired recently and the comprehensive flow simulation carried out with an unsteady Navier-Stokes code.

5.1.2 Dynamic Pressure Measurements

To provide a complete knowledge of the nozzle-rotor interaction phenomena the instanteneous unsteady dynamic pressure has been acquired (Lakshminarayana et al., 1998). The sensitivity and the high-frequency response of silicon based semiconductor strain gauge pressure transducers coupled with their small size make them very desirable for use in obtaining unsteady dynamic pressure fluctuations. The implementation of the dynamic pressure transducers in the turbine rig was driven by space limitations. The pressure transducers are inserted into chambers, which in turn are connected to the turbine airfoil surfaces through 0.5 – 0.8 mm diameter holes. The design objective is to achieve a frequency response of 40 kHz. The miniature sensors used are the Kulite model XCS-093 with a pressure range of maximum 5 psia. They are capable of measuring pressure fluctuations to an accuracy of 0.01 psia. Sixteen Kulite transducers are located along the chord at the midspan of the rotor blade. Seven transducers are on the pressure side and the remaining nine are located on the suction surface of the next blade in the same passage. A schematic showing the location of dynamic pressure transducers on the blade at midspan (16) and on the hub (endwall) surface (5) is shown in Fig. 5-1. The low-level signals from the dynamic pressure transducers are amplified in the rotating frame by using miniature amplifiers. The amplifiers rotate in the rotor frame and provide a high-level signal output before the signal reaches the slip-ring unit. These amplifiers are located inside the rotating instrumentation drum. The transducers were calibrated by inserting the entire blade in a pressure chamber as well as using the steady state static pressures on the blade before the experiment.

The dynamic pressure data from the rotor is transmitted through the rotating drum to a slip-ring unit. The slip-ring unit is of the brush type and has 150 channels. The slip-ring unit is housed in a cowling in front of the facility. Each ring carries four brushes made of silver graphite. The rings are made up of coin silver, which withstands up to current levels of 5 Amps. The brushes are individually removable and replaceable. The contact resistance is about 5 milliohms maximum.

A completely automated data processing system is built around a computer with a clock rate of 7MHz. The data is triggered by an encoder on the turbine shaft. Approximately 167 (1 million samples at 6000 samples/rev.) revolutions of data are acquired. This was ensemble-averaged to derive revolution periodic, which is then decomposed into blade periodic (average-passage) and blade aperiodic pressures. The procedure used for data processing is similar to that described in the last section. The latter represents the deviation of the individual passage from the average passage. A typical set of processed data for x/C_x=0.285 is shown in Fig. 5-3. The blade aperiodic quantity is small for most passages and appreciable only in three or four passages. Only the blade periodic data are presented and interpreted here.

5.2 Numerical Procedure

To simulate rotor unsteady flow, time dependent boundary condition were imposed at rotor inlet. Velocity and the pressure distributions were based on the experimental data at 24.59% of the rotor chord upstream of the leading edge. Data was obtained using a five-hole probe in a stationary frame of reference. To impose an accurate unsteady boundary condition, the measured pressure and velocity fields (moving in rotor frame of reference) were superposed with the rotor potential field based on a steady prediction (steady in the rotor frame of reference).

In order to apply periodic boundary conditions, the flow in five rotor passages was calculated. This provides a vane-to-blade ratio equal to 4:5, close to the actual ratio of 23:29.

5.3 Sensitivity Studies

To analyze the grid sensitivity, numerical simulations have been carried out using three grids: 101X61, 181X91, and 211X181. The distance between the first grid point and the wall varied from y+=0.9 for the coarse grid to y+=0.3 for the fine grid. Steady flow predictions based on 181X91 and 211X181 girds are identical. A numerical simulation of the unsteady flow imposes an additional requirement on the grid density outside the boundary layer. An earlier analysis of the influence of the artificial dissipation (Chapter 3) has been used to estimate the required mesh distribution in the middle of the passage. The axial gap in the turbine stage is equal to 27.6% of the rotor chord. Hence, the nozzle wake defects are substantial. At least ten Fourier harmonics are needed for an accurate representation of the inlet velocity field. The amplitude of the 10th harmonic is 2% of the wake defect. According to the previous analysis, the finest grid (211X181) provides enough spatial resolution to model the whole spectrum of the inlet wake. A numerical simulation based on 181X91 grid may lead to excessive decay of the 8th and higher harmonics due to the artificial dissipation. A comparison of the numerical prediction of the unsteady flow based on these two grids indicates that utilization of the coarser grid (181X91) results in a 3% smaller local wake defect due to the artificial dissipation. No other significant differences have been observed. To minimize CPU time, most of the simulation studies were carried out using 181 X 91 gird.

The accuracy of the numerical simulation depends on the appropriate choice of the number of physical time steps as well as the number of inner pseudo-time steps. Current simulations were carried out with 1000 physical time steps per period. Even though it was found that 500 time steps were enough for the accurate temporal resolution, the solution had features of numerical instability. This problem was eliminated when the number of physical time steps was increased to 1000. An investigation of the dependency of the solution on the number of inner iterations indicated that an accurate prediction of the unsteady pressure field required about 7 inner iterations. An accurate resolution of the velocity and turbulence field required 15 inner iterations.

5.4 Time-Averaged Flow Field

A comparison between the predicted (steady) and measured surface pressure distribution is shown in Fig. 5-4 and Fig. 5-5. The comparison is done for four cases (summarized in Table 5-1). Very good agreement between the predicted and the experimental data is achieved for the design point (Fig. 5-4) as well as for the flows with moderate incidence angle (Fig. 5-5). For the case C with the inlet flow angle equal to –4.75°, the numerical simulation predicts flat pressure distribution along 60% of the chord on the pressure surface. The experimental data indicate that the pressure on the pressure surface decreases up to 30% of the chord and increases from 30 to 60% chord. This discrepancy is attributed to the known deficiency of the k-ε turbulence model in accurately predicting the extent of flow separation. The three-dimensional nature of the separation bubble may also contribute to this discrepancy. At β=-4.75°, the predicted separation bubble extends from x/C_x=0.1 to x/C_x=0.6. Its thickness is about 25% of the blade spacing at x/C_x=0.3.

A comparison of the blade surface pressure distribution at different operating conditions indicates that the flow is not sensitive to the moderate variation in the incidence angle and the prediction is excellent at these conditions. A lower inlet flow angle moves the stagnation point towards the suction surface. For the largest incidence angle, the stagnation point is located at x/C_x = 2%. At β =-4.75° the flow near the leading edge undergoes significant modification. A strong separation bubble develops on the pressure side of the blade due to high turning of the fluid particles near the leading edge. The resulting pressure field leads to a compressor-like behavior from the leading edge to x/C_x =18% of the chord.

The predicted (time-averaged) and measured (cycle-averaged) relative total velocity distribution at several axial locations at design condition (A) are shown in Fig. 5-6. The prediction is excellent at all locations except at x/C_x = 110%. One of the severest tests on the code is the ability to capture a large gradient in velocity. Near the leading edge, the excellent agreement at x/C_x=-5% provides confidence in the code. The wake depth is captured at x/C_x = 110%, but the predicted wake width is smaller than the measured one. This may be attributed to three-dimensional effects or the cycle averaging procedure. The predicted passage average angle at the exit is 67.4°. This compares well with the measured and design values of 64.3° and 67°, respectively. These results indicate that the time-averaged flow field is predicted accurately especially in the passage and upstream of the passage.

5.5 Unsteady Pressure Field on the Blade Surface (Design)

Before commenting on the nature and magnitude of unsteady pressure, it should be remarked here that the blading for the Penn State HP turbine was designed to limit over-acceleration on the suction surface just off of the leading edge (Lakshminarayana et al., 1992). On any turbine blade, the flow is subject to high acceleration around the leading edge region on both the suction and the pressure sides. In both cases, there may be a subsequent undesirable diffusion. However, a local diffusion, however small, is of more concern on the suction side where it may constitute a significant disturbance to the (laminar) boundary layer. In the present blading design, it was possible to trade one off against the other by precise tailoring of the leading edge geometry and adjustment to the leading edge inclination (i.e., incidence). Generally, only a very slight tendency to overspeed was tolerated on the suction surface as it was felt that a very minor increase in the pressure surface diffusion would not significantly affect the blade performance. The suction peak is located near the mid-chord location.

The measured and predicted steady pressure and unsteady envelope at the design condition as well as steady pressures are plotted in Fig. 5-4. The predicted amplitude of unsteady pressures agrees quite well with the measured values. The amplitudes are small near the leading edge on both surfaces. This is due to the fact that the blading is not very sensitive to incidence changes due to inherent design. The incidence angle changes (Table 5-1, Fig. 5-5) from 2.06° to - 7.6° had no significant input on the steady pressures. The maximum amplitude occurs near 28% chord on the suction surfaces and decreases gradually to insignificant values as the trailing edge is approached (Fig. 5-4). There is a significant difference between this data and those due to Dring et al. (1982), who observed maximum values at the leading edge. This may be due to large flow acceleration near the leading edge and closer rotor-stator spacing. The amplitudes (Fig. 5-4) are small on the pressure surface and once again decrease gradually to small values as the trailing edge is approached.

It should be remarked that even though the agreement between the measured and predicted steady pressures on the suction surface is not exact from 30% to 50% chord, the amplitudes of unsteady pressure are in good agreement.

The periodic variation of blade pressures on the suction surface at selected rotor chord locations are shown and compared with the predictions in Fig. 5-7. As mentioned earlier, the amplitudes are highest near the $x/C_X=0.28$ and decrease to insignificant values near the trailing edge. The prediction is very accurate at $x/C_X=0.071$ and 0.28. Discrepancies are observed aft of the midchord. The measurement shows larger decay in the amplitude than the prediction.

The space-time distribution of unsteady pressures ($\Delta C_{p'}$) on both surfaces along all measurement locations are shown in Fig. 5-8. Such plots can provide a valuable overview of the flow physics associated with the wake-rotor interactions. On the suction surface, the measurement shows a maximum value at about 28% of the chord. The phase angle of the peak values (marked HS) on the suction side changes rapidly as the flow progresses downstream due to large changes in the convection velocity of the nozzle wake. The first low value on the suction side (LS1) also moves at about the same phase as the peak (HS). But the second minimum (LS2) is nearly at constant phase. On the other hand, the peak values on the pressure side occur near the leading edge. One of the unusual features is the presence of two peaks (HP1, HP2) on the pressure side. As indicated earlier and in Fig. 5-2, the inflow has both the pressure gust and the velocity gust. As the two approach the leading edge, the phase angle between the two distortions change and the pressure gust seems to have a more profound effect on the pressure surface than on the suction side. Another interesting feature is that, except for the leading edge, the peaks move at nearly constant phase as the flow progresses downstream along the pressure surface. Some of these features are similar to those observed by Dring et al. (1982), but major differences are in the location of peaks on the suction side. This is due to the differences in the blading design.

The first three harmonics of the unsteady pressure on the suction surface are plotted and compared with the predictions in Fig. 5-9. The experimental data indicate that the first harmonic is the dominant component and this component is predicted quite well by the code. The predictions reveal two maxima; one near the leading edge and the other near 28% chord downstream. Since there is no data available at the leading edge, the presence of the first peak cannot be confirmed. But the minima observed near the 5% of the chord location is predicted accurately. The second harmonic shows a peak close to the 50% of the chord, but the predicted peak is further downstream. The occurrence of the peak in second harmonic can be attributed to the transfer of energy from the first harmonic to the second harmonic in the freestream unsteadiness. This is clear from the fact that the first harmonic decreases rapidly near the midchord and the peak in the second harmonic appears at this location. This is due to the dominant effect of two counter-rotating vortices (see discussion below) that are developed on either side of the wake and the weaker nozzle wake effect. This effect is overpredicted by the code. During the numerical simulations, it was observed that the amplitude of the second harmonic is sensitive to the local wake velocity defect. The measured values of the third harmonic are negligibly small.

5.6 Unsteady Pressures at Off-Design Conditions

The space-time history of unsteady pressures at the off-design condition (Case C, Table 5-1) is shown in Fig. 5-10. The relative flow at this operating condition is nearly axial, and the incidence is $-44.9°$ (Fig. 5-1). The peak unsteady pressures on both surfaces occur near the leading edge. One of the salient features of the distribution on the suction side is the change in the phase angle of the unsteady pressure as flow propagates downstream. The blade up to 20% of the chord behaves like a compressor. The relative velocities on the suction side of the turbine (pressure surface) are small up to about 20-30% of the chord (Fig. 5-5, Case C). Hence, the disturbance is nearly at constant phase up to about 30% of the chord on the suction side. Significant changes occur beyond this location and the unsteady pressure decays very rapidly. This rapid decay is caused by major viscous effects within the passage due to the severe off-design conditions. The unsteady pressures decays more rapidly on the pressure surface. This is caused by a possible flow separation and a bubble near the leading edge of the pressure surface at this operating condition. The unsteady pressure on the pressure side (such as the suction surface) increases significantly.

The measured values are compared with predictions at selected chordwise locations in Fig. 5-11. Here again, the agreement is very good near the leading edge, especially on the suction surface. As indicated earlier, the predicted flow separation on the pressure side may not be accurate, and this may account for the discrepancy at $x/C_X=0.3$ on the pressure surface.

The chordwise distributions of the unsteady pressure amplitude at all operating conditions (Table 5-1, Cases A, B, C, and D) are shown in Fig. 5-12. There are two major effects involved here; the time-averaged incidence changes and the reduced frequency changes. Cases A and B are carried out at the same speed, with Case B being at a higher mean incidence. The data on the suction surface shows that the amplitudes are slightly higher for Case B at most locations. The dominant effect is downstream of the leading edge ($x/C_X=0.28$ on suction surface, 0.14 on the pressure surface). Cases C and D have the same mass flow and Reynolds number, with Case C at more severe off-design condition. The data for Case D follows trends very similar to those of Cases A and B. As indicated earlier, due to large negative incidence for Case C, the peak unsteady pressures are similar on both the suction and the pressure surfaces and have the fastest decay on the pressure side. The amplitudes are highest for this case on the pressure side. One of the interesting features of all of this data is that the peak pressure for all operating conditions (Cases A, B, C, and D) occur downstream of the leading edge on both surfaces. This has a significant impact on the leading edge cooling. The present design seems to have reduced unsteady wake-interaction effects near the leading edge through aerodynamic design.

5.7 Unsteady Flow Field Due to Rotor-Stator Interaction

A brief description of the data acquired from the LDV inside the passage at the midspan of the turbine rotor is given above. This data is compared with the predictions in this section.

To account for the non-uniformity of the rotor absolute flow field, measurements were made at six tangential locations, equally spaced over a nozzle pitch (Fig. 5-1), in the absolute frame of reference. These six tangential locations represent six different relative positions between the nozzle and the rotor. The derived flow field corresponds to the fixed "rotor shaft positions," not real time. More details on the experimental procedure and experimental measurements can be found in Zaccaria and Lakshminarayana (1997b). To enable a comparison of the measured "rotor shaft phase-locked" blade-to-blade flow field with the numerical prediction, the data from the computation has been processed in the same way as the experimental technique. The derived blade-to-blade distributions of the wake defect and the unresolved unsteadiness (eq. 5-2) in the absolute frame of reference are shown in Fig. 5-13 and Fig. 5-14, respectively. It should be remarked here that the unresolved unsteadiness consists of both the random fluctuations due to turbulence as well as the blade periodic fluctuations, which is found to be small in this single-stage turbine. The velocity field is shown for the position N1 (Fig. 5-13, bottom station); while the unresolved unsteadiness distribution is plotted for the position N4 (Fig. 5-14, top station). Due to the blade shadow and lack of seeding, no experimental data is available in the unshaded (white) region. The velocity represents the periodic unsteadiness due to the nozzle wake $\tilde{V}$ (ensemble average minus the time average, eq. 5-3). A comparison between the data and the prediction shows good agreement with the location and defect in the nozzle wake. The numerical prediction moderately under-predicts the level of the wake defect between $x/C_x=0$ and $x/C_x=0.2$ (Fig. 5-13, Fig. 5-15). The measured unresolved unsteadiness and the predicted turbulence intensity, (Fig. 5-14) indicate that the peak intensities are predicted reasonably well, but the wake width based on the unsteadiness shows that the computation has a larger diffusion (into the freestream) compared with the experimental data.

Even though the “rotor shaft phase-locked” flow field can be used to analyze the development of the unsteady flow in a rotor passage due to the wake-rotor interaction, it is more appropriate to consider the instantaneous flow field. “Rotor shaft phase-locked” representation is used only to compare the measured velocity field with the numerical prediction. All subsequent discussion is based on the time accurate (instantaneous) flow field.

5.8 Discussion of Unsteady Flow Physics

As indicated earlier, the vane-blade ratio used in the computation is 4:5; hence the unsteady flow field is computed in five rotor passages. Hence, all the simulation data shown in this and subsequent sections shows predictions in five rotor passages.

The unsteady velocity, pressure, turbulence field, and the unsteady relative total pressure coefficient shown in Fig. 5-16, Fig. 5-17, Fig. 5-18, and Fig. 5-19 respectively, reveal the development of the rotor unsteady field caused by the nozzle wake-rotor interaction. Based on the unsteady velocity, the nozzle wake appears as a negative jet moving towards the suction side (Fig. 5-16). The nature of such impingement depends on the inlet velocity triangle and the wake defect. The location and propagation of the nozzle wake can be clearly identified by examining all the instantaneous properties: unsteady velocity $(V-\overline{V})$, static and stagnation pressure, and turbulence field. The shape of the turbulence wake is very close to that of the entropy wake, which is normally used to identify the wake position. For the sake of brevity, the unsteady entropy distribution is not shown here.

The wake segment is initially straight (Fig. 5-16). Due to the potential effect and the blockage caused by the leading edge, it is stretched, distorted, and diffused as it approaches the rotor leading edge. Further downstream, the wake is chopped and transported at the local convection speed as a separate segment. Due to a large convection velocity near the suction side, spreading of the suction leg of the wake segment is much faster. When the wake segment reaches the trailing edge of the pressure surface, the wake is chopped on the suction side of the leading edge (Fig. 5-16).

As observed by others, the wake propagation through the passage generates a system of the counter-rotating vortices. Analysis of the unsteady flow shows two main sources of unsteady pressure on the blade surface. The interaction of counter-rotating vortices with the passage flow is the primary source of the unsteady pressure field beyond 20% of the chord (Fig. 5-17). The second source is the interaction due to pressure gust associated with the nozzle wake. A rapid decay of the inlet unsteady pressure field limits the influence of the pressure gust to the leading edge region. The interaction of the pressure gust with the blade at the leading edge generates a zone of high pressure on the suction side (Fig. 5-17).

Additional simulations were carried out to investigate the contribution of the velocity gust and the pressure gust due to the nozzle wake and the rotor blade. In the first case, only the velocity defect is present; the second case has only pressure gust. Distribution of the instantaneous velocity and pressure fields for these three inlet conditions are shown in Fig. 5-20. In the absence of the velocity defect, the pressure gust generates a system of counter-rotating vortices with rotation in a direction opposite to those induced by velocity gust. Near the leading edge, the variation in the surface pressure due to the velocity gust and the pressure gust has a phase angle variation of nearly 180°, as shown in Fig. 5-21, at $x/C_x = 0.71$. At this location, the pressure gust has a dominant effect. As a result, combined flow has only one peak related to the pressure gust.

An interesting feature of the pressure gust-blade interaction is that it generates a significantly smaller pressure oscillation on the pressure side near the leading edge in comparison with the suction side. This can be explained by the shorter interaction time on the pressure side.

In the absence of the pressure gust, pressure oscillations are small within the initial 15% of the chord. The only significant effect of this interaction is the decreased skin friction coefficient on the pressure surface. At moderately off-design flow conditions, this phenomenon may lead to an earlier development of the separation bubble due to the nozzle-wake blade interaction and may generate significant additional losses.

Beyond 20% of the chord, the pressure gust has a minimal impact on the unsteady pressure field on the suction surface (Fig. 5-22). Downstream of this location, the interaction between the nozzle wake induced counter rotating vortices develop a high-pressure zone upstream of the nozzle wake center and a low-pressure zone downstream. This unsteady pressure system propagates downstream on the suction surface at the convection velocity (i.e. velocity at the boundary layer edge near the suction surface). The location of the maximum pressure is close to the location of the maximum wake defect. Downstream of $x/C_x = 0.7$, the unsteady pressure decays due to a decreased intensity of counter-rotating vortices.

Interaction between the passing wake and the pressure surface is significantly weaker because of a very small variation of the velocity field in the vicinity of the blade downstream of $x/C_x = 0.3$. The resulting amplitude of the unsteady pressure on the suction surface is less than one-third of those at the pressure surface.

The measured and predicted unsteady pressure coefficient on the suction surface at the design condition is shown in Fig. 5-22. Many of the features were described earlier. The measurement does not show the effect of the pressure gust near the leading edge, as there is no data available at this location. But the trend from 5% to 20% of the chord indicate that the distribution is similar to the predictions. The distribution beyond 20% of the chord shows the major influence of the velocity gust and the associated counter-rotating vortices. Predictions are in good agreement with the data. Both measurements and predictions indicate that unsteady pressures are negligible beyond about 70% of the chord.

5.9 Nozzle Wake Decay Through the Rotor Passage

The nozzle wake is a source of additional mixing losses in turbine passages. Physics of the wake mixing consists of two main components: viscous dissipation and inviscid effects (chopping, stretching, distortion, area changes etc.). The wake decay due to the viscous dissipation results in losses, while the inviscid effects are the reversible process. In some cases, wake ingestion can be used to increase the efficiency of the propulsion system (Smith, 1993).

Based on experimental and analytical investigations, Hill et al. (1963), suggested a wake decay model in a diffusing flow, which includes both the viscous and the inviscid effects. Van Zante et al. (1997) developed an inviscid wake model for the two-dimensional compressor blade row. This model estimates the inviscid decay of the wake defect as a function of the cascade flow parameters. The wake propagation in a turbine is more complex in nature when compared to those in a compressor. Due to a strong variation of the flow velocity in both the streamwise and the pitchwise directions, the wake is highly distorted and can not be considered as straight or slightly bent segments. To analyze the wake stretching in a turbine, it should be considered as a set of segments undergoing stretching/compression under significantly different local conditions.

An understanding of the viscous and inviscid contributions to the wake mixing is essential for minimization of the mixing losses. An analysis of the wake mixing based on the viscous and inviscid prediction is carried out to investigate the physics of the nozzle wake decay in a rotor passage. Three following cases are simulated:

1) Base flow, viscous simulation (includes inviscid effect)

2) Base flow, inviscid simulation

3) Modified base flow, viscous simulation; no unsteady pressure variation at inlet. This case denoted as 'no pressure gust'

A comparison of the wake decay in the absolute frame of reference for all cases is shown in Fig. 5-15. At the trailing edge, the nozzle wake defect based on the inviscid prediction is three times larger than that predicted by the viscous simulation. For locations upstream the leading edge in addition to the distribution of the maximum wake defect, minimum wake defect distribution is plotted at same locations. These lines correspond to the wake propagation along path II, Fig. 5-16, (see discussion below) and denoted 1a, 2a, 3a for cases 1,2,3, respectively.

Viscous and inviscid predictions have a different wake decay rate inside the rotor passage, but a similar wake flow pattern exists at all locations. This enables a comparison between the inviscid and the viscous wake decay at different locations inside the rotor passage, even though the local wake defect is different in viscous and inviscid predictions. It is assumed (and verified through the numerical modeling) that at each particular location the inviscid rate of the wake decay is not a function of the local wake velocity defect. Thus, the inviscid contribution to the wake decay from the viscous solver can be compared with those based on the inviscid simulation despite the difference in local amplitude of the wake defect.

Table 5-2 Zone boundaries

Zone number	Beginning x/C_x	End x/C_x
1, max ΔV, corresponds to Path I, Fig. 5-16	-0.24	-0.1
1a, min ΔV, corresponds to Path II, Fig. 5-16	-0.24	-0.1
2	-0.1	0.05
3	0.05	0.25
4	0.25	0.6
5	0.6	outlet
Total	-0.24	outlet
Blade region	0.0	1.0

Different mechanisms contribute to the wake decay and mixing in a rotor passage. There are significant variations in the viscous/inviscid effects at each axial location. It is possible to segregate the rotor passage into zones based on the characteristics of the nozzle wake decay. The boundaries of the various zones are shown in Tab. 1. The first zone extends from the inlet computational plane to x/C_x=-10% upstream of the leading edge. In this region, the nozzle wake is advanced as a set of parallel segments convected by the mean flow. The wake segment, transported along path I (Fig. 5-16) undergoes stretching in the streamwise direction, due to a 20% decrease in the streamwise velocity. This effect is clearly seen in Fig. 5-15 (line 2), in the form of the increased inviscid wake defect. A decrease in the inviscid wake defect beyond x/C_x= -0.15 is associated with the potential effect, which is described below for the second zone. The wake segment traveling along path II (Fig. 5-16) undergoes an opposite process. Flow acceleration (40% increase in the local velocity) upstream of the suction surface results in a significant decrease in the wake defect (Fig. 5-15). The ratio of the maximum to minimum inviscid wake defect at x/C_x=0.1 is equal to 1.45. Viscous dissipation has a more profound influence on the wake propagation along path I in comparison with the Path II.

For each zone, the contribution of the viscous dissipation can be calculated as:

wake decay due to the viscous dissipation

$\delta\,\Delta V_{dis} = \delta\,\Delta V_{vis} - \delta\,\Delta V_{inv}$

change in the wake defect due to the inviscid effect $\delta\,\Delta V_{str} = \delta\,\Delta V_{inv}$

where $\Delta V = (V - \bar{V})/\bar{V}$ is a local wake defect, $\delta\Delta V$ - is the change in wake defect between the two axial locations, subscripts *inv,vis* -denote inviscid and viscous solution respectively.

Viscous contributions to the wake mixing, presented in Fig. 5-23 are defined as follows:

$$\frac{\delta\Delta V_{dis}}{\delta\Delta V_{dis} + |\delta\Delta V_{inv}|} \text{ and inviscid : } \frac{\delta\Delta V_{str}}{\delta\Delta V_{dis} + |\delta\Delta V_{inv}|}.$$

For zone N ≥ 2, the predicted inviscid wake at the inlet to the zone is scaled by the predicted viscous wake defect at the current location, i.e., $(\delta\ \Delta V_{inv})' = \delta\ \Delta V_{inv} * (\Delta V_{vis}/\Delta V_{inv})$.

Contributions of the potential effect are calculated as: $\delta\Delta V_{pot} = \dfrac{\delta\Delta V_{visnopot} - \delta\Delta V_{vis}}{\delta\Delta V_{vis}}$,

where the subscript *visnopot* denotes Case 3. A positive sign indicates that the pressure gust increases the wake decay. Similar to above, the wake defect scaling is used to normalize the wake $\delta\ \Delta V_{visnopot}$.

The inviscid mixing is responsible for 30% of the total wake decay along Path I (denoted as Zone 1 in Fig. 5-23). For Path II, intense stretching of the wake segment increases the inviscid contribution to about 50%. Downstream of x/C_x=0.1, only the propagation of the maximum wake defect is considered.

The essential difference between the first and the second zone (from 10% upstream of the leading edge to 5% of the chord from the leading edge) is the increased contribution by the pressure gust. Viscous simulation, without the unsteady pressure field at inlet (Case

3) predicts a significant increase in the maximum wake defect over the baseline (Case 3,Fig. 5-15). The comparison, shown in Fig. 5-20 can be used to interpret the influence of the moving pressure gust on the nozzle wake decay. This influence can be separated into two parts. The first effect is the generation of an additional favorable pressure gradient, resulting in enhanced mixing. At the inlet, the wake segment is located in the region of high pressure. When the wake is convected downstream, the region of high pressure is replaced with a zone of low pressure due to relative nozzle-rotor movement. A numerical simulation with "no wake" boundary conditions reveals another contributing factor in increased wake decay due to the pressure gust. Even though no time-dependent velocity component was presented at inlet, the moving pressure field generates jet-wake structure shown schematically in Fig. 5-20. The jet, associated with the moving pressure field, is located above the nozzle wake. Thus, the velocity at this side of the wake is increasing, contributing to the decay of the wake defect. Counter clockwise rotation of the wake segment leads to a compression of the wake segment near the leading edge of the pressure side. This counterbalances the decay in the wake defect due to the pressure gust. The combination of these two effects results in a smaller net change in the inviscid decay of the wake defect. Overall, the contribution of the viscous and inviscid mechanisms is approximately equal in this region (Fig. 5-23).

In the third region (Zone 3), which extents from 5% of the chord up to 25% of the chord, the location of the maximum nozzle wake defect is moving rapidly from the pressure side to the suction side (Fig. 5-16). After the nozzle wake is chopped at the leading edge, two counter-rotating vortices develop in the rotor passage. At x/C_x=10%, the slip velocity vector (Fig. 5-1) is pointed in the direction of the suction surface. Transport of a low momentum fluid from the pressure surface to the suction side is the dominant mechanism responsible for the amplification of wake defect in this region. The acceleration of the convection velocity in the direction of wake propagation leads to wake thickening and a further increase of the wake defect. A viscous dissipation contribution is only 60% of inviscid one in this region (Fig. 5-23).

At x/C_x =30% (Fig. 5-15), the wake is strongly bent with two legs extending from the suction to the pressure surface. A maximum wake defect is located on the suction side, closer to the wake center. The slip velocity is parallel to the streamwise direction. Further propagation of the wake segment containing a maximum wake defect can be considered through its rotation-free elongation-compression in the streamwise direction. Following the velocity field the wake defect is decreasing from x/C_x =30% to x/C_x=60%. The wake defect increases from x/C_x =60% to x/C_x =100%, since the streamwise total velocity decelerated by 13% (Fig. 5-15).

In both zones 4 and 5, the inviscid phenomenon is the major mechanism for the wake decay (Fig. 5-23) and it is responsible for more than 70% of changes in the wake defect. In zones 4 and 5, the wake decay can be estimated using the formula for inviscid stretching. The estimated values are as follows:

Table 5-3 Wake decay, zone 4 and 5

	Predicted	Inviscid stretching (estimated)
Zone 4	0.64	0.68
Zone 5	1.08	1.20

Within the blade passage, the inviscid stretching results in a net increase of the wake defect (Fig. 5-15, line 2). In summary, the viscous dissipation is responsible for 60% of the wake decay within the blade passage and for 75% of the wake decay from the inlet to the trailing edge.

5.10 Loss Generation Due To Unsteady Flow

The loss estimate is one of the most challenging tasks for the computational fluid dynamists. Numerical simulation based on different numerical solvers may result in an appreciable variation in the predicted losses (e.g., Venable et al. 1998). However, the prediction of the trend in losses is consistent. Based on a comparison between the predicted and measured flow characteristics presented earlier, a certain level of confidence is achieved in the predicted loss distribution. However, the absolute level of the predicted loss should be verified through a comparison with the measurement. An additional inviscid numerical simulation was carried out to assess the presence of the non-physical losses due to the numerical errors (artificial dissipation, grid influence, etc.). Grid identical to those in the viscous solver was used to ensure consistency. It was found that the time mean (the pitchwise mass-averaged) loss coefficient based on an inviscid calculation is less than 0.01 or less than 4% of the maximum time-mass averaged loss at the outlet based on the viscous solver prediction. This is an acceptable level of accuracy. The predicted flow and the pressure field can be used to analyze the distribution of losses through the passage as well as additional losses due to the presence of the nozzle wake.

Instantaneous distribution of the relative total pressure, shown in Fig. 5-19, reveals that the inlet flow pattern associated with the low total pressure inside the wake is followed by a zone of high and low unsteadiness in total pressure along the blade passage. Static pressure variation is the major factor contributing to the total pressure oscillation. The range of the total pressure variation at the location of the maximum nozzle wake-blade interaction ($x/C_x \sim 0.3$) is significantly higher than the time-average value of ζ. At this location, the local peak value of ζ varies from -1.5 to 0.5 near the suction surface, while the time-averaged loss coefficient is equal to 0.25 at the passage outlet (Fig. 5-24). The unsteady relative total pressure coefficient reaches its minimum (and correspondingly max. amplitude) near $x/C_x = 0.7$. Further downstream, a spot of low total pressure propagates downstream without significant change in its value. A zone of high relative total pressure undergoes a more rapid decay from $x/C_x = 0.7$ to $x/C_x = 1.5$. This is due to a more rapid mixing of the nozzle wake.

The pitchwise averaged loss coefficient, shown in Fig. 5-24, can be used to identify sources of increased losses due to the unsteady flow. The loss coefficient for the unsteady flow is based on the unsteady inlet total pressure. Thus, it includes only losses in the rotor passage. There is a sharp increase in $\bar{\zeta}$ upstream of the leading edge; an indication of the intense mixing in this region. This contribution accounts for 55% of the increased total loss coefficient in comparison with those based on the steady flow prediction. Additional losses within the blade passage contribute 34% to the total unsteady losses. The steady and unsteady loss distributions are practically parallel from 25 to 50% of the chord. Thus, the profile losses due to the rotor boundary layer are dominant in comparison with the mixing losses due to the nozzle wake decay within the passage. The time-averaged boundary layer properties beyond x/C_x=0.4 reveal higher values for suction surface momentum thickness in comparison with the steady flow prediction. This correlates well with the differences in $\bar{\zeta}$ based on the steady and the unsteady flow predictions. There is a moderate increase ($\bar{\zeta}$ ~0.07) in the loss coefficient downstream of the trailing edge. This may be attributed to the nozzle wake - rotor wake interaction. However, this level of $\bar{\zeta}$ increase is to small to be considered as reliable.

5.11 Unsteady Transitional Flow on the Suction Surface

An accurate prediction of the unsteady transitional flow is crucial in evaluating loses, efficiency, and cooling requirements of turbines. Very few attempts have been made to predict the unsteady transitional boundary layer on a turbine blade using the full Navier-Stokes solver.

A major feature of the unsteady flow in the present turbine rotor is the location of the maximum unsteadiness in the surface pressure, which is at x/C_x=0.3 (s/C_x=0.45), (Fig. 5-22). This is close to the location of the transition onset, thus significantly affecting the flow in the transition region. An accurate prediction of the pressure field is crucial to the prediction of the unsteady transitional zone.

Space-time distribution of the unsteady turbulence field, due to the interaction of the nozzle wake with blade surface boundary layer, is shown in Fig. 5-25. t/T=0 line corresponds to the flow conditions in Fig. 5-16. Various zones in the unsteady boundary layer can be classified as follows (shown in Fig. 5-25 and Fig. 5-26):

L - laminar region

TR1 - wake induced transitional strip

TU1 - wake induced turbulent strip

TR3 - transition between wakes

TR2- wake turbulence induced transition between wakes

TU2 - turbulent flow between wakes

TR4 - transitional strip behind passing wake

The unsteady nature of the transitional process makes it difficult to identify the beginning and the end of the transition. For a steady flow simulation, the identification of the inception and the end of the transition can be based on the local turbulence field and verified through an analysis of other flow characteristics (i.e., skin friction coefficient, shape factor, etc.). It is found that this approach cannot be used in an unsteady flow due to a phase lag between different flow variables and properties in the transitional region. Hence, the location of the onset and the end of the transition is based only on the predicted turbulence field. The position of the transition inception is calculated as the position where $F(\mu_t^m)$ reaches its maximum value along the path on a space-time diagram (Fig. 5-25). $F(\mu_t^m)$ is the first derivative of μ_t^m along the wake path at the boundary layer edge and μ_t^m is the maximum value of the eddy viscosity inside the blade boundary layer at any given space-time position.

The location of the maximum value of k at the end of the transitional zone was chosen as the location of the end transition. This criteria correlates well with the predicted value of the local- maximum skin friction coefficient.

The variation of the predicted unsteady skin friction coefficient on the suction surface is shown in Fig. 5-26. As indicated earlier, from $x/C_x=0$ to $x/C_x= 0.25$ the pressure gust is the primary source of the unsteady pressure in the blade (Fig. 5-22).

Beyond $x/C_x = 0.2$, the wake defect and the counter-rotating vortex system generate a combination of high-pressure and low-pressure zones, which are convected in the streamwise direction. In the laminar region, the surface pressure variation is the primary source of the boundary layer disturbance. The observed variation of the skin friction coefficient along Path 1-2, 1a-2a as well as 3-4, 3a-4a, shown in Fig. 5-26 can be explained on the basis of the unsteady pressure gradient (favorable and adverse) at these locations (Fig. 5-22)

Near $x/C_x=0.3$ ($s/C_x=0.45$) an interaction of the blade boundary layer with the nozzle wake increases the velocity at the boundary layer edge (Fig. 5-16). At this location (Fig. 5-22 and Fig. 5-25), the Reynolds number, based on the momentum thickness, (Re_θ) is 12% higher over the time-averaged value, reaching a value of $Re_\theta=230$. The boundary layer development along this path (going through point 1 in Fig. 5-26) undergoes wake induced transition at $s/C_x=0.68$. Transition within the wake induced transitional strip is characterized by a maximum increase in the turbulence kinetic energy as well as the maximum value of the unsteady skin friction coefficient. After the boundary layer becomes fully turbulent, the nozzle wake disturbance leads to a wake induced turbulent strip (TU1). The transformation of the kinetic energy of the velocity fluctuation into the turbulence kinetic energy generates an increased level of k across the boundary layer in comparison with the zone of the turbulent flow between wakes (TU2). Declining pressure fluctuations and wake defect decay are the reasons for the vanishing shear stress fluctuations in the wake induced strip beyond 80% of the chord.

A laminar flow in the region following the wake has a moderately decreased level of Re_θ=200 at 30% of the chord (Fig. 5-26, Point 2). The boundary layer development behind the nozzle wake is characterized by a significantly delayed transition inception, which occurs at s/C_x=0.98. Flow remains transitional up to the trailing edge (Zone TR4). Unlike the wake induced transition strip or the transition region between wakes, the turbulent kinetic energy does not undergo a rapid increase in the transition region, with further relaxation to the level of those in the developed turbulent boundary layer. The turbulent kinetic energy increases monotonically; raising from a low laminar value to those in the end of the transitional zone. An analysis of the boundary layer development in this region leads to the conclusion that the diffusion of the turbulence kinetic energy between the freestream and the turbulent zones upstream and downstream are the primary mechanisms responsible for the amplification in k.

The zone in between the passing wake is not a subject .to an additional pressure gradient or other disturbance associated with the wake-blade interaction. Nevertheless, there is an earlier transition inception near s/C_x=0.70 and t/T=0.5. A comparison of the turbulent kinetic energy (Fig. 5-25), and the blade-to-blade turbulence field (Fig. 5-18) shows an elevated level of turbulence in the boundary layer due to the maximum diffusion of the nozzle wake turbulence at this location. In the absence of the velocity disturbance, this high turbulence level (about 5% increase in Tu_t) is the primary source of earlier transition in Zone TR2. A numerical simulation with no turbulence fluctuation in the nozzle wake confirmes this hypothesis. If there is no elevated level of turbulence in the nozzle wake, Zone TR2 moves upstream and closer to Zone TR1, merging with Zone TR3 (transition between wakes).

The boundary layer in the Zone TR2 has a lower increase in the momentum thickness and has a lower level of eddy viscosity. Thus, losses in this region are lower in comparison to those at the wake induced transition/turbulent strips, but a little higher than that in the region of pure transition between wakes (Zone TR3).

The flow in the Penn State turbine has a high level of freestream turbulence. For this type of flow, the transition occurs through the bypass mechanism. The transition inception occurs at the location where an outer disturbance causes generation and growth of turbulent spots. The length of the transitional region depends on the spot spreading angle and their growth. These characteristics are functions of a number of parameters; local momentum thickness, pressure gradient, Mach number, etc. At zero pressure gradient, the leading edge of the turbulent spot propagates at $0.88W_\delta$, while the trailing edge has the propagation velocity equal to $0.5W_\delta$. The low Re k-ε model, originally developed for the fully turbulent flow, models the transitional process through the diffusion of the freestream turbulence and a local balance between the turbulence production and the dissipation rate, which depend on the distribution of the velocity in the boundary layer. The unsteady flow results in the unsteady transition on a blade surface. Disturbances, caused by the passing wake, lead to an earlier generation of the turbulent spot, which may form a turbulent strip. Turbulent spot growth and propagation mechanisms are essentially the same as in the case of the steady transition. The propagation velocities of the leading and the trailing edge of the wake induced turbulent strips are equal to those of the turbulent spot (i.e., $0.88W_\delta$ and $0.5W_\delta$. correspondingly). This is confirmed by the measurement (e.g., Halstead et al., 1995). Development of the calmed region, which is located behind the wake induced transitional/turbulent strips, is another crucial element in the unsteady transitional process. The trailing edge of the calmed region propagates at $0.3W_\delta$. This region has laminar characteristics, but has an elevated level of shear stresses. This can be considered as the relaxation zone between the turbulent and the laminar zones. Higher resistance to the separation and low boundary layer losses associated with a calmed region are beneficial.

The low Re k-e model lacks the physics associated with the turbulence spot development and can model the transition process only in an "global fashion". In the numerical prediction, the unsteady velocity fluctuation caused by the wake-blade interaction is the primary source responsible for the earlier transition. The maximum value of the average turbulence kinetic energy and the maximum value of the k fluctuation across the boundary layer occur at the same location. After the transition inception, two major mechanisms are responsible for the further development of the predicted transitional strip - the convection of the transitional zone at the local propagation speed, which is smaller than the wake propagation speed, W_δ at the boundary edge. The second mechanism is the advection of the velocity disturbance with variable velocity across the boundary layer. It was found that the propagation speed of the transitional strip TR1, defined as a path along maximum k in Fig. 5-25, is equal to $0.66W_\delta$. This is higher than the propagation velocity equal to $0.55W_\delta$ at the location of the maximum turbulent kinetic energy across the boundary layer. Investigation of the time-space distribution of the velocity and turbulence across the boundary layers reveal that this increase is due to a greater speed of the velocity disturbance propagation; the second contributor to the development of the unsteady transitional zone. From Fig. 5-25 and Fig. 5-26 the leading edge velocity of the transitional strip is estimated to be $0.9\text{-}1.W_\delta$, while the trailing edge velocity is about $0.5\text{-}0.55W_\delta$. As stated above, the transition in Zone TR2 is due to an elevated level of freestream turbulence, which is convected at the local propagation speed. Therefore, the propagation speed of the transition strip is equal to the local convection velocity inside the boundary layer ($0.55W_\delta$).

Zone B (Fig. 5-25 and Fig. 5-26) has several features of the calmed region. A low level of the turbulent kinetic energy and eddy viscosity in this region is similar to those observed in a laminar flow. At the same time, it has an elevated level of shear stresses in comparison with the shear stress in the laminar zone. Phase lag between the maximum amplitude of k and the maximum amplitude of C_f at the transition inception (about 5% of t/T, Fig. 5-25 and Fig. 5-26) results in higher shear stresses in the zone above the wake induced transitional strip. This phase lag diminishes further downstream and is equal to zero at the end of the transition. There is a significantly delayed transition onset in Zone B. A low level of the momentum thickness in combination with low eddy viscosity results in significantly smaller boundary layer losses. Nevertheless, this region lacks another crucial feature of the calmed region. A predicted shear stress profile does not have "relaxing" distribution of C_f at the side of the calmed region. Experimental data indicate that the trailing edge of the calmed region is propagating at $0.3W_\delta$. In the prediction, the line of a zero momentum thickness variation, which can be considered as a boundary of the region B, has a propagation velocity equal to 47% of W_δ.

5.12 Rotor Wake Development

Numerical modeling accurately predicts the decay of the rotor wake defect (Fig. 5-27). Both the experimental data and the numerical simulation show a rapid decay of the rotor wake velocity defect. Analysis of the instantaneous velocity field (Fig. 5-28), as well as the wake space-time distribution at $x/C_x = 1.32$ (Fig. 5-16), may be used to understand the rotor wake development.

The development of the rotor wake is influenced by its interaction with segments of the nozzle wake. The nozzle wake propagation and its distortion in the rotor passage, discussed earlier, result in a zone of decelerated flow, which is located near the suction surface. A similar zone, with significantly smaller amplitude, propagates along the pressure surface (Fig. 5-16). Due to the differences in the convection velocity, the phase lag between these two spots is $t/T \approx 0.35$ at the trailing edge. Downstream of the trailing edge, the interaction between the rotor wake and these two nozzle wake segments is the primary source of rotor wake unsteadiness with a variation in the suction side velocity playing a dominant role. Analysis of the pitchwise distribution of the total velocity reveals the presence of the rotor wake (Fig. 5-28) and the suction side, and pressure side nozzle wake segments within about 5% of the chord downstream of the trailing edge (Fig. 5-28). Downstream of $x/C_x = 1.05\%$, the suction side wake segment merges with the rotor wake. The phase lag between the suction side segment and the pressure side segment of the nozzle wake gives a rise to fluctuation in the rotor wake at the double nozzle wake frequency, but with a significantly smaller amplitude.

A comparison of the predicted rotor wake development with the LDV measurements shows that the rotor wake development is simulated correctly (Fig. 5-27). The merging of the suction side nozzle wake segment with the rotor wake and the presence of the pressure side wake segment far downstream is simulated correctly (Fig. 5-28).

Even though a good correlation is achieved for the rotor wake velocity defect, the current solver underpredicts the wake semi-width. There is a discrepancy between the predicted and the measured wake turbulence levels in the wake region. Measured turbulence field shows a very complex three-dimensional anisotropic nature of the rotor wake turbulence. Hence, it can not be adequately modeled using the k-ε model.

5.13 Off-Design Flow

The numerical simulation at the off-design condition (1100 Rpm) has been carried out to derive an additional insight on the unsteady flow physics. Reduced frequency for this condition is $\Omega = 7.32$.

Only the unsteady blade surface pressure distribution has been measured for this operating condition. Due to a lack of the experimental data on the inlet boundary conditions, the wake profile at the design condition has been utilized for the numerical simulation. Velocity and pressure distribution, shown in Fig. 5-29, indicates a significant change in the overall flow pattern at the off-design condition. Due to an increased reduced frequency, there are more nozzle wake segments in the rotor passage in comparison with the design case. Another significant factor is the development of a strong separation bubble on the pressure surface, which extends from $x/Cx = 5\%$ to $x/Cx = 65\%$. In the zone of the maximum thickness ($x/Cx = 0.35$) the separation zone occupies nearly 25% of the rotor passage. There are two factors leading to differences between the design and off-design conditions. The unsteady pressure field on the suction surface does not undergo significant adjustment beyond those caused by an increased reduced frequency (Fig. 5-29).

The interaction between the nozzle wake and the separation bubble results in amplified unsteady pressure on the pressure surface. Predicted unsteady velocity (Fig. 5-29) indicates that the nozzle wake generates a vortex pattern in the separation zone. Additional pressure fluctuation associated with the vortex structure is the source the increased variation in the surface pressure. Based on the space-time distribution, it is possible to identify three major regions on the pressure surface. From the leading edge to x/Cx = 0.20, vortex generation and its downstream propagation leads to a zone of high/low pressure regions propagating at local convection speed. A comparison of the experimental and measured pressure distribution at x/Cx = 0.14 (Fig. 5-11) shows that the numerical prediction was able to capture this phenomenon. For x/Cx ≥ 0.2, the propagation of the vortex structure does not directly affect the surface pressure. The phase change is negligible. This can be seen in the measured pressure distribution (Fig. 5-10). A comparison of the measured and predicted pressure at x/Cx =0.3 (Fig. 5-11) reveals a phase lag between the measured and the predicted data. This is an indication that the numerical simulation overpredicts the extent of the separation bubble. This may be due to several factors: 1) possible three-dimensionality of the flow in this region; 2) deficiency of the k-ε turbulence model for the case of a strong separation bubble. Downstream of the separation bubble (x/C_x = 0.65), the distribution of the unsteady pressure is similar to those at the design condition.

An overall comparison between the measured and the predicted pressure field shows that the numerical simulation predicts the unsteady pressure field fairly well.

5.14 Effect of Inlet Turbulence

Additional simulation studies have been carried out with different freestream turbulence intensities at inlet. The design condition had a 7% turbulence intensity in the free stream at the inlet. The additional simulation includes a freestream turbulence intensity of 2% and 15% (which is closer to that existing in aircraft engines). The major feature is the decay of the nozzle wake. The amplitude of unsteady pressure distribution shown in Fig. 5-30 reveals that the freestream turbulence intensity plays a major role. The wake decay is slower and unsteadiness is higher at the low turbulence intensity and decreases significantly as the turbulence intensity is increased to 15%. This is confirmed by the nozzle wake defect plotted in Fig. 5-31.

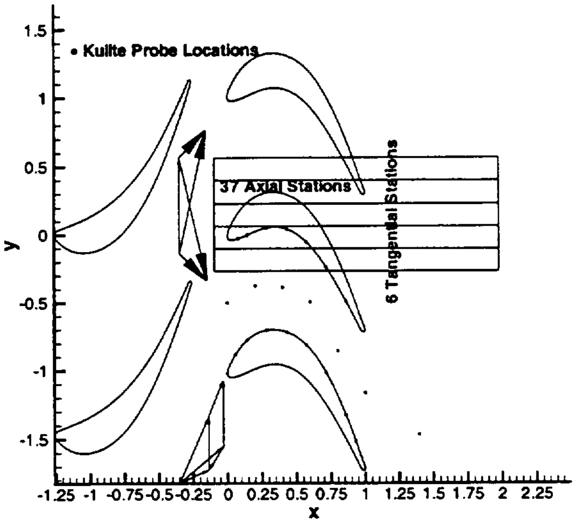
• Kulite Probe Locations
37 Axial Stations
6 Tangential Stations
1.5
1
0.5
0
-0.5
-1
-1.5
y
-1.25
-1
-0.75
-0.5
-0.25
0
0.25
0.5
0.75
1
1.25
1.5
1.75
2
2.25
x

Fig. 5-1 LDV and Kulite measurement locations in rotor passage (velocity triangle is based on design)

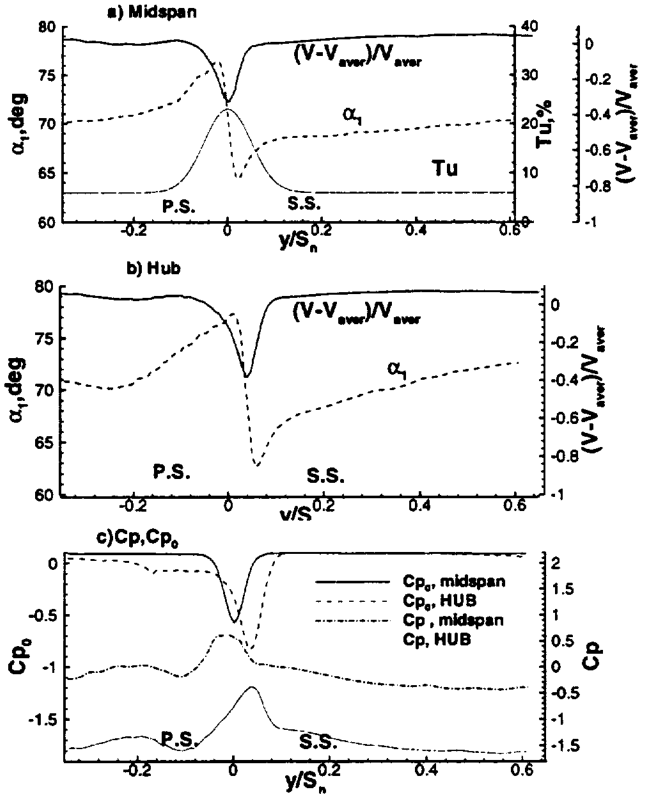

Fig. 5-2 Variation of rotor inlet static and stagnation pressure coefficients, velocity and turbulence quantities at x/c_x =-0.244, design conditions (case A)

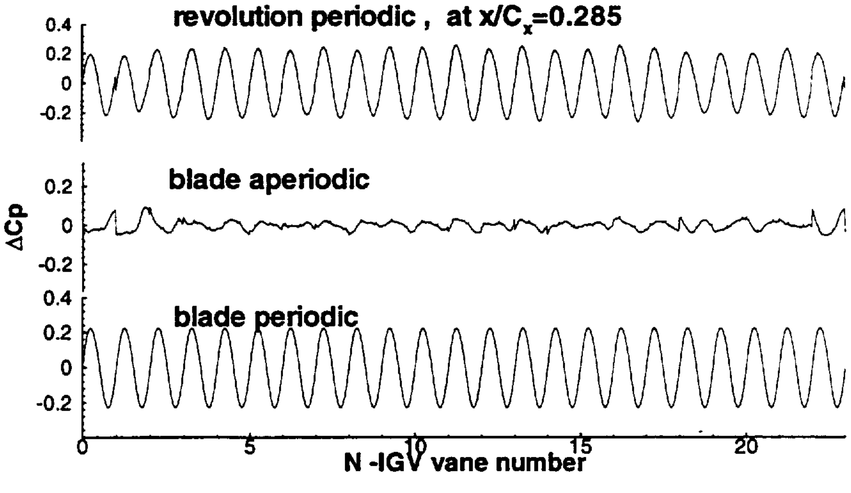

Fig. 5-3 Decomposition of the revolution periodic data into blade periodic (average passage) and blade aperiodic

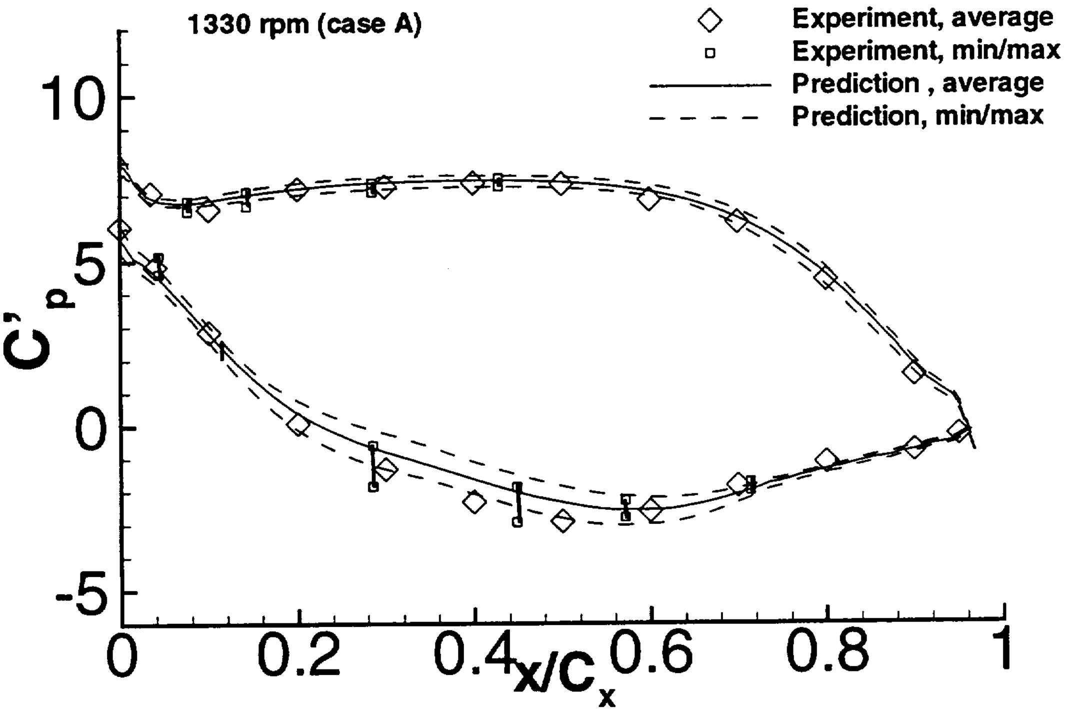

Fig. 5-4 Averaged blade pressure and unsteady pressure envelope at design conditions, (midspan)

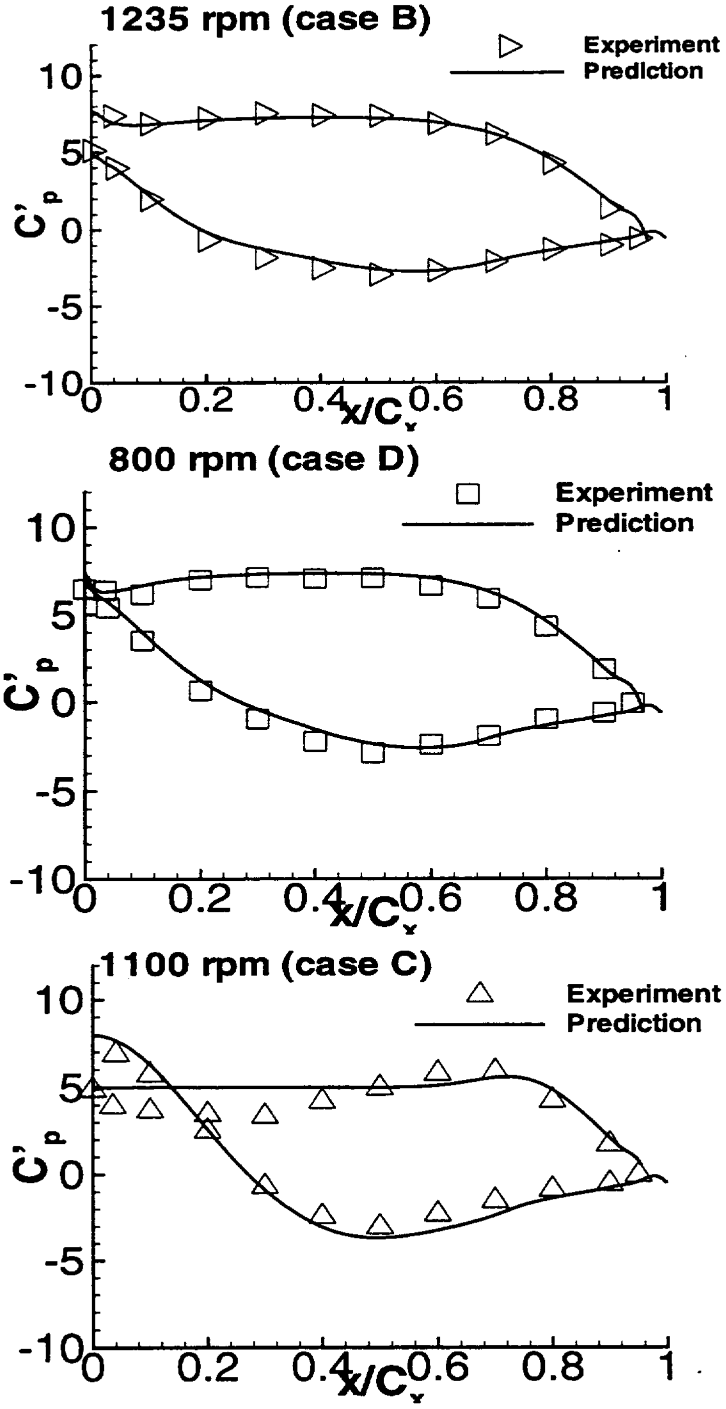
1235 rpm (case B)

800 rpm (case D)

1100 rpm (case C)

Fig. 5-5 Averaged blade pressure coefficient on the rotor blade midspan at off design

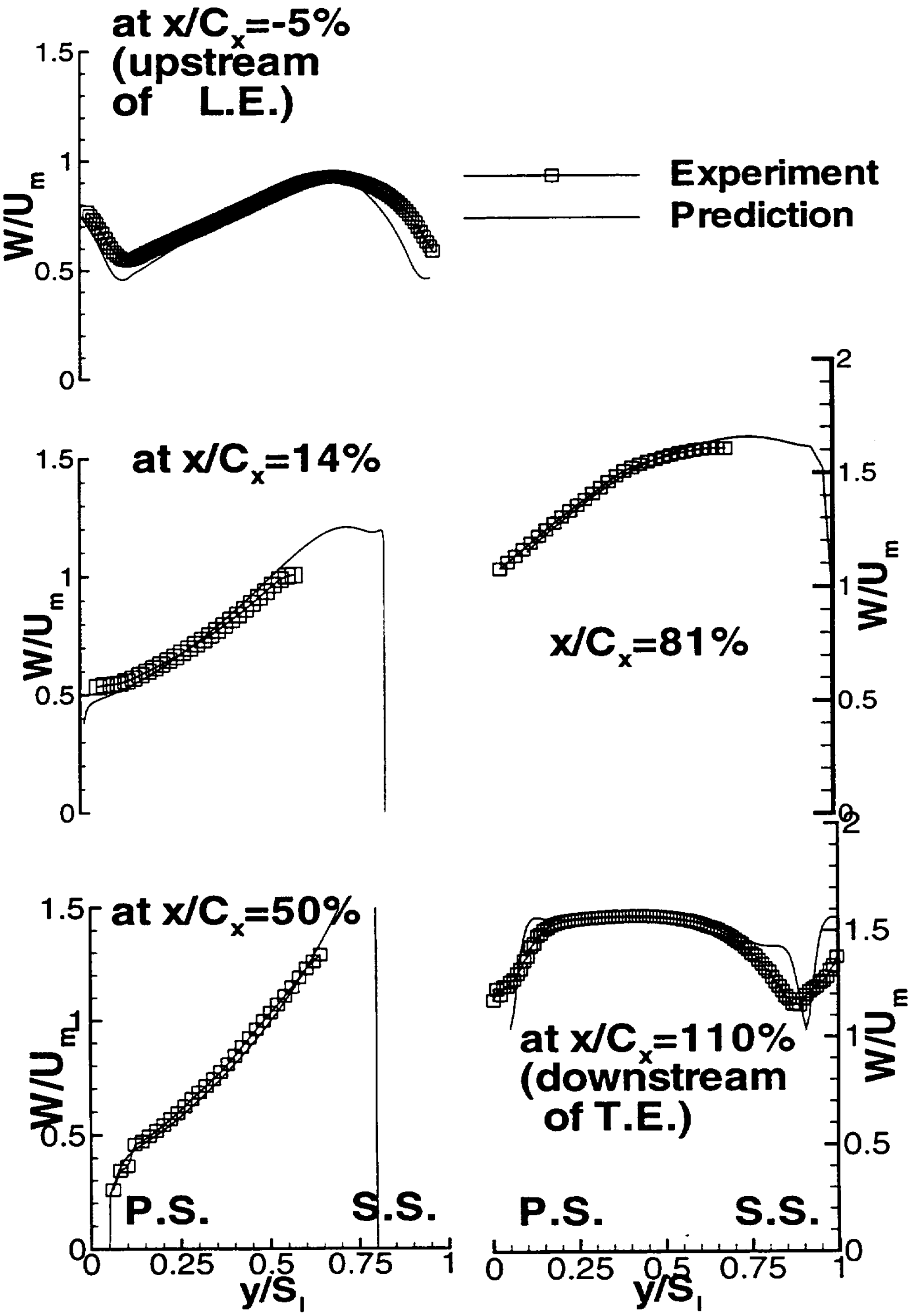

Fig. 5-6 Blade-to-blade distribution of relative velocity

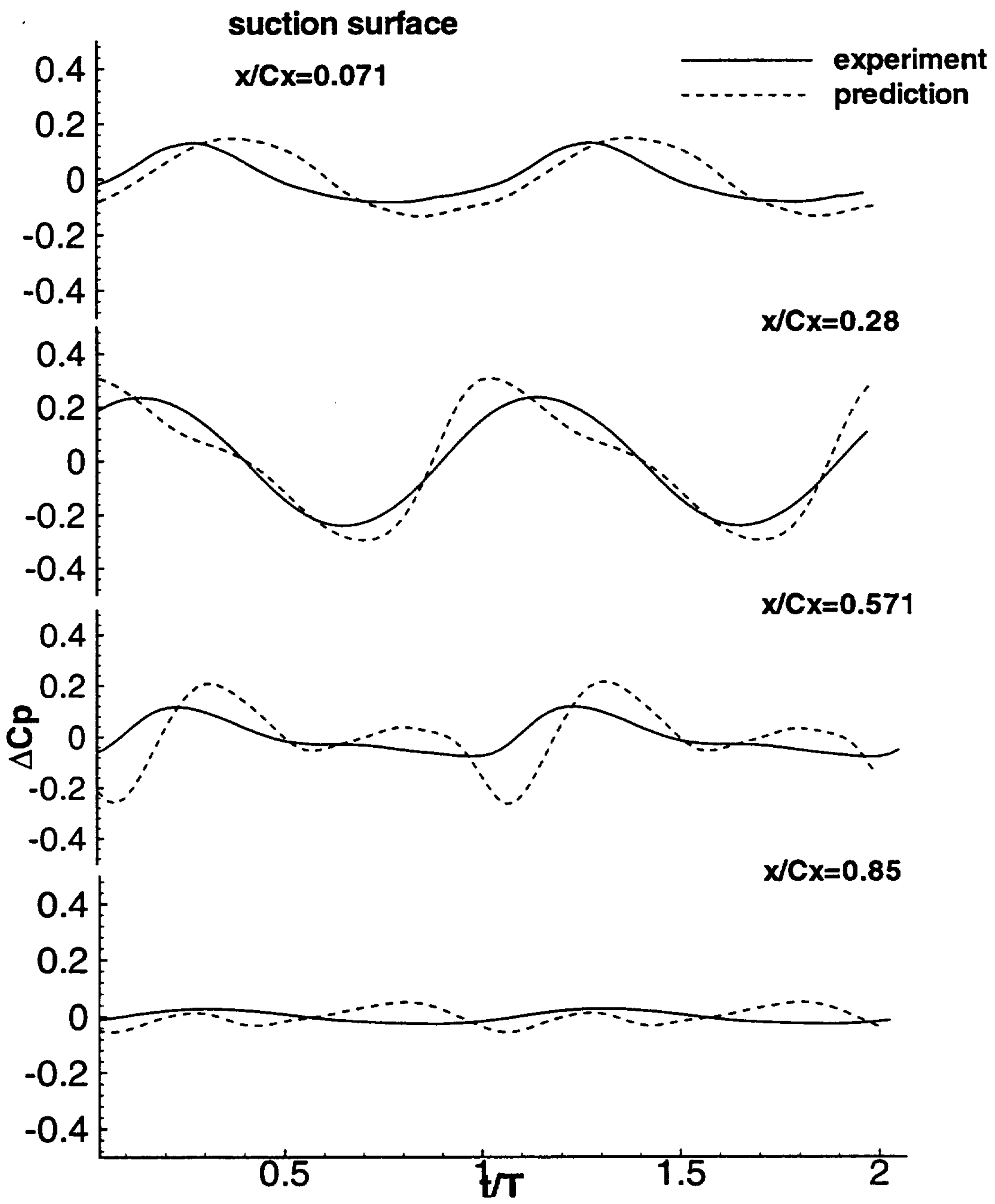

Fig. 5-7 Measured and predicted time history of unsteady pressures on the suction surface (design condition)

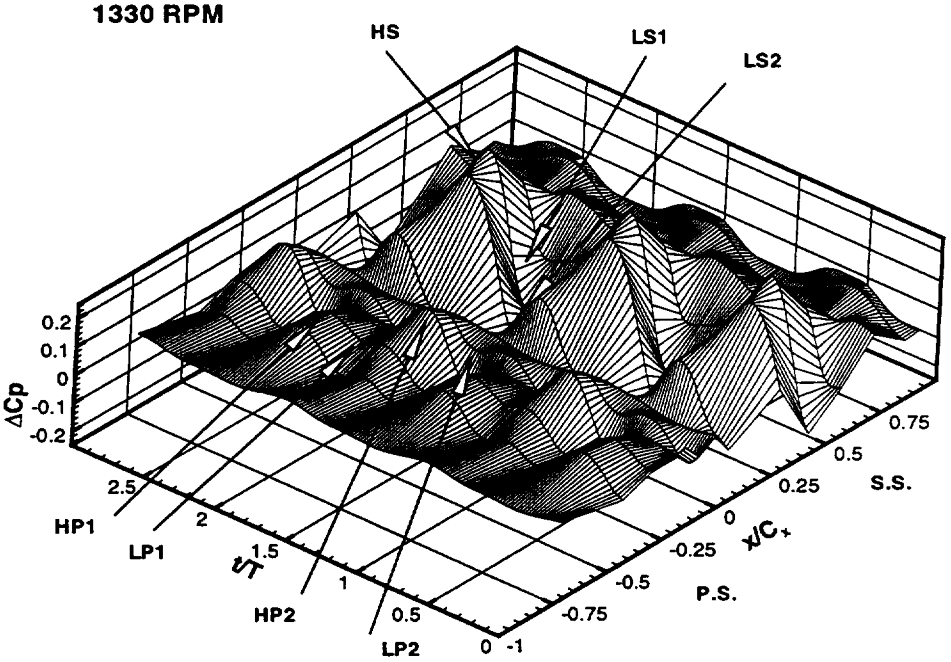

Fig. 5-8 Measured space-time distribution of blade unsteady pressure, case A (design)

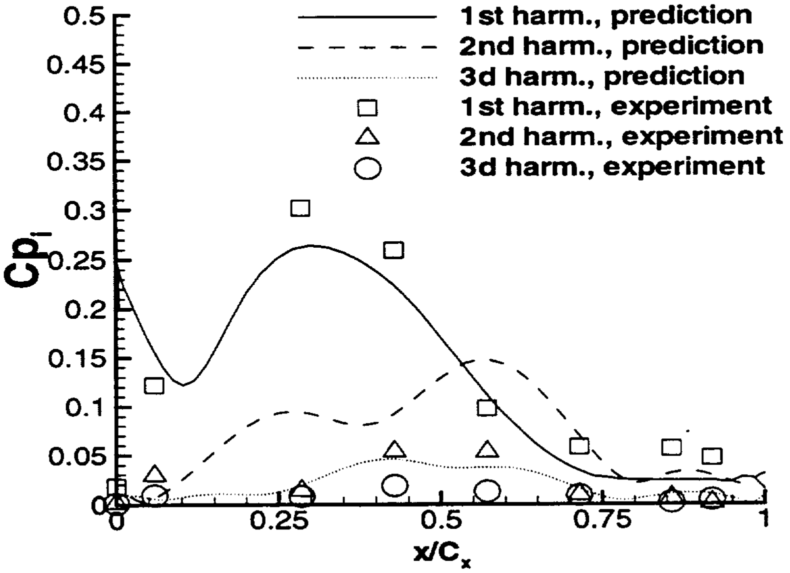

Fig. 5-9 Measured and predicted harmonics of blade unsteady pressure suction surface

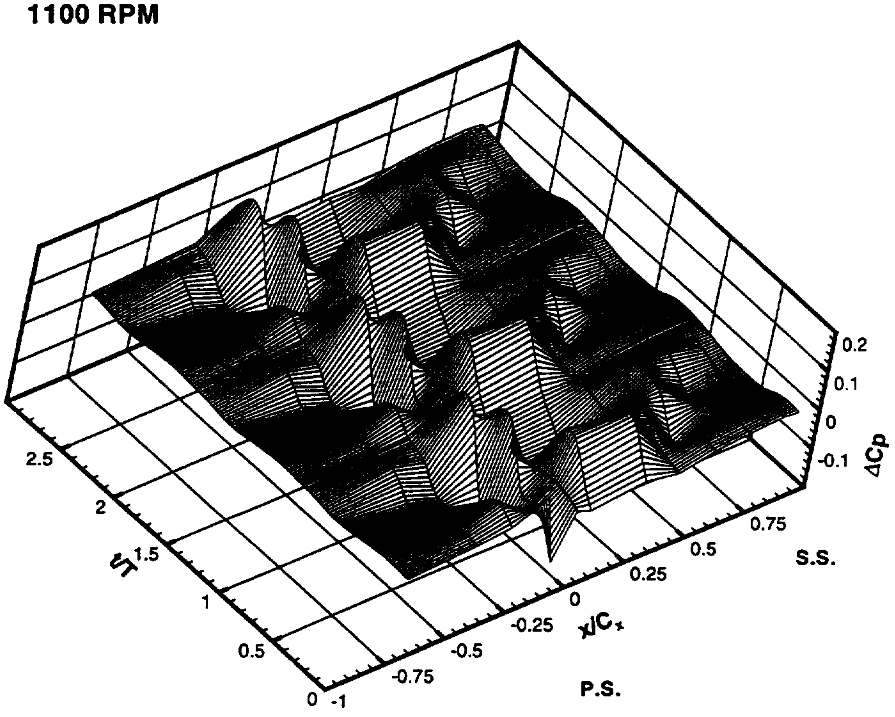

Fig. 5-10 Measured space-time surface pressure distribution at midspan, case C

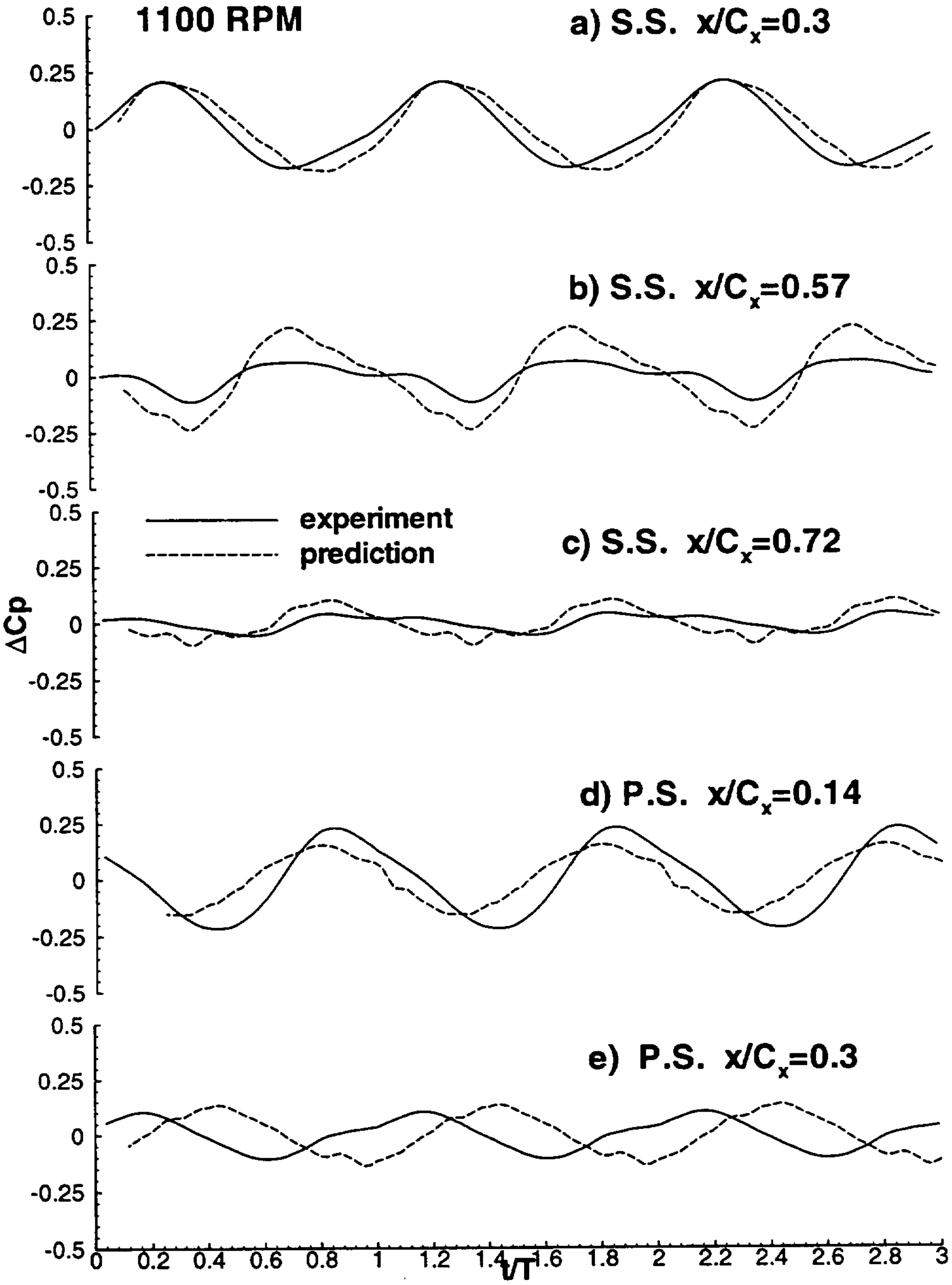

Fig. 5-11 Measured and predicted time history of unsteady pressure, case C (off design)

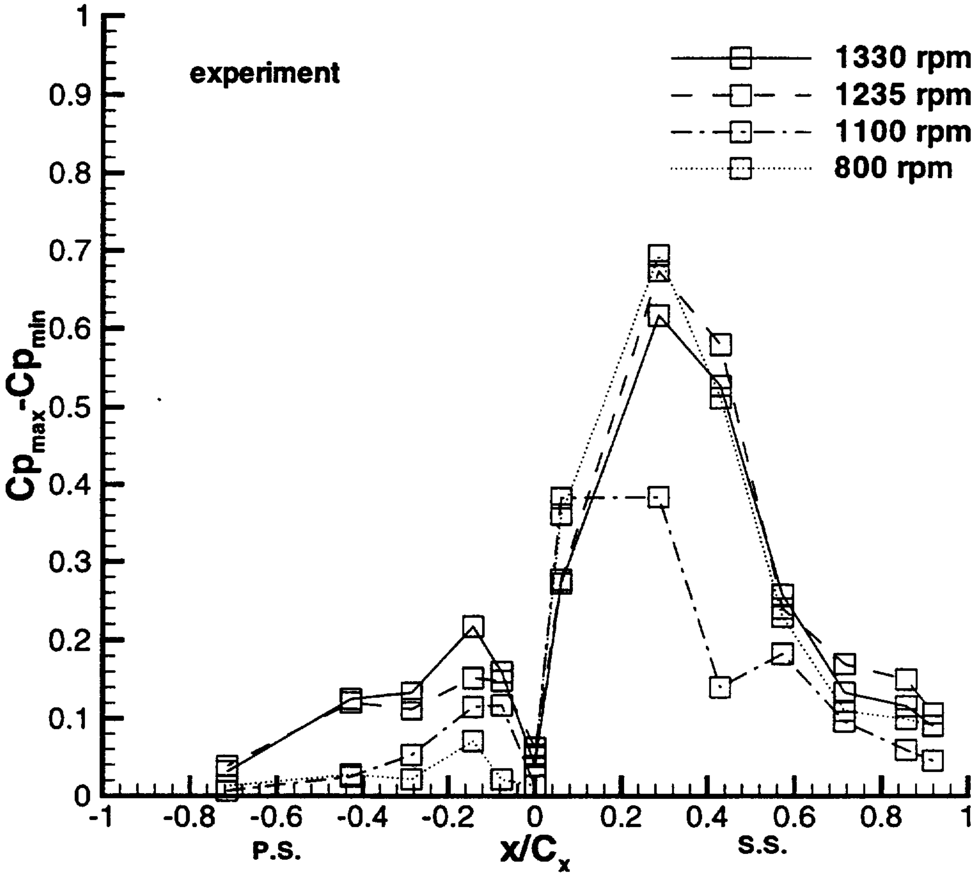

Fig. 5-12 Maximum variation of surface unsteady pressure, cases A-D

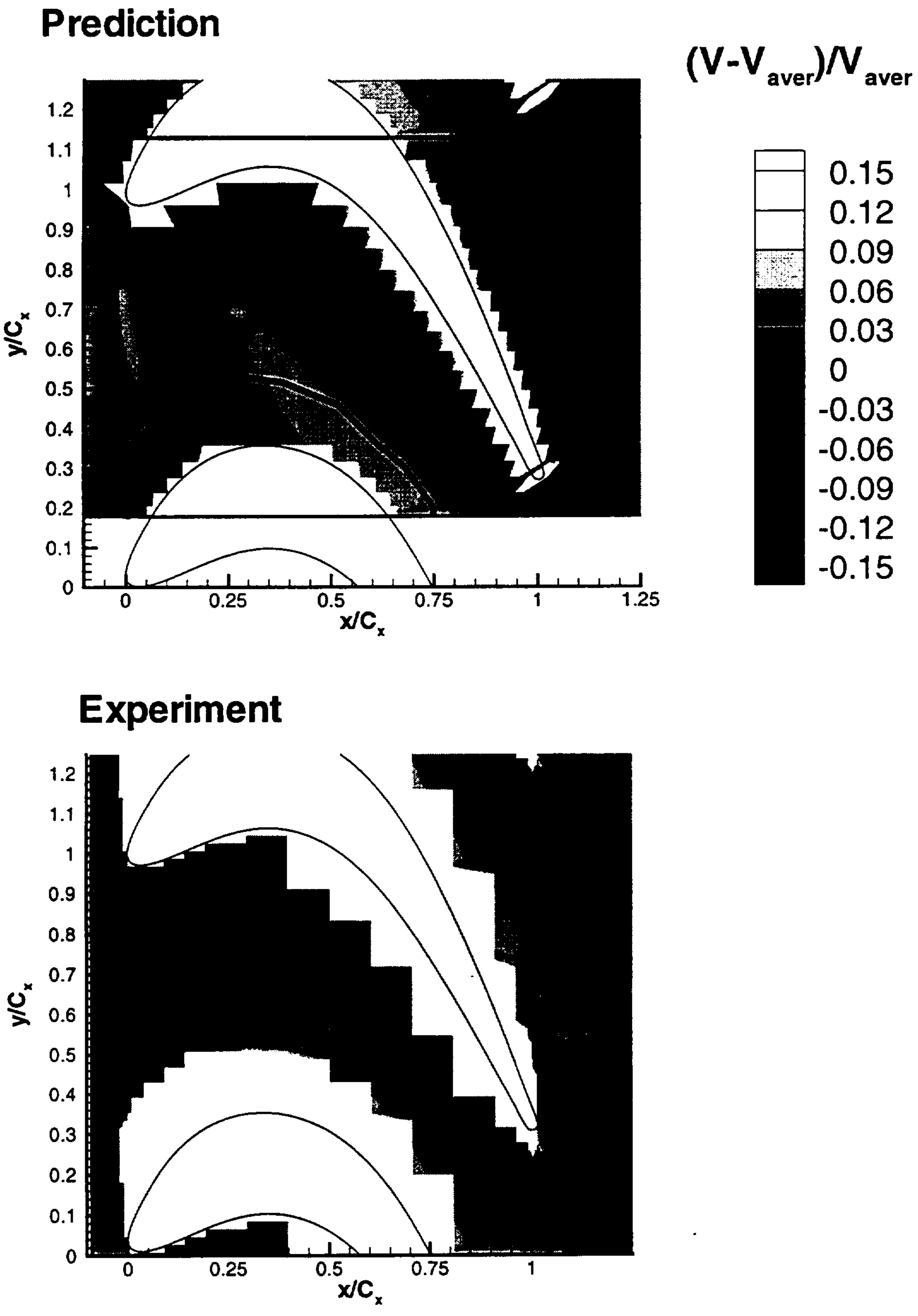
Prediction

Experiment

Fig. 5-13 Nozzle wake defect at the nozzle-LDV position N1

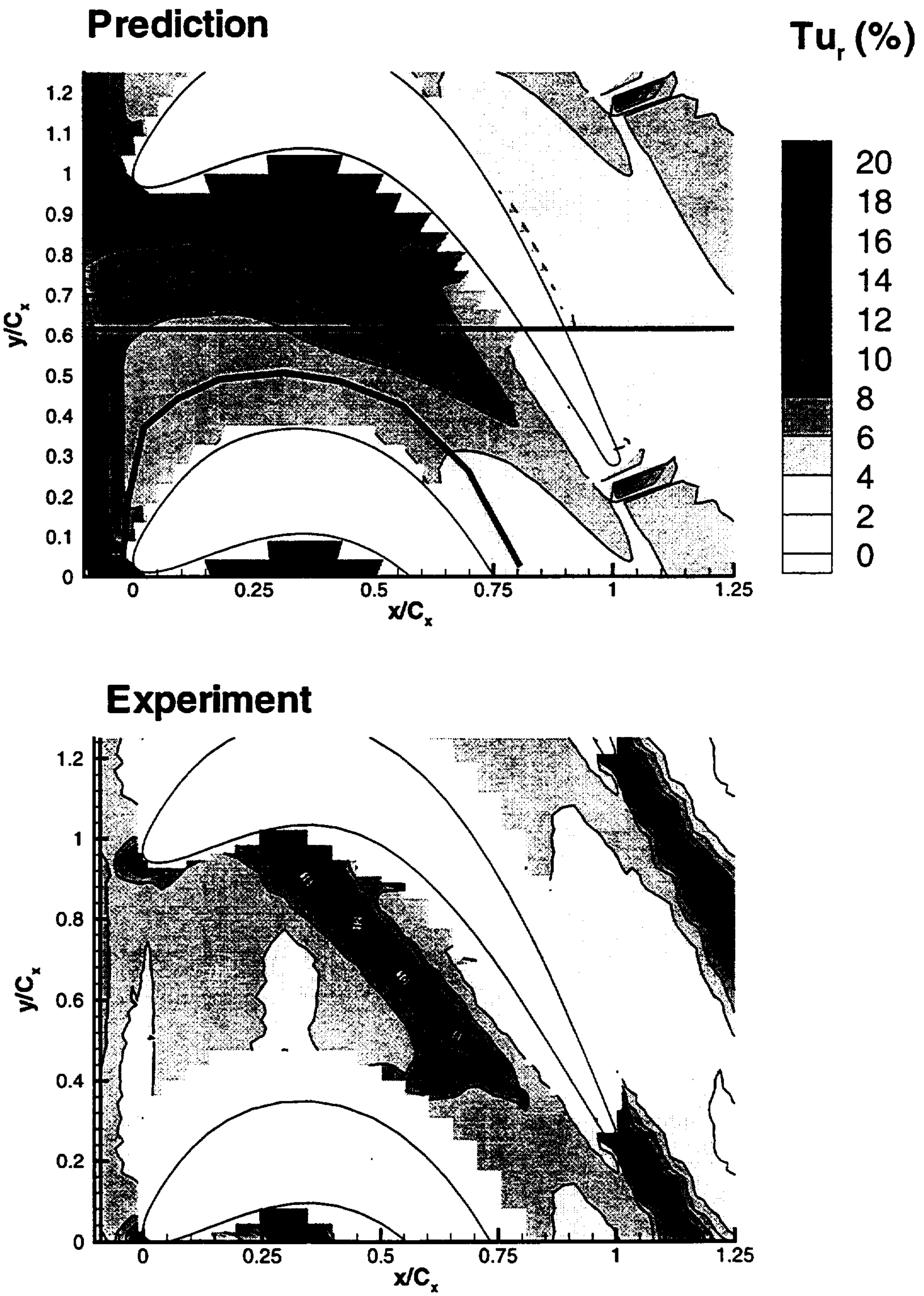

Fig. 5-14 Unresolved unsteadiness at nozzle-LDV position N4

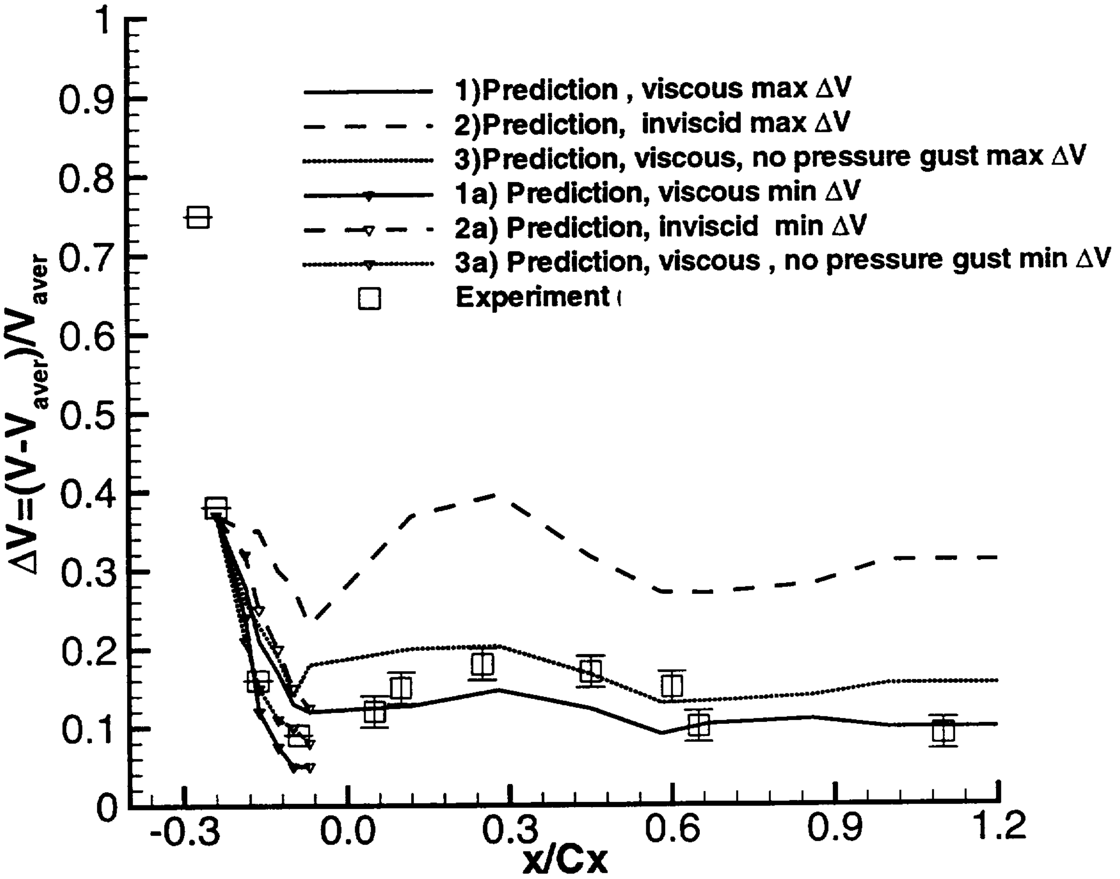

Fig. 5-15 Wake defect decay

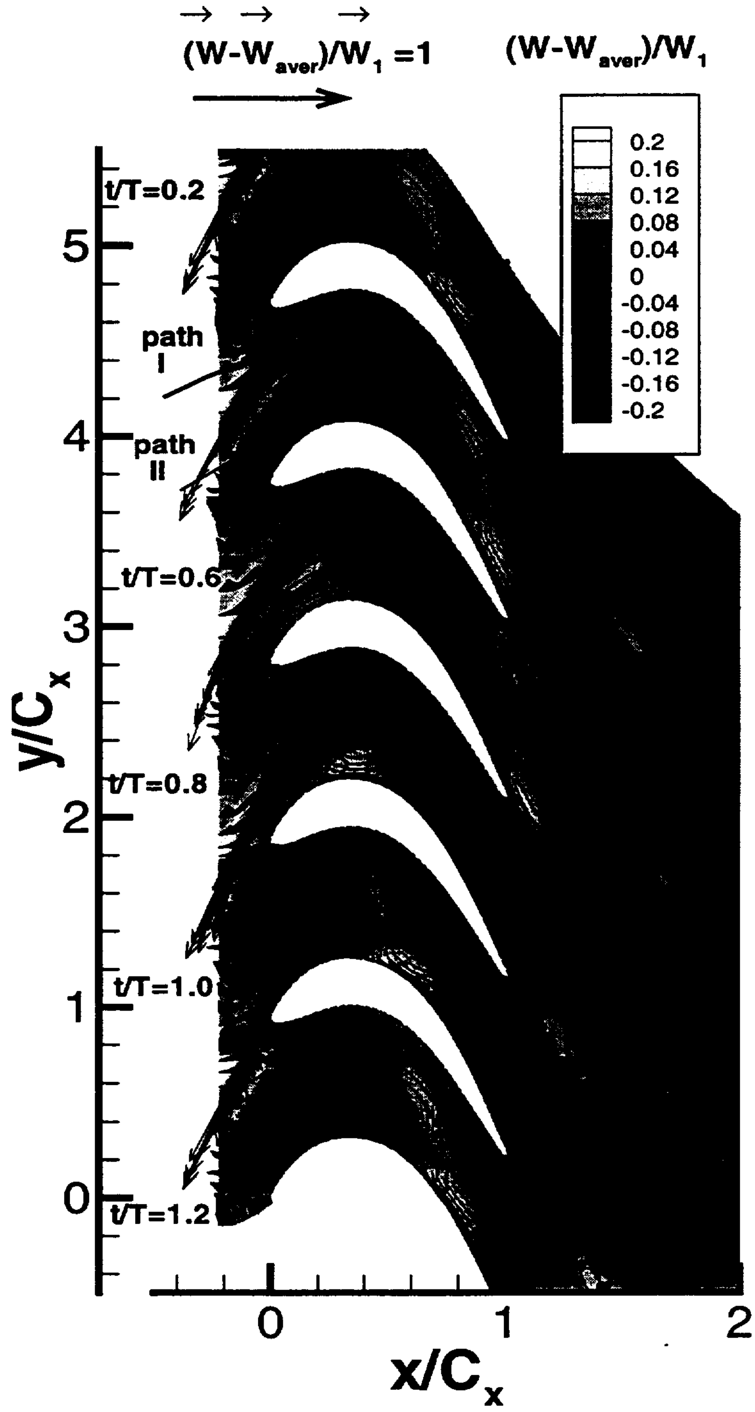

Fig. 5-16 Unsteady velocity field in the rotor passage

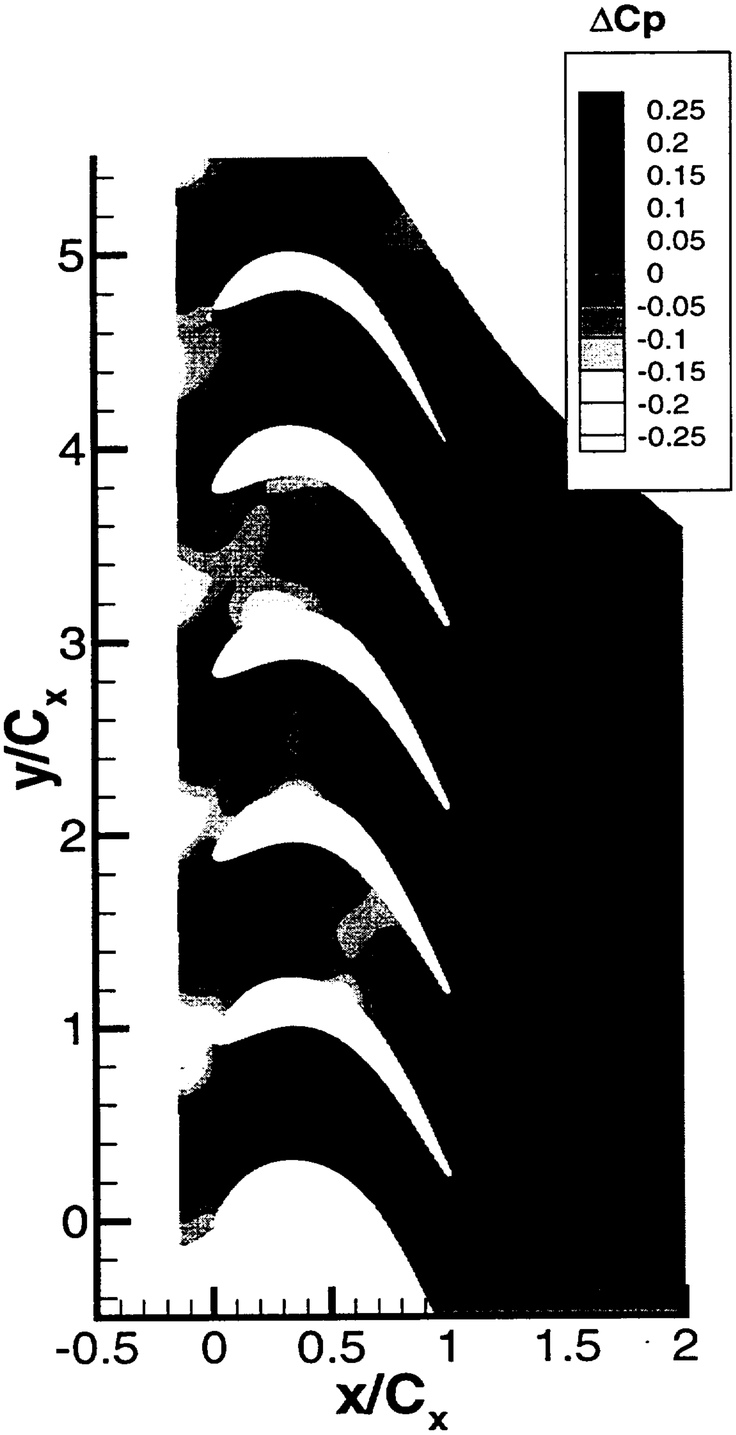

Fig. 5-17 Unsteady pressure field inside the rotor passage

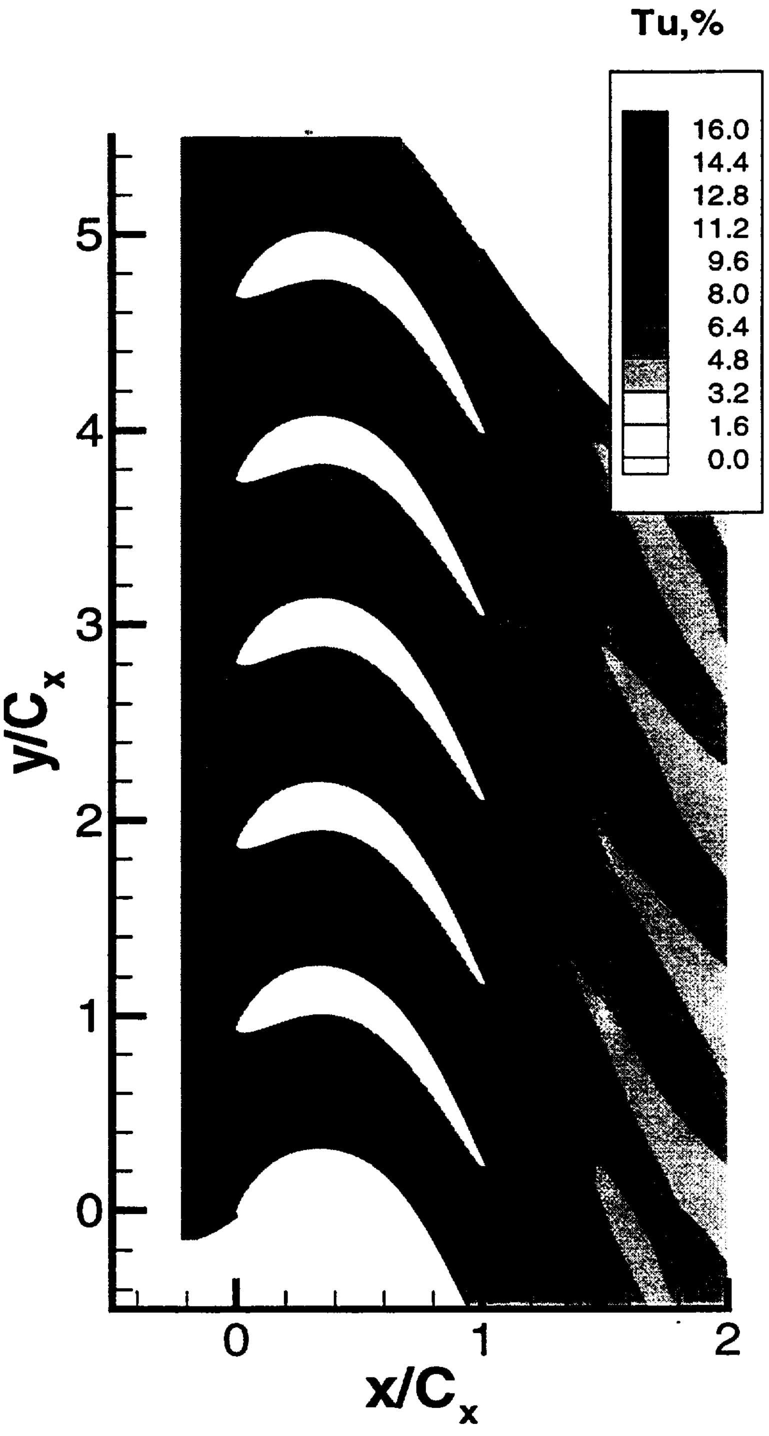

Fig. 5-18 Transport of the nozzle wake turbulence in the rotor passage

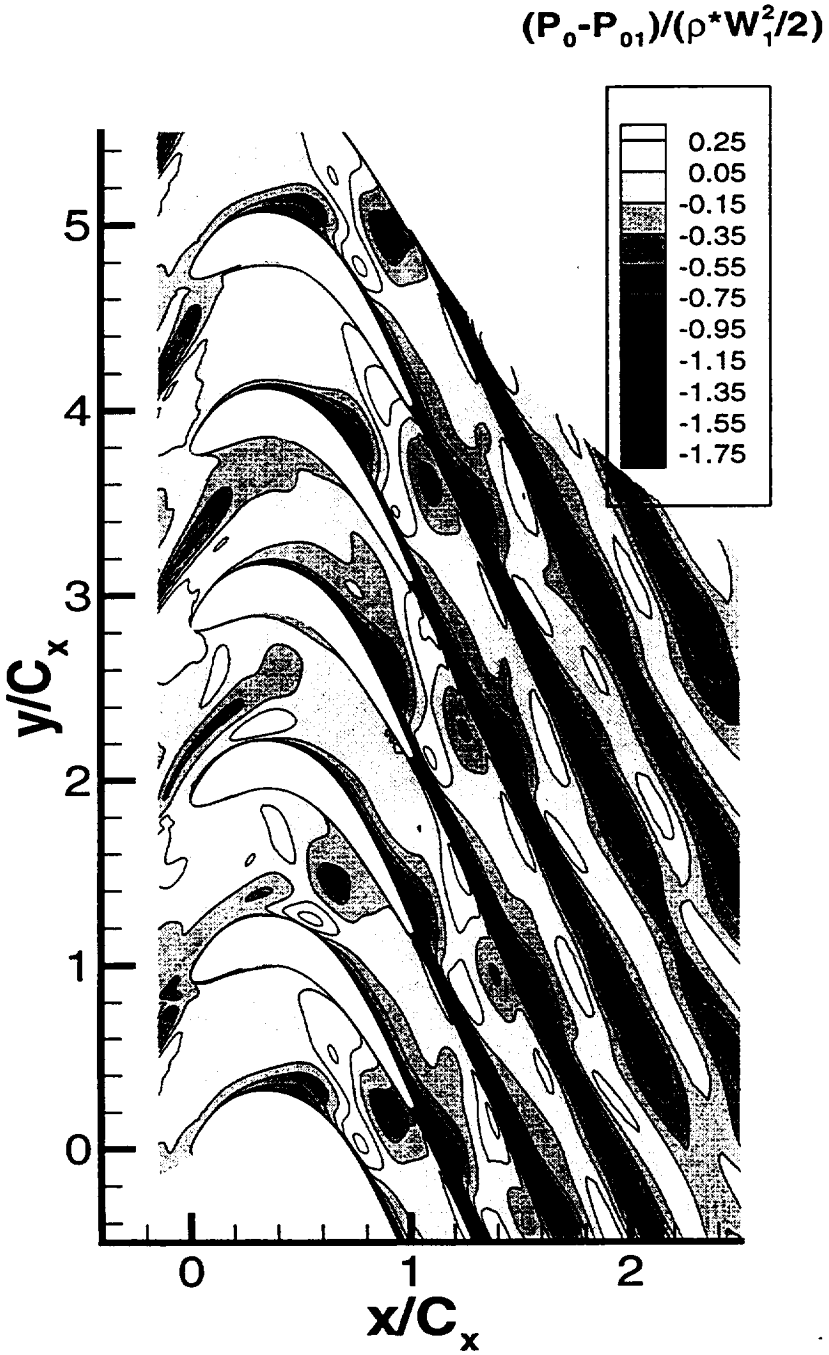

Fig. 5-19 Normalized unsteady relative total pressure coefficient

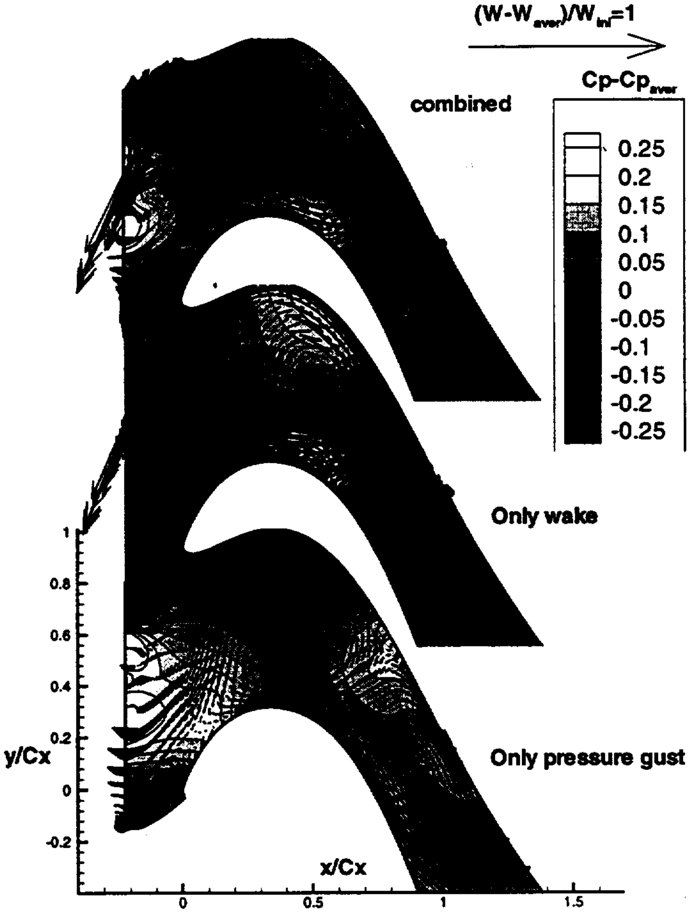

Fig. 5-20 Unsteady velocity and pressure field with different inlet B.C.

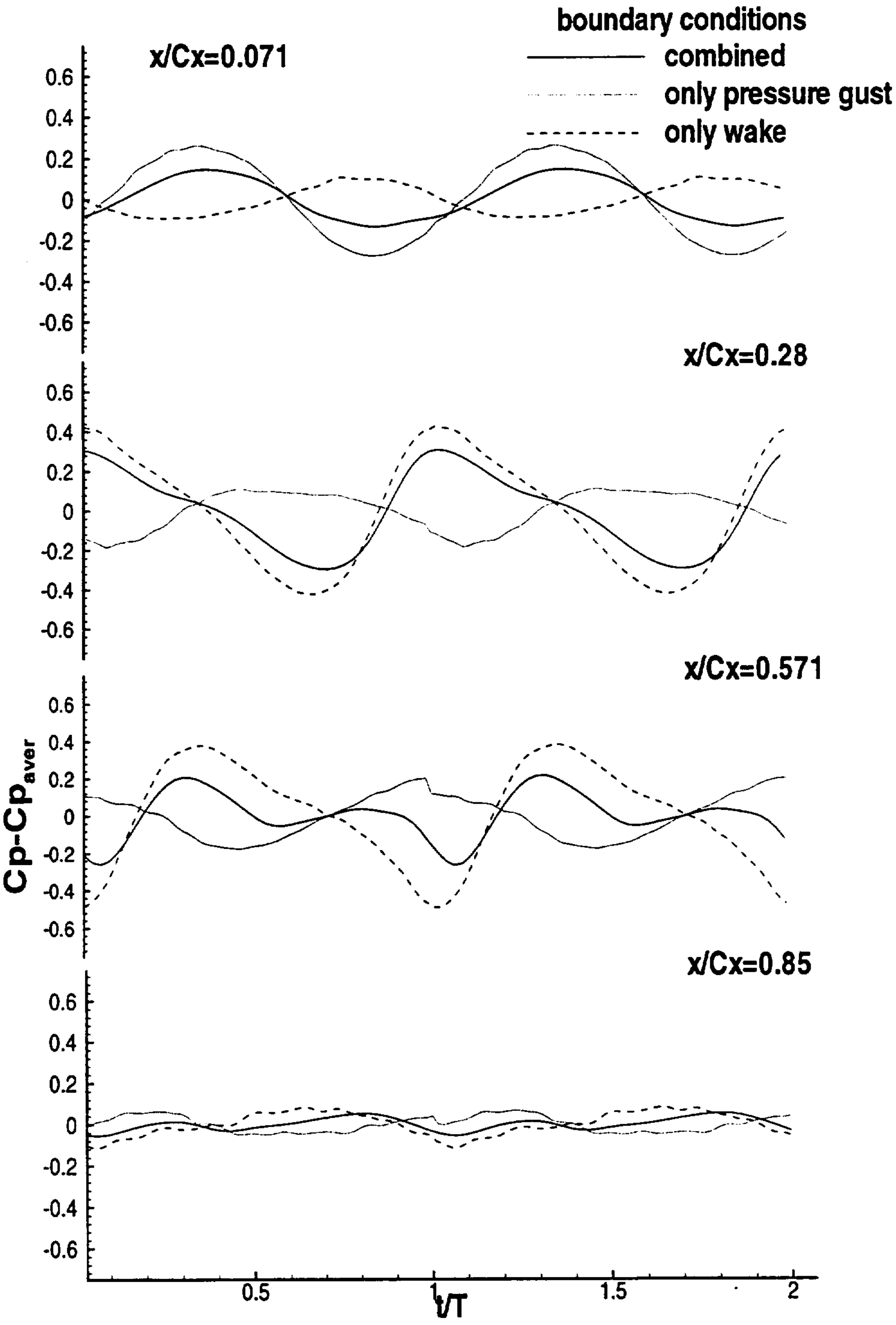

Fig. 5-21 Measured and predicted time history of the surface pressure with different inlet B.C.

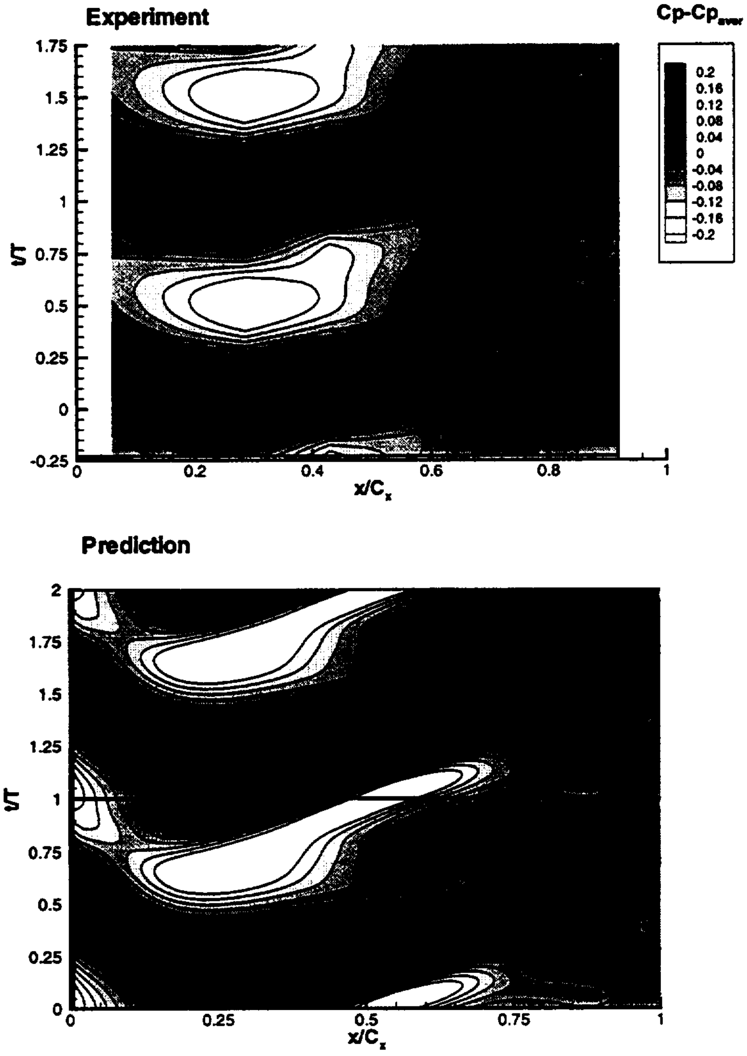

Fig. 5-22 Unsteady pressure coefficient, suction surface

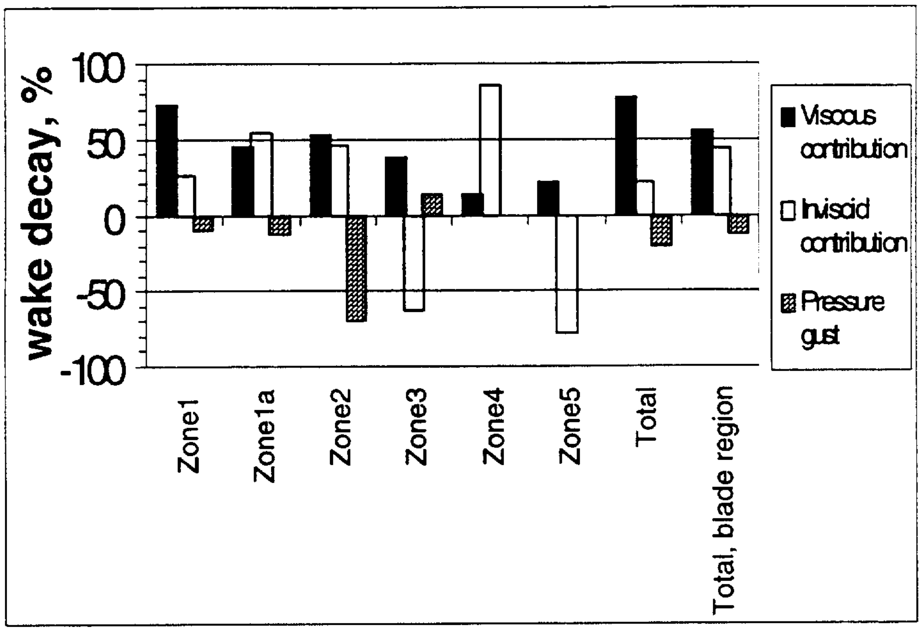

Fig. 5-23 Wake decay balance

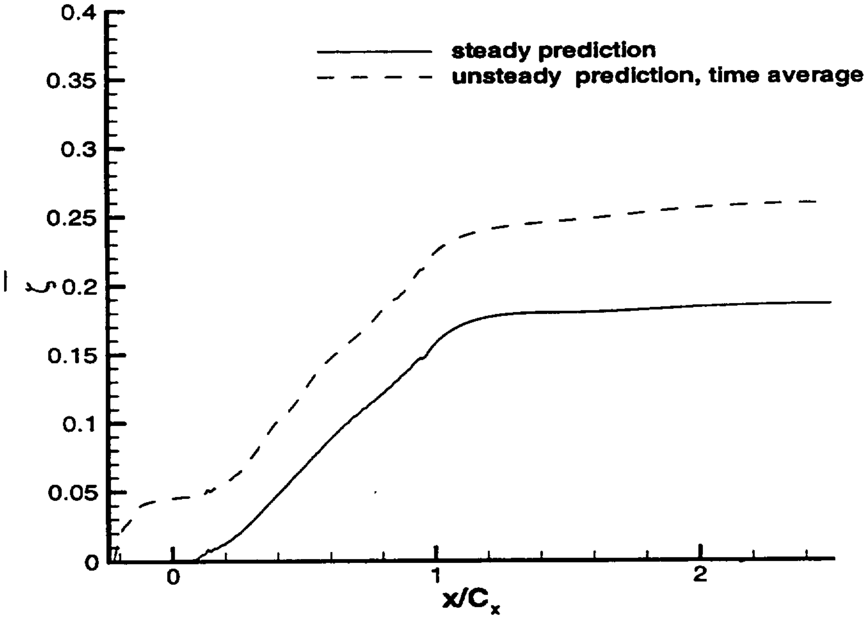

Fig. 5-24 Mass average loss coefficient

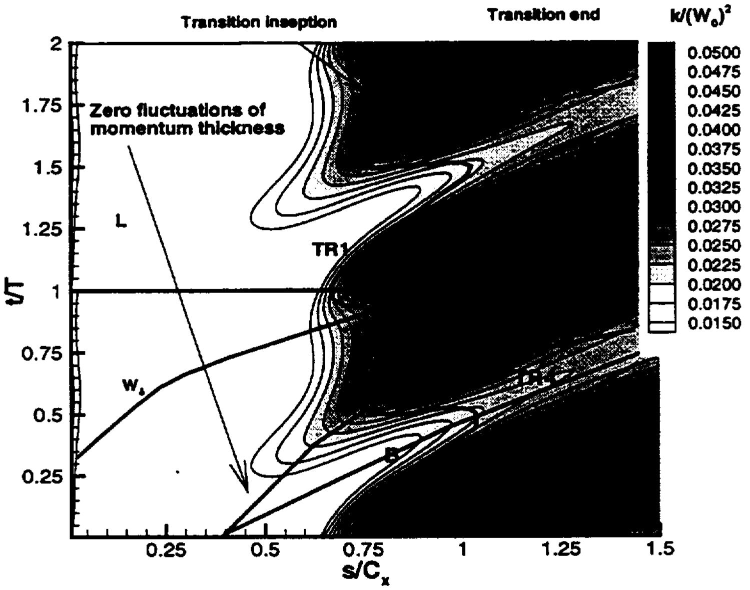

Fig. 5-25 Maximum turbulence kinetic energy in the boundary layer, suction surface

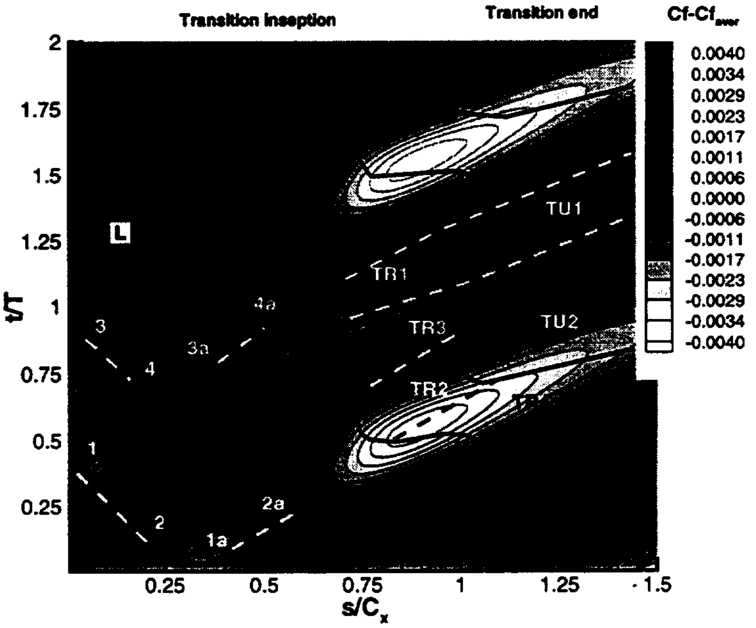

Fig. 5-26 Unsteady skin friction coefficient, suction surface

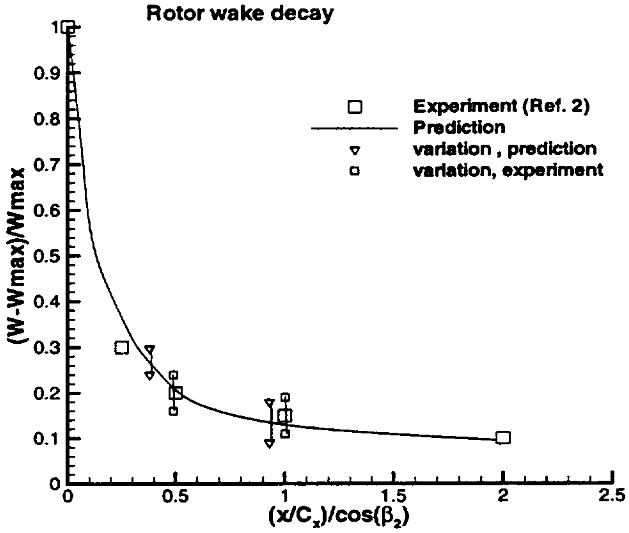

Fig. 5-27 Rotor wake decay as a function of streamwise distance distance

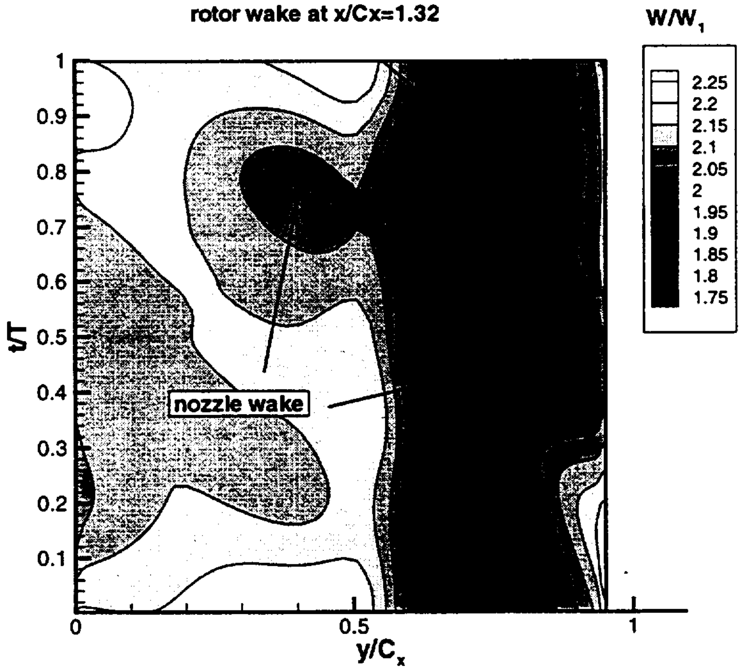

Fig. 5-28 Space-time distribution of the total velocity at x/C$_x$=132%

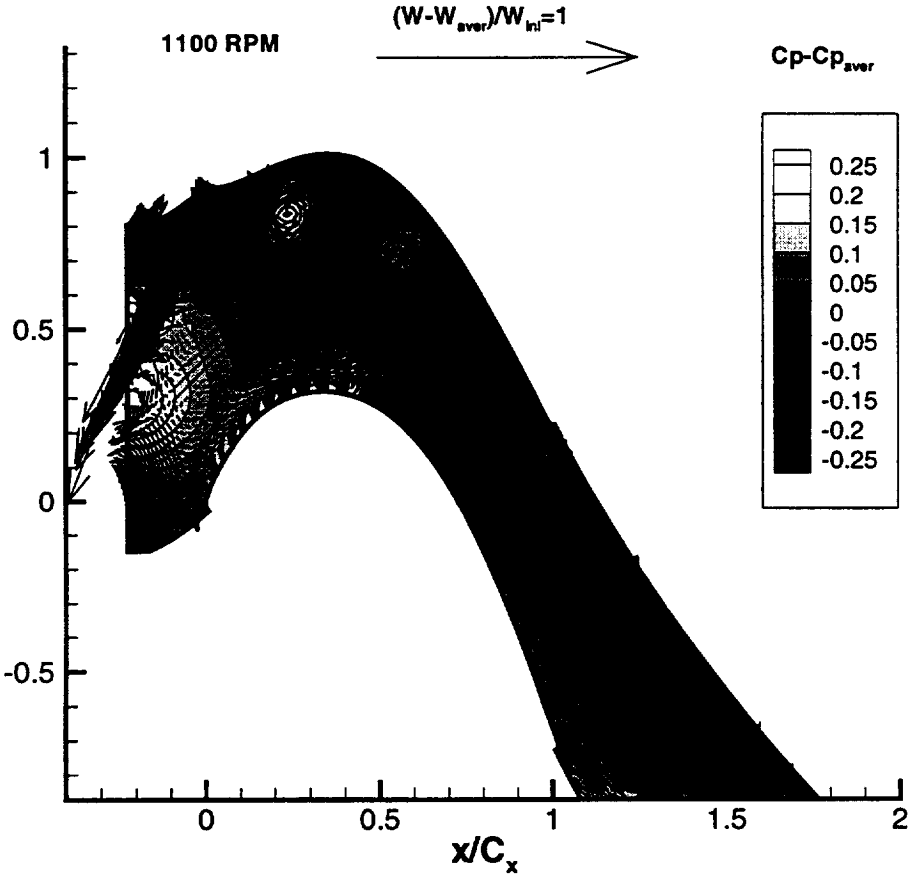

Fig. 5-29 Unsteady pressure and velocity fields, case C

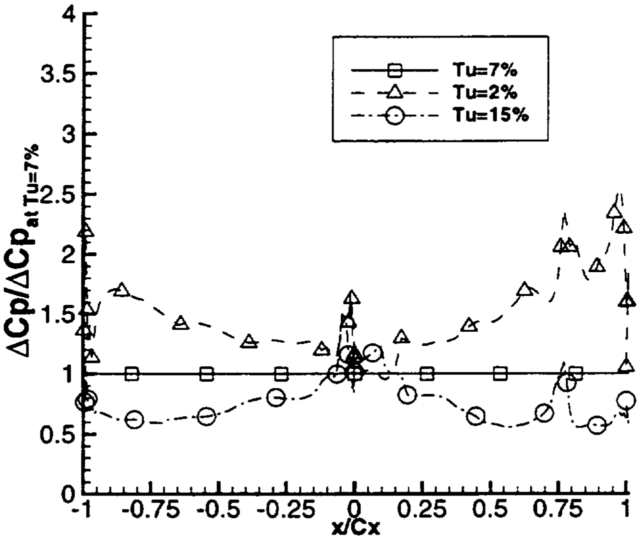

Fig. 5-30 Variation of the maximum blade unsteady pressure at different inlet turbulence levels

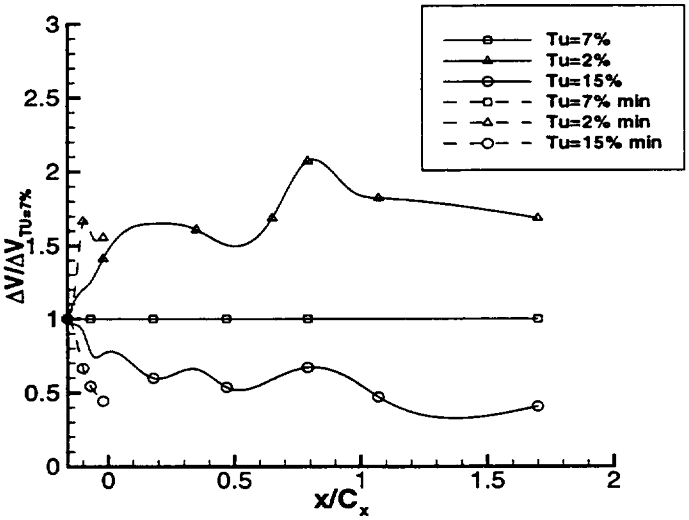

Fig. 5-31 Variation of the maximum wake defect at different inlet turbulence levels

Chapter 6

NUMERICAL SIMULATION OF THE TRANSITION OVER LAMINAR SEPARATION BUBBLE

The flow in a low pressure turbine stage of the aircraft engine is complicated by the variation of the flow conditions. A significant change in the ambient condition results in notable variations in the stage Reynolds number. Modified boundary layer development affects losses, efficiency, and heat transfer characteristics of the stage. At cruise condition, the flow Reynolds number may be less than half of the value of the take-off condition. This may result in a separated flow and efficiency degradation. The development of a reliable prediction technique is very important in the design of efficient machines and may lead to an improved efficiency and weight/thrust characteristics. The transition in a low-pressure turbine may occur in either bypass form, similar to those observed in high pressure turbine, investigated in the previous chapter, or through the development of a separation bubble, depending on the Reynolds number between the take-off and the cruise condition.

Considerable effort has been spent in the investigation of the ability of different turbulence models to predict various types of transitional flows. Nevertheless, very few investigators were focused on turbomachinery flows with the transition over a laminar separation bubble, especially at a high level of freestream turbulence (Michelassi et al., 1997, transonic turbine , Huang and Xiong., 1998, low pressure turbine).

The objective of the research presented in this chapter is to gain a detailed understanding of the unsteady transitional flows in low-pressure turbines, with emphasis on separation-induced steady transition. The test case chosen for this study is the simulation of the separation and the transition of the flow over the suction surface of low-pressure turbine cascade blade investigated experimentally by Qiu and Simon (1997). The influence of the free stream turbulence and pressure gradient is investigated. An existing Navier-Stokes unsteady flow solver is used. Three low-Reynolds number forms of two-equation turbulence models have been incorporated and tested for accuracy. In order to overcome the over-prediction of the turbulence kinetic energy and the dissipation rate near the leading edge, several modifications of the production terms have been incorporated in the code as well as the Algebraic Reynolds Stress Model.

6.1 Description of the Test Case

The experimental data in a simulated LP turbine cascade have been used to assess the ability of the numerical solver. A schematic of the facility is shown in Fig. 6-1 (Qiu and Simon, 1997). The cascade flow was simulated using a channel with a convex and concave wall profiled as suction and pressure surfaces of a turbine blade. A flow suction device was utilized to simulate periodic flow near the leading edge. Experiments were carried out with the inlet flow velocity ranging from 3 to 12.5 m/s, which corresponds to Re number from 50, 000 to 200, 000. A number of turbulence generators were utilized to generate the flow with 0.5, 2.5 and 10% inlet turbulence intensities. Boundary layer characteristics were measured using a hot-wire probe. Coordinates of measurement locations are given in Table 6-1. According to Qui and Simon (1997), the uncertainty in the mean velocity is 3.6%, and the fluctuating velocity is 4%.

Table 6-1 Location of the experimental data points on the suction blade surface

N	x/C_x	N	x/C_x
P1	0.	P8	0.6889
P2	0.0398	P9	0.7457
P3	0.2111	P10	0.8173
P4	0.3778	P11	0.8593
P5	0.4667	P12	0.9111
P6	0.5506	P13	0.9728
P7	0.6247		

6.2 Numerical Procedure

Numerical simulation shows that for the LP turbine flow, the utilization of the explicit ARSM does not modify the solution outside the boundary layer, but may cause a stability problem. To avoid this instability and minimize the CPU time, the ARSM is used only up to twice the boundary layer thickness from the blade surface.

Experimental data were acquired assuming two-dimensionality of the flow. However, turbulent and especially transitional fields are essentially three-dimensional. To address this feature, the numerical simulation based on the ARSM/ k-ε approach is carried out using a three-dimensional solver. The symmetry boundary condition in the spanwise direction forces the mean flow to be two-dimensional. Nevertheless, the turbulence field contains the spanwise component of the Reynolds stresses.

Experimental data were acquired in a “channel” type configuration, while an original “cascade” configuration was chosen for the numerical simulation. The utilization of the bleeding device to model the cascade flow may lead to a discrepancy in the flow angle in the vicinity of the leading edge. To verify the potential effect of this discrepancy, a numerical simulation of the cascade flow at different inlet flow angles have been carried out. A comparison of the predicted and the measured blade pressure distribution indicates that the best prediction has been achieved at the design flow angle (Fig. 6-2).

Another potential source of the discrepancy between the “channel” and “cascade” configurations is the flow near the trailing edge. An extension wall employed in the experiment provides a smooth development of the boundary layer beyond the point of the virtual trailing edge. In contrast, the flow over a real trailing edge is characterized by a sudden change in the flow angle, local variation of the pressure, etc. The numerical experiment shows that, in the case of the attached flow, utilization of either approach leads to a practically identical solution except in the region 5% upstream of the leading edge. However, the flow prediction based on “cascade” configuration results in significant instability as soon as the reattachment point moves downstream of the trailing edge. In order to reduce the effect of this phenomenon, but keep the “cascade” approach, the blade has been extended using an extension wall with zero thickness for cases with a separation bubble.

The numerical investigation requires a verification to ensure the grid independence. A number of grids (121 x 71, 141 x 91, and 241 x 181; or 121x71x3 in the case of ARSM/k-ε model etc.) have been utilized to study the grid dependency on the solution. The maximum distance between the surface and the first grid point varies between y+=0.8 for the course grid to y+=0.12 for the finest grid. At x/c_x=0.65, coarse grid has 20 grid points within the boundary layer and 8 grid points within the laminar sublayer. The fine grid has 35 and 15 points correspondingly. Numerical predictions based on coarse and fine grid are very close to each other. In some cases, the fine grid solution was not stable in the transition region over a separation bubble. The difference between the solutions based on fine and coarse grid is minimal for the converged solution. All the reported simulation data in this paper is based on 141 x 91 grid. Additional discussion on the code verification is presented later.

The numerical simulation of the transitional flow in turbomachinery cascades reveals the deficiency of the standard k-ε model in predicting the flow with a high free stream turbulence. Non-physical increase in the turbulence intensity near the stagnation point may "contaminate" the boundary layer turbulence and trigger an earlier transition. An elevated level of the turbulence at the mid-passage, in the zone of maximum flow acceleration, leads to a higher level of freestream turbulence (ΔTu= 3-4%) at the boundary layer edge. The modifications of the k-ε model described in Chapter 3 is used to predict turbulence filed near the leading edge and at midpassage accurately. After the incorporation of the production term modification, the inlet distribution of the dissipation rate is set to provide the measured kinetic energy along the boundary layer edge.

6.3 PREDICTION USING k-ε MODEL

6.3.1 Case Re=200000, Tu=10%

The distribution of the surface pressure predicted by different turbulence models is compared with the experimental data in Fig. 6-2. Since the flow is fully attached at this Reynolds number, the pressure increases monotonically along the rear part of the suction surface. There is no difference between the blade pressure distribution predicted by various turbulence models. Flow with Re = 200,000 and Tu=10% is fully attached on the suction surface (Fig. 6-3). The flow with Re=50,000 and Tu=10% has transition over laminar separation bubble as shown in Fig. 6-4.

In the laminar part of the boundary layer (experimental locations P2-P7, Table 6-1), the predicted velocity field exactly match the measured values. For brevity, this comparison is not shown. Velocity and turbulence intensity profiles at locations P8-P13 are shown in Fig. 6-5. The beginning and the end of the transition, as well as the separation location predicted by various turbulence models, are compared with the data in Table 6-2

Table 6-2 Inception and length of the transition, separation and reattachment points, Re=200000, Tu=10%.

	Experiment	Prediction FLB model	Prediction CH model	Prediction LB model
Transition inception, x/C_x	71%	~65%	57-59%	61%
End of transition, x/C_x	81%	82%	94%	80-82%
Separation, x/C_x	attached[1]	attached	75%	attached
Reattachment, X/C_x	-	-	no reattachment	

[1] Flow visualization indicates the presence of a very small separation bubble at x/C_x=0.7

In the laminar boundary layer, the prediction based on the LB model is identical to those based on the FLB model. The turbulence intensity profile shows that the CH model predicts an amplification of the turbulent kinetic energy in the laminar boundary layer. While the eddy viscosity predicted by the CH model is four-five times higher than the eddy viscosity derived from the simulation based on the FLB or LB models, it is still small. The ratio of eddy viscosity to laminar viscosity is about 4 and this part of the boundary layer has laminar features. The primary source of this increase is the lack of turbulent dissipation to compensate for an increase in the turbulent kinetic energy near the leading edge, rather than generation inside the boundary layer. The increased level of turbulence intensity predicted by the CH model contributes to an earlier transition.

The simulation based on the CH model predicts the transition at about 58% of the chord. The best agreement between the measured and the predicted velocity profile is achieved in simulations based on FLB and LB models. At locations P8 and P11 the predicted velocity profiles are identical to the experimental data. Between P8 and P11 the measured profile is less steep in comparison with the numerical solution. The transition inception is predicted at about 4% of the chord upstream of the measured location. The numerical simulation predicts a shorter transition and hence the flow field is near the end of the transition at the location P10. The turbulence profile is very close to 'fully developed' profiles. As a consequence of this, the predicted velocity profiles at P9-P10 are closer to turbulent profile when compared to the data.

The main drawback of the CH model is the existence of a very thin separation zone near the 75% of the chord. The CH model, based on y+, is known for its poor performance in separated flows. The CH model overpredicts the turbulence intensity in the turbulent boundary layer by 50-70%.

6.3.2 Case Re=50000, Tu=10%

Reduced Re number results in the development of a medium size separation bubble (Fig. 6-4). The separation zone is characterized by the presence of a flat zone in the pressure distribution at x/Cx~0.75 on the suction surface of the blade (Fig. 6-2b). A solution based on the FLB model correctly predicts this trend, which shows an earlier return to an adverse pressure gradient. As confirmed by the velocity profiles, this is due to a smaller separation bubble and earlier reattachment of the flow. In spite of the presence of the separation bubble in the simulation based on FLB and CH models, the region of constant pressure is not clearly predicted by these two models.

Velocity profiles are plotted in Fig. 6-6. Experimental data indicates that the flow separates at about 74% of the chord and the transition to turbulence occurs over a laminar separation bubble at about 81% of the chord. All three models predict a laminar separation at the same location; x/Cx=71% of the chord. The length of the laminar region inside the separation bubble varies for different models. The CH model gives the transition immediately after the inception of the separation at 71% of the chord. A simulation based on the FLB model predicts the transition inception at 78% of the chord, with distance between the separation point and inception of transition equal to 7%, which is close to the measured value.

The transition to turbulence over the separation bubble is characterized by the inception of the transition in the shear layer with further penetration through the separation zone. The maximum turbulence intensity is located farther from the wall in comparison with high Re cases (Fig. 6-6). Contrary to the measured data, the numerical simulation predicts strong backward flow inside the separation flow, (point P10). An additional turbulence production due to the higher shear stresses in the zone of separated flow increases the turbulence intensities in the separation bubble. The predicted turbulence profile has a smoother distribution, and its maximum is located closer to the wall in comparison with the experimental data. In the case of FLB and LB models, an increased level of turbulence in the separation zone leads to a smaller thickness of the separation bubble and an earlier reattachment. A comparison between the numerical simulation and the data is given in Table 6-3.

Table 6-3 Inception and length of the transition, separation and reattachment points, Re=50000, Tu=10%.

	Experiment	FLB model	CH model	LB model
Transition inception, x/C_x	76%	78%	72%	75%
End of transition, x/C_x	>p13 97.28%	84%	85%	86%
Separation, x/C_x	70%	71%	72%	72%
Reattachment, X/C_x	91%	93%	no reattachment	no reattachment

6.3.3 Case Re=50000, Tu=2.5%

This case is the most difficult to compute. A low level of turbulence at a low Re number leads to an inherently unsteady flow with an unsteady separation bubble and transitional zone. Even though the results presented in this paper is based on the steady solution, the analysis of the convergence and unsteady flow simulation indicate the need for an implementation of the time accurate simulation to achieve better resolution of the flow physics. No results for the LB model is presented, because attempts to stabilize the solution using increased artificial dissipation resulted in total damping of the separated flow. For the CH and FLB models, the flow has moderate fluctuation in the size and extent of the separation bubble. The data presented is calculated as an average of these fluctuations. This variation affects the rear part of the separation region and does not influence the location of the separation point and the transition inception point.

A comparison between the predicted and the measured surface pressure distribution is shown in Fig. 6-2c. Both models underpredict the extent of the separation bubble, which results in a shorter zone of constant pressure. A comparison of the measured and the predicted velocity and turbulence intensity profiles (Fig. 6-7) shows similar trends to the cases described earlier. The numerical solver overpredicts the turbulence intensity in the transition zone; while for the flow with high freestream turbulence level, the maximum turbulence intensity is underpredicted (similar to Re=200000 case with Tu=2.5% and Tu=10%). There is no peak in turbulence fluctuations above the separation bubble in the transition region. The prediction based on the FLB model has a smaller separation bubble thickness and an earlier reattachment. The size of the separation bubble is equal to the experimental data at point P9, about 1/2 of the experimental value at point P10 and 1/3 at point P11. For the FLB model, the variation in the thickness of the separation bubble was 50%. A low level of the freestream turbulence delays reattachment from the 85% to 99% of the chord. A comparison between the numerical simulation and the data is given in Table 6-4.

Table 6-4 Inception and length of the transition, separation and reattachment points, Re=50000, Tu=2.5%.

	Experiment	Prediction FLB model	Prediction CH model	Prediction LB model
Transition inception, x/C_x	81%	~80%	~78%	69%
End of transition, x/C_x	96%	86%	88%	97%
Separation, x/C_x	69%	71%	69%	72%
Reattachment, X/C_x	no reattachment	99%	no reattachment	90%

6.4 Prediction Using Hybrid ARSM/K-ε Model

Experimental data for the transition over a laminar separation bubble (e.g., Wang and Hatman, 1998) shows a strong redistribution of the turbulent kinetic energy between components in the transition zone. Peaks of u' and v' are equal to each other, while in the attached turbulent boundary layer v' is equal to 40% of the u' component. The k-ε model is unable to capture this redistribution as well as the overall anisotropy of the turbulence field associated with the transition process. A numerical simulation based on the hybrid k-ε/ARSM has been carried out to investigate the ability of this model to improve the prediction of the transition flow over the LP turbine blading. Results of the current research as well as previously reported simulations (e.g., Abid et al., 1995) indicate that a numerical solution strongly depends on the k-ε model used. A comparison of the prediction based on hybrid models with different low Re k-ε (CH, FLB, LB) led to the conclusion that transition inception is controlled by the k-ε model and is close to those predicted by a corresponding k-ε model. Therefore, the FLB model has been chosen as the model with the best results based on the previous computations.

Results of the numerical simulation based on hybrid k-ε/ARSM are identical to the prediction based on k-ε approach. High Re case is characterized by the transition in an attached boundary. Maximum shear stresses are located close to the blade surface in the region where viscous residual is calculated using k-ε approach. ARSM part is used only for the outer layer. Therefore, the influence of the hybrid approach is minimal. In contrast, the shear layer above the separation zone is located in the zone where viscous residual is calculated using ARSM. Thus, the hybrid approach has a more profound effect. For the high Re case (Re=50 000, Tu=10%), this effect is minimal and can be seen only in the turbulence field. The utilization of a hybrid model moves the peak of the fluctuation velocity further from the wall, and closer to the measured location. There is only a minor change in the predicted velocity field. A comparison between the predicted and the experimental data for the case with Re=50, 000 and Tu=2.5% (Fig. 6-8) reveals an improvement in both predicted velocity and turbulence.

Current numerical simulations have been carried out without the pressure strain terms. As a result, the w' component is equal to the v' component. An analysis of the turbulent case indicates that the streamwise component has about 50% of the total turbulent kinetic energy, while v' and w' have 25% each. No significant change in the balance between the different components is found in the transition region (no more than 5% variation). Hybrid turbulence model overpredicts maximum amplitude of the fluctuation velocity similar to k-ε model. However, redistribution of the turbulence energy between turbulence components plays a major role in improving the velocity prediction .

6.5 Prediction Using k-ε Model in Conjunction with the Transition Model

A numerical simulation of the transitional flows based on the turbulence model generally does not provide an adequate level of accuracy and robustness. Incorporation of transition models is a potential way to improve the transition prediction. Transition models use an empirical or a semi-empirical correlation to calculate the inception and end of transition, as well as the intermittency distribution in the transition region zone. A number of models were developed to calculate the inception and end of transition in an attached flow. The most common approach is the calculation of the transition inception using an empirical correlation and the calculation of the intermittency distribution using the approach suggested by Dhawan and Narasimha (1958), in conjunction with the correlation for the non-dimensional spots breakdown parameter (e.g., Gostelow and Walker, 1991; Mayle, 1991). In the current research, a model by Abu-Ghannam and Show (1980) is utilized for the transition prediction in an attached flow:

$$\mathrm{Re}_{\theta tr} = 163 + \exp\left[F(\lambda) - \frac{F(\lambda)\cdot Tu}{6.91}\right]$$

$$F(\lambda) = \begin{cases} 6.91 + 12.75\cdot\lambda + 63.64\cdot\lambda^2 \cdots if\lambda \le 0 \\ 6.91 + 2.48\cdot\lambda - 12.27\cdot\lambda^2 \cdots if\lambda > 0 \end{cases}$$

where: $$\lambda = \frac{\theta^2 (\frac{\partial p}{\partial x})}{\mu U_e}$$

transition is completed when:

$$\mathrm{Re}_\theta = 2\,\mathrm{Re}_{\theta tr}$$

Intermittency distribution is based on Dhawan and Narasimha (1958)

Transition models for separated flows correlate the distance between the separation and the transition inception. In the current paper the model due to Davis et al. (1985) is used:

$$\mathrm{Re}_{xtr} - \mathrm{Re}_{xs} = 25\cdot 10^3 \log_{10}\left[\coth(17.32 Tu_e)\right]$$

As in the case of the attached flow, an intermittency distribution is based on Dhawan and Narasimha (1958) formula. Even though this relation was suggested for the attached flow, a comparison presented in Qui and Simon (1997) indicates that it can be applied to the separated flow.

Utilization of the transition model provides a more reliable prediction in comparison with the "pure" turbulence model. Nevertheless, the transition model has a number of weak points. Empirical correlations are based on data that has a significant spread. The accuracy of the transition model deteriorates as flow parameters deviate from those used for the derivation of the model. A comparison between the predicted distribution and the measured data shows that the transition model used predicts an earlier transition. Therefore, this discrepancy may be attributed to the inaccuracy of the transition model. In addition to the models described earlier, calculations with the transition model based on the measured intermittency factor have been carried out to investigate an effect of the "ideal" transition model. For the attached flow case (Re=200, 000, Tu=10%), there is no significant difference in the predicted velocity and turbulence fields because the predicted transition inception based on Abu-Ghannam and Shaw correlation is located upstream of the "natural" transition inception predicted by a "pure" turbulence model. For the separated flow, the transition model used is practically identical with the experimental data for the case with Re=50, 000 and Tu=10%. However, as described in Qui and Simon (1997), for other cases with a high freestream turbulence, the correlation was not perfect.

Different approaches can be used to incorporate an intermittency distribution. Methods based on a separate solution for the laminar and turbulent parts show potential for the improved flow prediction (e.g., Steelant and Dick, 1996). Nevertheless, for engineering applications it is more advantageous to have a single solver throughout the flow field. This is especially preferred from the point of view of the model extension to three-dimensional flows in turbomachines. Two methods are tried for the incorporation of the intermittency factor into the existing code. In the first method, an additional damping function F (γ) is utilized for the calculation of the eddy viscosity (this case of the transition model utilization is denoted as Var.1):

$\mu_t = \frac{k^2}{\varepsilon} c_\mu f_\mu F(\gamma)$, where $F(\gamma)=\gamma$

This approach implicitly assumes that the eddy viscosity based on local scales is 'turbulent' in nature. If the distribution of the turbulent kinetic energy and the turbulent dissipation rate are transitional in nature, this approach may lead to an underprediction of the local eddy viscosity due to the 'double' damping. Assuming that the eddy viscosity in the transition region can be calculated correctly using the same expression for μt as for the turbulent part, the intermittency distribution can be utilized only through the modification of the turbulent equations. An additional damping function based on γ is applied only to the calculation of the production term (this case is denoted as Var. 2):

$P = P * F(\gamma)$, where P is the turbulence production

Mean flow is affected implicitly through the eddy viscosity.

In the transition zone, the intermittency distribution has complex two-dimensional distribution. Most of the transition models vary intermittency only in streamwise direction. Based on experimental distribution, the calculations have been carried out with the variation of the γ in both streamwise and crossflow directions. Overall six combinations of transition model incorporations have been analyzed; there are two ways to incorporate intermittency distribution into solver (Var.1 and Var. 2) and three different distributions of the intermittency factor:

1) Step distribution: $\gamma=0$, for $x<x_{tr}$ and $\gamma=1$, for $x>x_{tr}$

2) One dimensional:$\gamma(x) = Max_y(\gamma(x,y))$ or :$\gamma(x)$ base on transition model

3) Two-dimensional : $\gamma=\gamma(x,y)$

All cases are calculated using the FLB turbulence model, which gave the best prediction among the CH, LB, and FLB models.

In attached flow transition, the implementation of the transition model does not have any significant effect on the velocity and turbulence distribution. No significant influence of the method of the implementation of the transition model (Var. 1, Var. 2, or type of γ) is found. As stated above, the utilization of Abu-Ghannam and Shaw correlation predicts an earlier transition in comparison with both the experiment and the prediction based on "pure" turbulence model. The current approach may only postpone the transition inception. Therefore, the prediction based on the "pure" turbulence model and the transition model produce practically identical flow fields. Simulation with the experimental distribution of the intermittency factor improves the prediction the turbulence kinetic energy distribution in the vicinity of the transition inception and an earlier end of the transition. Nevertheless, there is no improvement in the velocity distribution at location P10.

In contrast to the high Re cases, the way the transition model is incorporated and the type of intermittency distribution used has a profound effect on the prediction of low Re flow (Fig. 6-9). The incorporation of the transition model with the direct effect on the eddy viscosity (Var. 1) resulted in the development of the larger separation bubble in comparison with the experimental data (Fig. 6-9). The separation zone extends beyond the location of the trailing edge. Utilization of the two-dimensional distribution of the intermittency factor led to a further increase in the separation bubble size. The flow prediction based on the application of the intermittency distribution to the calculation of the production term (Var.2) leads to the prediction of a much smaller separation bubble and reattachment near the trailing edge. The predicted height and extent of the separation zone are closer to the measured values, which is a consequence of the delayed inception of transition. However, an overall deviation of the predicted velocity profile from the experimental data is greater in comparison with the "pure" turbulence model for all cases except the "step" transition model. This is due to the double damping of the eddy viscosity in a transition zone. Even though γ distribution indicates that the transition zone should extend beyond the trailing edge, all but one (one-dimensional model, Var. 1) has the end of the transition upstream of the trailing edge. A numerical prediction based on the one dimensional distribution and "step" distribution in conjunction with Var. 2 gave the most accurate prediction of the separation bubble size and location, even though it does not improve the turbulence intensity distribution in comparison with the simulation without the transition model.

6.6 Effect of Artificial Dissipation on the Transition Prediction

The stability consideration requires an analysis of the differential approximation of the original PDE, which is not possible. Numerical experiments are carried out to study the influence of the artificial dissipation on the transition prediction. The major objective of the current validation is to establish the limits of its influence.

A number of realizations of the artificial dissipation terms have been analyzed. The original version of the code employed a hybrid second/fourth order artificial term with a switch based on the local turbulence field. Velocity scaling and eigenvector scaling are incorporated to keep the artificial dissipation at a minimum level in the boundary layer. Nevertheless, an analysis of the turbulence kinetic energy in the transition zone (Fig. 6-10b) indicates that the level of the artificial dissipation reaches 50% of the source term (Pk - ε) for the base case. The base case has k_{2ke}=0.01, which is about twice the minimum level required to avoid odd-even decoupling. To minimize the level of the artificial dissipation, the artificial dissipation term was modified to include only the streamwise variation of k. The k balance based on this modification is shown in Fig. 6-10c. All calculations presented in this paper are based on this modified approach, even though it does not affect the prediction beyond a small zone of high gradients in the transition region.

The effect of utilizing only the fourth-order artificial dissipation term in turbulence transport equations has been also investigated (for mean flow equations the artificial dissipation is always based on fourth-order terms). This approach does not alter the result of the analysis presented below (beyond absolute values of the artificial dissipation coefficient). However, the employment of only the fourth-order artificial dissipation leads to a significantly increased sensitivity of the code to the turbulence field development near the leading edge. A moderate flow disturbance generates a significant increase in the turbulence kinetic energy, which decreases rapidly downstream. Numerical modeling shows that this increase can not be explained as a transition with relaminarization further downstream, because it may be reproduced at any location within the first 30% of the chord by placing the source of potential disturbance (e.g., locally skewed grid).

The predicted location of the separation inception, beginning and end of transition and reattachment point as a function of the artificial dissipation is shown in Fig. 6-11. Both the insignificant as well as excessive levels of artificial dissipation result in an earlier transition. The values of k4 and k_{2ke} vary from the level below the stability limit to a level at which the artificial dissipation causes a significant non-physical diffusion.

It should be noted, based on the previous experience with the solver, that the recommended variation of the k_{2ke} was 0.01 – 0.02. Within this range, the variation of the predicted and measured location of the transition inception is within 2.5% of the chord. An earlier transition inception results in a smaller separation bubble (Fig. 6-11 and Fig. 6-

12). However, the variation of the artificial dissipation in the mean flow equation does not significantly influence the predicted mean flow profile (Fig. 6-13).

The primary source of the early transition in the case of a small k_{2ke} is a slight numerical instability of the scheme. For $k_{2ke} \leq 0.075$, a moderate odd-even decoupling generates a premature transformation from the laminar to the turbulent boundary layer. An increase in the artificial dissipation also results in an earlier transition inception. It is possible to identify zones with a different behavior of the scheme. For simulations with $k_{2ke}<0.02$, the variation of the artificial dissipation term affects only the transition inception, but the transition length is essentially constant. This fact indicates that, within this range, the artificial dissipation acts as a destabilizing factor. A comparison of the streamwise distribution of the turbulent kinetic energy based on differing values of k_{2ke} shows that slope of k is constant; i.e., the transition zone is shifted upstream without diffusion of the k field. Therefore, in this zone, the artificial dissipation is similar to the physical disturbances (freestream turbulence, noise etc.). For $k_{2ke}>0.02$, the artificial dissipation leads to both an earlier transition and an increased transition length. This is the consequence of the streamwise/stream diffusion of the turbulent kinetic energy.

The influence of the artificial dissipation in the mean flow equation on the predicted velocity and turbulent fields is presented in Fig. 6-13. In contrast to the k_{2ke} variation, the variation of k_4 does not affect the accuracy of the mean flow, except at very high levels of artificial dissipation.

6.7 Concluding remarks

Comparison between the prediction and the experimental data formally shows more accurate prediction of the transition inception for cases with the transition over a separation bubble. However, the development of the attached, transition and turbulent boundary layers is not very sensitive to even relatively high error(~4 % of the chord) in the predicted transition inception. In contrast, the development of the separation bubble is strongly affected by the small variation in the transition prediction. Moderate delay in transition inception results in significant enlargement of the separation bubble and correspondingly notable increase in profile losses. To be reliable, the numerical solver should provide the prediction of the transition inception with an accuracy equal to 1-2% of the cord. Further research is needed to achieve this goal. Numerical investigation, presented in this Chapter, shows very strong effect of solver characteristic on the transition development for the flow with the transition over a separation bubble. Therefore, further development should be concentrated not only on the transition model/turbulence model development but also on the model coupling with the numerical solver to control the influence of the scheme characteristic on the transition development.

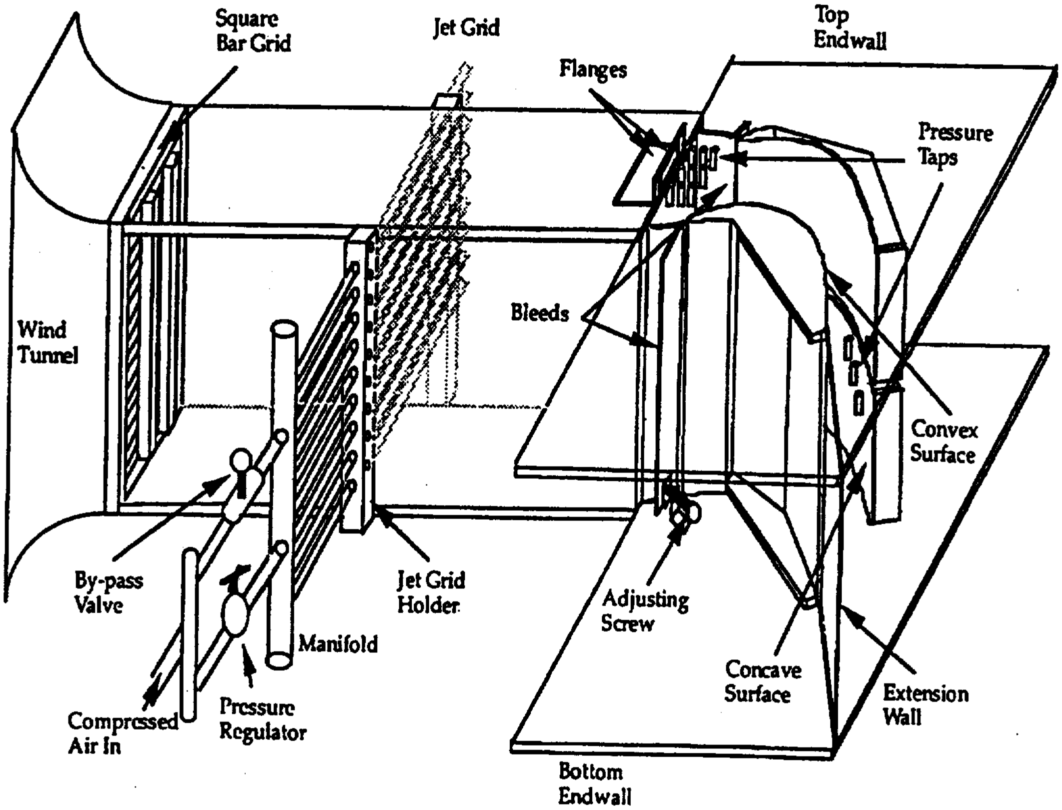
Square Bar Grid
Jet Grid
Top Endwall
Flanges
Pressure Taps
Wind Tunnel
Bleeds
Convex Surface
By-pass Valve
Jet Grid Holder
Adjusting Screw
Manifold
Concave Surface
Extension Wall
Compressed Air In
Pressure Regulator
Bottom Endwall

Fig. 6-1 Schematic of the experiment

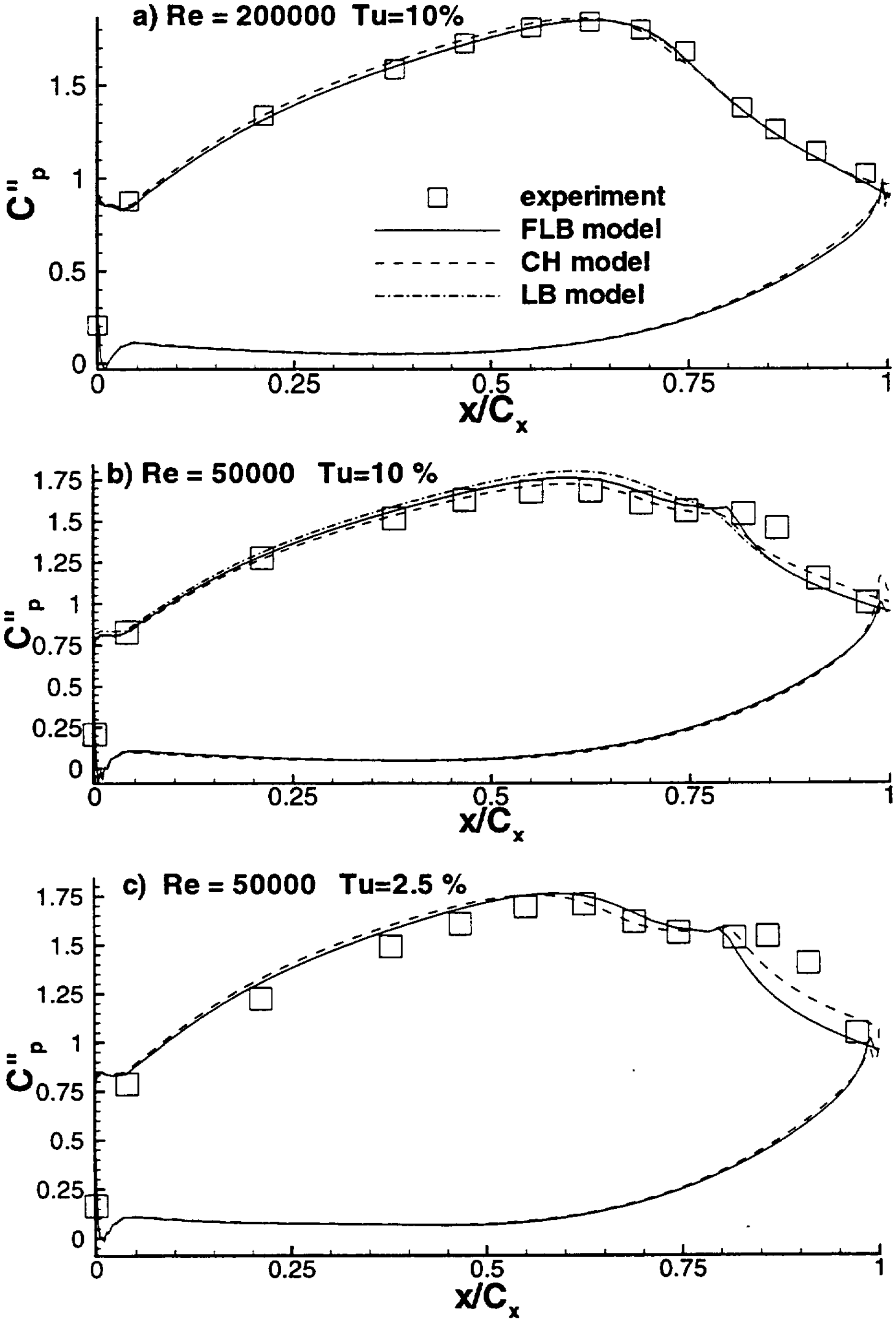

Fig. 6-2 Surface pressure distribution

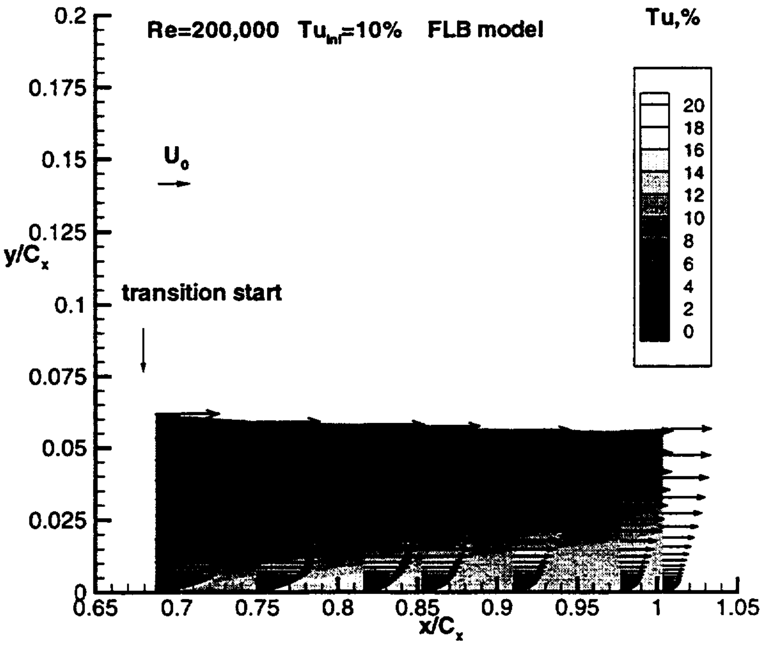

Fig. 6-3 Transition in attached boundary layer

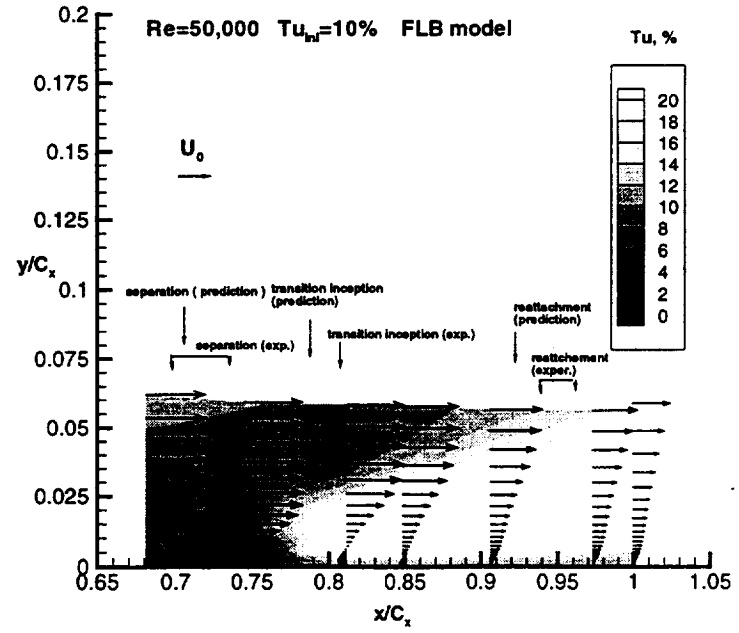

Fig. 6-4 Transition over a laminar separation bubble

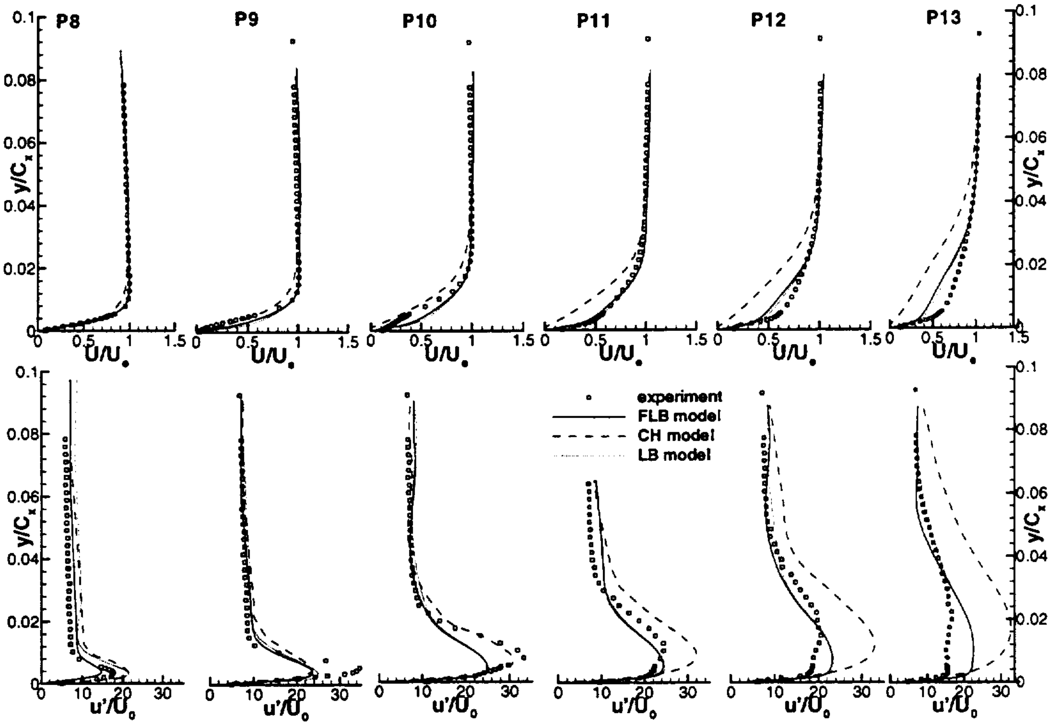

Fig. 6-5 Velocity and turbulence intensity, Tu=10%, Re=200000

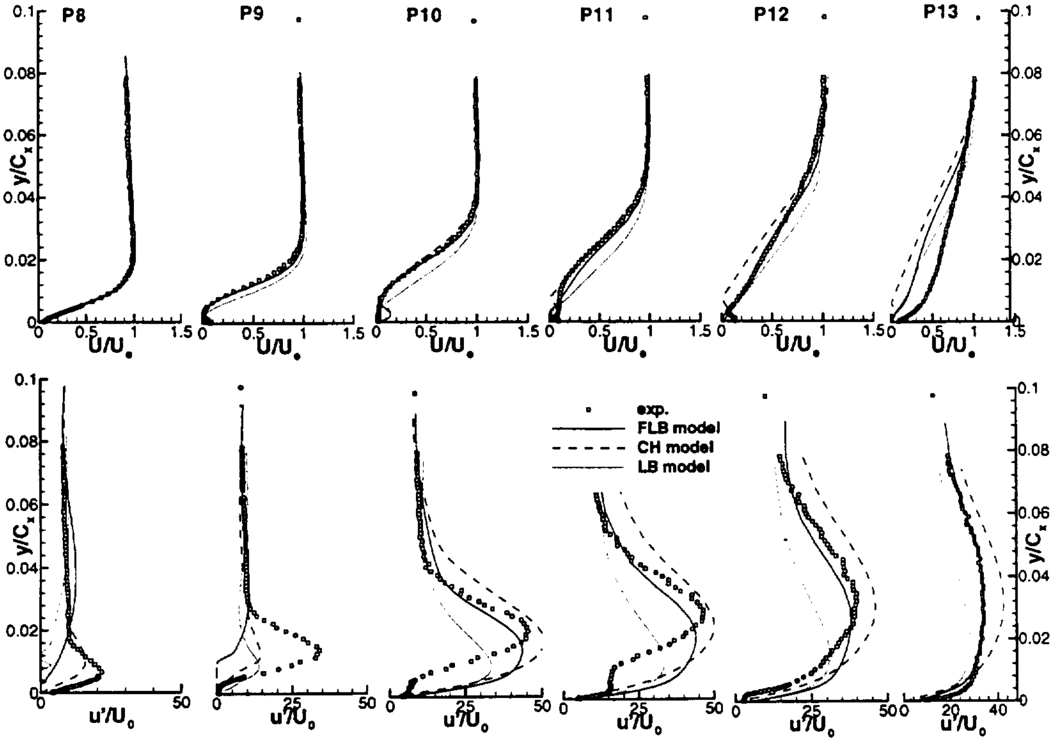

Fig. 6-6 Velocity and turbulence intensity, Tu=10%, Re=50000

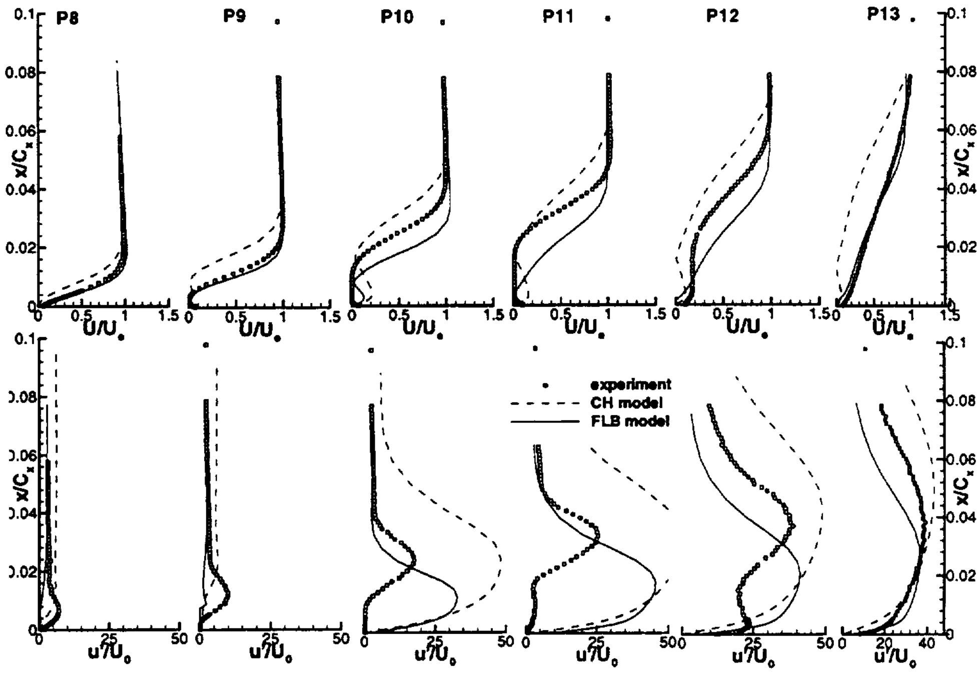

Fig. 6-7 Velocity and turbulence intensity, Tu=2.5%, Re=50000

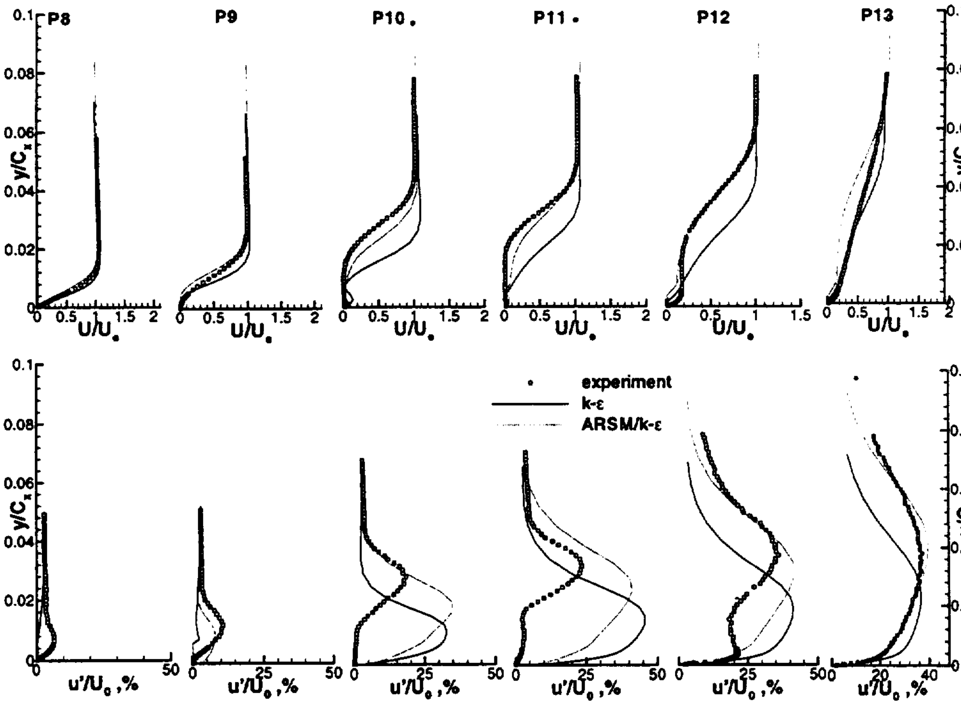

Fig. 6-8 Velocity and turbulence intensity, Tu=2.5%, Re=50000, prediction based on hybrid ARSM/k-ε approach

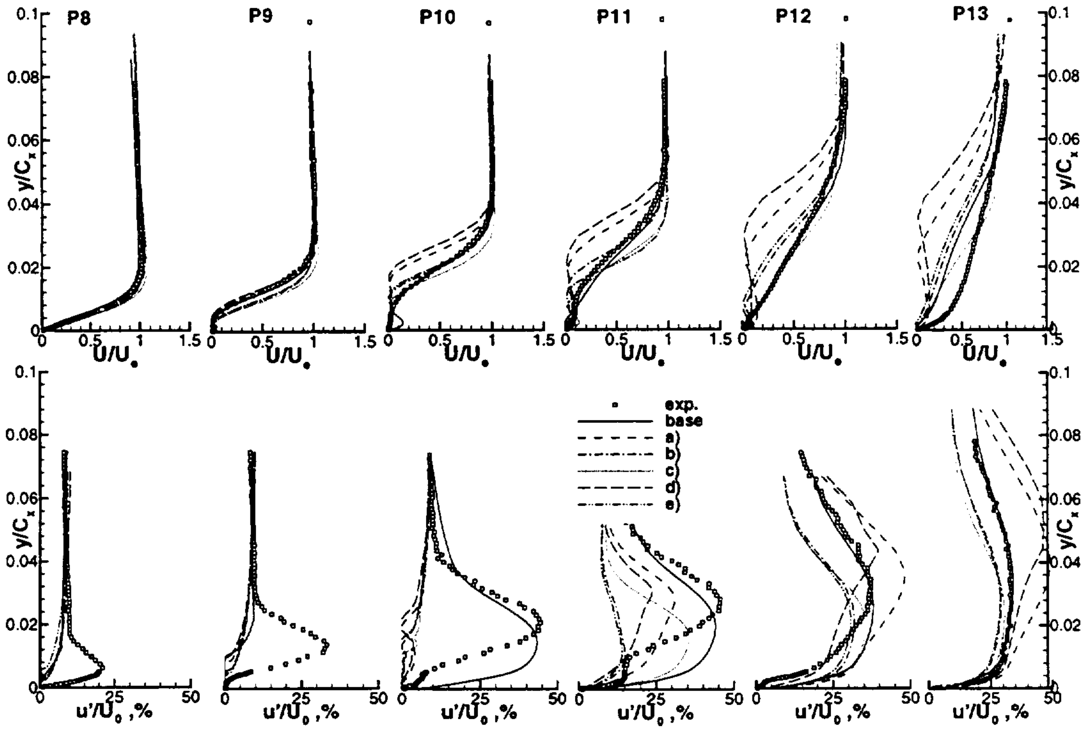

Fig. 6-9 Velocity and turbulence intensity, Tu=10%, Re=50000, effect of the transition model utilization a) 1d model Var1, b) 1d model Var2, c) "step" model, d) 2d model Var1, e) 2d model Var2

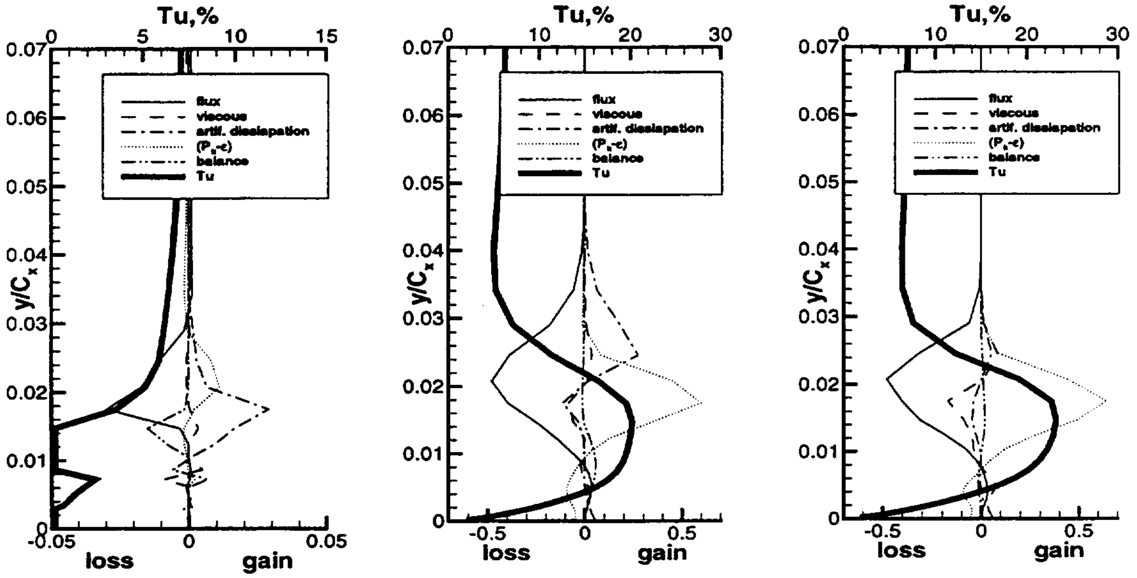

a) x/Cx=77%

a) x/Cx=81%

a) x/Cx=81%, modified

Fig. 6-10 Turbulent kinetic energy balance, Tu=10%, Re=50000

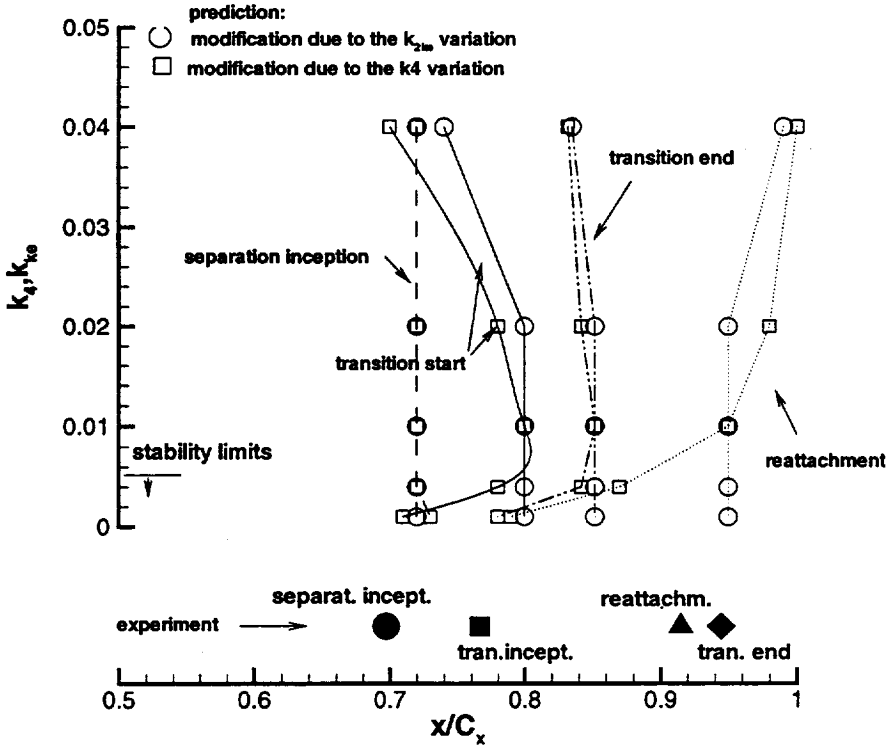

Fig. 6-11 Effect of artificial dissipation on predicted location of transition and separation inception, , Tu=10%, Re=50000

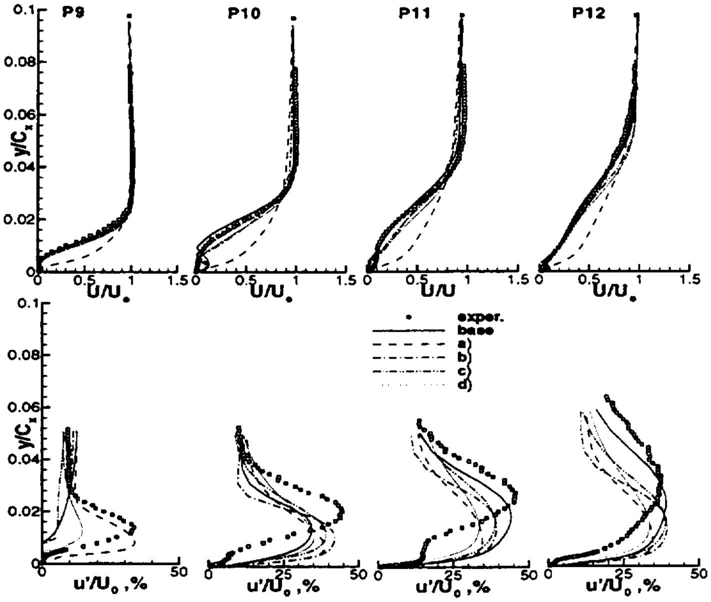

Fig. 6-12 Influence of the artificial dissipation; Tu=10%, Re=50000
k_4=0.01 a) k_{2ke}=0.001 b) k_{2ke}=0.004 c) k_{2ke}=0.02 d) k_{2ke}=0.04

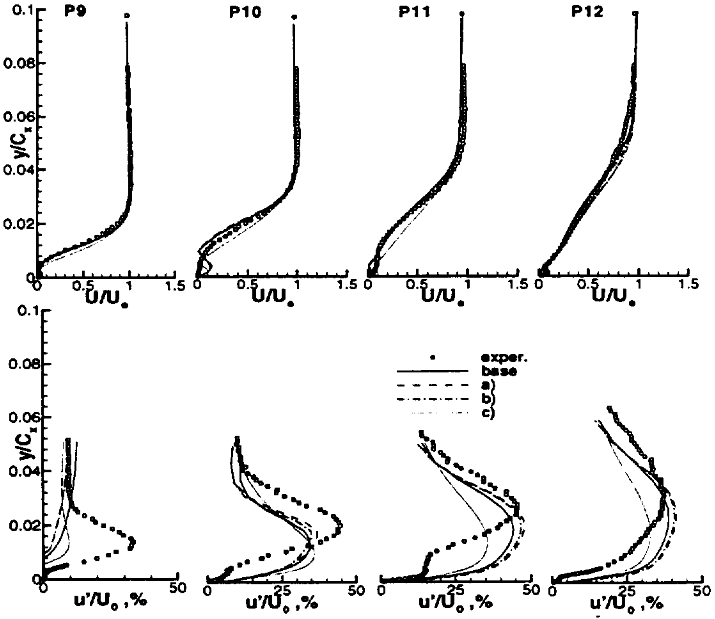

Fig. 6-13 Influence of the artificial dissipation, Tu=10%, Re=50000
k_{2ke}=0.01 a) k_4=0.001 b) k_4=0.02 c) k_4=0.04

Chapter 7

NUMERICAL SIMULATION OF LEADING EDGE FILM COOLING

Numerical simulation of two dimensional steady and unsteady transitional flows presented in previous chapters provides a foundation for accurate modeling of turbomachine aerothermodynamics. Turbine film cooling flow and secondary flows, including tip gap flow are two major problems that have profound effect on the characteristic of turbomachinery performance. The ability of the numerical solver to predict these phenomena should be established. Numerical simulation of the three-dimensional leading edge film cooling flow, discussed in this chapter, has been performed to accomplish this objective and gain a better understanding of the vortex structure due to the cooling jet-main flow interaction. The heat transfer and the flow phenomena associated with the leading edge film cooling are very complex. A thin boundary layer near the stagnation point, large pressure gradient, and the presence of the curvature effect make the numerical modeling including the grid generation extremely complicated. This is further complicated by the compound angle injection. Very few attempts have been made to simulate such flows. The research presented in this chapter is limited only to the steady state approximation of the leading edge film cooling due to the large CPU resources required for adequate temporal resolution of the unsteady phenomenon. Multiblock version of the solver, described in Chapter 2, has been utilized for the numerical modeling.

This has been found to be crucial for the accurate prediction of the flow in film cooling multidomain configurations.

7.1 Flat Plate Film Cooling

The film cooling on a flat plate with an injection from a row of holes, measured by Pietrzyk et al., (1990) was chosen as a case to test the code and establish a numerical procedure for the numerical simulation with cooling flow injection. A similar configuration was computed by Leylek and Zerkle (1993) (incompressible code) and Fabian (1995) (ADPAC developed by Hall et al., (1994)). The inlet flow velocity was 20 m/s. Blowing ratio $M = \frac{(\rho U)_{\text{injection}}}{(\rho U)_{\text{meanflow}}} = 2$. Ratio of the hole length to the hole diameter l/d was 3.5. Inlet turbulence intensity was T_u=0.5%. The computational domain was divided into 3 blocks: plenum, hole, and main part. Grid (Fig. 7-1) was generated using Genie+ grid generator in conjunction with an algebraic grid generator for the grid point distribution inside the holes. The grid size was 81x31x31 for the main block, 31x17x17 for the hole, 21x33x33 for the plenum. To ensure a stable and converging calculation, the numerical simulation was carried out through the number of steps. During the first step a flow initialization was carried out in separate blocks. Two dimensional calculation was performed to generate initial flow distribution in the main block. Multidimensional flow in a cooling hole was calculated using constant outlet static pressure. Hole inlet pressure was set to provide the required massflow. The next step consist of a coupled calculation of the flow in the plenum and the hole, preserving the prescribed blowing ratio. During the third step, the flow in the mainstream was calculated with a fixed jet velocity from the previous step to avoid the numerical instability and reverse flow from the main block into the hole. Finally, a coupled simulation of all three blocks was carried out to obtain a solution.

The result of the numerical prediction was compared with the experimental data and the numerical prediction based on the ADPAC code. The predicted and the measured distribution of the adiabatic effectiveness along the jet centerline is shown in the Fig. 7-2. Due to the high blowing ratio, the jet separates from the surface upstream of the cooling hole. This leads to a sharp decrease in the adiabatic effectiveness at s/d=3. The comparison of other flow characteristics (secondary vectors, crossflow temperature distribution) indicates a good correlation between the prediction and available data.

7.2 Leading edge cooling at compound angle

The configuration and experimental data by Cruse et al. (1997) are utilized for the numerical modeling of the leading edge film cooling aimed at validation and improved understanding of the flow and thermal physics. The schematic of the model is shown Fig. 7-3. The symmetry of the flow near the leading edge was simulated using the suction slot near the stagnation point. The cooled air (T= 166 K) was injected through two rows of holes. The first row was located along the stagnation line and the angle between the hole axis and the surface was 20°. The second row of holes was inclined at 25° to the upstream direction. The angle between the hole axis and the surface was 20°, which is the same as the corresponding angle for the first row. There were nine holes in each row, with the hole spacing equal to z/d=7.67. The length of the hole was equal to l/d=12. The upstream plate and the suction were adjusted to obtain a correct position of the stagnation streamline. The surface temperature distribution was measured using an infrared camera. Thermocouples were employed to measure the crossflow temperature distribution.

7.2.1 Numerical modeling

Based on the results of the preliminary analysis, the multiblock grid, presented in Fig. 7-4, was generated for a numerical simulation. It consists of 6 blocks: a plenum, 2 holes, a mainblock, an inlet, and an outlet block. The total number of grid points is 286199. A summary of the flow condition used is presented in Table 7-1.

Table 7-1 Flow conditions

Freestream Velocity (m/s), U_0	10	Mass Flow/ Hole (g/s)	0.725
Freestream Turbulence (%), Tu	0.5, 20.	Pressure (atm),p	1
Freestream Temperature, (C),T_0	27.5	Plate Conductivity (W/mK)	0.025
Average Mass Flux Ratio,M	2.0	Surface Roughness (m)	< 25
Jet/ Freestream density ratio, D	1.8	Hole Edge Radius (mm)	< 0.1

The excessive grid skewness may result in a nonphysical solution due to the increased level of the artificial dissipation. For the current topology, the angle between the hole wall and the cooling wall is equal to 20°. In the case of the structured grid used in the current simulation, the presence of the sharp angle requires an optimal redistribution of the local skewness near the hole-main block interface. It was found that the accuracy could be improved if some non-orthogonality is allowed near the hole walls as opposed to the case with the orthogonal grid near the hole wall and a higher concentration of skewed cells farther from the wall. The boundary conditions used in the numerical modeling are as follows (letters correspond to block faces shown in Fig. 7-4):

Table 7-2 Boundary conditions

a_1	Inlet (P^*, T^*, flow angle)
a_2	inlet (p,U, flow angle)
b	Periodic conditions
c	Symmetry conditions
d_1	no-slip conditions
d_2	wall function
e	outlet, constant static pressure

Interaction between the coolant jet and the mainflow results in a very complex flow field. The three-dimensional separation zone downstream of the cooling jet has an adverse effect on the overall heat transfer. This complexity requires the implementation of the low-Re number turbulence model instead of the wall function. While the use of the wall function can significantly reduce the computational time, it lacks the near wall physics required for an accurate resolution. To ensure an accurate prediction of the boundary layer flow in the main block, the first grid point was located at $y^+ \approx 1.2$.

The static pressure at the plenum inlet was set to provide the required massflow through the injection holes. The current experimental configuration has long holes, l/d=12. It has been found that after the developed flow regime is achieved near the hole entrance, the plenum flow does not affect the flow in the mainblock. Therefore, the plenum flow field is frozen during the final convergence to minimize CPU utilization. The pressure oscillation during the convergence process resulted in the development of the reverse flow into the hole from the mainblock. To avoid this and ensure a stable development of the jet, the pressure distribution for the hole is fixed during the initial part of the computation. After a fully developed jet is obtained in the mainblock, this limitation is relaxed.

In the first attempt, a low-Re turbulence model was also employed for the flow in the hole. Conformal (one-to-one) interblock interface requires that stretched grid lines from the near wall region inside the cooling hole should be extended throughout the main block. Thus, the quality of the mainblock grid is significantly reduced due to the presence of the zones with very stretched (in normal to the cooling surface direction) and skewed grid cells. Consequently, the numerical solution has suffered from an excessive numerical dissipation; and the predicted mixing of the coolant jet with mainflow has been strongly overestimated. The incorporation of the wall function for the boundary condition inside holes has enabled the generation of the grid with a more uniform distribution of the grid points on crossflow planes. The mainblock grid also has smoother characteristics (as a result of one-to-one interblock interface). Despite a minor sacrifice in the accuracy of the flow prediction in the coolant hole due to the utilization of the wall function, the accuracy of the mainblock flow prediction has improved significantly.

7.2.2 Comparison with the experiment

A comparison between the predicted and the measured surface adiabatic effectiveness is shown in Fig. 7-5. Smooth distribution of the adiabatic effectiveness in the vicinity of the stagnation line indicates the uniform spreading of the coolant flow from the bottom row of jets. In the numerical simulation, a re-circulation zone exists between the jet and the wall and; as a result, the coolant jet separates from the wall. Interaction with the main flow causes the reattachment of the jet at point A (Fig. 7-5a). The extended region of the cooled surface near point B (Fig. 7-5b) in the experimental data is an indication of the similar behavior (reattachment) of the jet. More intensive mixing and diffusion of the bottom jet in the experiment result a in a low surface temperature between upper holes (Fig. 7-5,point C). In the numerical prediction, the bottom coolant jet encircles the root of the top jet and is partially entrained by it. This contributes to the predicted low adiabatic effectiveness at point C, Fig. 7-5.

The lateral distribution (line plot) of the adiabatic effectiveness due to the presence of the upper cooling hole is plotted in Fig. 7-6 at several streamwise locations. The numerical simulation accurately predicts the amplitude and the position of the maximum cooling at s/d = 4.86. There are two main discrepancies between the predicted and the measured data; the predicted temperature decrease on the left side of the jet is less steeper than that in the experiment and, the predicted cooling effectiveness is lower than the measured values between z/d = 4.5 and z/d = 7. The difference between the predicted location of the maximum influence of the bottom jet is one of the factors contributing to this discrepancy. As indicated above, in the numerical prediction the bottom jet reattaches far to the left (A, Fig. 7-5a) as compared to the experiment (B, Fig. 7-5b). As a result, the rest of the coolant fluid from the bottom jet augments cooling on the left side of the top jet rather than in the region between z/d= 4 and 7. At s/d= 9.88 (Fig. 7-6c), the minor discrepancy between the predicted and the measured maximum adiabatic effectiveness indicates an underturning of the predicted jet trajectory. The discrepancy at lateral sides of the jet, observed at s/d=4.86, practically vanishes due to the mixing process.

The overall effectiveness of the film cooling process is represented by laterally average adiabatic effectiveness. A very good agreement between the measured and the predicted laterally averaged adiabatic effectiveness is achieved (Fig. 7-7). Even though a good agreement with the experimental (thermal) data was achieved on the surface, the numerical simulation underpredicts the temperature diffusion in the core of the jet. This characteristic can be found in all numerical simulations of film cooling. Under some conditions, this may lead to a more favorable prediction of the surface temperature distribution in comparison with the real configuration. A comparison of the predicted spanwise distribution of normalized temperature with measured values (Fig. 7-8) indicates that the normalized temperature in the core of the jet is 0.25 (s/d= 1.24) to 0.4 (s/d= 9.88) higher than the measured values. The isotropic nature of the turbulence model used is probably the major source of this problem. The turbulence field associated with the jet mainstream interaction is strongly anisotropic. k-ε turbulence models may not be suitable for the prediction of such flows. Another factor is the choice of the inlet turbulence dissipation rate. An inlet level of ε has less influence on the wall bounded flow, but may have a stronger influence on the free shear layer flows. Further evidence of this is presented later.

7.2.3 Discussion of aerothermal flow physics

A thorough understanding of the physics of the jet-mainstream interaction can contribute to an improved understanding of the primary sources of film cooling losses as well as factors contributing to the cooling effectiveness. The development of vortices due to the jet-mainstream interaction and its effect on mixing has a profound influence on the overall development of the film cooling flow, including the distribution of the coolant fluid and aerodynamic losses. The importance of tracking the vortex structure is emphasized by Sgarzi and Leboeuf (1997), and Walters and Leylek (1997). Sgarzi and Leboeuf (1997) suggested a classification of major vortices associated with the film cooling on a flat plate. In the case of the flat plate, there are five vortices: "kidney shaped" counter-rotating vortices in the core of the jet; "horse shoe" vortices due to the sudden deceleration of the boundary layer upstream the leading edge of the jet; "half wake" vortex pair in the zone of low pressure downstream of the jet.; "half wall" vortex pair induced by the "kidney" vortex; and "lip" vortex, due to the freestream jet- leading edge interaction. Visualization by Bario and Beral (1996) confirms the existence of these vortices. Walters and Leylek (1997) analyzed the source of different vortices as well as their influence on the jet injected over a flat plate. Based on this analysis, suggestions were made to improve the film cooling.

Leading edge film cooling through a compound angle injection results in a much more complex aerothermal field in comparison with the flat plate injection. Complexities arise due to the difference in the direction of the jet velocity and mainstream velocity, the three-dimensional turning of coolant jet, and the presence of strong streamwise pressure gradient.

The numerical solution is analyzed to examine the vortex structure, including the origin of various vortices and their contribution to the flow and thermal field development. A schematic representation of major vortices associated with the upper row of holes is shown in Fig. 7-9 - Fig. 7-12. Streamlines are plotted like ribbons; their twist corresponds to the magnitude of the local vorticity. The laminar boundary is very thin upstream of the jet. The amplitude of the "horse shoe" vortex (denoted as Ω_1, Fig. 7-9) is very weak. Streamlines downstream of the injection hole clearly indicate the presence of the "half wake" vortex (denoted as Ω_2, Fig. 7-9). The vorticity in the core of the jet induces a counter-rotating pair of vortices (denoted as Ω_3) which can be seen in Fig. 7-13a. The development of the "kidney" vortex in the core of a flat plate cooling jet was shown to have a first-order effect on the film cooling effectiveness. In the case of the leading edge film cooling at compound angle, a similar, but more complex, structure exists in the film cooling jet. It is possible to identify four main vortices. During the initial part of the jet path they are associated with the streamlines from the hole orifice. These streamlines are shown in Fig. 7-9 - Fig. 7-12. The major part of the cooling fluid is encountered in vortex Ω_{4b},.Fig. 7-11. This vortex rapidly dissipates (Fig. 7-13a, Fig. 7-14a, Fig. 7-15a). Downstream of s/d=11 it changes its sign. The cooling fluid associated with this vortex comes from the core of the jet. The part of the coolant fluid located closer to the right lateral side of the hole is organized into the vortex Ω_{4a}. The characteristic feature of this vortex is its high strength. At a distance far from the jet (Fig. 7-13c), it has a structure similar to those observed in a flat plate film cooling. The interaction between the jet and the mainflow also produces two counterclockwise rotating vortices Ω_{5a}, Fig. 7-11 and Ω_{5b}, Fig. 7-10. They have their origin at the upstream side of the hole (Ω_{5b}) and left lateral side of the hole (Ω_{5a}). The behavior of these vortices is similar to the clockwise rotating counterparts. The vortex Ω_{5b} decays rapidly, while vortex Ω_{5a} retains its strength far downstream (Fig. 7-13).

An understanding of the origin of the vortices is the basis for the improved jet-mainflow interaction. Walters and Leylek (1997) identified three potential sources of the "kidney vortex," (the boundary layer at the lateral side of the coolant hole, an axial secondary vorticity, and the lateral crossflow shear layer). The first one has a major influence on the development of the 'kidney' vortex. The analysis of the flow near the upper hole in the current simulation leads to a similar conclusion. Vorticity due to the boundary layer in the hole at sides A and B (Fig. 7-12) is the primary source of Ω_{5a} and Ω_{4a} vortices, as well as Ω_{4b}. Vorticity due to the boundary layer at the upstream side of the hole (C, Fig. 7-12) contributes to the vorticity Ω_{5b}. Crossflow shear layers predominantly affect the development of vortices, Ω_{5b} and Ω_{4b}. To analyze the contribution of different vortices to the overall interaction, the projection of the normalized vorticity in the main stream direction, a normalized temperature, and the loss coefficient for three different streamwise locations are plotted in Fig. 7-13, Fig. 7-14 and Fig. 7-15. The plane at s/d =4.2 is located near the upper hole. At this location, the jet undergoes a rapid turning from the crossflow direction to the mainflow as well as bending around the z axis. All four of the core vortices defined earlier are clearly seen in Fig. 7-15a. The distribution of the normalized total pressure has two major spots. The region in the core of the jet has a positive value of ξ. The stagnation region behind the jet has a low level of the total pressure (Fig. 7-15b). The presence of the low pressure zone, which extents 2.5d downstream of the trailing edge of the jet (Fig. 7-16) is the primary source of the strong crossflow, which can be seen upstream of the stagnation region (Fig. 7-17 and Fig. 7-18). The crossflow is compromised of the hot fluid and creates a zone of high temperature under the coolant jet. The combined effect of Ω_{5a}, and Ω_{4a} vortices and crossflow lifts and moves the zone of a low total pressure to the right (Fig. 7-14b). The pressure gradient also results in larger turning of the upper jet in comparison with the bottom jet. The experimental results indicate a higher skeweness of the thermal field than that observed in the numerical prediction at the left side of the jet at this location. It may be an indication that the numerical simulation undepredicts the strength of the Ω_{5b} vortex. Intensive mixing and dissipation due to the presence of Ω_{5b} and Ω_{4b} vortices decrease the value of the total pressure in the core of the jet. At s/d=6, the jet has practically completed its turning in the streamwise direction. Further downstream, the development of the jet is similar to that of the flat plate jet, except for the presence of the streamwise pressure gradient. The core of the jet reaches the shortest distance to the wall at about s/d=7; further downstream it lifts slowly.

One of the negative effects of counter-rotating vortices is an entrainment of the hot air under the cooling jet. Fig. 7-9 - Fig. 7-12 show that Ω_{5a} and Ω_{4a} vortices entrain hot fluid under the jet, pushing cold core fluid farther from the wall, hence decreasing the cooling efficiency. An analysis of the streamlines shows that Ω_{4a} and Ω_{5a} are a mixture of coolant and mainstream flows. Upstream of s/d~5, Ω_{5a} consists of hot air with the rest of the coolant fluid pushed closer to the jet center. Ω_{4b} and Ω_{5b} have a minimal entrainment of the surrounding hot fluid and predominantly consist of a cooling fluid with an increased temperature due to the diffusion.

The contribution of various vortices is summarized below:

1) The vortex Ω_{4a} has a strong impact on both the thermal efficiency (entrainment of the hot flow) and aerodynamic losses.
2) The vortex Ω_{5a} has a similar effect. Its contribution to the losses is smaller in comparison with those of Ω_{4a}. The presence of the stagnation region downstream of the jet is the primary source of the losses at the left side of the jet.
3) Vortices Ω_{4b} and Ω_{5b} have a much less adverse effect due to the rapid decay, caused by the strong dissipation near the root of the jet and a minor lifting of the jet core downstream.

4) The three-dimensional flow field arising from the second (upper hole) jet is shown in Fig. 7-17 and Fig. 7-18. The presence of the separation zone underneath the jet as well as the highly skewed free shear layer above the separation zone is clearly visible. The flow angle changes dramatically from the wall to the free stream. Such large and differing flow angles of the jet and the mainstream result in large velocity gradients and intense turbulent mixing. The jet-wake type of profile can be clearly seen in Fig. 7-17 and Fig. 7-18. The mixing of the two jets is completed in about six jet diameters. Large crossflow (spanwise flow) develops at the bottom of the jet, resulting in the thermal field observed (Fig. 7-17 and Fig. 7-18). These crossflows tend to lift the separation zone and move the hot spots away from the wall.

7.2.4 Mach number effect

All measurements of the film cooling configurations are performed at a very low Mach number, usually around 0.03-0.06. The Mach number in a real configuration is usually much higher. To analyze the effect of the Mach number on the leading edge film cooling, a numerical simulation of the configuration with M=2 and stagnation point located at s/d=0 is carried out with an inlet Mach number of 0.3. All other variables used for the test case are held constant. Maximum Mach number at the top of the cylindrical leading edge reaches 0.9. Due to the rapid acceleration of the flow, static temperature of the flow above the surface is much smaller than that at a low Mach number. To make a proper comparison between the high and low Mach number cases, the wall temperature in the case of the high speed flow is adjusted by a change in the kinetic energy at the edge of the boundary layer due to the local acceleration $\Delta T = \frac{u_{highMach}^2 - u_{lowMach}^2}{2C_p}$. A comparison of the corrected adiabatic effectiveness between the experiment and the numerical prediction at a low Mach number (Fig. 7-19) shows a mild increase in the jet diffusion at a high speed flow. Two major factors contribute to this behavior of the jet; a higher pressure gradient (Fig. 7-20) and the decreased diffusion of the jet due to the compressibility. Analyses of the flow near the stagnation line indicate that there is a moderate decrease in the separation zone under the bottom hole jet. Hence, the mixing process is increased due to the smaller lifting of the jet. The flow pattern in the vicinity of the top row of coolant holes does not indicate modifications of an aerothermal field due to the higher pressure gradient resulting from the increased Mach number. Consequently, the adiabatic effectiveness is not changed. Further downstream, the jet in the high-speed flow undergoes a rapid spreading. This is due to the influence of the negative pressure gradient.

7.2.5 Influence of the high inlet turbulence

The level of inlet turbulence in a real turbine is much higher than that used in laboratory experiments. To understand the influence of the high freestream turbulence intensity on the leading edge film cooling, a numerical simulation of the flow with 10%

inlet turbulence was carried out. This is close to the turbulence intensity encounted in real engines. A comparison of the laterally averaged adiabatic effectiveness for high and low freestream turbulence intensities (Fig. 7-21) indicates a decrease in the cooling effect near the bottom row of coolant jets. Cooling effect downstream of the top row of jets is modified only slightly.

The overall vortex structure resulting from the injection from upper holes is similar to that observed for a low turbulence case (Fig. 7-22a and Fig. 7-22b). An increase in the turbulence intensity leads to a more intense mixing and more rapid decay of the vortex system and results in a significantly low temperature of the jet core (Fig. 7-23a and Fig. 7-23b). The position and the amplitude of vortices are also modified due to a more intense turbulent diffusion. The most affected vortex is Ω_{4a} (Fig. 7-9 - Fig. 7-12 and Fig. 7-13a). Its amplitude is significantly reduced and is located closer to the wall at Tu=10% (Fig. 7-22a and Fig. 7-22b). This results in the smaller lifting of the Ω_{4b} vortex, containing the core of the coolant jet. The reduced intensity of Ω_{4a} vortex also decreases an entrainment of the hot ambient fluid under the coolant jet, therefore improving the cooling effectiveness. A distribution of the surface adiabatic effectiveness (Fig. 7-24) shows more intense spreading in the crossflow direction. This favorable effect of the increased turbulence (low entrainment and higher spreading) compensates for the intensified jet-core temperature diffusion. Therefore, the laterally averaged adiabatic effectiveness is modified only moderately (Fig. 7-5a and Fig. 7-24a).

Increased turbulence intensity significantly affects the flow structure in the vicinity of the coolant holes near the stagnation surface. The separation zone under the bottom jet shrinks by a factor of two in both the crossflow and in the normal to the wall direction (Fig. 7-25 and Fig. 7-26). The location of the jet core moves closer to the wall at a higher turbulence intensity. Another major modification is a smaller spreading of the jet in the streamwise direction. This is due to the lower intensity of the “kidney”-type vortex. At the low turbulence intensity level, the “kidney”-type vortex spreads to the lateral side of the jet before turning smoothly in the streamwise direction. At high inlet turbulence, coolant jet streamlines go parallel to the stagnation line until the jet turns suddenly in the streamwise direction; and without reattachment, finally mixes with the mainstream. The concentration of the jet streamlines along the stagnation line compensates only slightly for the increased turbulence diffusion.

7.2.6 Influence of the inlet turbulence length scale.

The development of the leading edge film cooling is controlled by the vortex structure located outside the boundary layer. In boundary layer flows, the freestream turbulence has a major influence on the flow development through its influence on the turbulence intensity at the edge of the boundary layer. Due to the intense mixing and an entrainment of the ambient fluid into the coolant jet core, the freestream turbulence dissipation rate and the corresponding length scale play a significant role in the leading edge film cooling effects.

To analyze the effect of the freestream turbulence length scale, a numerical simulation was carried out with an inlet turbulence intensity $T_u = 10\%$ and a higher length scale in comparison with the previous case. For the current calculation, the ratio of the eddy viscosity and the molecular viscosity is 120, while for the previous simulation (with $T_u = 10\%$) it is about 30. Smaller dissipation rate leads to only a minor increase in the turbulence intensity (about 1.5% near the bottom coolant hole row). The comparison of the lateral averaged adiabatic effectiveness at two differing length scales is shown in Fig. 7-27. A comparison of the surface adiabatic cooling effectiveness (Fig. 7-24) reveals a more intense increase in the surface temperature at the lower turbulence dissipation rate. The increased eddy viscosity moderately reduces the laterally averaged adiabatic effectiveness downstream of the upper hole. Examination of the aerothermal field indicates only a minor decrease in the intensity of the Ω_{4a} vortex (Fig. 7-22b and Fig. 7-22c). Therefore, there is no mechanism to compensate for the higher temperature diffusion similar to the previous case.

As indicated by Cruse et al. (1997), the experimental investigation gave a contradictory conclusion on the effect of the increased turbulence intensity. The modification of the mixing process due to the change in the length scale can be one of the factors contributing to these discrepancies. Elevated turbulence dissipation rate affects the jet core and correspondingly the vortex strength Ω_{4b}. A numerical simulation with a low freestream turbulence intensity overpredicts the temperature of the coolant jet core (Fig. 7-8). This simulation was carried out with a high freestream turbulence length scale. The observed trend due to the variation in the length scale (Fig. 7-23b and Fig. 7-23c) indicates that the inlet length scale employed for the baseline computation contributes to the observed discrepancy between the measured and the predicted jet core temperature.

7.3 Concluding remarks.

The numerical investigation indicates that the CFD analysis can be successfully employed for the prediction, simulation, and parametric study of the complex flows associated with the leading edge film cooling. However, great care should be exercised in the quality of the grid, the accuracy of inlet conditions, and the selection of the turbulence model.

The analysis of the aerothermal field due to a compound angle leading edge film cooling indicates the presence of the complex vortex structure much different from that observed for a flat plate. Interaction between the upper coolant jet and the mainflow generates four major vortices; Ω_{4a} , Ω_{4b} , Ω_{5a} , Ω_{5b}. These vortices originate respectively from the interaction of the mainflow with the coolant flow eminating from the right lateral side, core, left lateral side, and the upper side of the hole (Fig. 7-9 - Fig. 7-12). The vortices Ω_{4b} and Ω_{5b} decay rapidly and the vortex Ω_{4b} changes its sign beyond s/d=11. Vortices Ω_{5a} and Ω_{4a} are major contributors to aerodynamic losses and for a decrease in the adiabatic effectiveness through the entrainment of the hot fluid.

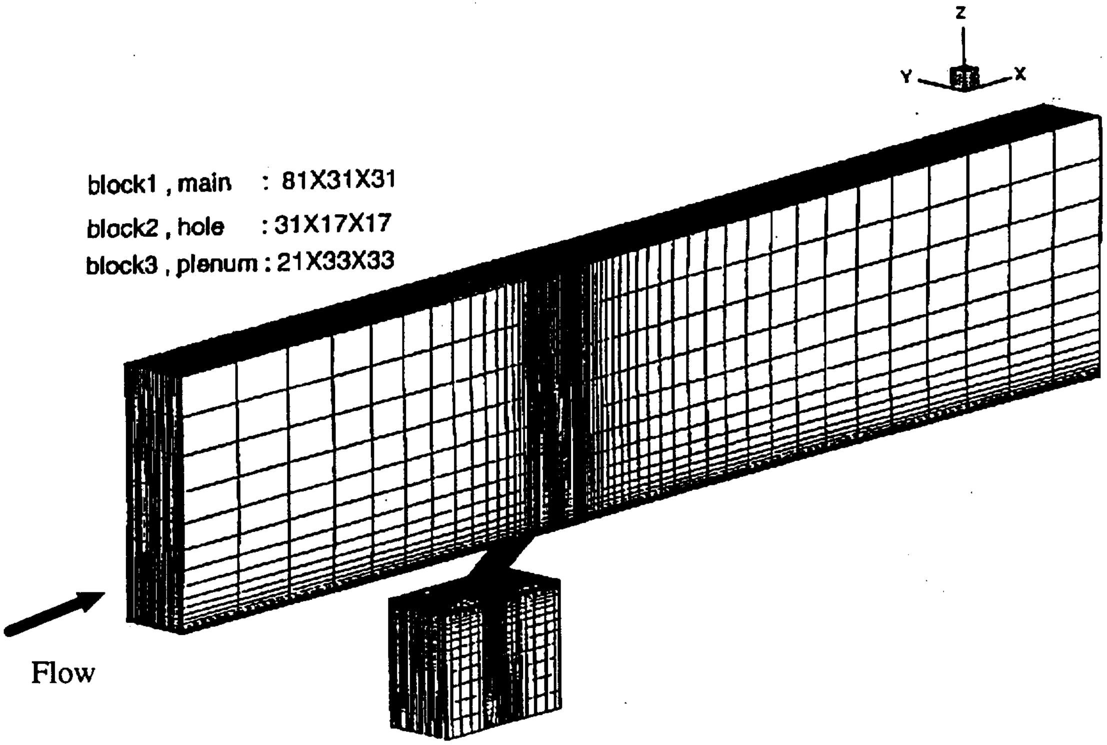
Z
Y
X
block1 , main : 81X31X31
block2 , hole : 31X17X17
block3 , plenum : 21X33X33
Flow

Fig. 7-1 Flat plate film cooling, grid

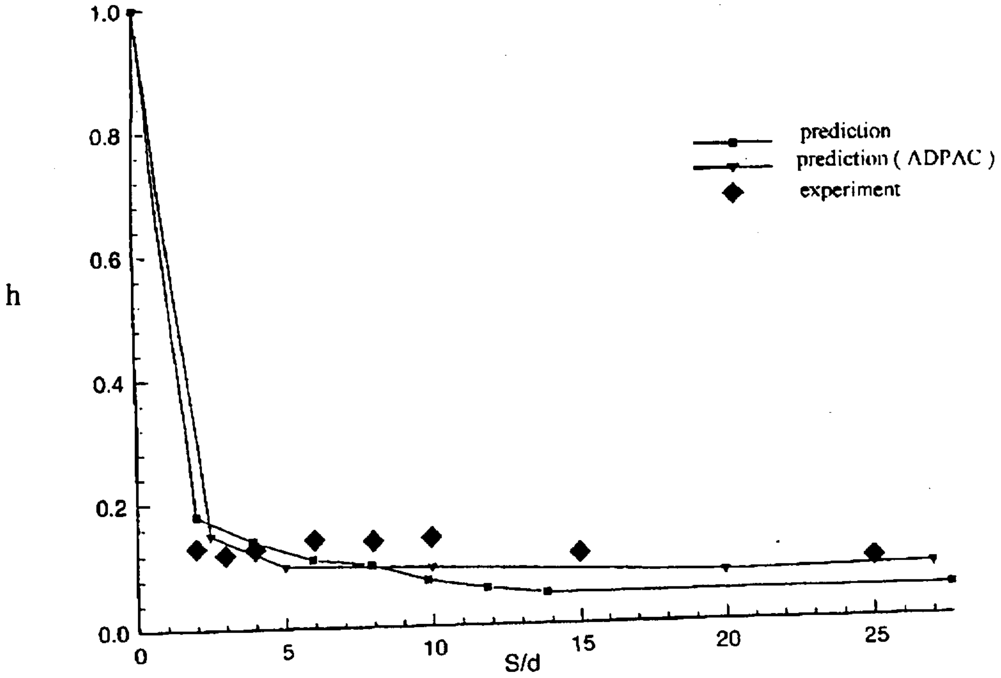

Fig. 7-2 Adiabatic effectiveness along the jet centerline

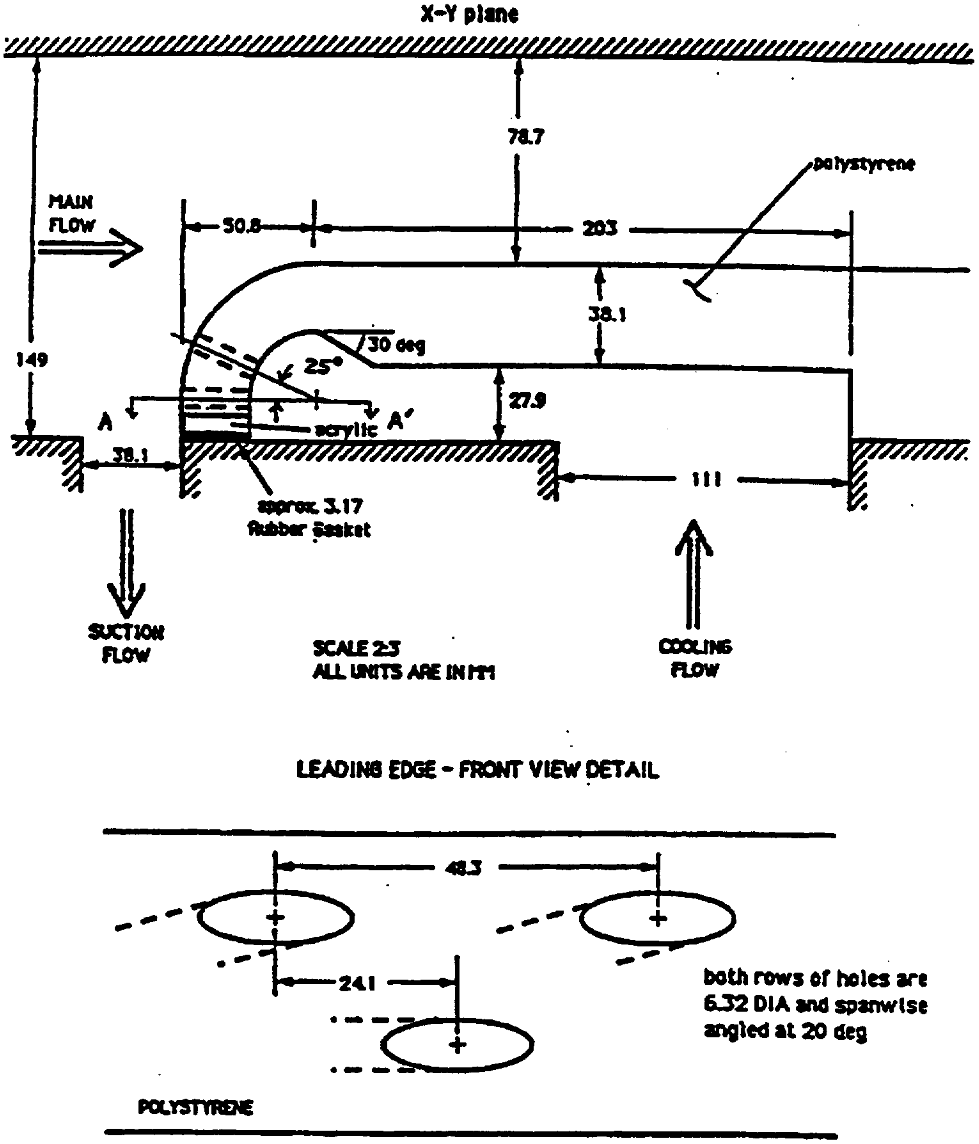
X-Y plane
78.7
polystyrene
MAIN FLOW
50.8
203
38.1
30 deg
25°
149
27.9
A
A'
acrylic
38.1
approx. 3.17
Rubber Gasket
111
SUCTION FLOW
SCALE 2:3
ALL UNITS ARE IN MM
COOLING FLOW
LEADING EDGE - FRONT VIEW DETAIL
48.3
24.1
both rows of holes are
6.32 DIA and spanwise
angled at 20 deg
POLYSTYRENE

Fig. 7-3 Schematic of the test case

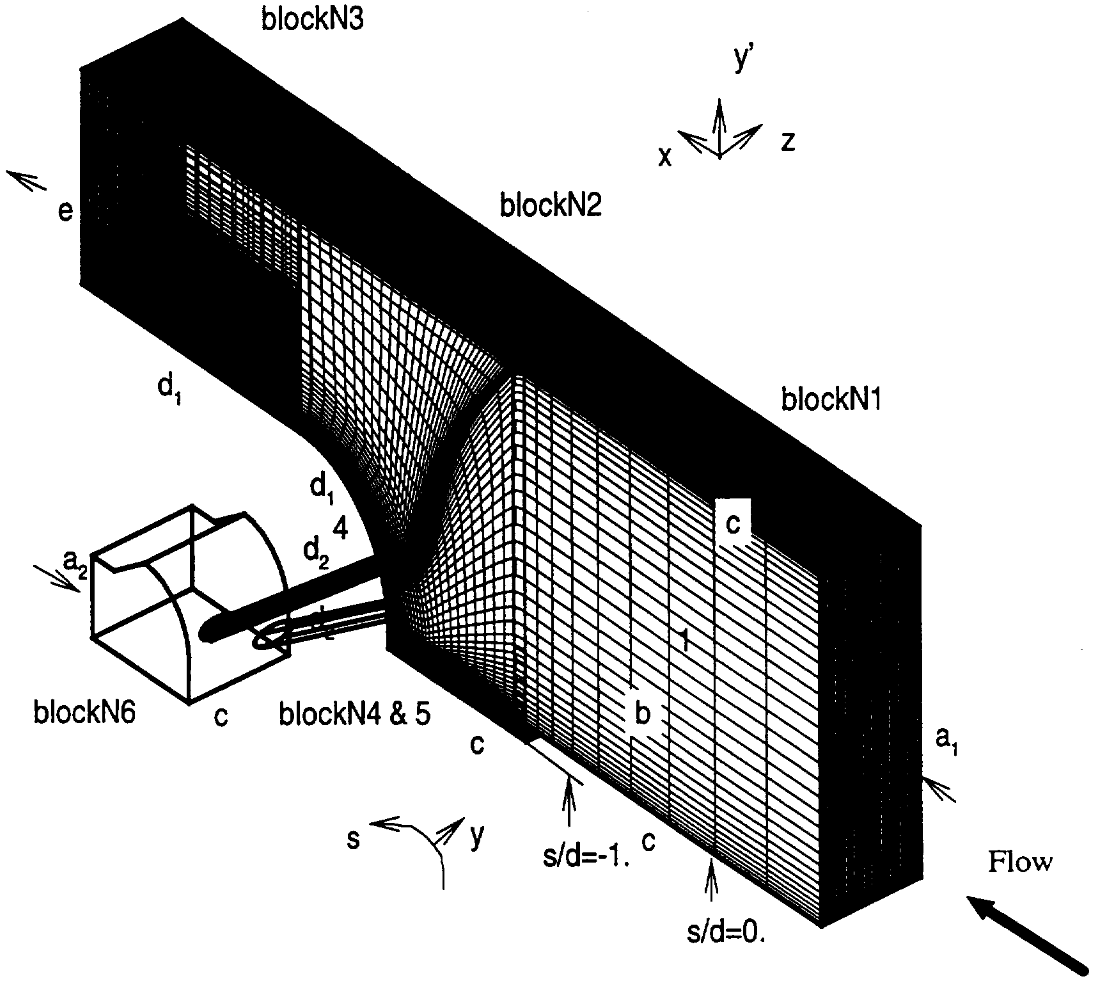
blockN3
y'
x
z
e
blockN2
d_1
blockN1
d_1
4
d_2
c
a_2
d_2
1
blockN6
c
blockN4 & 5
b
c
a_1
s
y
s/d=-1.
c
s/d=0.
Flow

Fig. 7-4 Grid structure and boundary conditions

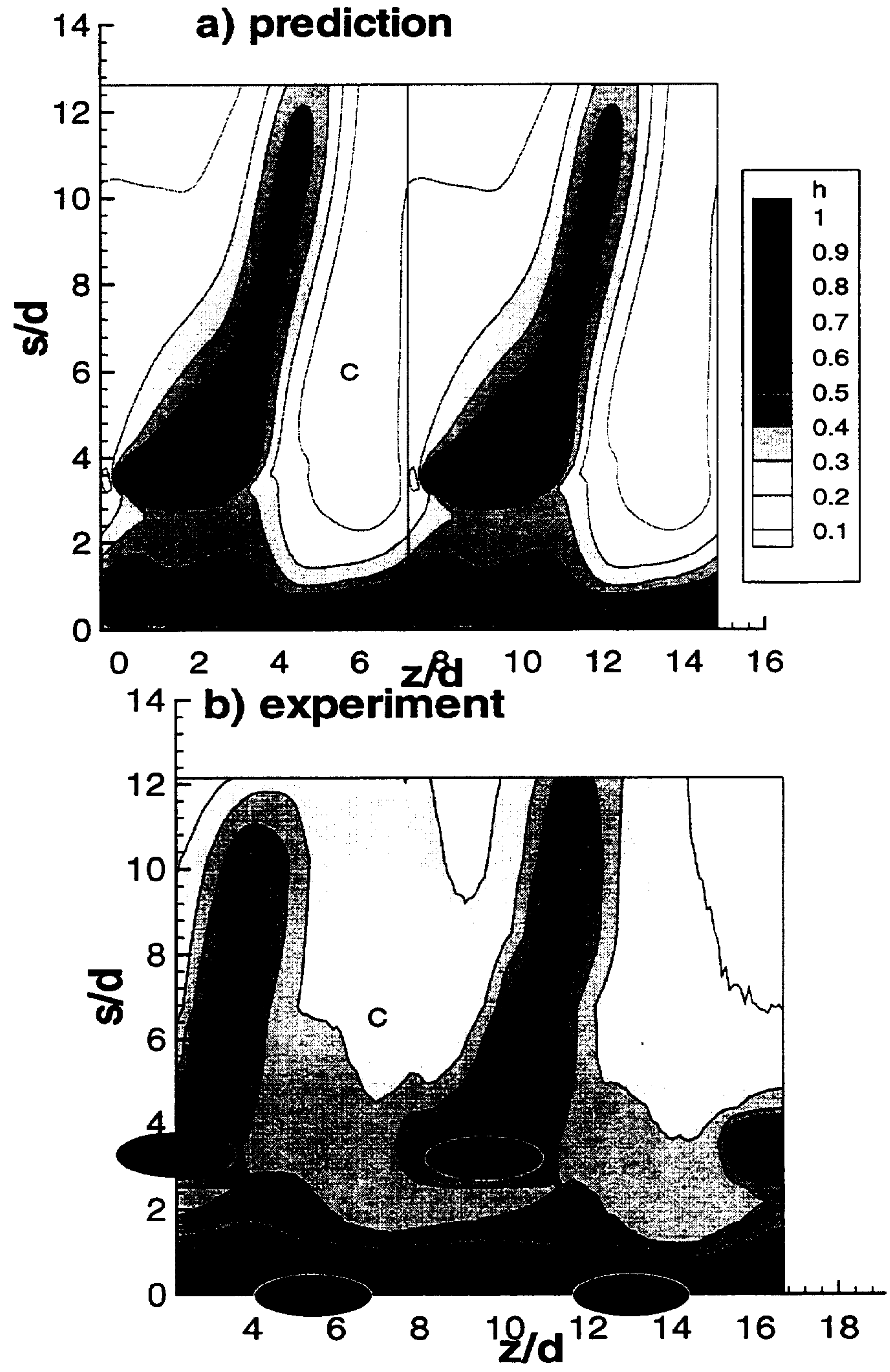

Fig. 7-5 Surface adiabatic effectiveness, Tu=0.5%

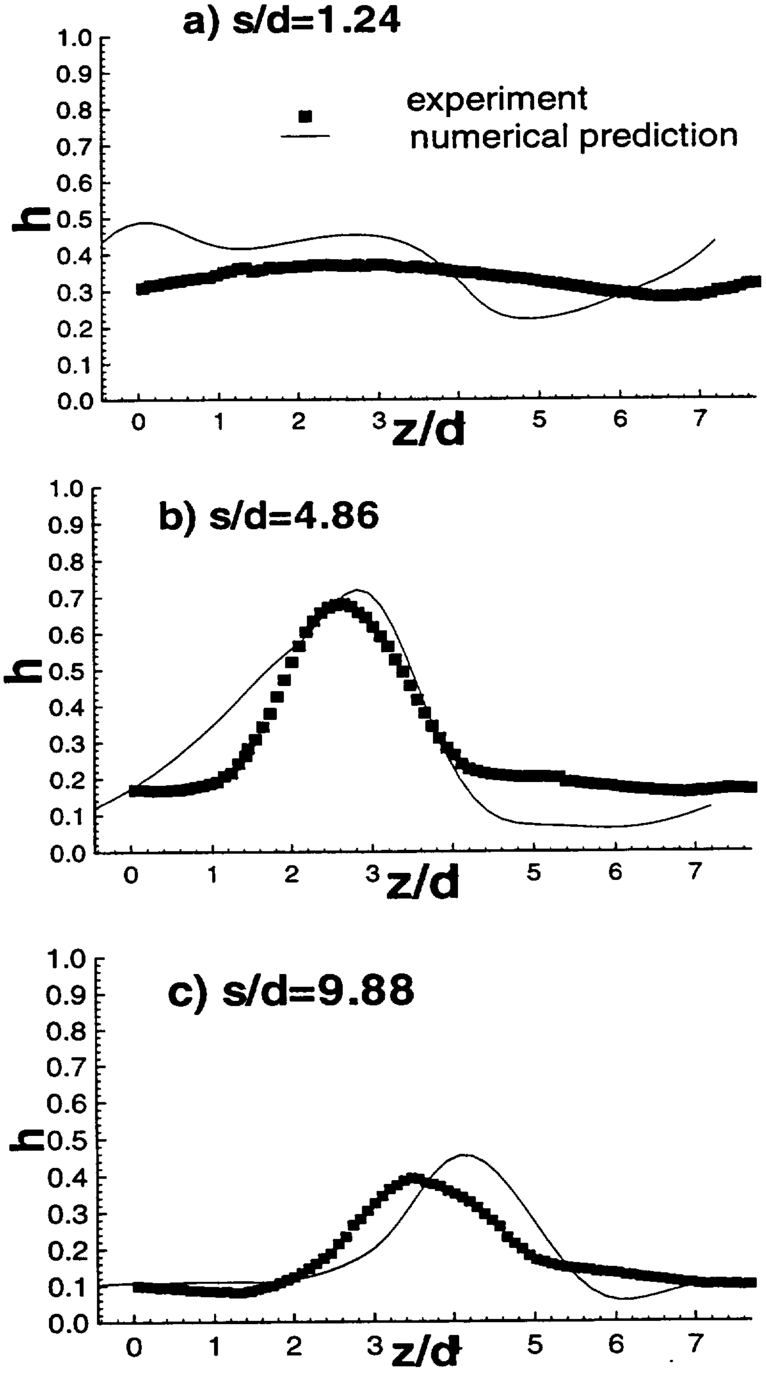

Fig. 7-6 Lateral distribution of adiabatic effectiveness, Tu=0.5% a) s/d=1.24; b) s/d= 4.86; c)s/d=9.88

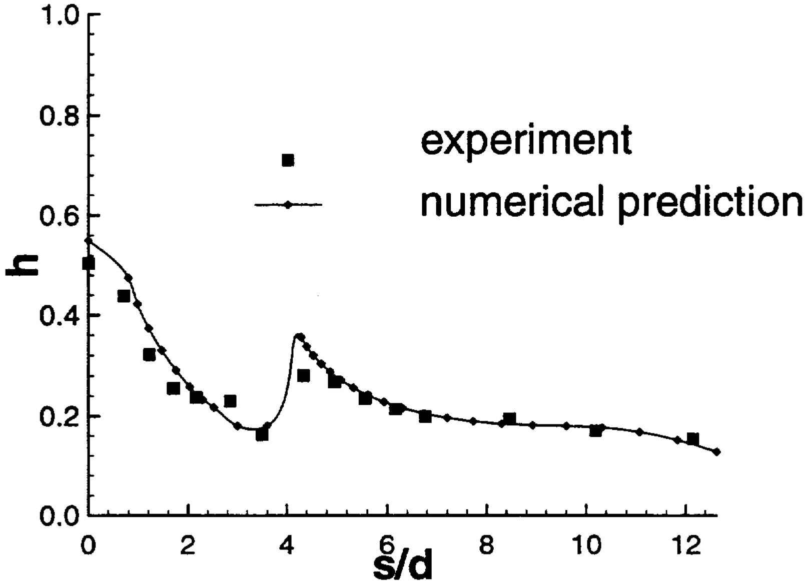

Fig. 7-7 Laterally averaged adiabatic effectiveness, Tu=0.5%

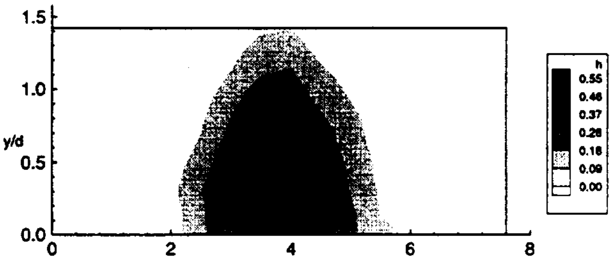

Experimental data

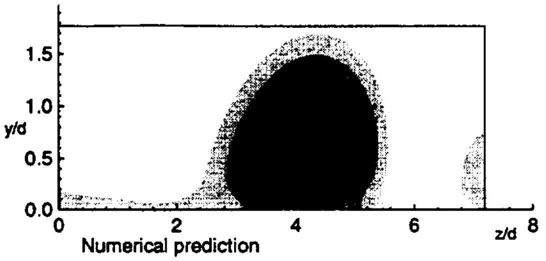

Numerical prediction

Fig. 7-8 Normalized temperature at s/d=9.88

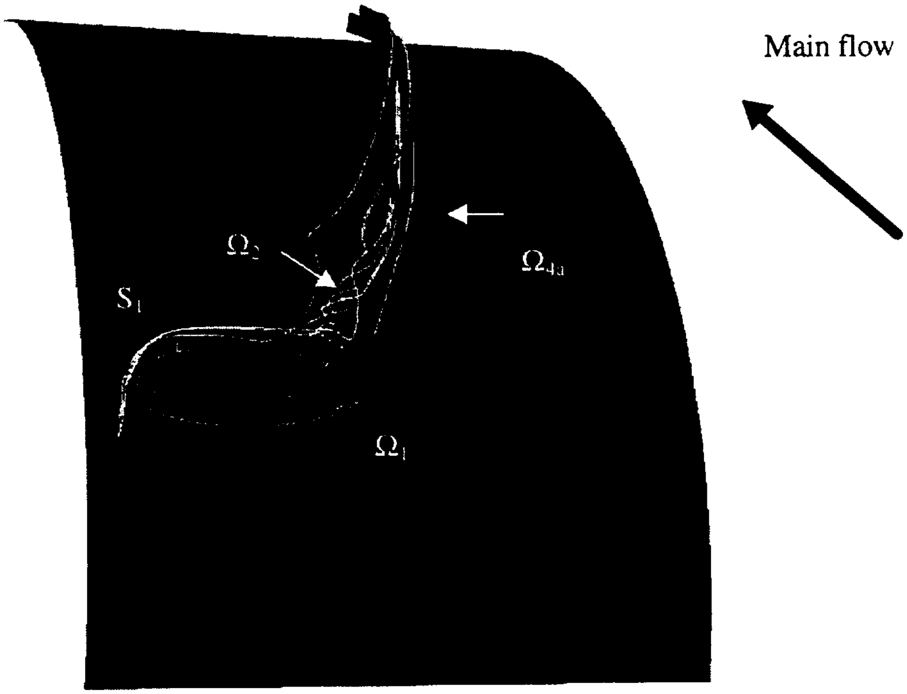
Main flow
Ω_2
S_1
Ω_{4a}
Ω_1

Fig. 7-9 Vortex structure due to the upper hole jet-mainstream interaction, a)

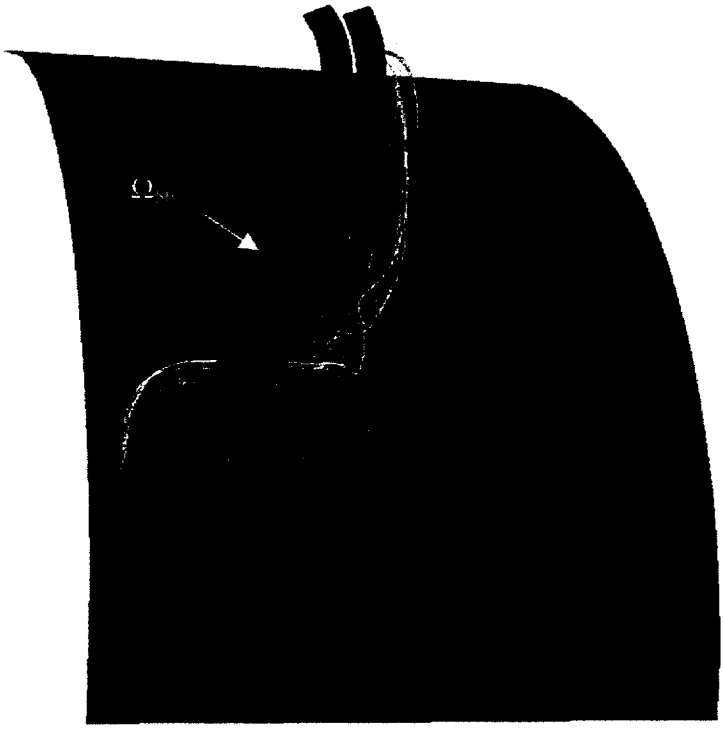

Fig. 7-10 Vortex structure due to the upper hole jet-mainstream interaction, b)

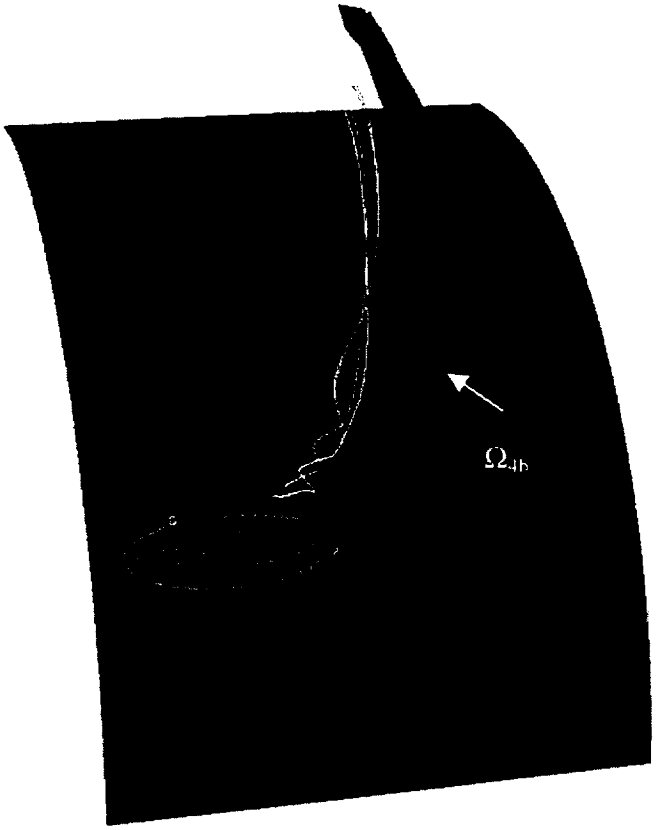

Fig. 7-11 Vortex structure due to the upper hole jet-mainstream interaction, c)

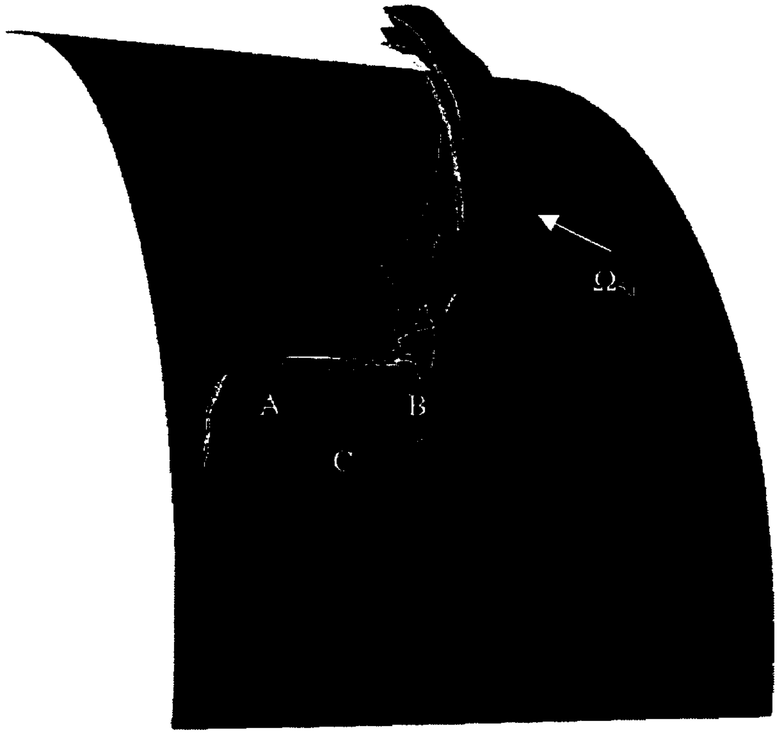

Fig. 7-12 Vortex structure due to the upper hole jet-mainstream interaction, d)

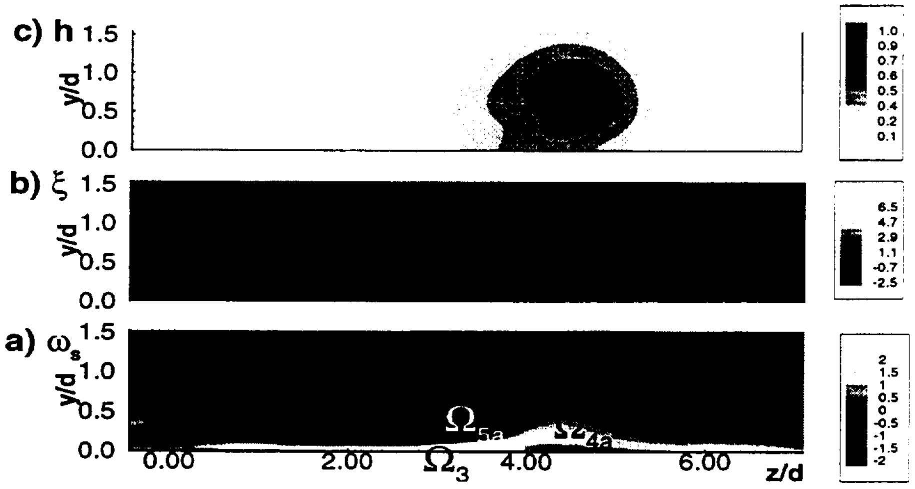

Fig. 7-13 a) Streamwise vorticity; b) normalized total pressure; c) normalized temperature at s/d=9.88

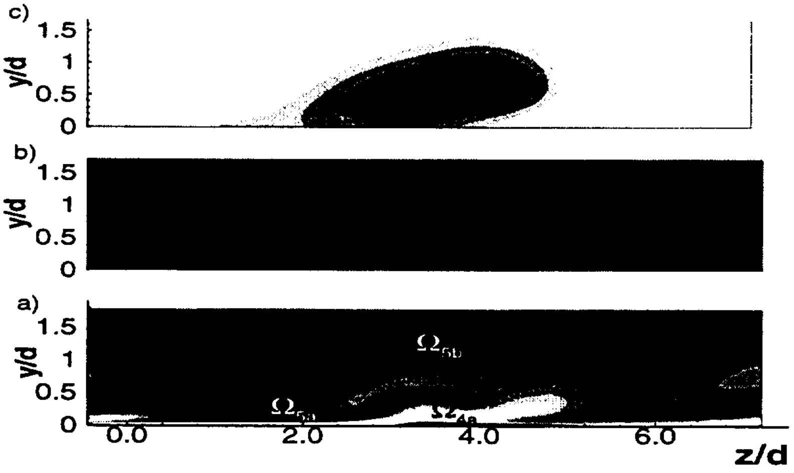

Fig. 7-14 a) Streamwise vorticity; b) normalized total pressure; c) normalized temperature at s/d=6

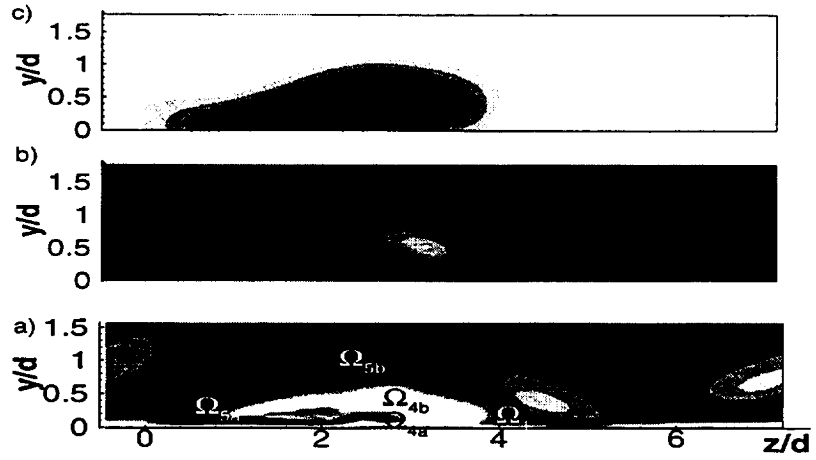

Fig. 7-15 a) Streamwise vorticity; b) normalized total pressure; c) normalized temperature at s/d=4.2

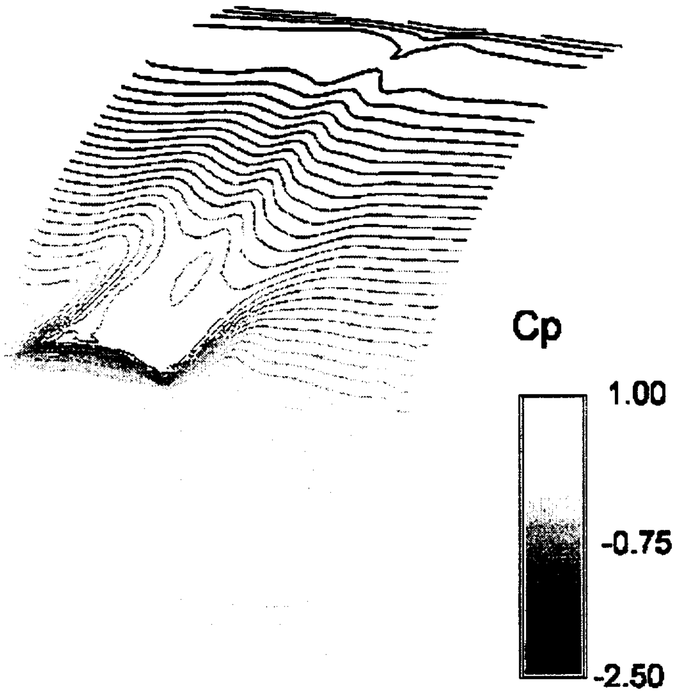

Fig. 7-16 Surface pressure distribution, Tu=0.5%

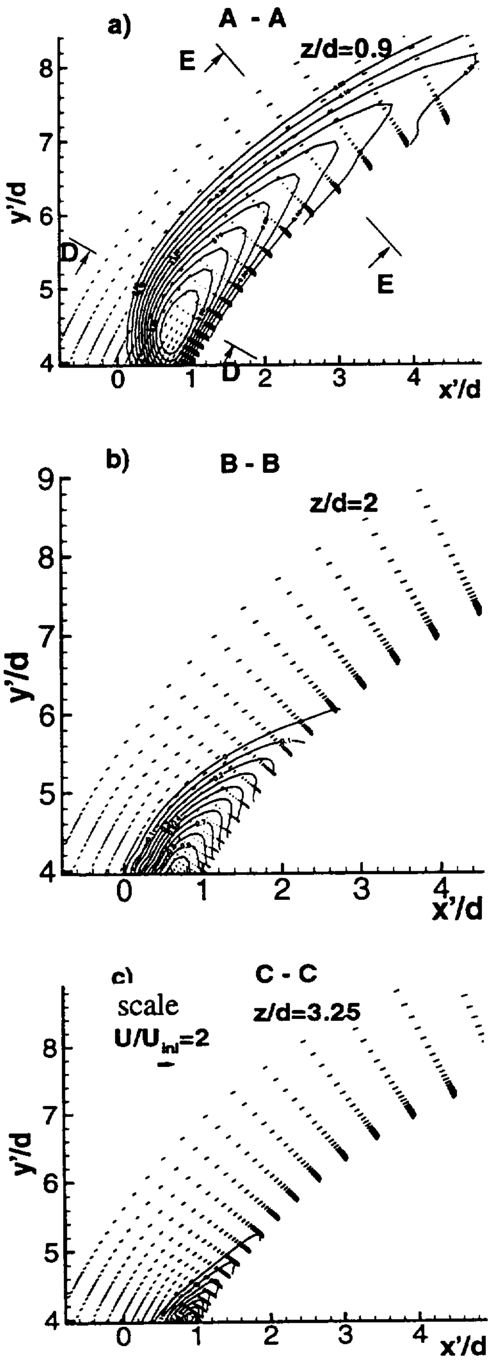

Fig. 7-17 Velocity distribution , Tu=0.5%, contours represent distribution of normalized temperature, h

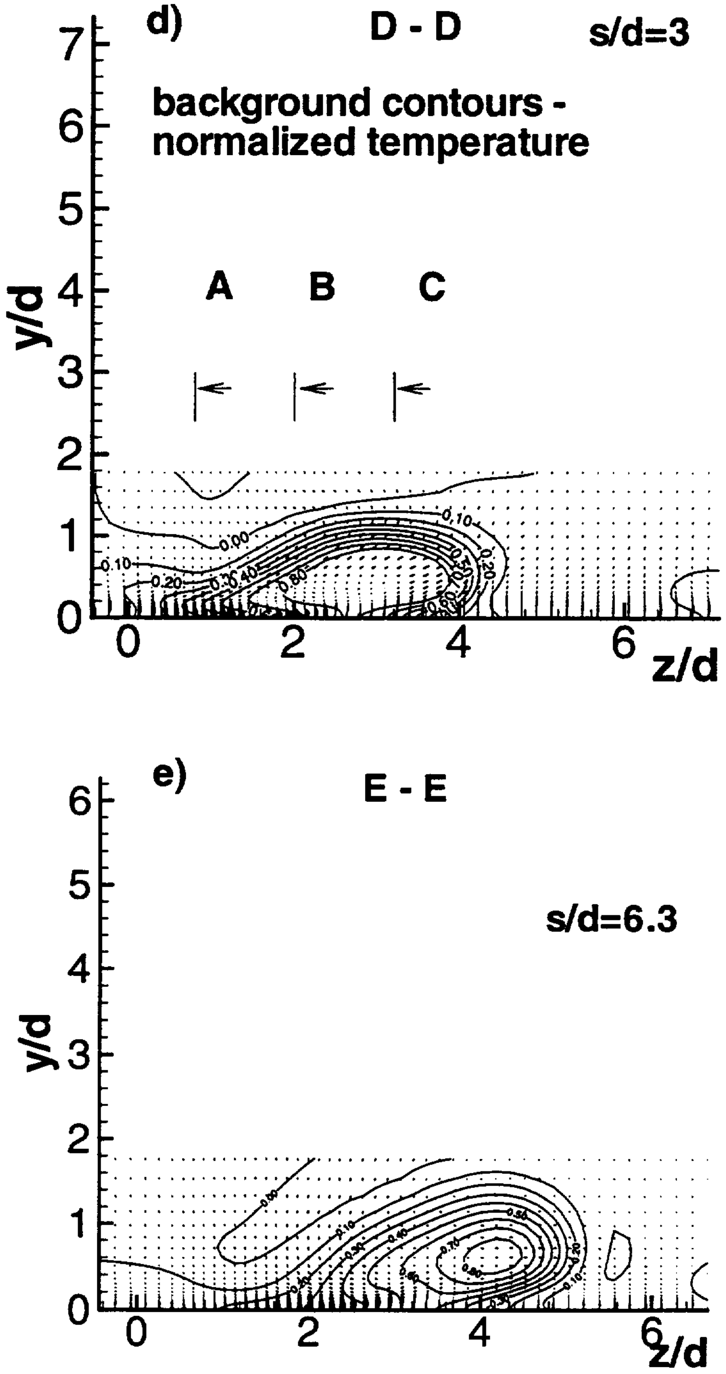

Fig. 7-18 Velocity distribution , Tu=0.5%, contours represent distribution of normalized temperature, h

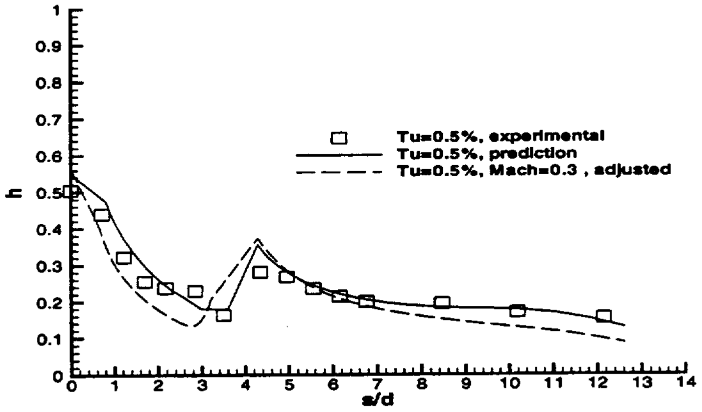

Fig. 7-19 Laterally averaged adiabatic effectiveness, influence of the Mach number

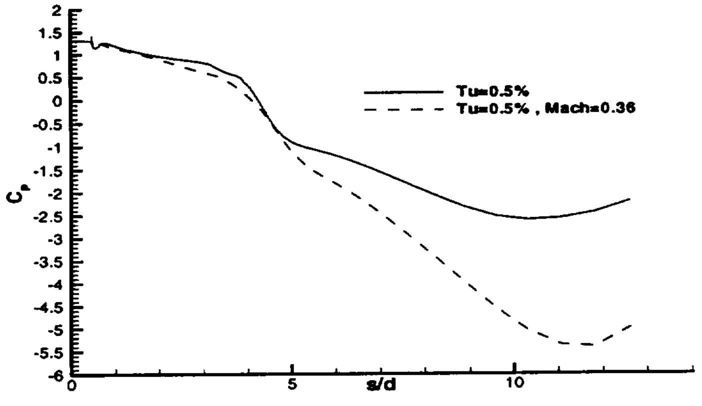

Fig. 7-20 Surface pressure distribution at z/d=5

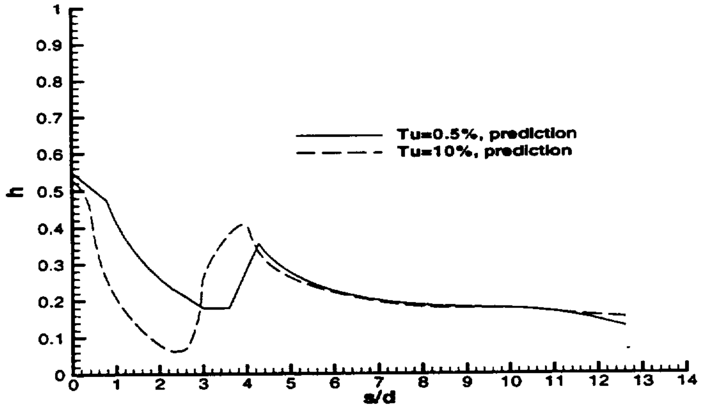

Fig. 7-21 Laterally averaged adiabatic effectiveness, influence of high turbulence intensity

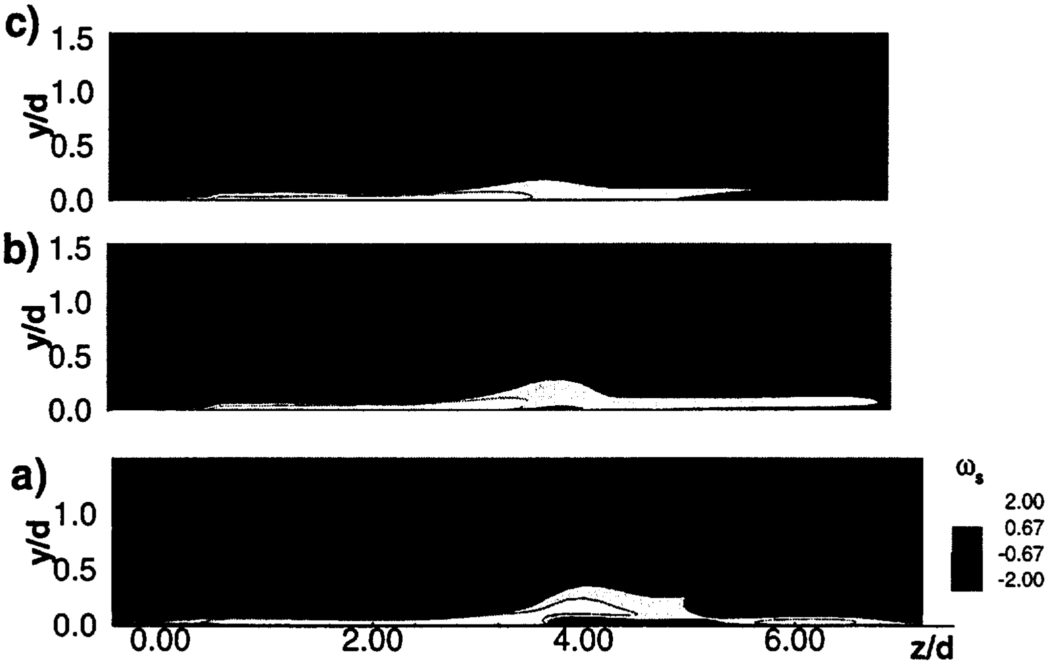

Fig. 7-22 Streamwise vorticity at s/d=8.4, a) Tu=0.5%, b) Tu=10, μ_t/μ_l=30, c) Tu=10%, μ_t/μ_l=120

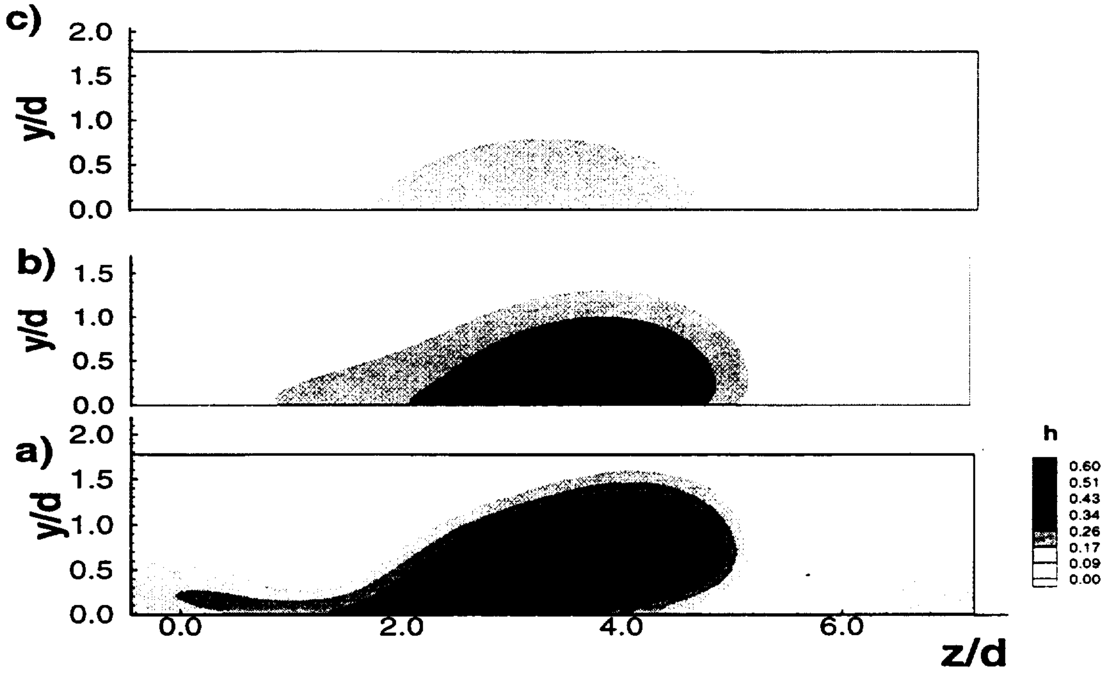

Fig. 7-23 Normalized temperature at s/d=8.4 a) Tu=0.5%, b) Tu=10%, μ_t/μ_l=30, c) Tu=10%, μ_t/μ_l=120

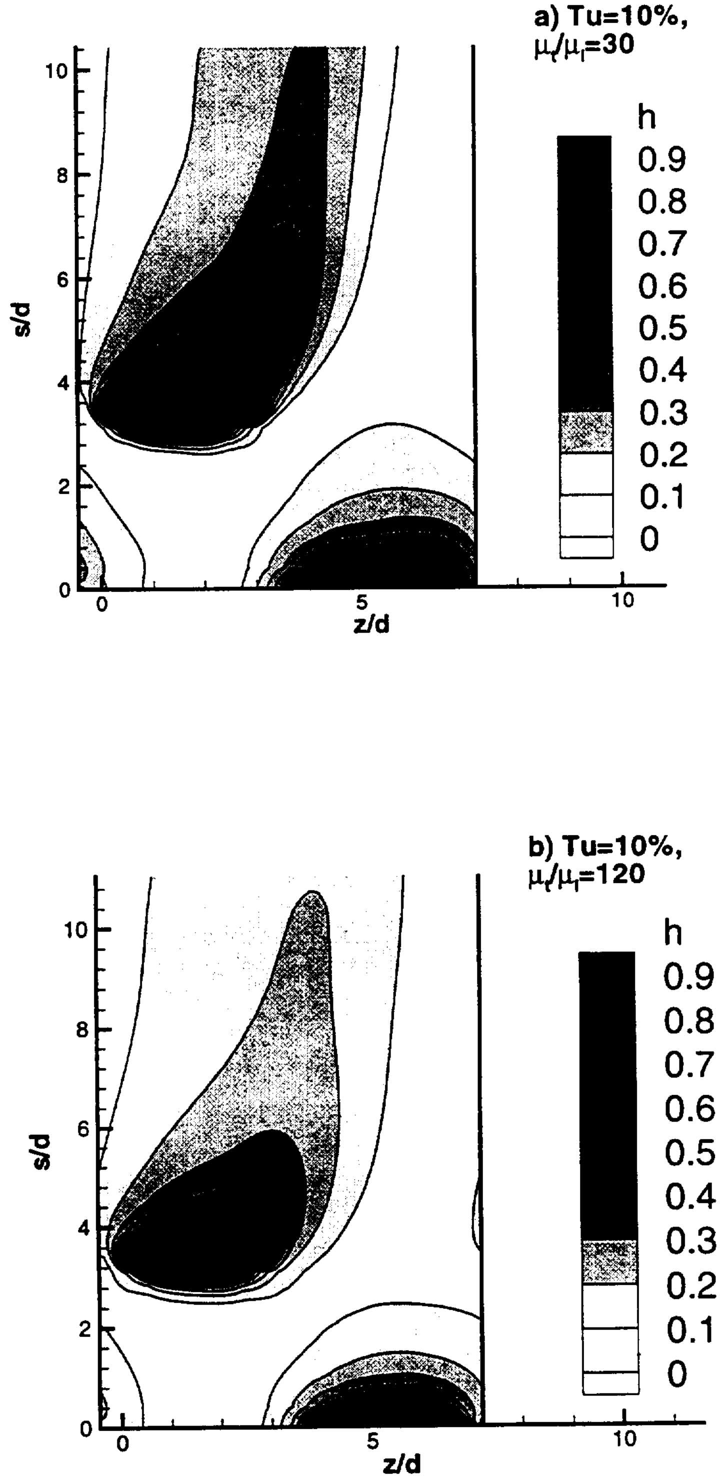

Fig. 7-24 Surface adiabatic effectiveness

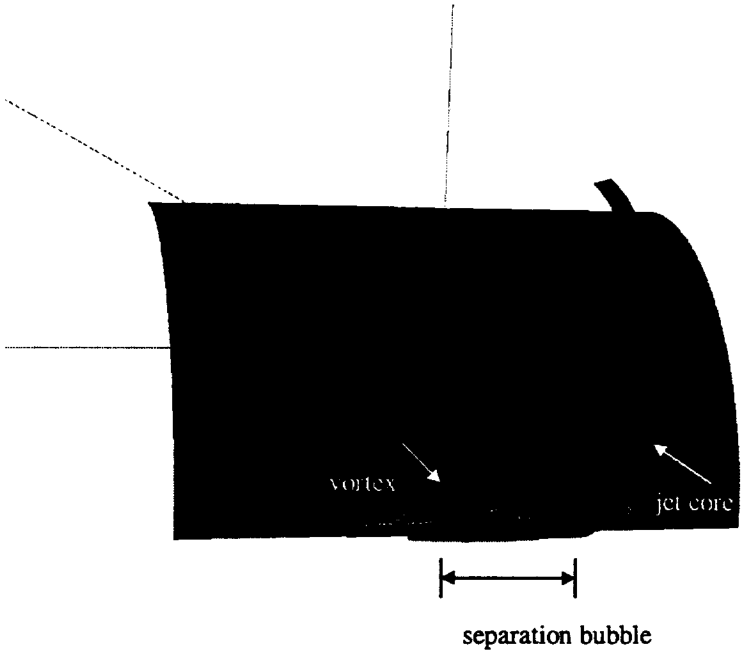
vortex
jet core
separation bubble

Fig. 7-25 Streamlines from the bottom hole, Tu=0.5%;

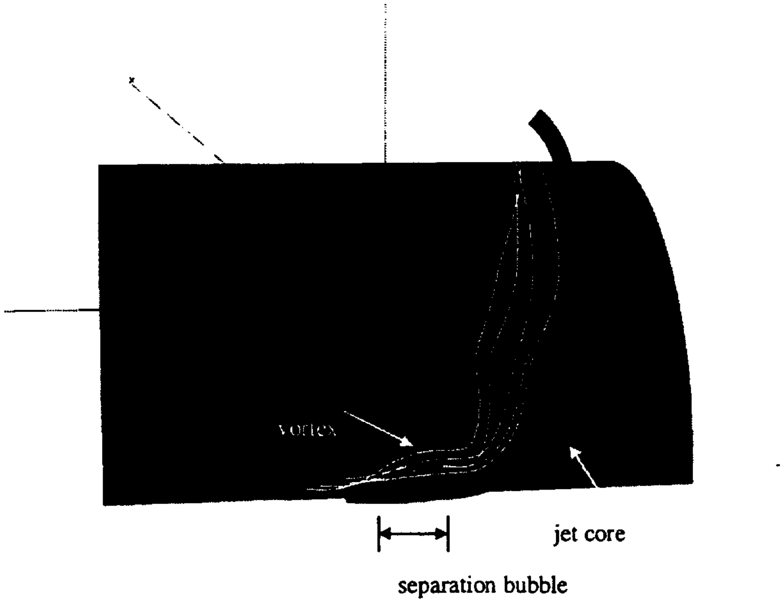
vortex
jet core
separation bubble

Fig. 7-26 Streamlines from the bottom hole, Tu=10%

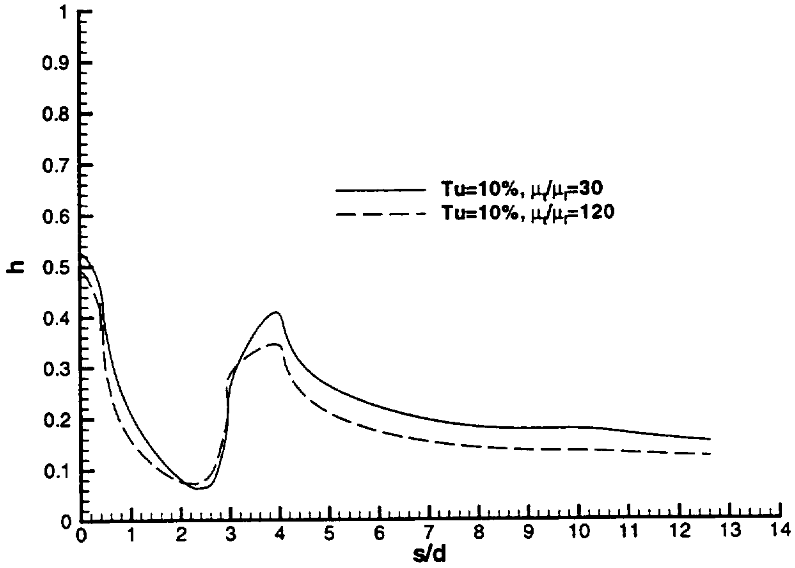

Fig. 7-27 Laterally averaged adiabatic effectiveness, influence of the length scale

Chapter 8

THREE DIMENSIONAL FLOW IN TURBINE ROTOR

Numerical investigation of the flow field in the Penn State rotor based on the utilization of the Navier-Stokes solver has been carried out to gain a better understanding of the secondary and the tip leakage flow development. Pressure gradient across the blade tip clearance results in the development of the jet-like tip clearance flow. Its interaction with the meanflow leads to the development of the tip vortex and modification of the casing secondary flow and vortex. Similar to the jet-flow interaction analyzed in the previous chapter, the vortex interaction and mixing result in additional losses. One of the objectives of this simulation is to identify features affecting the development of secondary and tip leakage vortices, as well as sources of secondary flow losses.

8.1 Computational details

The current investigation is an extension of the numerical simulation presented in Luo and Lakshminarayana (1997). The emphasis of this research is to improve the resolution of the flow in the tip region, including a detailed analysis of the tip vortex development and assessment of the utilization of an ARS turbulence model.

The embedded h-grid is utilized for the simulation of the flow in the tip region. There is a significant variation of velocity vector across the tip clearance due to the relative motion of the blade and casing. The maximum change in velocity amplitude reaches 90 m/s within 1mm distance. Thus, very dense grid is required for an accurate resolution of the tip clearance flow. A comprehensive grid dependency analysis is not feasible due to the enormous utilization of the CPU time. Only a partial grid dependency analysis has been carried out. The numerical simulation has been performed with 9, 12, and 18 grid points in the tip clearance height (0.9 mm, $\tau_c=(r_{cas}-r_{tip})/(r_{cas}-r_{hub})=0.75$). The difference between the solution based on 12 and 18 tip clearance grid points is considerably smaller than that based on 9 and 12 grid points within the gap. All results reported are based on the grid with 18 grid points in the gap. Similar analysis has been performed for the vortex region. Twenty- six grid points in spanwise-direction are utilized across the tip vortex zone. The total grid size is 104 (axial) X 60 (blade-to-blade) X 78 (radial). The outlet boundary is set at $x/C_x = 2$ downstream of the leading edge to ensure that there is no influence of the outlet boundary condition on the vortex structure development. Pitchwise average flow field based on the data by Zaccaria and Lakshminarayana (1995) is used to establish the inlet boundary conditions.

8.2 Comparison with the experimental data

Predicting strong secondary flow that exists in a turbine is known to be one of the most difficult tasks in CFD analysis. Results of the numerical modeling of the ERCOFTAC turbine test cascade reveal a large variation in the position and the amplitude of the secondary vortex predicted by various codes (Gregory-Smith, 1997). Current prediction of the flow in the Penn State rotor have been compared with LDV and pressure measurements by Ristic et al. (1998) and Xiao (1999) to establish confidence in the simulated results.

A previous numerical simulation of the flow in the Penn State turbine Rotor (Luo and Lakshminarayana, 1997) showed very good correlation between the predicted surface pressure distribution and design values from H_b=0.13 to H_b=0.90. Comparison presented by Xiao, 1999, also indicates very good correlation between the experiment and predicted values. The numerical simulations presented in this thesis, which are based on a refined grid, variable tip gap, and a k-ε /ARSM model, show that all these factors do not affect surface pressure at the blade location away from the casing region $H_b<0.94$. Thus that comparison is not presented here. However, the pressure distribution in the vicinity of the blade tip is strongly affected. Grid refinement has the most profound effect on the predicted pressure distribution near the tip clearance on the pressure side (Fig. 8-2).

The comparison presented in Fig. 8-2 shows very good correlation between the predicted and measured blade pressure distribution on the pressure side. The presence of the tip clearance flow affects the pressure distribution only from 97% of span to the casing. The pressure field is essentially two-dimensional in nature (i.e., no significant variation in radial direction) from H_b=50% to 97%. From 97% of the blade span, the velocity field undergoes sudden turning and acceleration as the flow enters the tip clearance. This leads to a rapid decrease in blade pressure near the tip from $x/C_x = 0.4$ to $x/C_x = 0.9$ in this region. This zone corresponds to the maximum tip-leakage mass flow at the pressure side of the gap. The low-pressure zone is relatively thin and extends from $Zg=(r-r_{tip})/(r_{cas}-r_{tip})=-0.2$ to $Zg = 0.5$. Grid density should be adequate not only in tip zone, but also below the blade tip to provide an accurate prediction of the flow in the flow acceleration zone. From Zg=0.5 to Zg=1 (casing) the pressure level is relaxing to the levels on the blade pressure surface. This is caused by the relative motion of the blade and casing, which generate the blockage near the casing and prevents or reduces the tip flow acceleration.

Predicted pressure distribution on the suction surface also correlates well with the experimental data (Fig. 8-3). The characteristic feature of the suction side pressure field is the development of the low-pressure zone at $x/C_x \sim 0.5$ near the blade tip. This pressure decrease is caused by the development of the tip vortex. The location of the minimum pressure can be used to identify the trajectory of the tip vortex (e.g., Ho and Lakshminarayana, 1996). A comparison between the predicted and measured location of the tip vortex path reveals earlier initiation of the tip vortex development in the case of the numerical simulation ($x/C_x \sim 0.58$ VS $x/C_x \sim 0.64$). At the blade trailing edge, the predicted distance between the vortex location and the endwall is higher than the measured value by about 1.5–2% of the blade span. One of the potential factors contributing to this discrepancy is the variation of the tip gap in the experiment. Design tip clearance is $\tau_c=1.1\%$, while the actual clearance varies from $\tau_c= 0.61\%$ to $\tau_c=0.9\%$. Base calculations have been carried out with $\tau_c=0.75\%$. Additional simulations discussed below have been performed to assess the influence of the small variation of the tip gap height on the predicted flow field.

Distribution of the axial velocity and axial vorticity at 10% of the chord downstream of the trailing edge is shown in Fig. 8-4 and Fig. 8-5. A comparison of the velocity field with the LDV data (Ristic et al., 1998) shows that the numerical solver correctly predicts reduced axial velocity zone near the suction side caused by the secondary and leakage flows. The zone of the reduced axial velocity extends to 50% of the pitch near casing and to 80% of the pitch near the hub. Both, the experimental data and the prediction reveal the zone of the reverse flow in the center of the tip vortex (Fig. 8-4). Distribution of the axial vorticity field shown in Fig. 8-5 may be used to identify major vortices; 1) casing wall passage vortex, 2) hub wall passage vortex, 3) tip leakage vortex, 4) scraping vortex (i.e. vortex caused by the relative motion of blade tip and casing) and 5) wake axial vortices. High flow turning results in the development of the passage vortices of significant strength. The hub wall passage vortex core is located at $H_b= 0.3$ and spreads one third of pitch in tangential direction. LDV data has two zones of the positive vorticity near the casing; 1a and 1b. A similar distribution can be observed in the predicted flow field (Fig. 8-5). However, measured axial vorticity in Zone 1a is significantly higher in comparison with the axial intensity in Zone 1b. Predicted axial vorticity distribution has an opposite trend. Normalized helicity, $\frac{\overline{\omega} \cdot \overline{W}}{|\overline{\omega}| \cdot |\overline{W}|}$, can be utilized to analyze vortex development (e.g., Kunz and Lakshminarayana, 1992). Normalized helicity tends to unity at the vortex center disregarding the vortex intensity. The distribution of the predicted normalized helicity indicates that at $x/C_x \sim 0.8$ the core of the casing wall passage vortex (defined as region with normalized helicity equal to unity) is separating into two parts. One is located closer to the casing and can be tracked to Zone 1a. The other part is transported downward and can be tracked to Zone 1b. Based on this analysis, both 1a and 1b are considered as elements of the casing wall passage vortex. A comparison between the predicted flow field in the rotor with tip clearance and without tip clearance indicates that this separation of the casing passage vortex into two zones exists even in the absence of the leakage flow. Both, the prediction and the experimental data, clearly show that the tip vortex is confined to the suction side tip corner. The maximum leakage vorticity occurs at H_b= 92% (prediction) and 94% (experiment). This correlates with the zone of low pressure on the suction side of the blade, which is discussed above. The tip clearance vortex extends to 20% in the pitchwise direction. The numerical simulation predicts a narrower tip clearance vortex. The wake development downstream of the trailing edge is three-dimensional in nature with a negative axial vorticity from 60 to 80% of the span and a positive axial vorticity in the lower 45% of the span. Interaction between the secondary flow and the wake, augmented by the rotation effects, is the primary mechanism responsible for the axial vorticity generation in the wake. Predicted wake axial vortices are more narrow than those observed in the experiment. This can be attributed to the interaction of the upstream nozzle wake with the rotor wake. This interaction, discussed in Chapter 5, makes the suction side of the rotor wake significantly thicker. The current simulation assumes a steady flow, thus the rotor wake-nozzle wake interaction effect is not captured.

A comparison between the predicted flow field with the preliminary results of the LDV measurements (Xiao, 1999) is shown in Fig. 8-6-Fig. 8-9. The axial vorticity field is mostly two-dimensional distribution at x/C_x = 50%, with the exception of the narrow zone near the casing, which corresponds to the development of the casing wall passage vortex.

Presence of a small zone of negative vorticity close to the blade tip indicates the inception of the tip clearance vortex. A comparison of the surface pressure distribution, presented earlier, indicates that the numerical simulation predicts earlier inception of the tip leakage vortex in comparison with the experiment. Therefore, predicted axial vorticity field at x/C_x=50% of the chord has a larger zone of high axial vorticity. At x/C_x = 80% (Fig. 8-9), the tip leakage vortex has grown significantly. The predicted axial velocity field indicates the presence of a stagnation zone in the core of the tip leakage vortex. This effect is weaker in the experimental data. However, the experimental data downstream of the leading edge (Fig. 8-4) contains a significant zone of the negative axial velocity, which is similar to the predicted flow. This discrepancy can be explained through a consideration of the tip vortex development. Presence of the reverse flow in the center of the tip leakage vortex, in combination with the fact that until 80% of the chord most of tip leakage flow is not entrained by the tip vortex, may lead to fewer LDV seeding particles in the center of the tip vortex. The tip leakage flow is essentially unsteady, therefore an experimental error may occur due to the variation of the position of the vortex core.

An overall comparison between the predicted flow field and the experimental data is good and enables a certain level of confidence in the predicted flow field required for the analysis of the secondary flow development presented below. The discrepancy noted may be attributed to two factors. First is the limitation of the flow model utilized, i.e., the steady state simulation based on the circumferential average of the rotor inlet flow field. Experimental measurements (Lakshminarayana et al., 1998) and two-dimensional unsteady simulation (Chapter 5) reveal a profound effect of the unsteady interaction on the flow field in rotor. Therefore, a steady state assumption may not capture some of the time-averaged features of the flow. The second factor is associated with deficiencies of the turbulence model. Ristic et al. (1998) measured strong anisotropy of the turbulence field downstream of the trailing edge. A further analysis is required to analyze the potential influence of non-isotropic turbulence on the accuracy of the prediction.

8.3 Vortex field development

Endwall boundary layers upstream of the rotor undergo strong modification as they enter the blade passage. Low momentum fluid located closer to the wall is transported towards the suction surface due to the blade-to-blade pressure gradient and streamline curvature. After the flow reaches the suction side, it develops into a passage vortices. Streamline and streamwise vorticity distribution (Fig. 8-10) illustrates the development of the secondary vortices in the rotor passage. Hub wall secondary flow impinges on the suction side of the blade at about 50% of the chord. At this location, it merges with the weak suction side horse shoe vortex. Further downstream, the hub wall passage vortex is transported away from the hub wall. At the trailing edge crossplane, the center of the hub vortex is located at 35% of the span. Development of the casing wall passage vortex is affected by the blade casing relative motion and by the leakage flow. Relative motion of the tip endwall contributes to a more intense transport of the casing boundary layer to the suction surface, in comparison with cascade flow. Casing boundary layer starts its final transformation into the passage vortex at x/C_x = 40% of the chord near the suction surface (Fig. 8-10). Starting at x/Cx=50% of the chord, the development of the tip leakage vortex affects the casing wall passage vortex intensity and pushes it away from the suction surface.

Relative motion of the casing wall results in a flow blockage (in pitchwise direction), preventing a development of the leakage flow within the first 30% of the chord and this strongly reduces the leakage flow further downstream. At x/C_x = 20%, the tangential transport of the casing boundary layer fluid results in a reverse leakage flow from the suction surface to the pressure surface (Fig. 8-11, streamlines originated at x/C_x=20% of the chord and Fig. 8-13). The fluid, located closer to the blade tip, is transported along the blade centerline and leaves the tip gap only at x/C_x = 50% of the chord (Fig. 8-14). This observation is supported by the distribution of the accumulated massflow rate through the gap plotted in Fig. 8-12. There is a weak negative tip leakage massflow rate up to 30% of the chord. Vector field at Zg = 0.33 indicates that the leakage flow entering the gap at the pressure surface near the leading edge leaves clearance only at x/C_x = 50%. Within 60% of the blade, a significant part of tip leakage flow originates at the suction surface rather than at the pressure side of the blade tip as a result of the casing wall crossflow boundary layer. Near the casing, this zone extends from the leading edge to x/C_x = 60% (Fig. 8-13) of the tip suction side. It shrinks to about 20% of the chord, from x/C_x =40% near the blade tip (Fig. 8-14). Further downstream, an increasing pressure gradient across the tip gap confines a zone of the reverse leakage flow to less than 5% of the tip clearance height near the casing wall. At x/C_x=55% of the chord, all streamlines initiated inside the gap propagates to the suction side of the blade, an indication of the normal pattern of the tip leakage flow (Fig. 8-11). The tip clearance flow originating at this location mixes with the mainflow without rolling up into a vortex.

A strong interaction between the leakage flow and the casing wall boundary layer immediately turns the leakage flow downwards and streamwise as it leaves the clearance at x/C_x = 60% (Fig. 8-14 and Fig. 8-16a). An analysis of the secondary velocity field indicates the presence of a vortex inception between the blade surface and the leakage flow. Further downstream, this vortex is transformed into a full scale tip leakage vortex (Figs. 8-16). However, streamlines paths clearly show the absence of the tip leakage fluid inside this vortex at x/C_x = 60% (Fig. 8-11 and Fig. 8-16).

The inception of the tip leakage vortex occurs around 50% of the chord, caused by the interaction between the tip leakage flow and the main flow. Increasing leakage massflow expands tip leakage jet penetration into the main flow (Fig. 8-16). However, as stated above, the leakage flow does not start to roll up into the vortex until 80% of the chord. An enlargement of the crossflow area between the leakage jet and the blade suction surface leads to a significant de-acceleration of the flow in this zone. Ultimately, the zone of weak reverse flow develops at the center of the vortex zone. Streamlines initiated at the location of the flow separation zone shown in Fig. 8-17 indicate that the core of the tip vortex comprises of the mainflow fluid rather than the tip leakage fluid until 85% of the chord. The stagnation zone in the core of the tip leakage vortex grows steadily from its initiation up to the trailing edge (Fig. 8-16). Downstream of the trailing edge, the zone of the reverse velocity disappears rapidly as a result of intense entrainment of the tip leakage flow into the core of the tip leakage vortex.

From 80% of the blade chord to the trailing edge, there is a continuous change in the amount of the leakage flow entrained by the tip leakage vortex and the tip leakage flow mixing with the mainflow as a plain jet. At x/C_x = 80% of the chord, only 10% of the tip leakage massflow ends in the tip leakage vortex (Fig. 8-16 and Fig. 8-18). At this location, most of the tip leakage fluid undergoes a quarter rotation as the outer layer of the tip leakage vortex and is then pushed downwards into the mainflow. Near the trailing edge, this part of the leakage flow is merging with the rotor wake (Fig. 8-18). Within the last 7% of the blade chord, practically all the tip leakage flow rolls up into the tip leakage vortex. The only exception is a thin zone near the casing wall. In this region, the scraping vortex prevents the flow from merging with the tip leakage vortex.

Accumulated massflow through the gap grows rapidly from 40% of the chord (Fig. 8-12). Maximum massflow rate is achieved from x/C_x = 70% up to the 90% of the chord. The percentage of the leakage flow, which is entrained by the tip vortex, increases nearly linearly from x/C_x = 80% of the chord to the trailing edge. Thus, the combined leakage massflow is equally split between the fluid, which is entrained by the tip vortex and the fluid which interacts with the mainflow as a plain jet.

8.4 Secondary and leakage flow losses

The complex structure of the vortices in the rotor and their interaction has a major influence on flow losses. There are three major sources of three-dimensional losses. The first source of losses is due to the presence of strong casing and hub passage secondary vortices. The second contributor is additional losses associated with the development of the tip leakage flow. The last source is the increased or, in some cases, decreased losses due to the interaction between the tip leakage vortex, secondary vortices, and the rotor wake.

The various zones of loss generation due to the leakage flow can be classified as:

1. Loss generation inside the tip gap, including losses due to the sudden contraction of the flow, tip and casing boundary layers, and a potential development of the separation zone;
2. Mixing losses inside the blade passage. These losses occur due to the dissipation of the tip leakage vortex and "plain" leakage jet-mainflow mixing loss;
3. Loss production associated with tip vortex development downstream of the trailing edge.

The numerical simulation is a valuable tool in the investigation of the sources of additional losses, as well as their distribution. However, the predicted losses based on CFD modeling are not very reliable in terms of their absolute values. No experimental data is available at this time; therefore, predicted losses can not be verified. Nevertheless, the author's experience and the information presented in literature show that CFD analysis provides reliable information in predicting the trend in loss distribution.

Axial distribution of the mass averaged loss coefficient, $(\varsigma = (\overline{P}_{01} - P_0)/(\rho_1 \overline{W}_1^2/2)$, is presented in Fig. 8-19. A comparison with the loss coefficient based on the two-dimensional simulation, presented in Chapter 5, shows that the secondary flow and tip leakage losses are responsible for about 50% of total rotor losses. This conclusion correlates well with experimental observations (e.g., Booth, 1985).

The presence of the secondary flow and the development of the tip leakage flow (Fig. 8-20) results in increased losses downstream of the trailing edge, while the presence of the axial vortices in the wake contributes to the increased level of losses in this zone. This observation is similar to those made by Ho and Lakshminarayana (1996), for the turbine cascade. Inside the blade passage, increased rate of loss generation, in comparison with two-dimensional flow, is observed from 50% of the chord as a result of the final entrainment of the casing and hub wall secondary boundary layers into corresponding passage vortices. Intensified loss production from x/C_x = 90% correlates well with the changing pattern of tip leakage – mainflow mixing. At this location, most of the leakage flow is entrained by the tip leakage vortex, resulting in additional losses.

Losses inside the tip clearance gap[1] are responsible for about 6-7% of the total additional losses (Fig. 8-19). This low value may be attributed to the absence of the flow separation inside the gap and on the blade pressure surface in the vicinity of the gap. However, the prediction of the separation zone is sensitive to the characteristics of the turbulence model used.

The secondary flow vortex structure is directly related to the distribution of the loss coefficient presented in Fig. 8-20. Development of tip and hub secondary vortices, which can be observed at $x/C_x = 60\%$ results in a zone of the low pressure near the tip and the hub wall respectively. Farther downstream, mixing of the secondary vortex is the primary source of losses up to the trailing edge. In the case of Penn State rotor, the presence of the tip leakage flow does not affect the loss generation due to the casing and hub passage vortices. This conclusion is based on a comparison of the loss coefficient distributions for the cases with and without tip clearance (Fig. 8-20 and Fig. 8-21). At $x/C_x = 80\%$, the loss coefficient distribution has a zone of the decreased total pressure located between the tip vortex center and the boundary layer (Fig. 8-20). Tip leakage flow streamlines initiated at x/C_x at 70% of the chord inside the gap indicate that these losses are due to the mixing of the tip leakage jet (i.e., part of tip leakage flow mixing with main flow without entrainment into the tip leakage vortex). Beyond this zone there is no indication of the additional losses caused by the mixing of the leakage flow outside the tip leakage vortex.

---

[1] Gap losses are calculated as the difference in the mass average stagnation pressure between the suction and the pressure sides of the gap, normalized by the ratio of tip leakage massflow to the total massflow

The development of the tip leakage vortex results in an extended zone of low pressure near the blade tip. The presence of the reverse flow in the vortex core minimizes the contribution of the zone of low total pressure inside the tip leakage vortex into overall losses. Downstream of the leading edge, massflow associated with the zone of the tip leakage vortex is higher. Therefore, the contribution of this zone in loss generation is more profound downstream of the trailing edge.

Due to the complex interaction between secondary vortices, leakage flow, and wake, it is very difficult to calculate contribution of various sources to total loss. It is estimated that the tip and the hub secondary vortices contribute 50% of the additional losses (i.e., losses in addition to the profile and plain wake mixing losses), while losses due to the tip leakage flow account for about 35% of the additional losses. The rest of the additional losses is due to the interaction of secondary vortex, the leakage flow and the wake (i.e., loss due to the presence of wake axial vortices, etc.).

8.5 Influence of the tip clearance height on the tip leakage vortex development.

A numerical simulation of the turbine rotor with different tip clearance heights has been carried out. The main objective of this investigation is to study the influence of clearance height on the amplitude and the structure of the secondary and leakage flows. In addition to gaining a better understanding, this simulation is useful in establishing a better interpretation of the comparison between the numerical and experimental results. This study will also provide guidance to the designer in optimizing the tip leakage effect. In the experimental rotor, the blade-to-blade variation of tip clearance is about 30% of its average value. Three cases have been investigated: with τ_c=1.1%, τ_c=0.61%, and no clearance (in addition to the base case with τ_c=0.75%). Even though zero clearance is physically not realizable, the relative motion of the blade and casing is preserved. A comparison of the leakage massflow at different tip clearances (Fig. 8-12) shows a nonlinear relation between the clearance height and the leakage massflow. The blade tip boundary layer and the casing boundary practically merge for the case of τ_c=0.61%. Therefore, leakage massflow at τ_c=0.61% is equal to less than one-third of those observed at the design value of tip clearance (τ_c=1.1%, Fig. 8-12).

There is no significant difference (beyond the moderate change in amplitude of vortices and position of the tip leakage vortex core) between the axial velocity and axial vorticity fields at x/C_x = 110% of the chord (Fig. 8-22 b,d and Fig. 8-4, Fig. 8-5) at various tip clearances. The position of the tip vortex center is located farther from the casing for the flow with τ_c=1.1%. This is due to the earlier inception of the tip leakage vortex caused by increased leakage flow. Based on the results of the numerical modeling, it is possible to estimate that 0.1% increase in clearance results in 1% change in the spanwise position of the tip leakage vortex. Despite the significant change in the size and amplitude of the tip vortex, as well as in the extent of the tip leakage vortex core reverse flow, the overall pattern of the secondary and leakage flows in the case of τ_c=0.61% is similar to the base case (Fig. 8-22). However, there is a significant redistribution between the leakage flow entrained by the tip leakage vortex. For the case with τ_c=0.61%, about 75% of the leakage flow is entrained into the vortex, while the base case has only 50% of the leakage flow rolled up into it. Mixing of the tip leakage vortex results in higher losses in comparison with “plain” jet mixing.

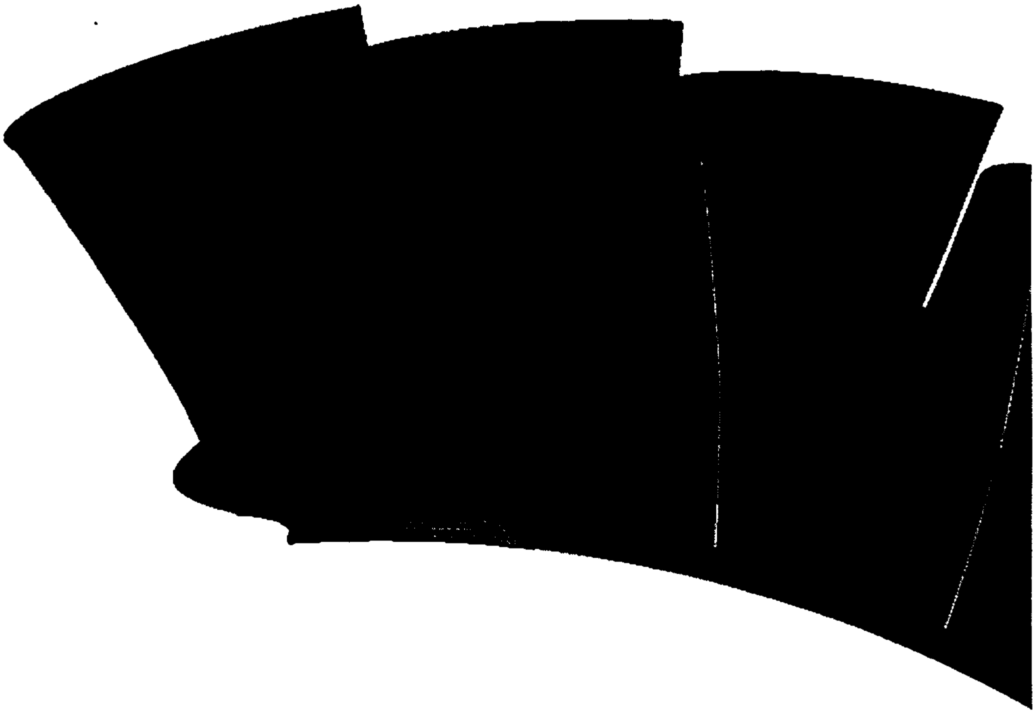

Fig. 8-1 Penn State rotor, computational grid

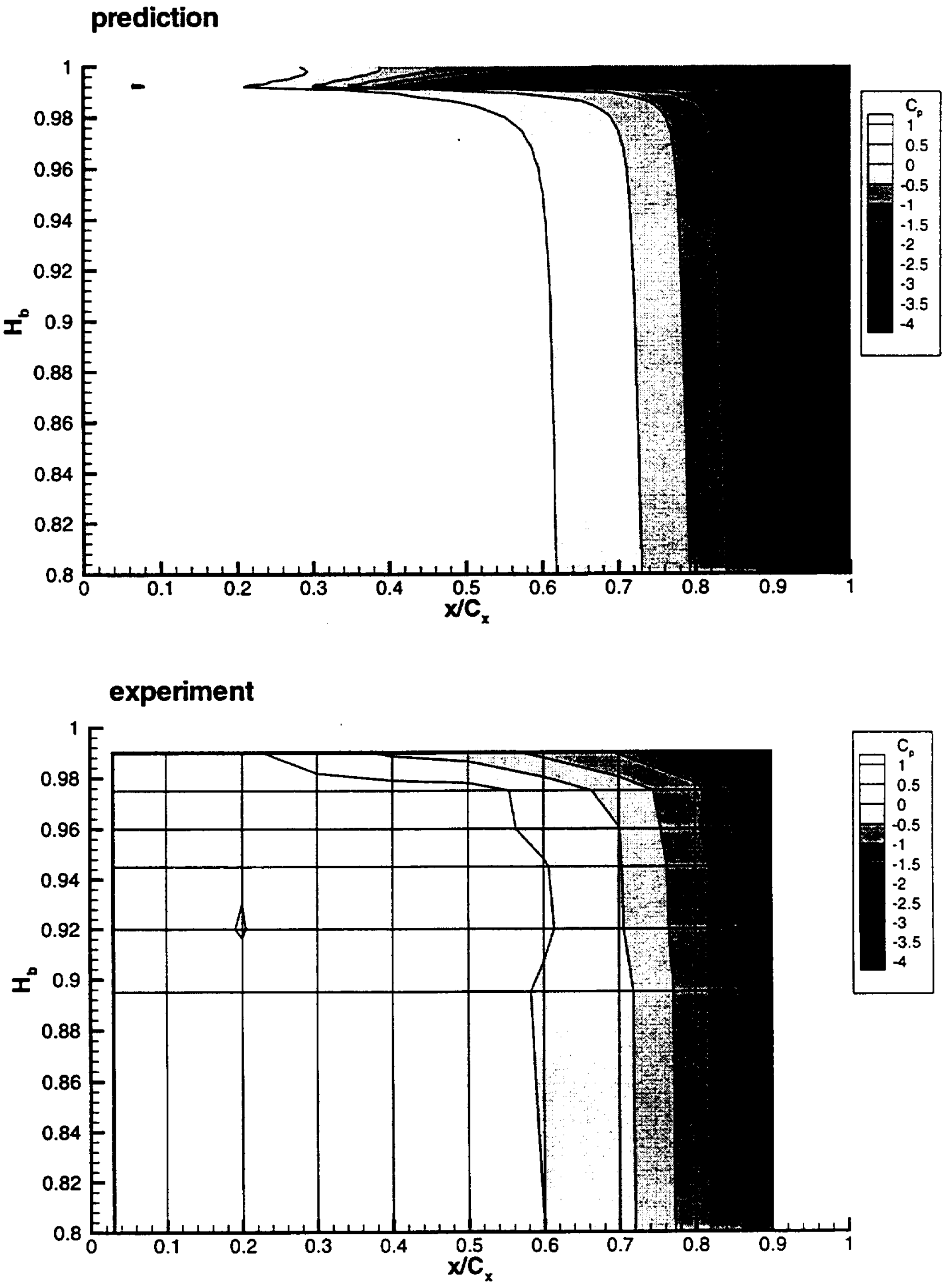

Fig. 8-2 Pressure distribution, pressure surface (tip clearance zone is also shown in the prediction)

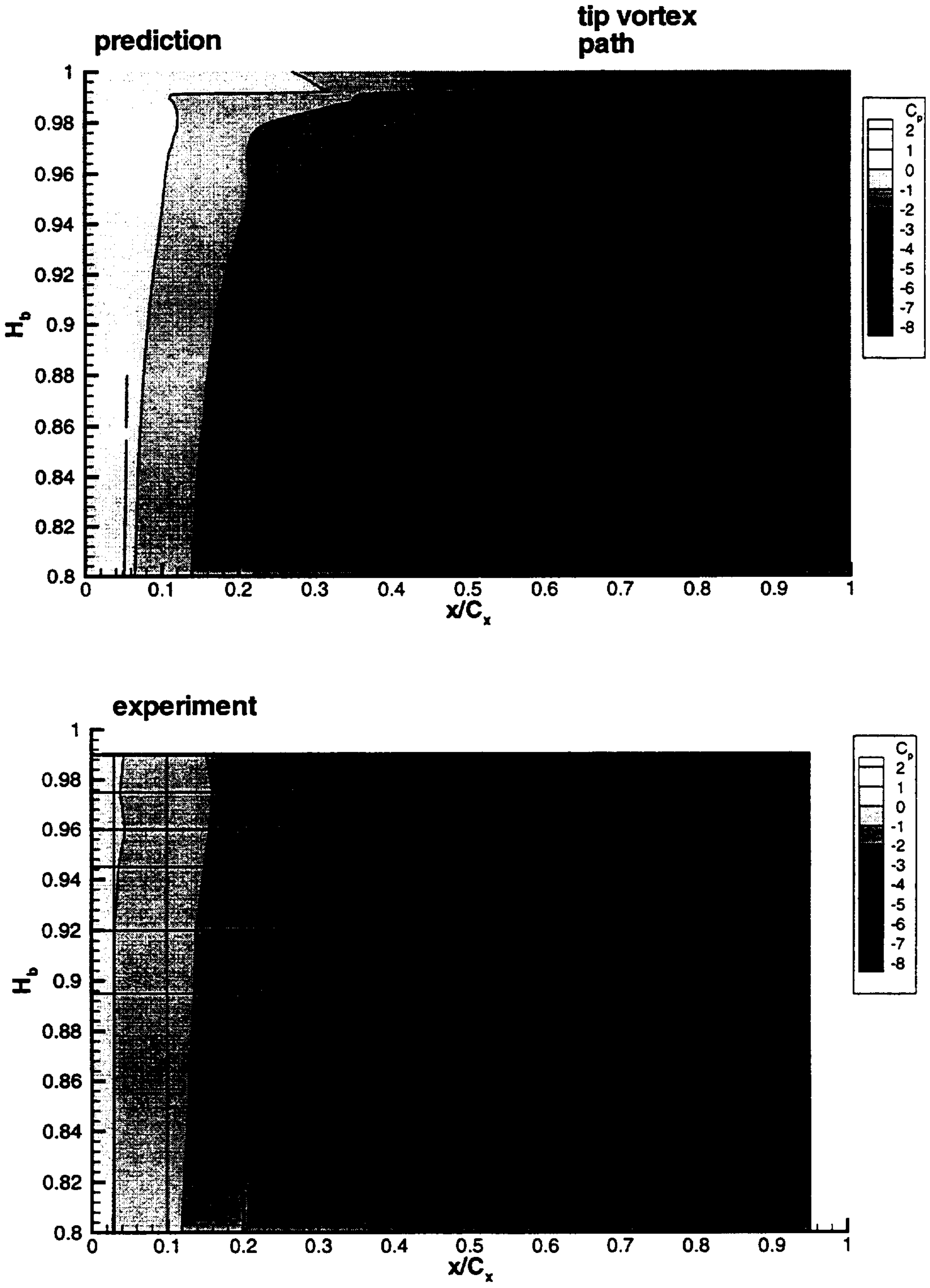

Fig. 8-3 Pressure distribution , suction surface (tip clearance zone is also shown in the prediction)

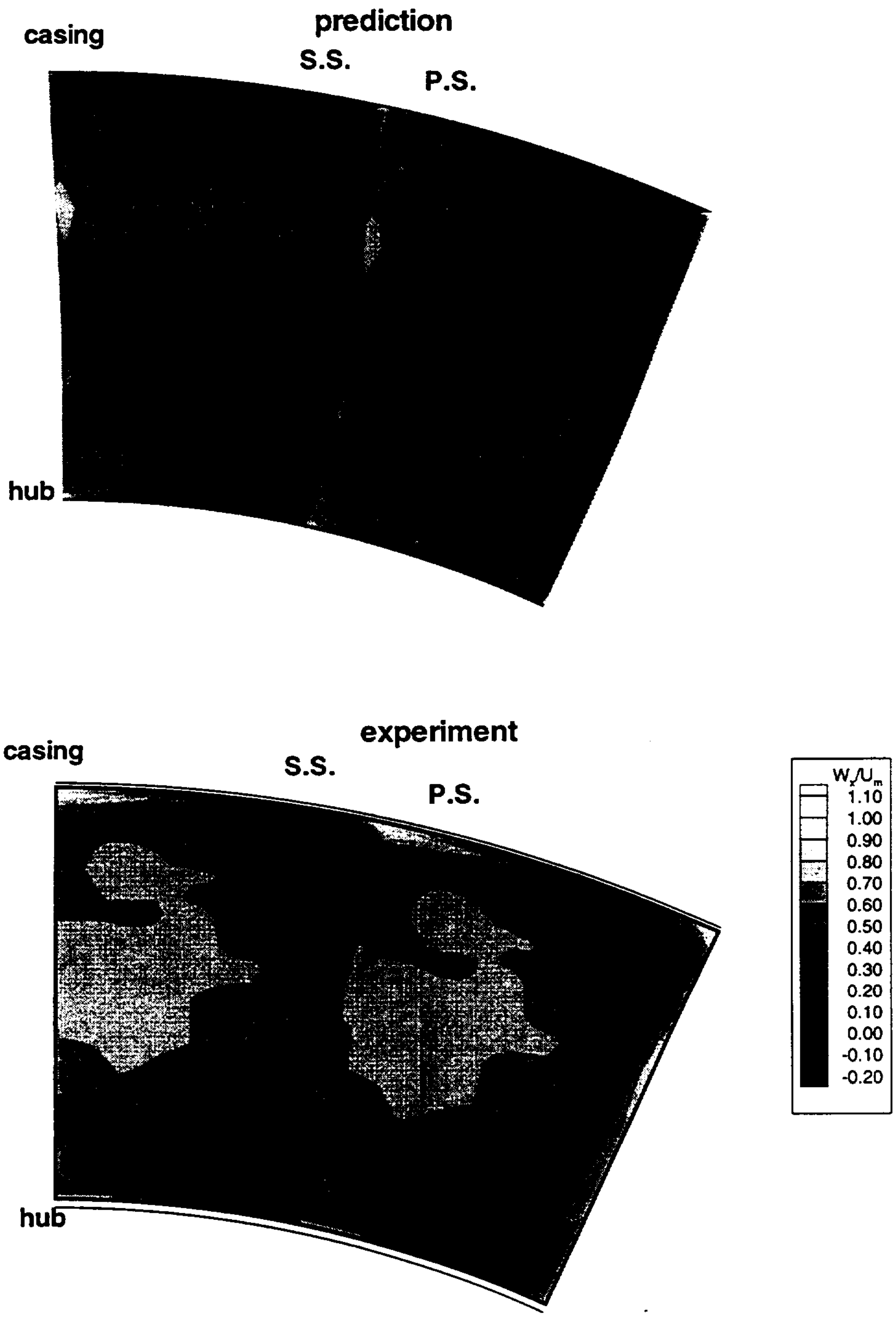

Fig. 8-4 Normalized axial velocity field at $x/C_x=1.10$

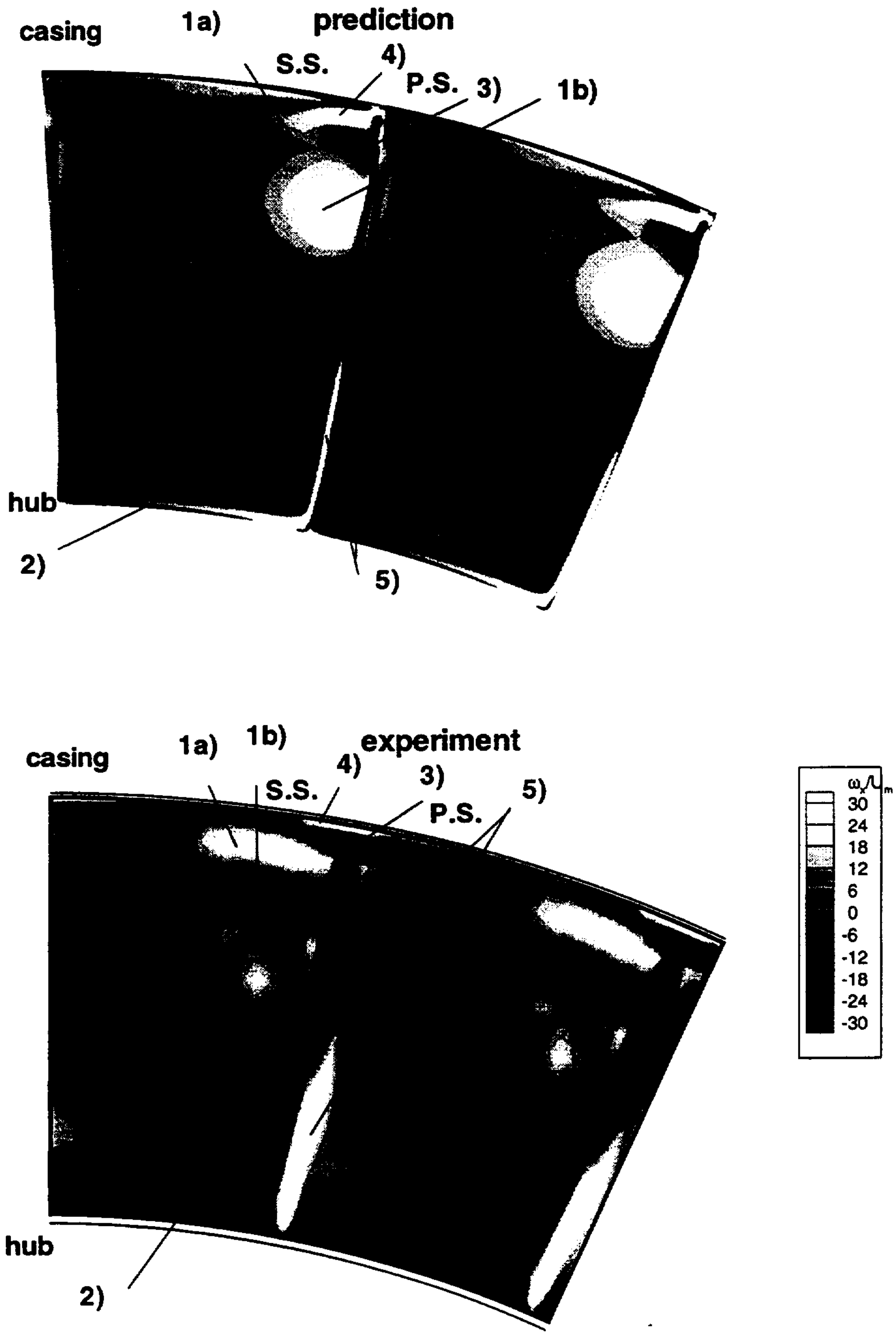

Fig. 8-5 Normalized axial vorticity at x/C_x=1.10

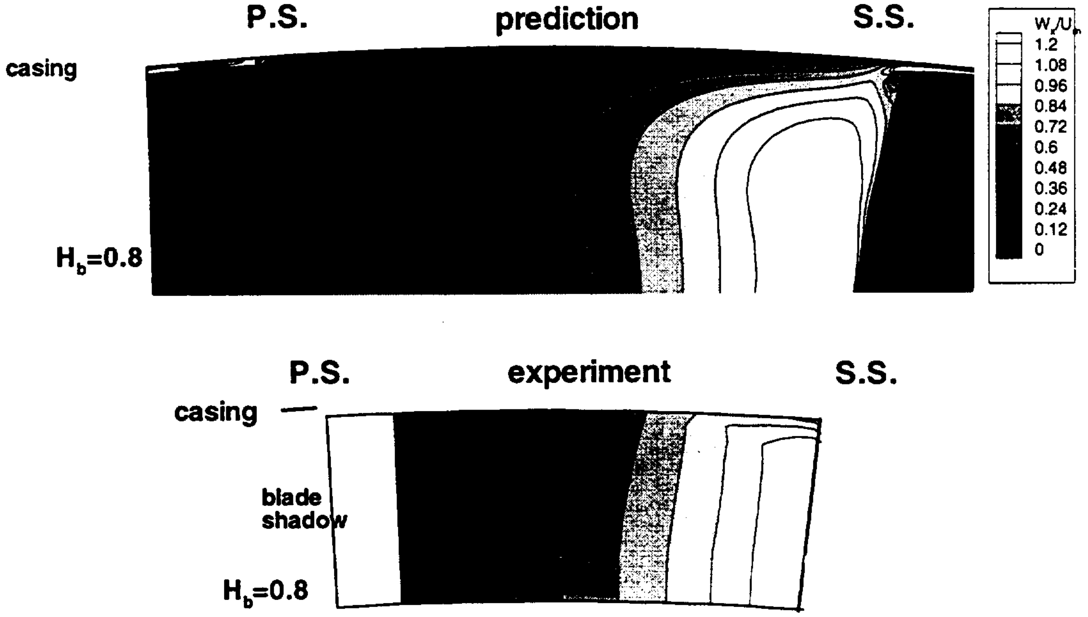

Fig. 8-6 Normalized axial velocity at x/C_x=50%

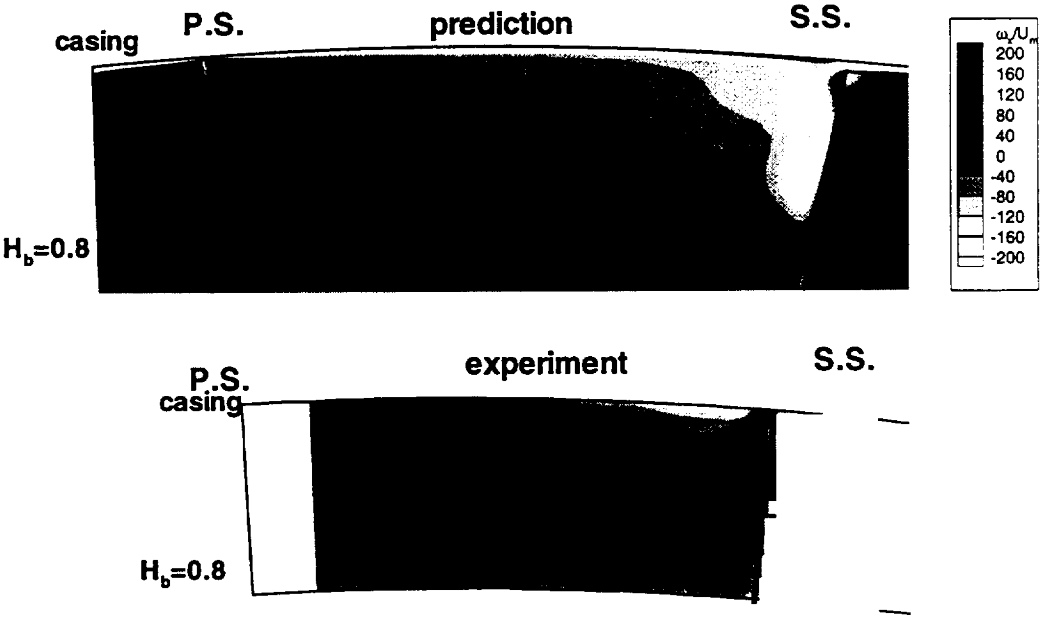

Fig. 8-7 Normalized axial vorticity at x/C_x=50%

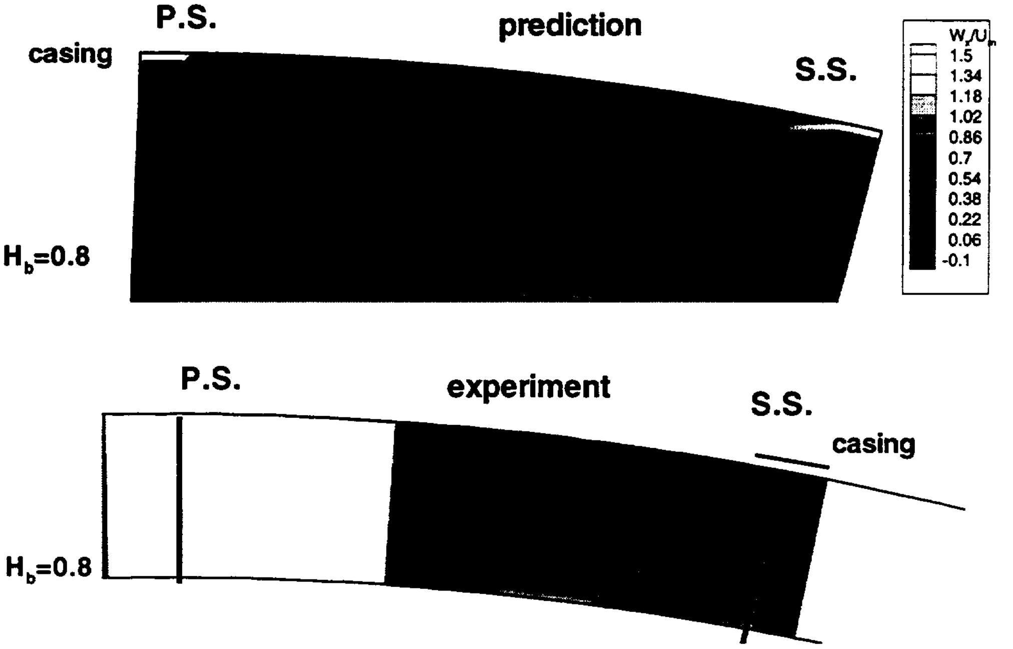

Fig. 8-8 Normalized axial velocity at x/C_x=80%

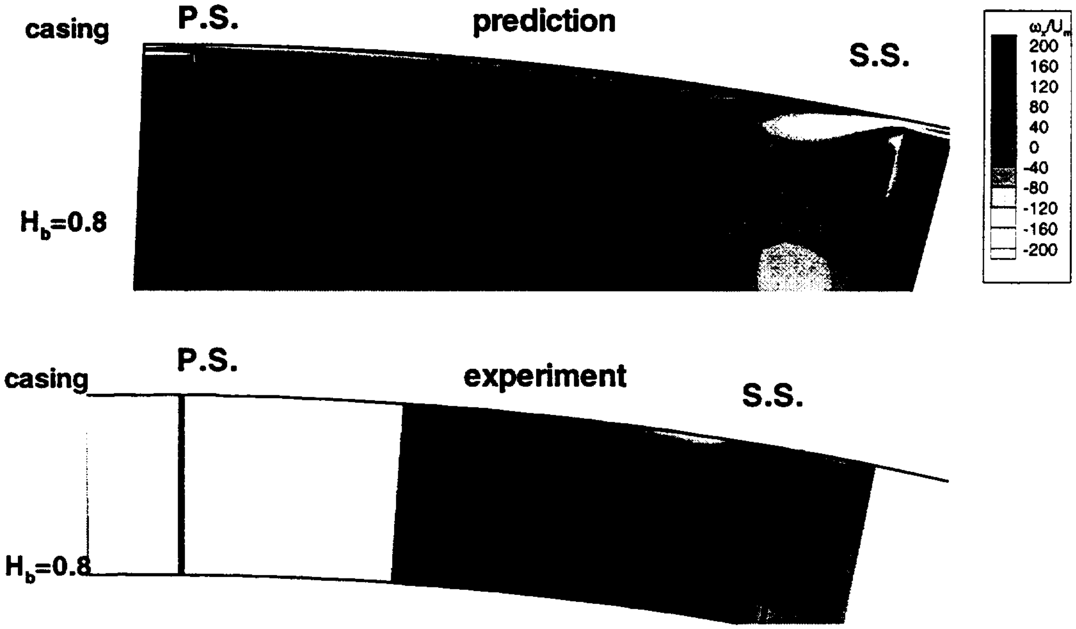

Fig. 8-9 Normalized axial vorticity at x/C_x=80%

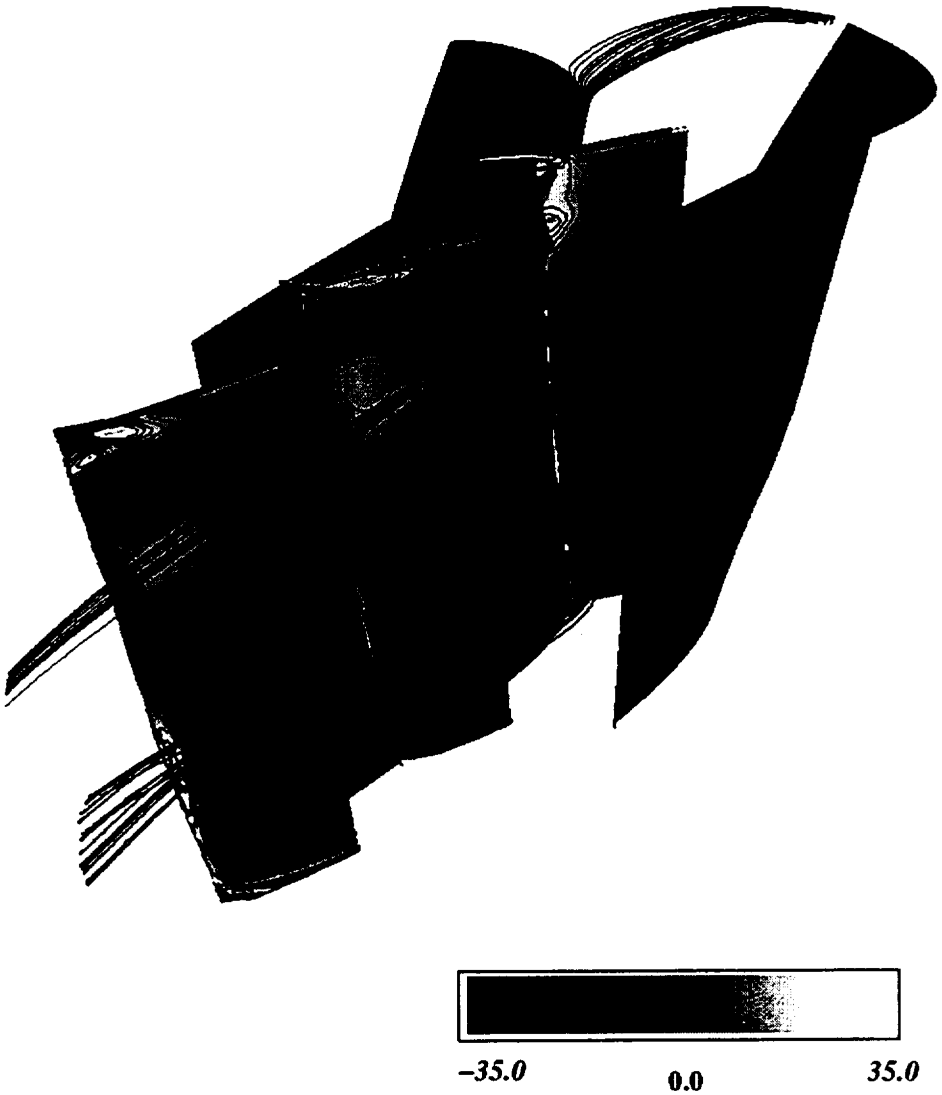

Fig. 8-10 Streamline vorticity ($\omega_s/2\omega$), crossflow planes are located at x/C_x=60%, x/C_x=80%, and x/C_x=110% respectively, streamlines are initiated 5% of the chord upstream of the leading in hub and casing boundary layers

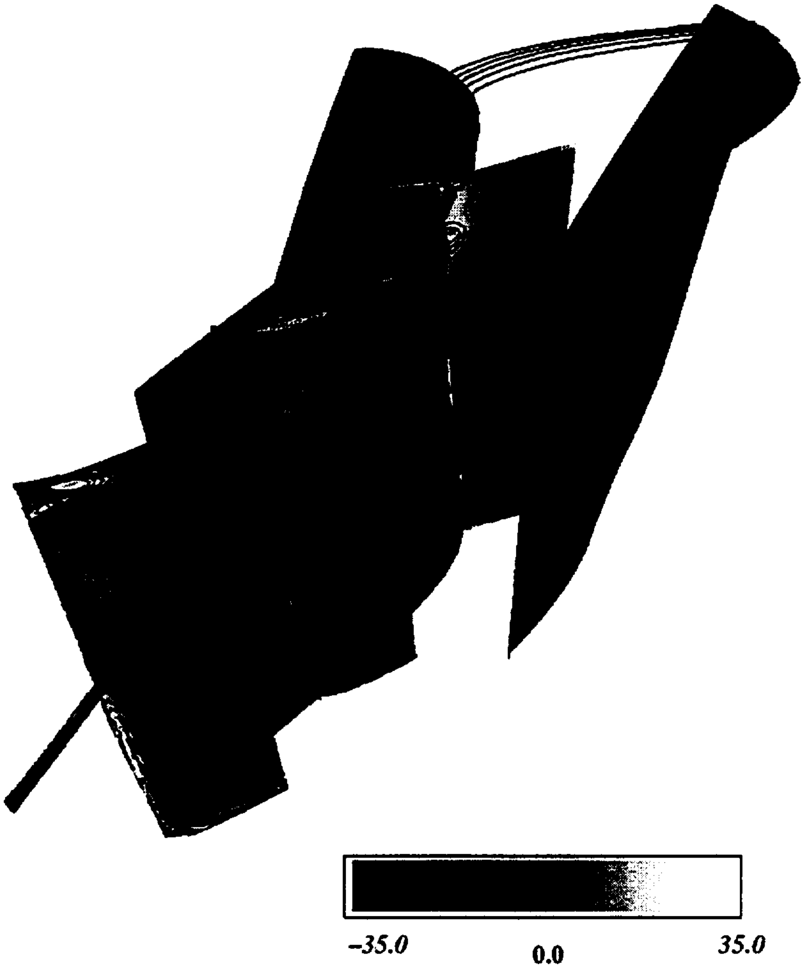

Fig. 8-11 Streamline vorticity ($\omega_s/2\omega$), crossflow planes are located at x/C_x=60%, x/C_x=80%, and x/C_x=110%, streamlines are initiated inside tip gap at 20% and 55% of the cord

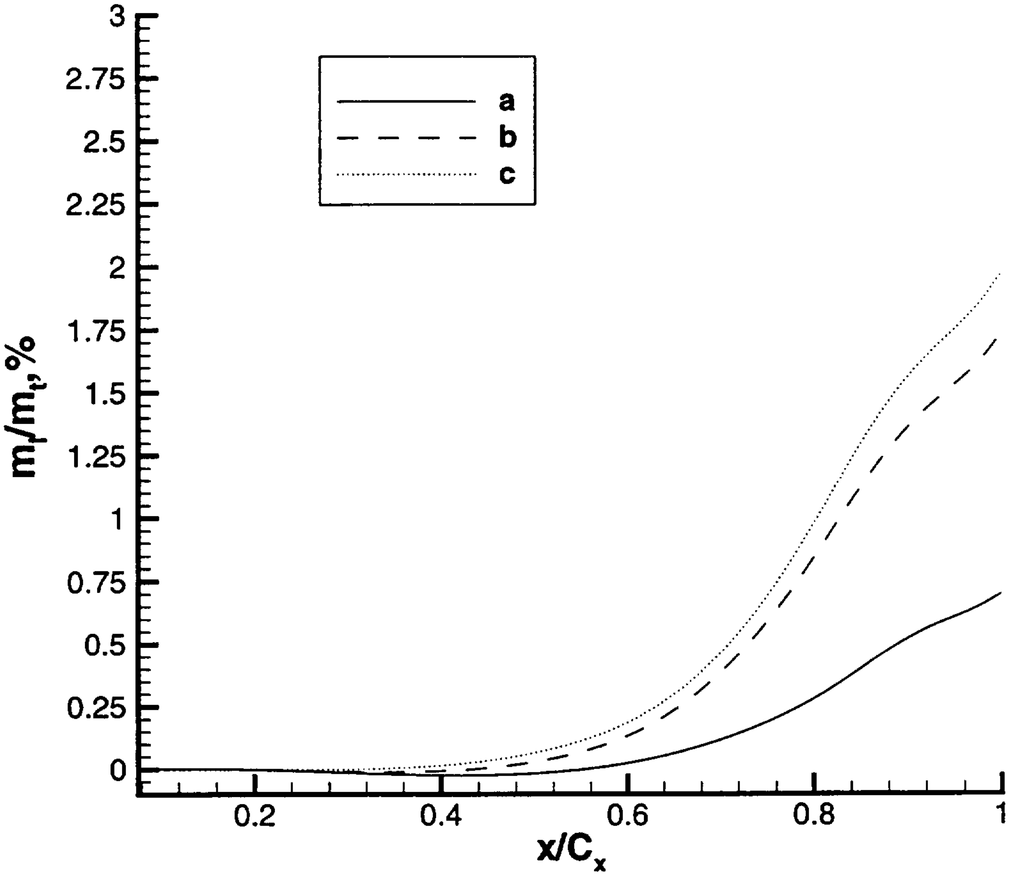

Fig. 8-12 Massflow through the tip gap a) case with τ_c=0.61%. b) case with τ_c=0.75%. c) case with τ_c=1.1%.

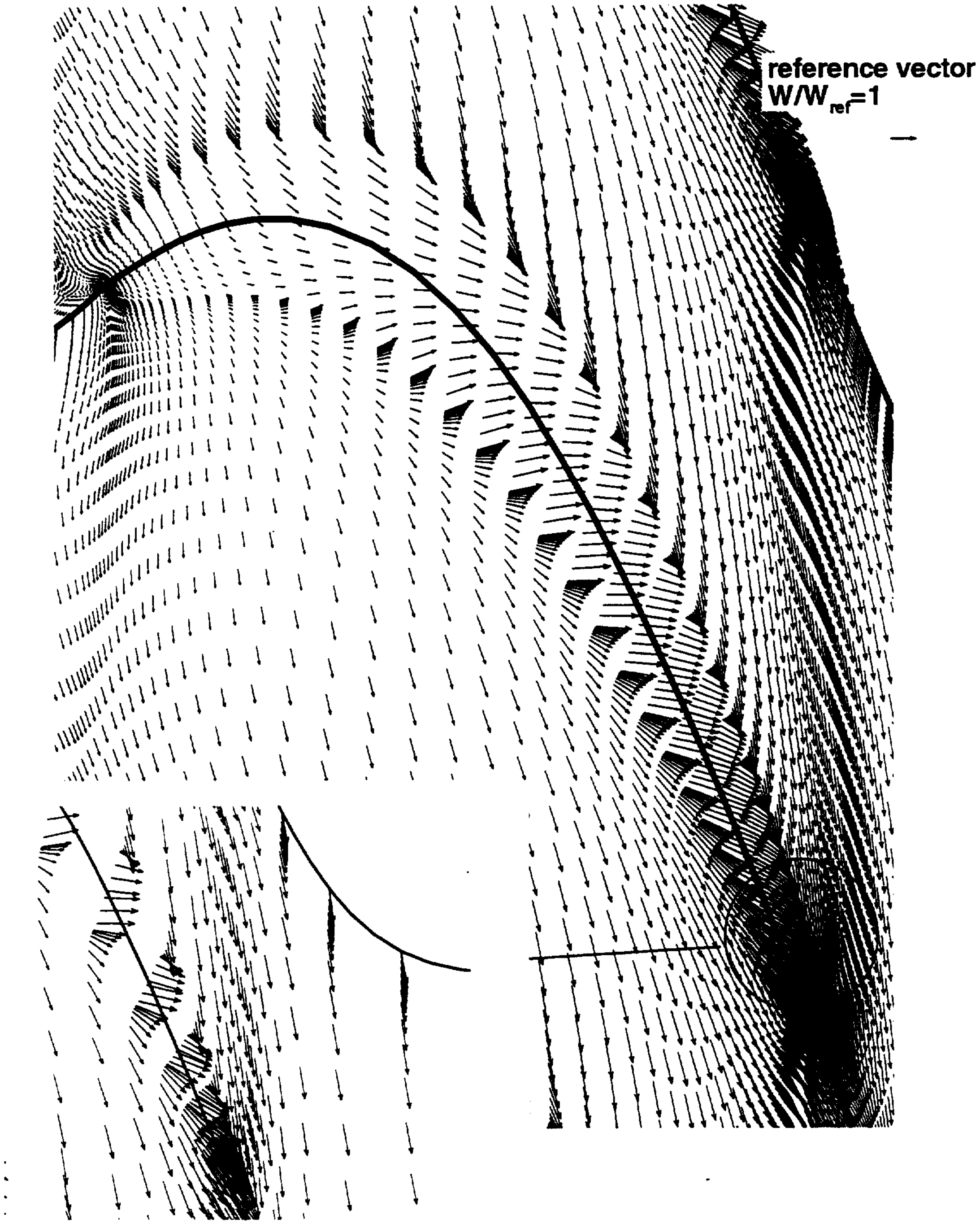

Fig. 8-13 Velocity field at Z_g=0.75

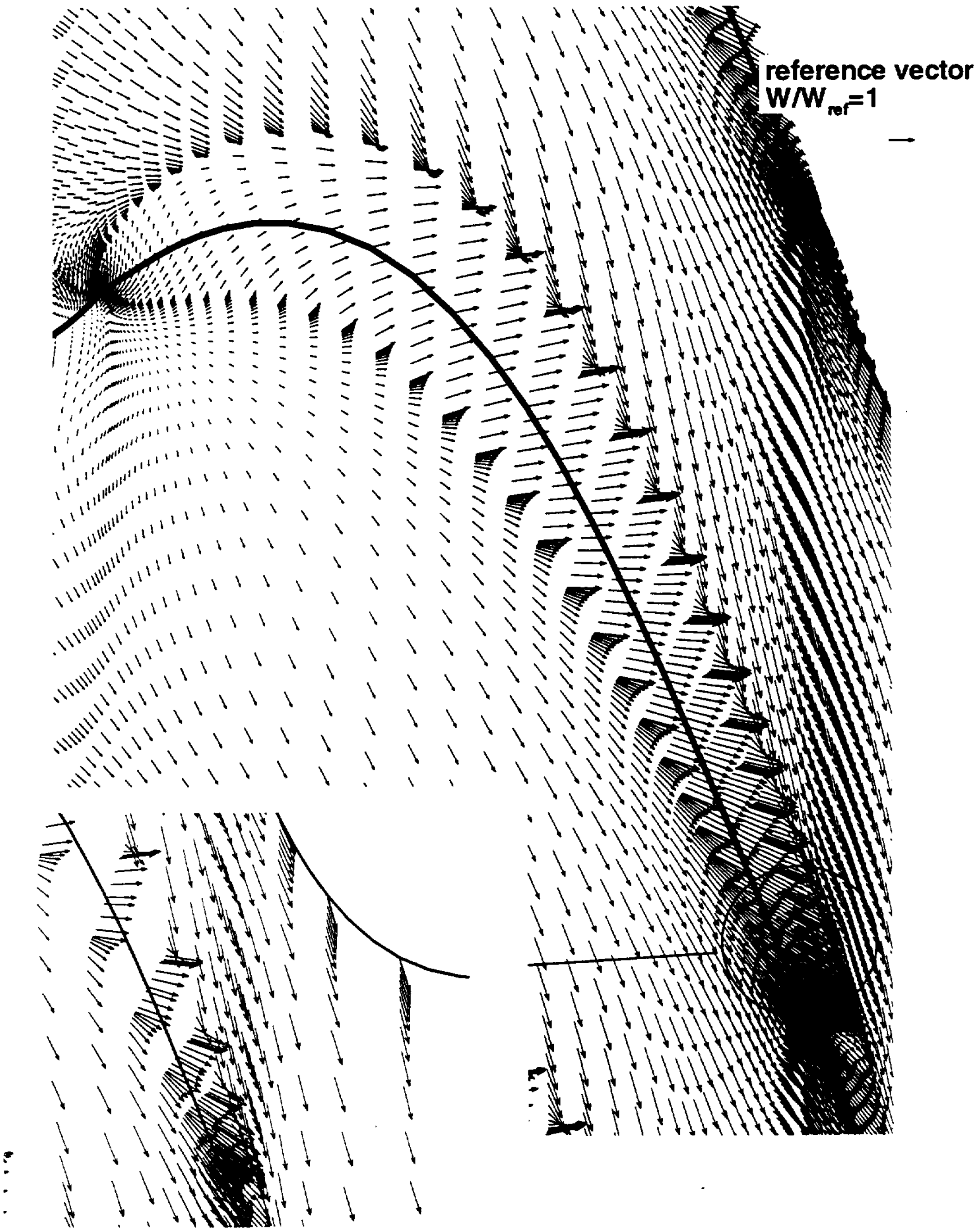

Fig. 8-14 Velocity field at Z_g=0.33

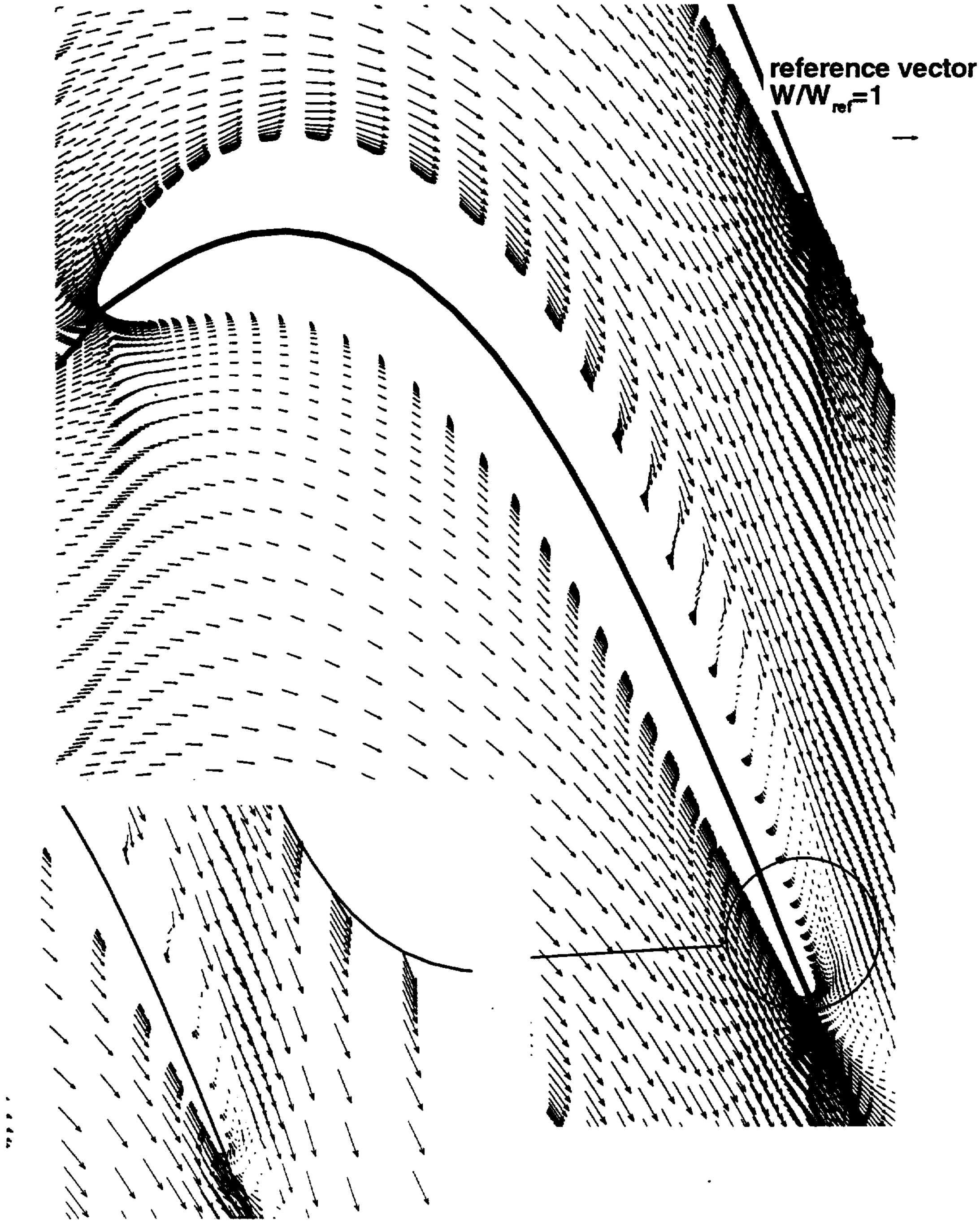

Fig. 8-15 Velocity field at Z_g=-10

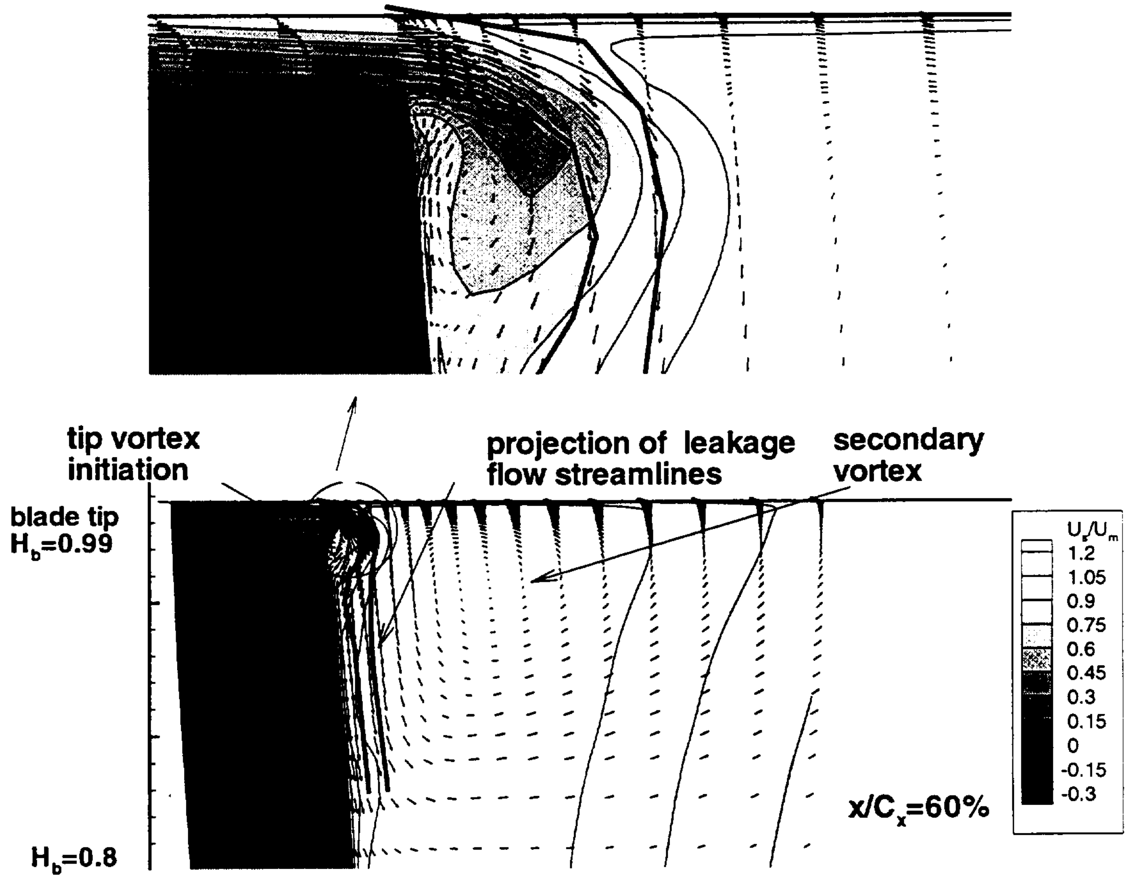

Fig. 8-16a Secondary velocity (calculated as velocity vector consisting of normal to the 2d design streamlines component and radial component), background contours - streamline velocity

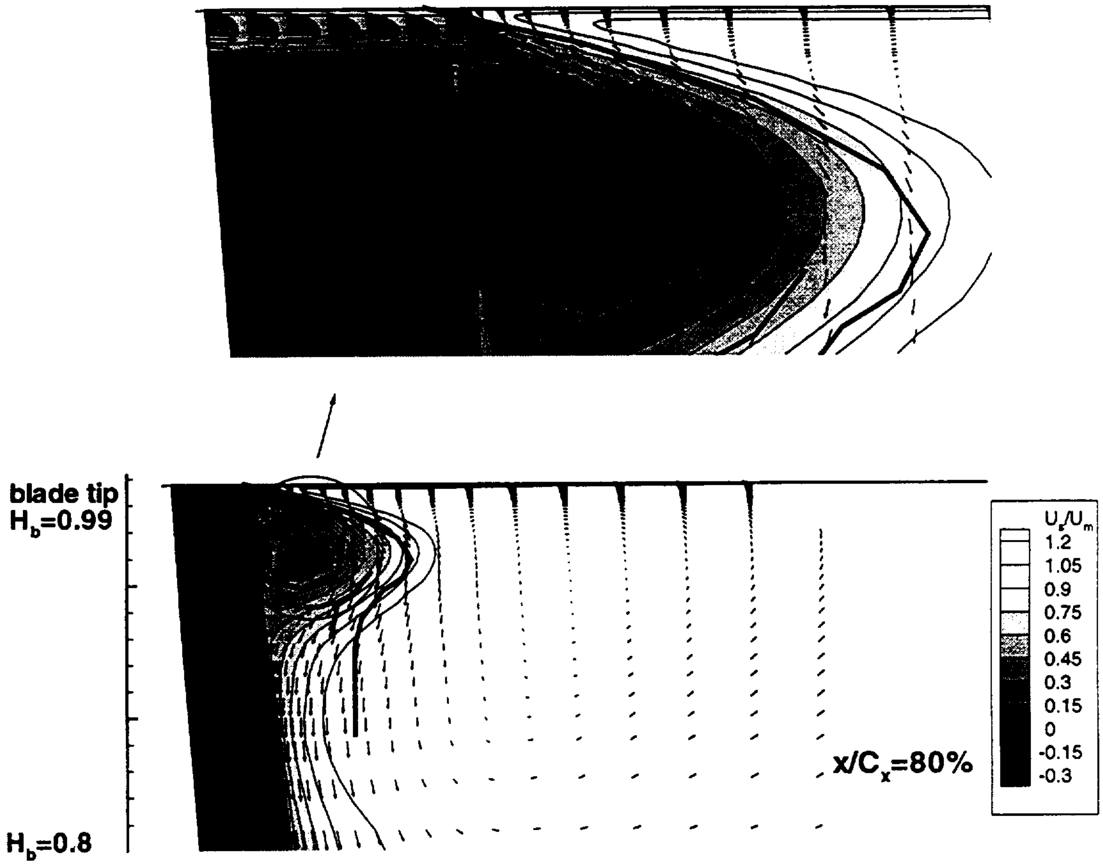

Fig. 8-16b Secondary velocity, background contours - streamline velocity

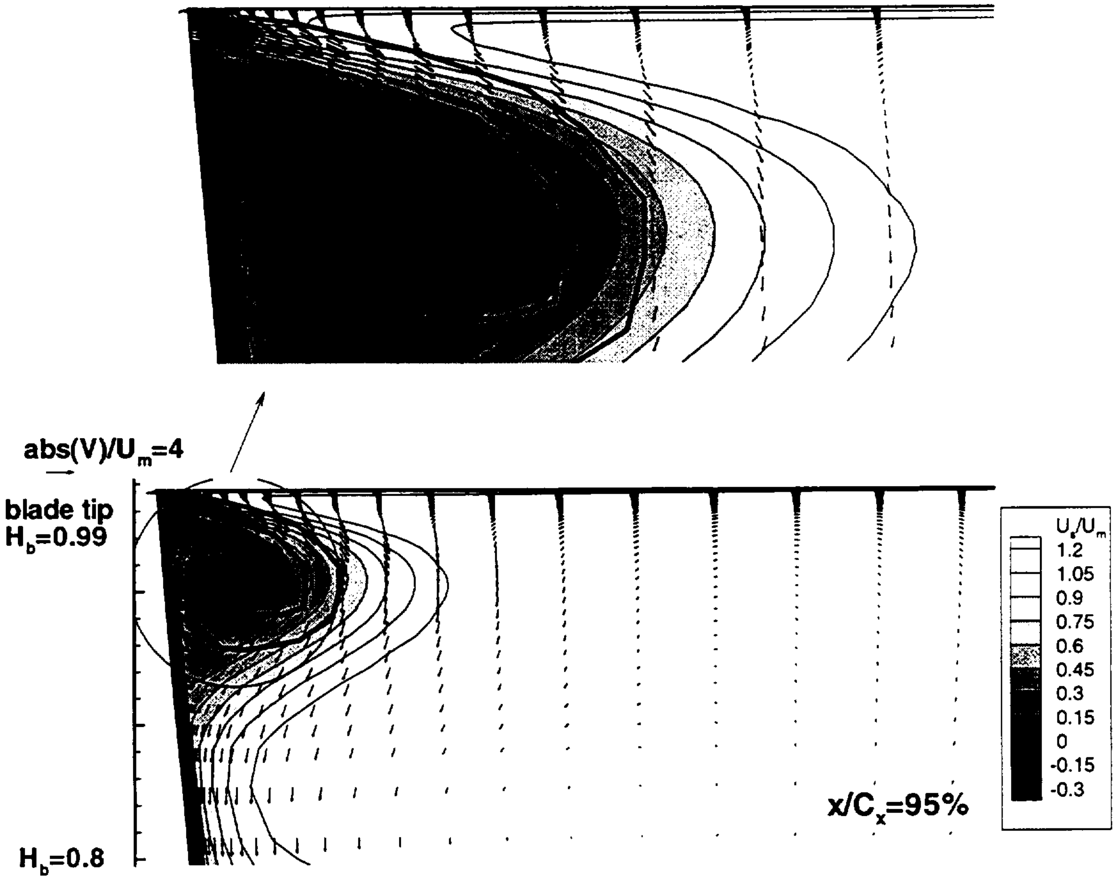

Fig. 8-16c Secondary velocity, background contours - streamline velocity

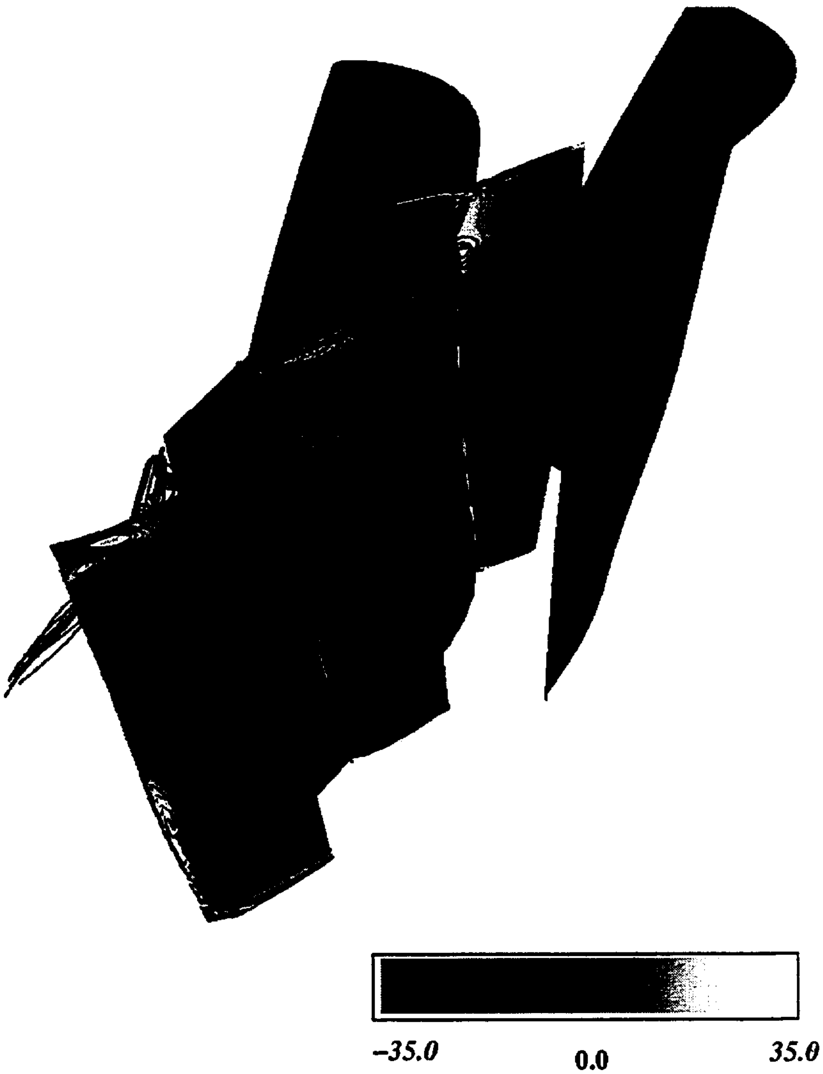

Fig. 8-17 Normalized streamline vorticity ($\omega_s/2\omega$), crossflow planes are located at x/C_x=60%, x/C_x=80%, and x/C_x=110%, streamlines are initiated at the location of the tip vortex inception and represent mean flow fluid particles

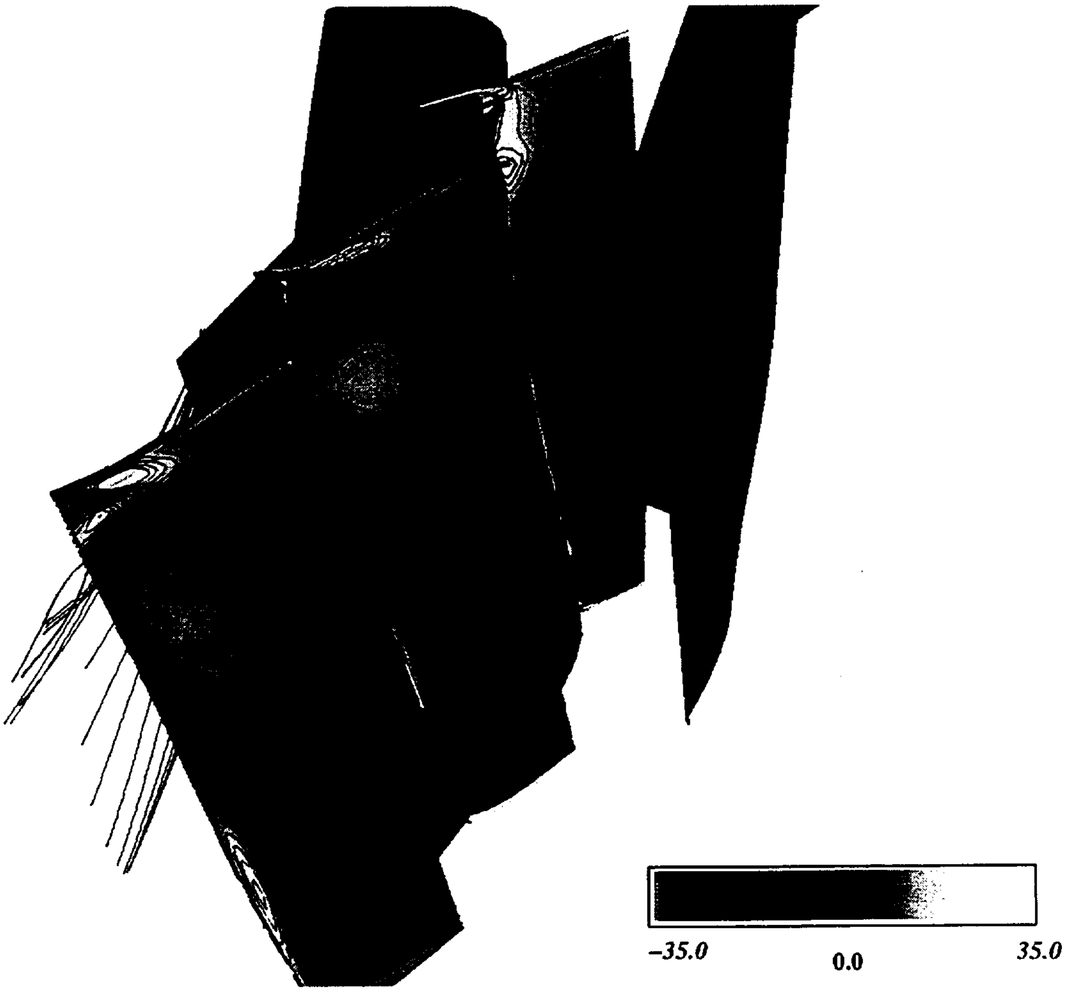

Fig. 8-18 Normalized streamline vorticity ($\omega_s/2\omega$), crossflow planes are located at x/C_x=60%, x/C_x=80%, and x/C_x=110%, streamlines are initiated inside tip gap at 70% and 90% of the chord

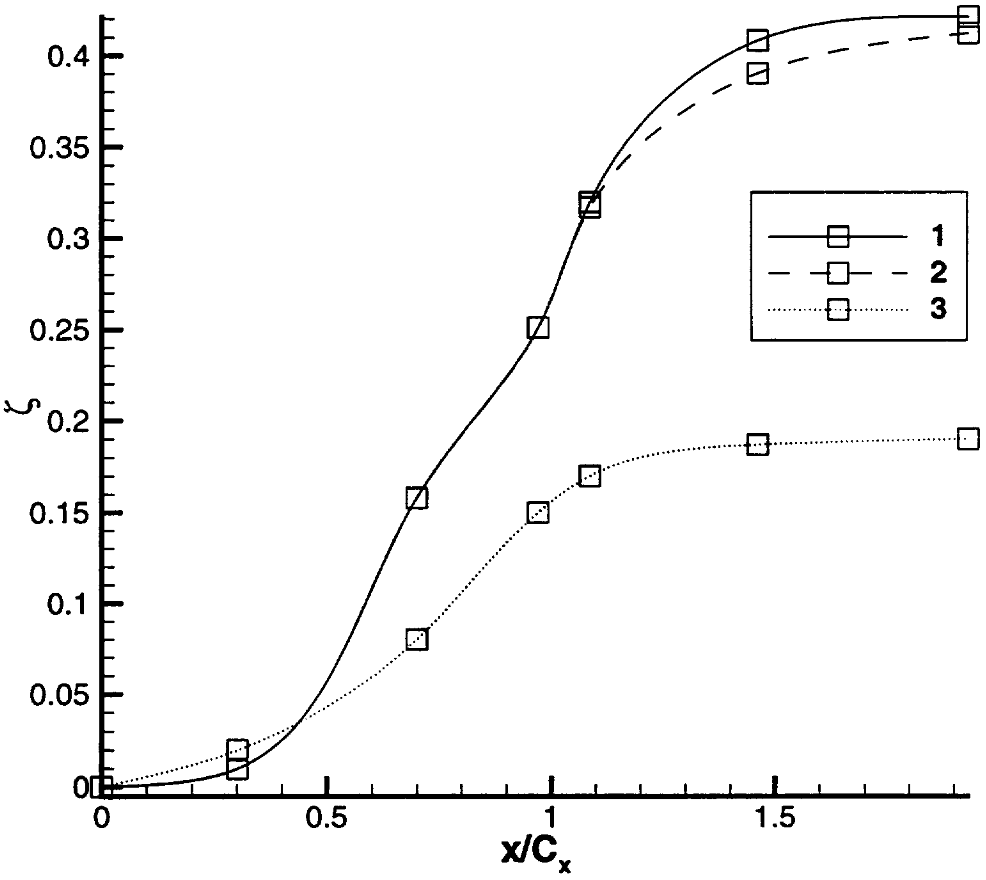

Fig. 8-19 Loss coefficient 1) case with τ_c=1.1%. 2) case with τ_c=0.75%. 3) Two-dimensional simulation

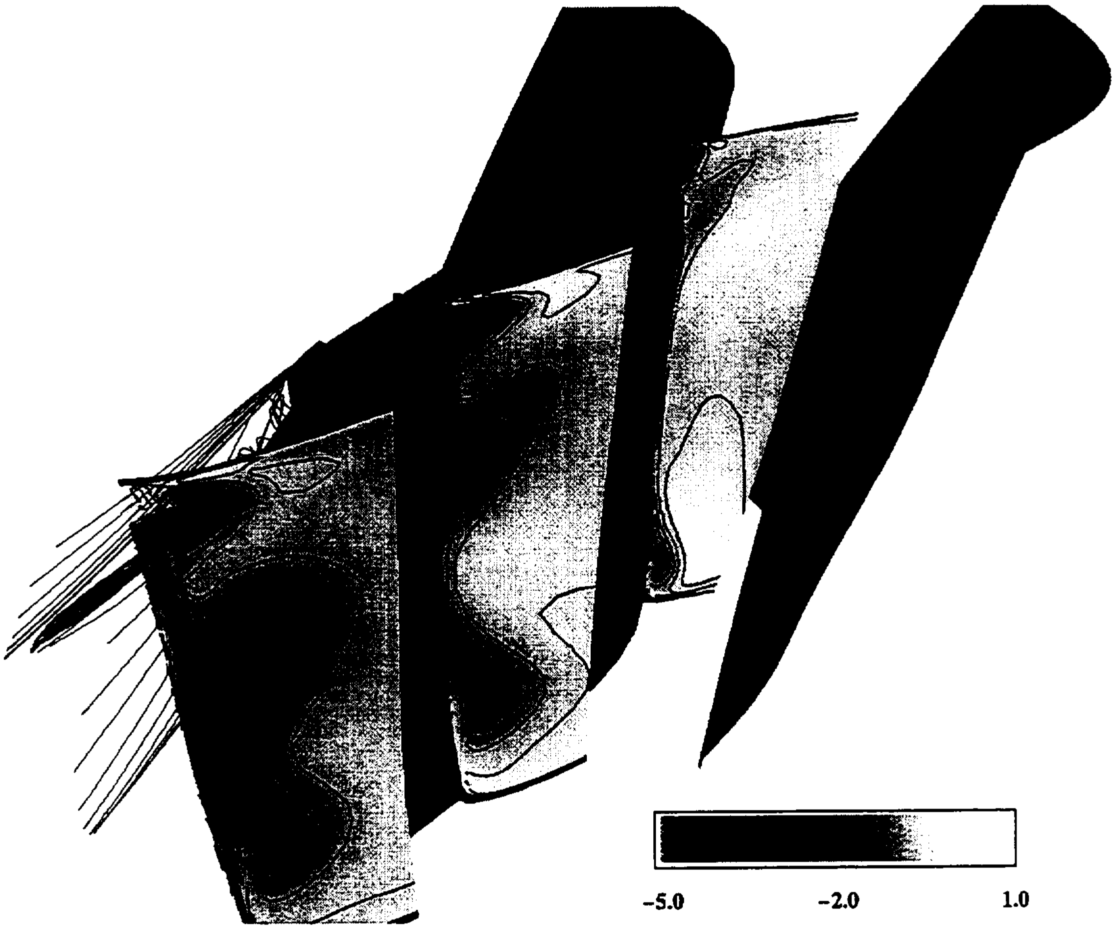

Fig. 8-20 Loss coefficient, ζ

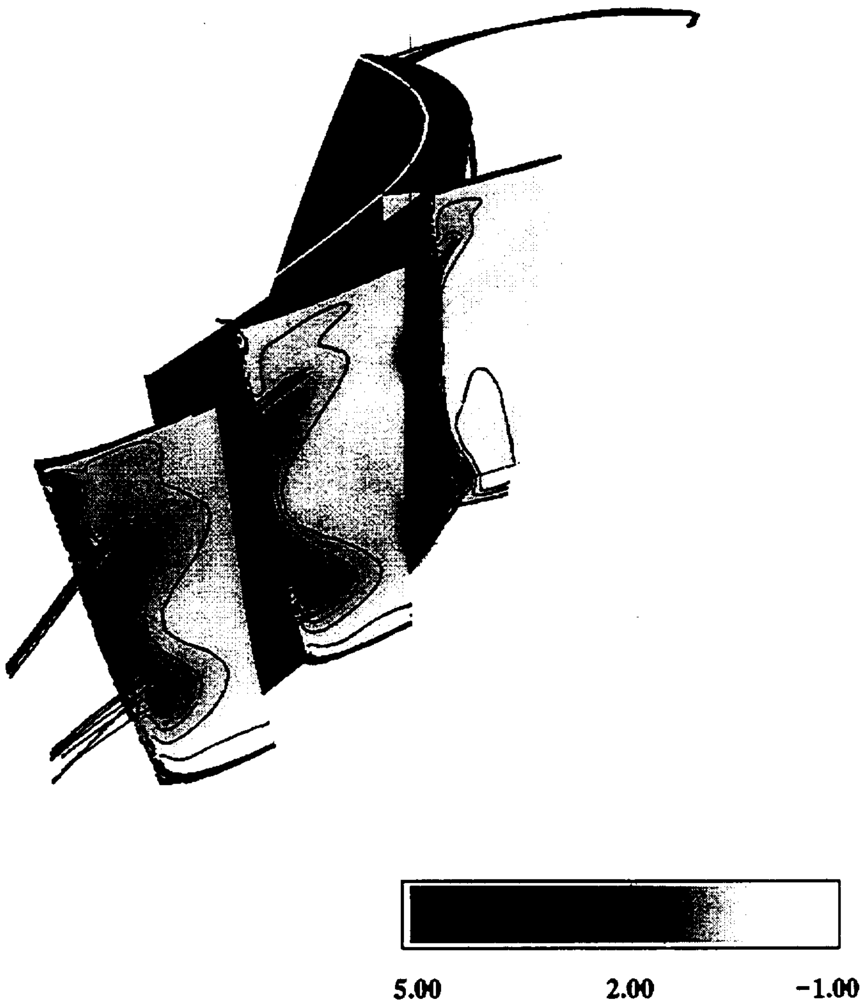

Fig. 8-21 Loss coefficient, ζ, no tip clearance

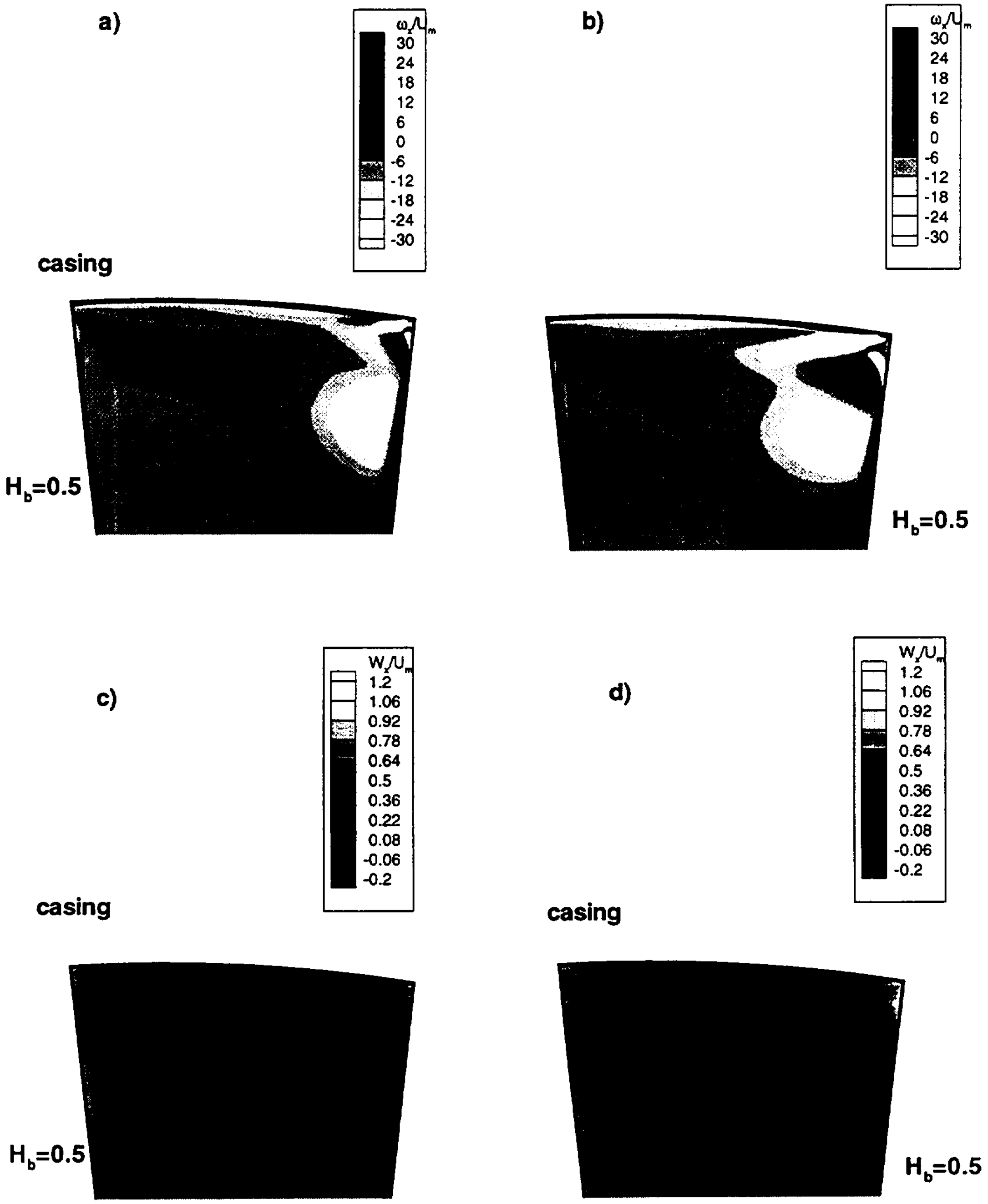

Fig. 8-22 a)-d) Flowfield at x/C_x=110%, influence of tip clearance height a) Normalized vorticity, 0.61% clearance a) Normalized vorticity, 1.1% clearance, c) Normalized axial velocity, 0.61% clearance, d) Normalized axial velocity, 1.1% clearance

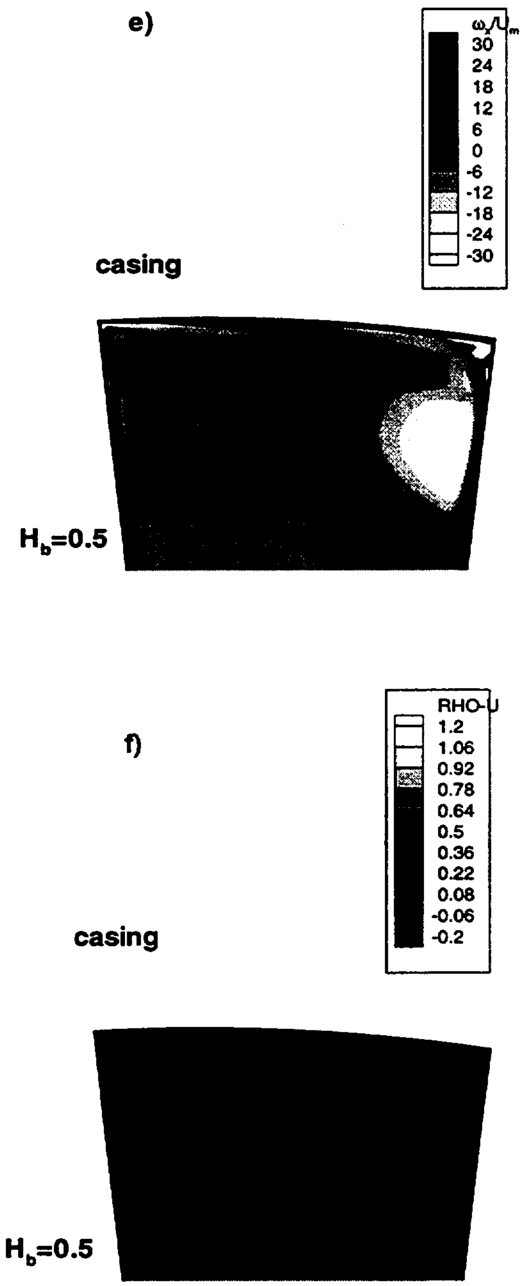

Fig 8-22 e)-f) Flowfield at x/C_x=110%, influence of tip clearance height e) Normalized vorticity, no tip clearance, f) Normalized vorticity, no tip clearance

Chapter 9

SUMMARY

9.1 Summary

A compressible unsteady Navier-Stokes solver has been developed to enable numerical simulation of complex turbomachinery flows. To improve the computational efficiency of the code, a pseudo-time acceleration technique has been employed in the conjunction with the explicit Runge-Kutta scheme. Utilization of the pseudo-time approach leads to the presence of additional source terms, thus affecting both the stability and the convergence characteristics of the original scheme. Von Neuman analysis has been carried out to assess different methods of the pseudo-time stepping implementation. Based on this analysis, a correction to the local time step required for the stable and efficient unsteady calculations has been established. Quality of the grid plays a significant role in the accuracy of the numerical prediction. The ability to use different grid topologies, which are more suitable for the particular flow condition, is beneficial for improved prediction capabilities. It is also helpful in reducing user's effort to generate the grid. The multiblock version of the code has been developed to make the code more flexible and more suitable for the numerical simulation of complex turbomachinery configurations such as multistage rotor-stator interaction, multidomain structure associated with film cooling, tip clearance flow etc.

Results of the numerical simulation based on the hybrid ARSM/ k-ε model depend on the k-ε component of the model, especially in the near wall region. This is especially noticeable in the transitional flows. Low Re number k-ε model based on distance to the wall and wall shear stress was replaced with the k-ε model based on local turbulence characteristic. This modification enables a better prediction of transitional and separated flows. Transition models have been incorporated in the code. This development is aimed at assessment of the numerical simulation of transition based on transition models against the prediction based on original turbulence models.

The numerical solver has been extensively validated against benchmark flows. A number of criteria, required for the accurate numerical simulation, have been established based on the results of the validation. A comparison of the predicted turbulence field with the experimental data indicates that the present solver strongly overpredicts the level of the turbulence intensity in regions with the dominant normal stress. The modification of k-ε model has been performed to reduce the predicted level of the turbulent kinetic energy near the leading edge and away from the blade surface. The Navier-Stokes procedure has been used to investigate the unsteady flow in turbine and compressor cascades. The nature of the upstream wake propagation through the stage, and its interaction with the blade passage flow have been analyzed. The contribution of various components (potential interaction, viscous dissipation, inviscid stretching) into the overall wake decay has been discussed. The assessment of low turbulence models for their ability to predict the development of the unsteady transitional boundary layer has been carried out.

Numerical modeling of the transition over a laminar separation bubble has been chosen to assess the ability of the numerical solver based on different turbulence models to accurately predict the complex flow phenomena associated with the flow in a LP turbine.

Finally, two cases of the flow with the complex vortex structure have been simulated. Numerical simulations of the leading edge film cooling and the tip vortex flow are aimed at a better understanding of the complex vortex flow caused by jet-mainstream interaction. Results of the numerical investigation are used to derive a better understanding of flow physics. Vortex structure is analyzed to identify sources of the aerodynamic losses and degradation in the heat transfer efficiency

9.2 Conclusions

Incorporation of the pseudo time stepping enables a significant improvement in the code performance. Required CPU time is from 5 to 25 times less than the CPU time required for the basic code, depending on the case. Utilization of the pseudo-time stepping is especially beneficial for the simulation of wake-blade row interaction. Navier-Stokes simulation requires only two-to-three times more CPU time in comparison with the Euler simulation, if the surface pressure distribution is of primary concern. Thus, the Navier-Stokes solver can be used as a replacement for the Euler code in a coupled Euler/boundary layer procedure. This will combine the efficiency and the accuracy of the unsteady boundary layer code with the ability of the Navier-Stokes code to predict accurate pressure distribution, upstream wake decay and the off-design and separated flow. The required CPU time in this case is about three times as much as the CPU time required for the original Euler/boundary layer solver.

The main result from the validation process is the establishment of the acceptable level of the artificial dissipation coefficient for accurate and stable solution. To provide an accurate flow simulation k_4 should be in a range from 0.005 to 0.015. This value of k_4 (the forth-order dissipation coefficient) is also adequate to provide the numerical prediction of the transition flow which is independent of the artificial dissipation. To obtain an accurate simulation of the upstream wake propagation through the turbomachinery stage, the grid should have at least twenty grid points per wave. However, this requirement can be moderately relaxed for high harmonics of the narrow wake (i.e., near wake). Rapid physical decay results in faster decay higher harmonics of the wake upstream of the leading edge. Thus the effect of artificial dissipation is not significant.

The modification of the k-ε model to eliminate overprediction of the turbulent kinetic energy near the leading edge and away from the blade surface is essential for accurate numerical simulation of transitional flows.

9.2.1 Unsteady transitional flow in compressor cascade

The ability of the Navier-Stokes code to predict the unsteady transitional flow on a turbomachinery blade is assesed. The unsteady pressure and velocity fields are in good agreement with the experimental data and the prediction from the Euler/boundary layer approach. The numerical solver is able to capture major zones (wake induced transitional strip, wake induced turbulent strip etc.) associated with the wake induced transition in a compressor cascade.

Another significant step is the assessment of k-ε turbulence models, including leading edge modifications. Best results are obtained using FLB model. The LB model predicts earlier inception of the transition and shorter transition length. Modification of the k-ε model is found to be essential for the accurate prediction of the unsteady transitional flow in the compressor cascade. The CH model fails to predict the unsteady transitional flow. The predicted boundary layer is turbulent from the leading edge, even with the modification of the k-ε model near the stagnation point.

The predicted momentum thickness reveals excellent agreement with the experimental data and the Euler/boundary layer prediction. Similar to the boundary layer solution, Navier-Stokes solver predicts higher level of time-average momentum thickness in comparison with the steady state solution. This is an indication of an increased loss due to the unsteady interaction

Interaction between the upstream wake and the stator wake results in shedding of unsteady vortices from the trailing edge and increased dissipation in the stator wake and, as a consequence, increased rate of decay of the stator wake.

9.2.2 Rotor-stator interaction in turbine stage

Comparison of the predicted unsteady flow filed with the LDV data and dynamic pressure measurements indicates that the predicted velocity and pressure fields in a turbine stage are in good agreement with the experimental data at the design and the off-design conditions. The measured unresolved unsteadiness and the predicted turbulence intensity show that the peak intensities are predicted reasonably well, but the wake width based on the unsteadiness shows that the computation has a larger diffusion (into the freestream) compared with the experimental data

The pressure gust has the most influence near the leading edge. Its influence in the development of the unsteady flow-field is limited to 15% of the blade chord from the leading edge. Beyond this, the wake-blade interaction through the development of the counter-rotating vortices in the blade passage, is the source of unsteadiness. The maximum variation in the unsteady pressure was observed at x/Cx = 0.28 on the suction surface.

Up to 15% of the chord, the viscous dissipation is responsible for 45% to 75% of the wake decay. Further downstream, the wake undergoes both the inviscid decay and the amplification inside the passage. The contribution of viscous dissipation is equal to 75% of the total decay and 58% of the decay in the passage. Most of additional losses due to unsteady flow occur upstream of the leading edge (~55%). Inside the blade passage, the nozzle wake mixing losses are small in comparison with blade profile losses. Increase in profile losses is attributed to the modification of the suction surface boundary layer due to the nozzle wake-blade interaction.

The numerical solver was able to predict most of the features associated with the wake induced unsteady transition (wake induced transitional strip, turbulent strip, etc.). Even though the k-ε model lacks physics of the bypass transition, the predicted development of various zones follows the trend observed in the experiment. The major exception is the calmed region. The predicted region downstream of the wake induced transitional strip possesses some characteristics of the calmed region. However, this region can not be identified as a calmed region because it lacks other essential features of the calmed region, such as propogation of the zone trailing edge at $0.3W_{\delta}$.

The nozzle wake interaction with the rotor wake leads to an increased unsteadiness observed in both the experiment and the prediction. The suction side segment of the nozzle wake merges with the rotor wake, causing fluctuations in the rotor wake. The phase lag between the suction side segment and the pressure side segment of the nozzle wake gives rise to fluctuation in the rotor wake at double the nozzle wake frequency, but with a significantly smaller amplitude.

There is a significant change in the overall flow pattern at the off-design condition. Due to an increased reduced frequency, there are more nozzle wake segments in the rotor passage in comparison with the design case. Another significant factor is the development of a strong separation bubble on the pressure surface within 15% of the chord near the leading edge. The interaction between the nozzle wake and the separation bubble results in amplified unsteady pressure on the pressure surface. Predicted unsteady velocity indicates that the nozzle wake-separation bubble interaction generates a vortex pattern in the separation zone, thus increasing unsteadiness in this zone.

9.2.3 Transition to turbulence over laminar separation bubble in LP turbine

A numerical simulation of the flow in a low-pressure turbine was carried out to assess the ability of different turbulence models to predict transitional flow at different Re and turbulence levels. Best results have been obtained with the FLB model (without the transition model). Implementation of the hybrid k-ε/ARSM improves the prediction for Re = 50,000, Tu = 2.5%. While having minimum impact in all other cases, this modification contributed to the redistribution of the turbulent kinetic energy between various components in the transition region.

Utilization of the transition model does not result in an improved flow simulation. Analysis of the turbulence characteristics in the transition zone shows that the lack of improvement is due to interference between the transition model and the low Re turbulence model. In the current prediction, the transition inception from the "pure" k-ε model is located only about 2% of the chord upstream of the measured location. An enforcement of the transition through the intermittency function leads to a double damping of turbulence in the transition zone.

A number of factors have been found to be essential for an accurate prediction of the transition. The first factor is the need to limit the turbulence production near the leading edge to ensure an accurate development of the laminar boundary layer. Implementation of the fourth-order artificial dissipation in k-ε equations, without modification for the leading edge flow, may lead to the development of the pseudo-turbulent boundary layer. The solver with a mixed second/fourth-order artificial dissipation is less sensitive to this problem due to its ability to avoid an immediate transition inception near the leading edge at high levels of turbulence intensity. A second factor is the need to modify the freestream turbulence equation. This problem, as well as the first one, is due to the poor performance of a standard k-ε model in the case of strong normal stresses. Without the adjustment of the freestream turbulence, the turbulence intensity may be over-predicted by 2-3%. The elevated level of the turbulent kinetic energy may affect the transition inception prediction.

The establishment of the reliability range for the numerical solver is needed for its wider acceptance for the design problems. Even though grid independency has been verified through the numerical modeling, a further analysis shows that the predicted transition location is affected by the level of artificial dissipation. For small values of k_{2ke}, the variation of the artificial dissipation acts as a disturbance (i.e., affecting the transition inception without diffusing k in the transition zone). This makes the assessment of the reliability of the prediction more complex. In addition to grid and turbulence model characteristics, the numerical scheme (i.e., form of differential approximation) and numerical details (e.g., the way the realizability of k is ensured) do contribute to the variation in the transition prediction. For the current solver, the potential error associated with this phenomenon can be estimated to be 2% of the chord for the location of inception of transition. For the attached flow, the level of accuracy achieved can be considered as acceptable even without utilization of the transition model. To ensure a reliable prediction of the separated flow cases, this level should be improved because even a moderate variation in the predicted transition inception results in a significant variation of the separation bubble.

9.2.4 Leading edge film cooling

The numerical investigation indicates that the CFD analysis can be successfully employed for the prediction, simulation, and parametric study of the complex flows associated with the leading edge film cooling. However, great care should be exercised in the quality of the grid, the accuracy of inlet conditions, and the selection of the turbulence model.

The analysis of the aerothermal field due to a compound angle leading edge film cooling indicates the presence of complex vortex structure much different from that observed for a flat plate. Interaction between the upper coolant jet and the mainflow generates four major vortices, pair of core vortices and pair of outer vortices. These vortices originate respectively from the interaction of the mainflow with the coolant flow emanating from the right lateral side, core, left lateral side, and the upper side of the hole. The outer vortices decay rapidly. Core vortices are major contributors to the aerodynamic losses and for a decrease in the adiabatic effectiveness through the entrainment of the hot fluid.

Following conclusions can be made:

1) The compound angle injection and the resulting large and differing flow angles of the jet and the mainstream result in large velocity gradient and a "jet-wake"

structure, leading to intense mixing. Large crossflow development results in the lifting of the jets and movement of hot spots away from the wall.

2) Numerical simulation at a higher inlet Mach number shows only a small decrease in the cooling effectiveness due to the compressibility and modified pressure gradient effects.

3) High turbulence intensity leads to a decrease in the cooling effectiveness near the stagnation surface. The development of the flow above the second row of holes at the high turbulence level is controlled by two opposing trends; increased turbulence dissipation and modification of the vortex structure leading to a decrease in the hot fluid entrainment. The freestream turbulent length scale has a significant effect on the balance between these two phenomenon.

4) The predicted cooling effectiveness and the flow-field are very sensitive to the inlet turbulent length scale. Increased length scale results in decreased effectiveness and faster decay of the vortices. Specification of the correct turbulence dissipation ratio or the length scale is one of the crucial elements for an accurate prediction of the leading edge film cooling effects.

A more accurate prediction of the film cooling effects may be achieved through an improved turbulence model. The incorporation of the higher order anisotropic turbulence model and the modification of the constant turbulent Prandtl number assumption may improve the accuracy of the vortex simulation. Additional investigations should be carried out to assess the influence of the curvature effect on this type of flow.

9.2.5 Secondary flow in turbine including tip leakage flow

Development of the tip leakage flow is characterized by significant velocity and pressure gradients that exist in the tip gap and its vicinity. According to the result of the grid refinement analysis, it is essential to have at least 15 grid points within the gap for an adequate numerical resolution of the flow. The sudden contraction of the flow generates a low-pressure zone below the blade tip on the pressure surface. Therefore, grid also should be highly clustered at least two tip gap heights below the blade tip.

There is a good correlation between the predicted and the measured blade pressure distribution. The comparison between the predicted flow-field and the LDV data also reveals good correlation downstream of the trailing edge. However, the numerical prediction indicates an earlier development of the tip leakage vortex. Pitchwise width of the tip leakage vortex is smaller in comparison with the experiment. These discrepancies can be attributed to the limitation of the physical model, especially to the steady state approximation and isotropic nature of the turbulent model.

Development of the leakage flow in the rotor significantly differs from that observed in a cascade. Relative motion of the blade and casing blocks the development of the tip leakage flow. Massflow through the tip gap reaches its maximum at 85% of the chord. Leakage flow leaving the tip clearance is only partially rolled up into the tip leakage vortex. At 50% of the chord, all the leakage flow mixes with the mainflow as a "plain" jet, while at 93% all leakage flow leaving the gap is entrained by the vortex. Tip vortex starts at around 50% of the chord as a radial separation zone on the suction surface. It immediately moves away from the blade surface and grows steadily until the trailing edge. The core of the tip leakage vortex mostly consists of the mainflow fluid entrained at the vortex inception up to the 90% of the blade. In the case of the intense tip leakage vortex growth, a zone of reverse flow develops in the core of the tip leakage vortex, increasing the flow blockage due to the tip leakage flow.

A comparison between the three-dimensional prediction, and two-dimensional prediction of pitchwise mass average loss coefficient shows that the secondary and leakage flow losses are responsible for about 50% of total losses. The prediction shows a relatively small contribution of the tip leakage flow (less then 30% of the additional losses). This can be attributed to the relatively small clearance (less then 1% of the blade span) in Penn State rotor. Most of the losses due to the tip leakage flow occur downstream of the trailing edge through the tip vortex mixing.

A smaller tip clearance results in decreased leakage flow. It also leads to an increased percentage of the tip leakage fluid entrained by the tip leakage vortex. Therefore, the decrease in losses is less prominent, because of higher losses associated with the flow entrined by the tip leakage vortex.

9.3 Recommendations for the future work.

Reliable prediction of the calmed region can be beneficial for the improved blade design, especially potential improvement in stage weight characteristics. Even though the accuracy of the unsteady transition flow prediction is comparable with the steady transition prediction, some essential features of the calmed region are not captured. This includes such characteristics as the propagation velocity of the calmed region near the trailing edge. Improved turbulence modeling is needed in order to get better resolution of the wake induced transition.

The numerical prediction of the separated flow in LP turbine is very sensitive to the accuracy of the transition inception. Small error in the predicted location results in considerably modified height and extent of the separation bubble. Further analysis is required to ensure a more stable and reliable simulation. Numerical solver should be modified to eliminate the dependency of the predicted transition on the numerical realization.

Complex vortex structure due to the film cooling is known to possess non-isotropic turbulence nature. The ratio of eddy viscosity coefficients in streamwise and spanwise directions are significantly different from unity. This ratio can be as high as 20. Additional research is required to explore the effect of non-isotropy in turbulence on the accuracy of the vortex flow simulations.

Present compressible numerical solver was successfully employed for the flow simulation with relatively low flow Mach number. However, code utilization for calculations of three dimensional, low speed flow results in code computational efficiency degradation, especially for cases with significant variations in the total energy distribution. An incorporation of the preconditioning may be beneficial for computationally more efficient modeling of low Mach flows.

Appendix A

LINEARIZED SOLUTION OF THE WAVE PROPAGATION

Let us consider sinus wave propagation:

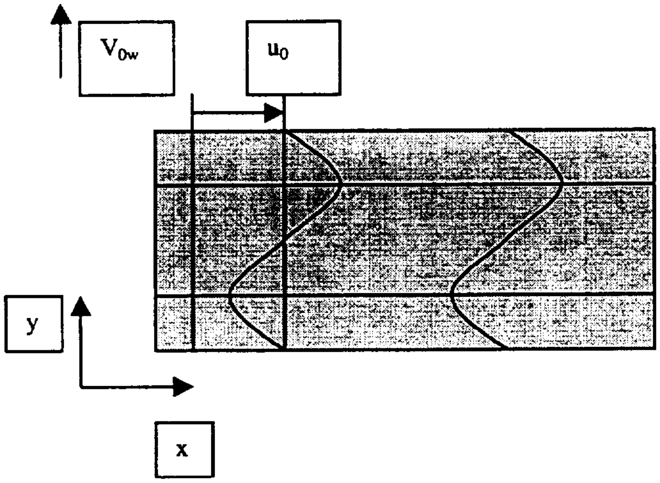

Governing laminar incompressible equations can be written:

$$\begin{cases} \frac{\partial u}{\partial t}+u\frac{\partial u}{\partial x}+v\frac{\partial u}{\partial y}=\nu(\frac{\partial^2 u}{\partial x^2}+\frac{\partial^2 u}{\partial y^2})+D_x \\ \frac{\partial v}{\partial t}+u\frac{\partial v}{\partial x}+v\frac{\partial v}{\partial y}=\nu(\frac{\partial^2 v}{\partial x^2}+\frac{\partial^2 v}{\partial y^2})+D_y \end{cases}$$

[A-1]

Artificial dissipation (assuming isotropic dissipation) is given by

$$D=\begin{cases} k_4(\frac{1}{\Delta t}\frac{\partial^4 u}{\partial x^4}(\Delta x)^4+\frac{1}{\Delta t}\frac{\partial^4 u}{\partial y^4}(\Delta y)^4) \\ k_4(\frac{1}{\Delta t}\frac{\partial^4 v}{\partial x^4}(\Delta x)^4+\frac{1}{\Delta t}\frac{\partial^4 v}{\partial y^4}(\Delta y)^4) \end{cases}$$

[A-2]

where u and v are x and y components of the total velocity.

Solution for the eq. [A-1] can be found in the form:

$$u = u_0(1 + A(x)\cos(2\pi\varpi(y - V_{0w}t))$$

$$v = V_{0w} - u_0\frac{\partial A(x)}{\partial x}\frac{1}{2\pi\varpi}\cos(2\pi\varpi(y - V_{0w}t) \qquad [\text{ A-3}]$$

Solution for A(x) can be obtained by the substitution of [A-3] into [A-1],

In this case equation for the x-component can be rewritten as:

$$u^2{}_0\frac{\partial A(x)}{\partial x}\cos(\cdot) =$$

$$\upsilon_{\text{eff}}(u_0\frac{\partial^2 A(x)}{\partial x^2}\cos(\cdot) + (2\pi\varpi)^2 A(x)(-\cos(\cdot)) - \frac{k_4\Delta x^4}{\Delta t}(u_0\frac{\partial^4 A(x)}{\partial x^4}\cos(\cdot) + (2\pi\varpi)^4 A(x)(\cos(\cdot))$$

[A-4]

where (•)=(y-V_{0w}t)

Linearization assumption, A(x) <<1, has been used to derive this expression.

Cell aspect ratio is assumed equal to unity, i.e., $\Delta x \sim \Delta y$

Equation [A-4] can be non-dimensionalised using wave length : $\breve{x} = x/l$, where l - is length of the wave.

$$\frac{\partial A(\breve{x})}{\partial \breve{x}} =$$

$$\frac{1}{\text{Re}_w}(\frac{\partial^2 A(\breve{x})}{\partial \breve{x}^2} + (2\pi\varpi)^2 A(\breve{x})) - \frac{k_4\Delta\breve{x}^4}{\Delta t u_0 l^3}(u_0\frac{\partial^4 A(\breve{x})}{\partial \breve{x}^4} + (2\pi\varpi)^4 A(\breve{x}))$$

[A-5]

Where Re_w is Reynolds number based on the wave length.

If CFL = 1 then

$$\frac{k_4\Delta x^4}{\Delta t u_0 l^3} = k_4\frac{\Delta x^3}{l^3}\frac{\Delta x}{\Delta t u_0} = k_4\frac{\Delta x^3}{l^3}\frac{1}{CFL} = k_4 n^3\frac{1}{CFL}$$

[A-6]

where n is the number of grid points per wave length.

Making additional assumptions

$$\frac{\partial^2 A(\breve{x})}{\partial x^2} << (2\pi\varpi)^2 A(\breve{x})$$

$$\frac{\partial^4 A(\breve{x})}{\partial x^4} << (2\pi\varpi)^4 A(\breve{x})$$

This assumption is based on the dominance of the crossflow component of the dissipation over a streamline one.

Then, solution for [A-5] can be written as:

$$A(\breve{x}) = A_0 \exp[(-2\pi\varpi)^2 (\frac{1}{\mathrm{Re}_w} + k_4 \frac{(2\pi\varpi)^2}{n^3})\breve{x}]$$

For the freestream wave/wake propagation, discussed in chapter 3, u and v are the functions of $(y-V_{0w}t+V_{0w}/u_0x)$. This problem may be reduced to the problem considered above using coordinate transformation : $\xi = y - V_{0_w} x$

BIBLIOGRAPHY

Abhari, R.S., and Epstein, A.H., 1994, "An Experimental Study of Film Cooling in Rotating Transonic Turbine," *Journal of Turbomachinery*, Vol. 116, pp. 63-70.

Abid, R., and Rumsey, C., and Gatski, T., 1995, "Prediction of Non-Equilibrium Turbulent Flows with Explicit ARSM," *AIAA Journal*, Vol.33, No.11.

Abu-Ghannam, B. J., and Shaw, R., 1980, "Natural Transition of Boundary Layers- The Effects of Turbulence, Pressure Gradient and Flow History," *Journal of Mechanical Engineering Science*, Vol. 22, No. 5, pp. 213 - 228.

Adamczyk, J.J., and Mulac, R. A., and Celestina, M. L., 1986, "A Model for Closing the Inviscid Form of the Average-Passage Equation System," ASME Paper 86-GT-227, pp. 1-9.

Alonso, J. J., and Jameson, A., 1994, "Fully-Implicit Time-Marching Aeroelastic Solutions," AIAA Paper 94-0056, pp.1-13.

Arndt, N., 1993, "Blade Row Interaction in a Multistage Low Pressure Turbine," *Journal of Turbomachinery*, vol. 115, p. 137.

Arnone, A. and Pacciani, R., and Sestini, A., 1994, "Multigrid Computations of Unsteady Rotor-Stator Interaction Using the Navier-Stokes Equations," AD-Vol. 40, ASME Winter Annual Meeting, Chicago, pp. 87-95.

Arnone, A., and Liou, M-S., and Povinelli, L.A., 1995, "Integration of Navier-Stokes Equation Using Dual Time Stepping and Multigrid Method," *AIAA Journal*, Vol. 33, No. 6. pp. 985-990.

Bario, F., and Beral, C., 1996, "Cooling Jet and Boundary Layer Interaction on the Suction Surface of a Turbine Inlet Guide Vane.", 3rd International Symposium on Aerothermodynamics of Internal Flows, Beijing, China, Sept 1-6, pp 615-621.

Behnia, M., Parneix, S., and Durbin, P., 1996, "Simulation of Jet Impingement heat transfer with the k-ε-v^2 Model", Center for Turbulence Research. Annual Research Briefs, pp 3-16.

Bergeles, G., and Gosman, A.D., and Launder, B.E., 1977, " The Near-Field Character of Jet Discharged Through a Wall at 30° to Mainstream," *AIAA Journal*, Vol 14, pp. 499-504.

Bogard, D.G., and Schmidt, D.L., and Tabbita, M., 1996, "Characterization and Laboratory Simulation of Turbine Airfoil Surface Roughness and Associated Heat Transfer," ASME Paper, 96-GT-386, pp. 1-7.

Booth, T.C., 1985, "Importance of Tip Clearance Flows in Turbine Design," VKI Lecture Series 1985-05, "Tip Clearance Effects in Axial Turbomachines".

Busby J.A., Davis, R.L., Dorney D.J., Dunn M.G., Haldeman C.W, Abhari R.S., Venable, B.L., Delaney R.A., 1998, "Influence of Vane Blade Spacing on Transonic Turbine Stage Aerodynamics, " Part 2: Time Resolved Data and Analysis," ASME Paper 98-GT-482.

Chevray, R., and Kovasznay, L. S. G., 1969, "Turbulence Measurements in the Wake of a Thin Flat Plate," *AIAA Journal*, Vol. 7, No. 8, pp. 1641 - 1643.

Chien, K-Y., 1982, "Predictions of Channel and boundary-Layer Flows With a Low-Reynolds-Number Turbulence Model," *AIAA Journal*, Vol. 20, No. 1, pp. 33- 38.

Cooper, D., Jackson, D.C., Launder, B.E., and Liao, G.X., 1993, "Impinging Jet Studies for Turbulence Model Assessment", Part I: "Flow-Field Experiments", *Int. Journal Heat Mass Transfer,* Vol.36, No. 10, pp. 2675-2689.

Craft, T.J., Graham, L.J.W., and Launder, B.E., "Impinging Jet Studies for Turbulence Model Assessment", Part II: "An Examination of the Performance of Four Turbulent Models," *Int. Journal Heat Mass Transfer*, Vol.36, No. 10, pp. 2675-2689.

Craward, M.E., and Kays, W.H., and Moffat, R.J., 1980, "Full-Coverage Film cooling; Part II: Heat Transfer Data and Numerical Simulation", ASME *Journal of Engineering for Power* , Vol. 102, pp. 1006 - 1012.

Crumpton, P.I., and Giles, M.B., 1995, "Implicit Time Accurate Solutions On Unstructured Dynamics Grids," AIAA-95-1671-CP, pp. 284 - 293.

Cruse W.M., Yuki, U.M., and Bogard D.G., 1997, "Investigation of Various Parametric Influences on Leading Edge Film Cooling," ASME Paper 97-GT-296.

Dailey, L.D., and Pletcher, R.H., 1995, "Evaluation of Multigrid Acceleration for Preconditioned Time-Accurate Navier-Stokes Algorithms," AIAA Paper 95-1668-CP, pp. 253 -363.

Davis, R.L., Carter, J.E., and Reshotko, E., 1987, "Analysis of Transitional Separation Bubbles on Infinite Swept Wings," *AIAA Journal*, Vol. 25, No 3, March, pp. 421-428.

Dhawan, S., and Narasimha, R., 1958, "Some Properties of Boundary Layer During the Transition from Laminar to Turbulent Flow Motion," *Journal of Fluid Mechanics*, Vol.3, pp.418-436.

Dorney D.J., and Davis, R.L.,1991, " Navier-Stokes Analysis of Turbine Blade Heat Transfer and Performance" AGARD 77th Symposum, CFD Techniques for porpulsion applications, San Antonio, TX, May 27-31, 1991

Dorney, D.J., and Verdon J.M., 1994, "Numerical Simulations of Unsteady Cascade Flows," *Journal of Turbomachinery*, Vol. 116, pp. 665-675.

Dring, R.P., Joslyn H.D., Hardin L.W., and Wagner J.H. ,1982 "Turbine Rotor-Stator Interaction," *Journal of Engineering for Power*, Vol. 104, pp. 729-742, 1982.

Emmons, H.W., 1951, "The Laminar-Turbulent Transition in Boundary Layer, Part 1," *J. of Aero. Sci.*, Vol. 18, pp. 490-498.

Erdos, J.I., and Alzner, E., and McNally, W., 1977, "Numerical Solution of Periodic Transonic Flow through a Fan Stage," AIAA Journal, Vol. 15, No. 11, pp. 1559-1568.

Fabian J.C.,1995, "On the Film Cooling of Turbine Blades", MS Thesis,Graduate School of the Ohio State University,pp. 1-79.

Fan, S., and Lakshminarayana, B., 1994, "Computation and Simulation of Wake-Generated Unsteady Pressure and Boundary Layers in Cascades, Part 2: Simulation of Unsteady Boundary Layer Flow Physics," ASME Paper 94-GT-141, Int. Gas Turbines and Aeroengine Congress and Exposition, The Hague, Netherlands, June 13-16, pp. 1-16.

Fan, S., and Lakshminarayana, B., 1996, " Time Accurate Euler Simulation of Interaction of Nozzle Wake and Secondary Flow in an Axial Turbine Stage Using Non-reflecting Boundary Conditions," *J. of Turbomachinery*, Vol. 118, No. 4, pp. 663-678.

Fan, S., and Lakshminarayana, B., and Barnett, M., 1993, "Low-Reynolds-Number k-ε Model for Unsteady Turbulent Boundary-Layer Flows," *AIAA Journal*, Vol. 31, No. 10, pp. 1777-1784.

Fan, S., and Lakshminarayana, B.,1996 "On the prediction of wake Generated Unsteady pressure and boundary layers in Turbomachinery Cascades," *J. of Turbomachinery* Vol. 118., No1, pp 96-122.

Fourmaux, A., 1994, "Assessment of a Low Storage Technique for multi-stage Turbomachinery Navier-Stokes computations," ASME Winter Annual Meeting, Chicago, AD-Vol. 40, pp. 97-103.

Furukawa, M., Inoue, M., Saiki, K., and Yamada, K., "The Role of Vortex Breakdown in Compressor Rotor Aerodynamics," ASME Paper 98-GT-239.

Garg, V.K., and Abhari, R.S., 1996, "Comparison of Predicted and Experimental Nusselt Number for a Film-Cooled Rotating Blade," ASME Paper 96-GT-223, pp. 1-15.

Giles, M.B., 1988, "Calculation of Unsteady Wake/Rotor Interaction," AIAA Journal of Propulsion and Power,Vol 4, N4, pp. 356-362

Goldstein, B.J., and Echert, E.R.G. , and Ito, 1987, "Film Cooling in a Plane Turbine cascade," Special First Int. Symposium on Transport Phenomena, Honolulu, HI, Apr.28-May 3, pp. 37 - 43.

Gostelow, J.P., and Blunden, A.R., 1989, "Investigations of Boundary Layer Transition in an Adverse Pressure Gradient," *J. of Turbomachinery*, Vol. 111, pp.366-375.

Gostelow, J.P., and Walker, G.J., 1991, "Similarity Behavior in Transitional Boundary Layer Over a Range of Pressure Gradient and Turbulence Levels," *J. of Turbomachinery*, Vol. 112, pp. 198-205.

Gregory-Smith, D.G., 1997, "Secondary and Tip-Clearance Flows in Axial Turbines," "CFD Modelling of Secondary Flows," *von Karman Institute for Fluid Dynamics*, Lecture Series 1997-01.

Gregory-Smith, D.G., et al. 1988, "Turbulence Measurements and Secondary Flows in a Turbine Rotor Cascade," ASME Paper 88-GT-244.

Hall, E.J., and Topp, D.A., and Heidegger, N.J., and Delaney, R. A., 1994, "Investigation of Advanced Counterrotation Blade Configuration Concepts for High Speed Turboprop Systems," NASA Contractor Report 195359, Task 8 -Cooling Flow/Heat Transfer Analysis, Final Report.

Halstead, D.E., Wisler, D.C., Okiishi, T.H., Walker, G. J., Hodson, H. P., and Shin, H-W., 1995, "Boundary Layer Development in Axial Compressors and Turbines" - Part1 and Part4 , *J. of Turbomachinery*, Vol. 119, January, pp 114-140, Part 2, *J. of Turbomachinery*, Vol. 119, April, pp 225-237, Part 3, *J. of Turbomachinery*, Vol. 119, July, pp 426-441

Hathaway, M., "Unsteady Flows in a Single-Stage Transonic Axial Flow Fan Rotor," NASA TM 88929, 1986.

He, L., 1989, "An Euler Solution for Flows Around Oscillating Blades, " ASME Paper 89-GT-279, pp.1-9.

He, P., and Licu, D., Salcudean, M., and Garshore, I.S., 1996, "Leading Edge Film-Cooling: Computations and Experiments Including Density Effects," ASME Paper 96-GT-176, pp. 1 - 11.

Hill, P.G., Schaub, U.W., and Senoo, Y., 1963, "Turbulent Wakes in Pressure Gradients", ASME *Journal of Applied Mechanics*, pp. 518 – 524.

Ho, Y.H. and Lakshminarayana, B., 1994 "Computational Modeling of Three-Dimensional Endwall Flow through a Turbine Rotor Cascade with Strong Secondary Flows," *J.of Tturbomachinery*, Vol 118, No2, p250-261

Ho, Y.H., and Lakshminarayana, B., 1993 , "Computation of Unsteady Viscous Flow through Turbomachinery Blade Row due to Upstream Rotor Wakes", J. of Turbomachinery Vol 117, No1, pp 541-552, October

Hodson, H.P.,1985 "Measurements of Wake Generated Unsteadiness in the Rotor Passages of Axial flow Turbines," *Journal of Engineering for Gas Turbines and Power*, Vol. 107, P. 468, 1985.

Hodson, H.P., and Shin, H-W., 1995, "Boundary Layer Development in Axial Compressors and Turbines Part 1 of 4: Composite Picture," ASME Paper 95-GT-461, International Gas Turbine and Aeroengineering Congress & Exposition Houston, Texas, June- 5-8, pp. 1-16

Huang, P.G., and Xiong, G., 1998, "Transition and Turbulence Modeling of Low Pressure Turbine Flows", AIAA Paper-98-0339, AIAA 36th Aerospace Science Meeting and Exhibit, January 12-15, Reno, Nevada.

Jin, G., and Braza, G. J., 1994, "Two-Equation Turbulence Model for Unsteady Separated Flows Around Airfoils," *AIAA Journal*, Vol. 32, No. 11, pp. 2316 -2317.

Jones, W.P., and Launder, B.E., 1972, "The Prediction of Laminarization with a Two-Equation Model of Turbulence," *Int. J. of Heat and Mass Transfer*, Vol. 15, pp. 301-314.

Joslyn, D., and Dring, R., 1992, "Three-Dimensional Flow in a Axial Turbine: Part 1-Aerodynamic Mechanisms," ASME *J. of Turbomachinery*, Vol. 114, pp.61-70.

Kang, D.J., and Lakshminarayana, B., 1988, "Numerical Prediction of Unsteady Transitional Boundary Layer Caused by Rotor-Stator Interaction," *J. of Propulsion and Power*, Vol. 14, No 6, p. 916, Nov.-Dec.

Kruse, F., 1977, "Investigation of Temperature Distribution Near Film Cooling Airofoils," AGARD CP 229.

Kunz, R., and Lakshminarayana, B., 1992, "Three-dimensional Navier-Stokes Computations of Turbomachinery Flows Using an Explicit Numerical Procedure and a Coupled k-ε Turbulence Model", *J. of Turbomachinery*, Vol.114, pp. 627-642, July.

Lakshminarayana, B., 1970, "Methods of Predicting the Tip Clearance Effects in Axial Flow Turbomachinery," *J. of Basic Engineering*, Sept., pp. 467-482.

Lakshminarayana, B., 1986, "Turbulence Modeling for Complex Shear Flows," *AIAA Journal,* No. 12, pp. 1900 - 1917.

Lakshminarayana, B., 1996, "Fluid Dynamics and Heat Transfer of Turbomachinery", John Wiley & Sons Inc., Chapter 7.

Lakshminarayana, B., Camci, C., Halliwell, I., and Zaccaria, M., 1992, "Investigation of Three-Dimensional Flow Field in a Turbine Including Rotor/Stator Interaction", Part 1: Design, Development and Performance of Turbine Facility, AIAA Paper 92-3325.

Lakshminarayana, B., Chernobrovkin, A., and Ristic, D., 1998, "Experimental and Numerical Study of Unsteady Viscous Flow Due to Rotor Stator Interaction in Turbines. Part 1: Data, Code, and Pressure Field", ASME Paper 98-3595, p. 1-15.

Lam, C.K.G., and Bremhost, K., 1981 "A Modified Form of the k -ε Model for Predicting Wall Turbulence," *Journal of Fluids Engineering*, Vol. 103, September, pp. 456 - 460.

Langston, L.S., Nice, M.L., and Hooper, R.M., 1977, "Three-Dimensional Flow Within a Turbine Blade Passage," ASME *J. of Engineering for Power*, Vol. 99, pp. 21-28.

Launder, B.E., and Spalding, D.E, 1974, "The Numerical Computation of Turbulent Flows" *Computer Methods in Applied Mechanics and Engineering,* Vol. 3, pp. 269-289.

Leylek, J. H., and Zerkle, R. D., 1993, "Discrete-Jet Film Cooling: A Comparison of Computational results with experiments," ASME Paper 93-GT-207, pp. 1- 14.

Luo, J. and Lakshminarayana, B., 1997 "Three-Dimensional Navier-Stokes Analysis of turbine rotor and Tip-Leakage Flow Field", 43rd ASME/IGTI Meeting, ASME Paper 97-GT-42

Margason, R. J.,1993, "Fifty Years Of Jet in Cross Flow Research," AGARD, CP-534, pp. 1-41.

Mayle, R. E., 1991, "The Role of Laminar-Turbulent Transition in Gas Turbine Engines," *J. of Turbomachinery*, Vol. 113, pp. 509-537.

Mayle, R. E., and Paxson, D.E., 1991, "A New Look at Transition," *J. of Fluid Mechanics.*

Melnik, R.E., Siclari, M.J., Marconi, F., Barber, T.J., and Verhoff, A., 1995, "An Overview of a Recent Industry Effort at CFD Code Certification," AIAA Paper 95-2229, June.

Melson, L. D., and .Sanetrik, M. D., and Atkins, H. L., 1994, "Time-accurate Navier-Stokes calculations with multigrid acceleration,." Sixth Copper Mountain Conference on Multigrid methods, Copper Mountain, April, 4-9 1993, pp.423 - 437.

Michelassi, V., Rodi, W., and Gieb, P.-A., 1997, "Experimental and Numerical Investigation of Boundary-Layer and Wake Development in a Transonic Turbine Cascade," ASME Paper 97-GT-483.

Narasimha, R., 1957, "On the Distribution of Intermittency in the Transition Region of a Boundary Layer," J. Aero. Sci., Vol. 24, pp.711-712.

Patel, V. C., Rodi, W., and Scheuerer, G., 1984, "Turbulence Models for Near-Wall and Low Reynolds Number Flows: A Review," *AIAA Journal,* Vol. 23, No. 9, pp. 1308 - 1319.

Pietrzyk, J. R., and Bogard, D.G., and Crawford, M. E., 1990, "Effects of Density Ratio on the Hydrodynamics of Film Cooling," *Journal of Turbomachinery*, Vol. 112, July, pp. 437 - 443.

Qiu, S. and Simon, T. W., 1997, "An Experimental Investigation of Transition as Applied to Low Pressure Turbine Suction Surface Flows," ASME 97-GT-455, ASME Turbo Expo 97, Orlando, Florida, June 1997.

Rai, M.M., 1987, "Navier-Stokes Simulations of Rotor/Stator Interaction Using Patched and Overlaid Grids," *Journal of Propulsion and Power,* Vol. 3, No. 5, pp. 387-396.

Rao, K.V. and Delaney, R.A, "Vane Blade Interaction in a Transonic Turbine," AIAA Papers-92-3323, 3324, Parts 1 and 2, 1992.

Reynolds, B., and Lakshminarayana, B., and Ravindranath, A., 1979, "Characteristics of the Near Wake of a Compressor Rotor," *AIAA Journal*, Vol. 17, pp. 959 - 969.

Ristic, D., Lakshminarayana, B., and Chu, S., 1998, "Three-Dimensional Flow Field Downstream of an Axial Flow Turbine Rotor," AIAA 98-3572.

Rodi, W., 1976, " New Algebraic Relation for Calculation of the Reynolds Stresses," ZAMM Vol. 56, p.219

Savill, A.M., 1992 "Synthesis of T3 Case Prediction," *in Numerical Simulation of Unsteady Flows and Transition to Turbulence*, Cambridge University Press, pp. 404-443.

Savill, A.M., 1997, "COST-ERCOFTAC Transition SIG. Evaluation of Turbulence Models for Predicting Transition in Turbomachinery Flows," Minnowbrook II, Workshop on Boundary Layer Transition in Turbomachines, September 7 – 10.

Schaub, U.W., Vlasic, E., and Moustapha, S.H., 1993, "Effect of Tip Clearance on the Performance of a Highly Loaded Turbine Stage," AGARD-CP-537, "Technology Requirements for Small Gas Turbines," Paper 29, October 1993.

Schmidt, R.C., and Patankar, S.V., 1991, "Simulating Boundary Layer Transition With Low-Reynolds-Number K-ε Turbulence Models: Part 1 - An Evaluation of Prediction Characteristics," *Journal of Turbomachinery*, Vol. 113, January, pp. 1-26.

Schubauer, G.B., and Klebanoff, P.S., 1955, "Contribution to the Mechanism of Boundary-Layer Transition," NACA TN 3489.

Schulz, H.D., Gallus, H.E., and Lakshminarayana, B., 1990, "Three-Dimensional Separated Flow Field in the Endwall Region of an Annual Compressor Cascade in the Presence of Rotor-Stator Interaction," *Journal of Turbomachinery*, Vol. 112, pp. 669-690.

Senoo, Y., and Ishida, M., 1987, "Deterioration of Compressor Performance Due to Tip Clearance of Centrifugal Impellers," *J. of Turbomachinery*, Vol. 109, p.55.

Sgarzi, O., and Leboeuf, F., 1997, "Analysis of Vortices in Three-Dimensional Jets Introduced in a Cross-Flow Boundary-Layer," ASME 97-GT-517, International Gas Turbine and Aeroengine Congress and Exhibition, Orlando, Florida, June 2-5 1997, pp. 1-12.

Shokin, J.I., and Janenko, N.N., 1985, "Method of Differential Approximation in Application to Gas Dynamics," Novosibirsk, "Nayka", pp. 1-365, (In Russian)

Simon, F.F., and Ashpis, D.E., 1996, "Progress in Modeling of Laminar to Turbulent Transition on Turbine Vanes and Blades," *Int. J. of Heat Transfer and Fluid Flow.*

Sjolander, S.A., 1997, "Secondary and Tip-Clearance Flows in Axial Turbines," "Overview of Tip-Clearance Effects in Axial Turbines," *von Karman Institute for Fluid Dynamics*, Lecture Series 1997-01.

Smith, L.H. Jr., 1993, "Wake Ingestion Propulsion Benefit", *Journal of Propulsion and Power*, Vol. 9, No. 1, Jan.-Feb., pp. 74 –82.

Steelant, J., and Dick, E., 1996, "Modeling of the Heat Transfer in Bypass Transitional Boundary Layer Flows," *International Journal for Numerical Methods in Fluids,* Vol. 32, pp.193-220.

Strahle, W. C., Sigman, R. K., and Meyer, W. L., 1987, "Stagnating Turbulent Flows," *AIAA Journal*, Vol. 25, No. 8, pp. 1071 - 1077.

Tekeishi, K., Aoki, S., Sato, T., and Tsukagoshi, K., 1991, "Film Cooling an a Gas Turbine Rotor Blade," ASME Paper 91-GT-291.

Van Zante, D., Adamczyk, J., Strazisar, A., and Okiishi, T., 1997, "Wake Recovery Performance Benefit in a High-Speed Axial Compressor", ASME Paper 97-GT-535.

Venable, B.L., Delaney, R.A., Busby, J.A., Davis, R.L., Dorney, D.J., Dunn, M.G., Haldeman, C.W., and Abhari, R.S., 1998, "Influence of Vane Blade Spacing on Transonic Turbine Stage Aerodynamics, Part 1: Time-Averaged Data and Analysis," ASME Paper 98-GT-481.

Venkateswaran, S., and Merkle, C.L., 1995, "Dual Time Stepping and Preconditioning for Unsteady Computations," AIAA 95-0078, 33th Aerospace Sciences Meeting and Exhibit, January, Reno, NV.

Verdon, J.M., 1989, "The Unsteady aerodynamics response to arbitrary modes of blade motion," *Journal of Fluids and Structures*, pp. 255 - 274.

Vogel D.T., 1996," Navier-Stokes simulation of the Flow Around a Leading Edge Film-Cooled Turbine Blade Including the Interior Cooling System and Comparison With Experimental Data," ASME Paper 96-GT-71, pp. 1 - 12.

Wadia, A.R., and Nealy,D.A., 1985 "Development of a Design Model for Airfoil Leading Edge Film Cooling," ASME Paper 85-GT-120.

Walters, D.K., and Leylek J.H., 1997, "A Detailed Analysis of Film-Cooling Physics. Part 1: Streamwise Injection with Cylindrical Holes," ASME Paper 97-GT-269.

Wang, T., and Hatman, A., 1998, "A Prediction Model for Separated-Flow Transition," ASME Paper 98-GT-237, Gas Turbine Congress and Exhibition, Stockholm, Sweden, June 2-5, 1998.

Wang, Z.J., and Yang, H.Q., 1994 "Unsteady flow simulation using a zonal multi-grid approach with moving boundaries," AIAA-94-0057, 32nd Aerospace Sciences Meeting and Exhibit, January, Reno, NV, pp. 1-11.

Weiss, J.M., and Smith, W.A., 1995, "Preconditioning Applied to Variable and Constant Density Flows," *AIAA Journal*, Vol. 33, No. 11, pp. 2050-2057.

Xiao, X., 1999, "An Experimental Investigation on the Tip Clearance Effects in an Axial Flow Turbine Rotor," (Thesis in preparation).

Yamamoto, A., 1989, "Endwall Flow/Loss Mechanisms in a Linear Turbine Cascade with Blade Tip Clearance," ASME *J. of Turbomachinery*, Vol. 111, pp.264-275.

Zaccaria, M., and Lakshminarayana, B., 1997,b "Unsteady Flow Field Due to the Nozzle Wake Interaction with the Rotor in Axial Turbine.: Part I -Rotor Passage Flow Field," *Journal of Turbomachinery*, Vol. 119, No. 2, pp. 201-224.

Zaccaria, M., and Lakshminarayana, B., 1995 "Investigation of the Three-Dimensional Flow Field at the Exit of a Turbine Nozzle," *AIAA Journal of Propulsion and Power*, Vol. 11, p. 55-63.

Zaccaria, M., and Lakshminarayana, B., 1997,a "An Experimental Investigation of Steady and Unsteady Flow Fields in Axial Flow Turbines," NASACR 4778.

REPORT DOCUMENTATION PAGE

Form Approved
OMB No. 0704-0188

Public reporting burden for this collection of information is estimated to average 1 hour per response, including the time for reviewing instructions, searching existing data sources, gathering and maintaining the data needed, and completing and reviewing the collection of information. Send comments regarding this burden estimate or any other aspect of this collection of information, including suggestions for reducing this burden, to Washington Headquarters Services, Directorate for Information Operations and Reports, 1215 Jefferson Davis Highway, Suite 1204, Arlington, VA 22202-4302, and to the Office of Management and Budget, Paperwork Reduction Project (0704-0188), Washington, DC 20503.

1. AGENCY USE ONLY (*Leave blank*)

2. REPORT DATE
July 1999

3. REPORT TYPE AND DATES COVERED
Final Contractor Report

4. TITLE AND SUBTITLE
Numerical Simulation of Complex Turbomachinery Flows

5. FUNDING NUMBERS
WU-523-26-33-00
NAG3-1736 and
NAG3-2025

6. AUTHOR(S)
A.A. Chernobrovkin and B. Lakshminarayana

7. PERFORMING ORGANIZATION NAME(S) AND ADDRESS(ES)
The Pennsylvania State University
Center for Gas Turbines and Power
153 Hammond Building
University Park, Pennsylvania 16802

8. PERFORMING ORGANIZATION REPORT NUMBER
E-11805

9. SPONSORING/MONITORING AGENCY NAME(S) AND ADDRESS(ES)
National Aeronautics and Space Administration
John H. Glenn Research Center at Lewis Field
Cleveland, Ohio 44135-3191

10. SPONSORING/MONITORING AGENCY REPORT NUMBER
NASA CR—1999-209303
PSU CGTP 9901

11. SUPPLEMENTARY NOTES

Project Managers, R. Boyle, (216) 433-5889, and D. Ashpis, (216) 433-8317, Turbomachinery and Propulsion Systems Division, NASA Glenn Research Center, organization code 5820.

12a. DISTRIBUTION/AVAILABILITY STATEMENT
Unclassified - Unlimited
Subject Categories: 02, 07, and 34 Distribution: Nonstandard

This publication is available from the NASA Center for AeroSpace Information, (301) 621-0390.

12b. DISTRIBUTION CODE

13. ABSTRACT *(Maximum 200 words)*

An unsteady, multiblock, Reynolds Averaged Navier Stokes solver based on Runge-Kutta scheme and Pseudo-time step for turbo-machinery applications was developed. The code was validated and assessed against analytical and experimental data. It was used to study a variety of physical mechanisms of unsteady, three-dimensional, turbulent, transitional, and cooling flows in compressors and turbines. Flow over a cylinder has been used to study effects of numerical aspects on accuracy of prediction of wake decay and transition, and to modify K-ε models. The following simulations has been performed. (a) Unsteady flow in a compressor cascade: Three low Reynolds number turbulence models have been assessed and data compared with Euler/boundary layer predictions. Major flow features associated with wake induced transition were predicted and studied. (b) Nozzle wake-rotor interaction in a turbine: Results compared to LDV data in design and off-design conditions, and cause and effect of unsteady flow in turbine rotors were analyzed. (c) Flow in the low pressure turbine: Assessed capability of the code to predict transitional, attached and separated flows at a wide range of low Reynolds numbers and inlet freestream turbulence intensity. Several turbulence and transition models have been employed and comparisons made to experiments. (d) Leading edge film cooling at compound angle: Comparisons were made with experiments, and the flow physics of the associated vortical structures were studied. (e) Tip leakage flow in a turbine. The physics of the secondary flow in a rotor was studied and sources of loss identified.

14. SUBJECT TERMS
Unsteady flow; Wakes; Turbomachinery; Turbulence; Transition; Separation; CFD; Turbulence modeling; Compressors; Turbines; Low-pressure turbine

15. NUMBER OF PAGES
323

16. PRICE CODE
A14

17. SECURITY CLASSIFICATION OF REPORT	**18. SECURITY CLASSIFICATION OF THIS PAGE**	**19. SECURITY CLASSIFICATION OF ABSTRACT**	**20. LIMITATION OF ABSTRACT**
Unclassified	Unclassified	Unclassified	